

University of Nevada, Reno

**Evaluation of Multi-scale Hyperspectral Reflectance and Emittance Image Data for Remote Mineral Mapping in Northeastern Death Valley National Park, California and Oasis Valley, Nevada**

A dissertation submitted in partial fulfillment of the requirements for the degree of Doctor of Philosophy in Geophysics

by

Zan Aslett

Dr. James V. Taranik/Dissertation Advisor

May, 2010

© Copyright 2010

Zan Aslett



THE GRADUATE SCHOOL

We recommend that the dissertation  
prepared under our supervision by

**ZAN ASLETT**

entitled

**Evaluation of Multi-scale Hyperspectral Reflectance and Emittance Image Data for  
Remote Mineral Mapping in Northeastern Death Valley National Park, California  
and Oasis Valley, Nevada**

be accepted in partial fulfillment of the  
requirements for the degree of

**DOCTOR OF PHILOSOPHY**

James V. Taranik, Ph.D., Advisor

Wendy M. Calvin, Ph.D., Committee Member

James R. Carr, Ph.D., Committee Member

Donald E. Sabol, Ph.D., Committee Member

Paul F. Starrs, Ph.D., Graduate School Representative

Marsha H. Read, Ph. D., Associate Dean, Graduate School

May, 2010

## Abstract

This dissertation focuses upon the analyses of hyperspectral reflectance and thermal emission image data to remotely detect and map surficial mineralogy in an arid environment in southern Nevada and southeastern California. It includes four manuscripts prepared for submission to peer-reviewed journals, which are presented as single chapters. The research involves the use of longwave-infrared (LWIR) hyper- and multi-spectral measurements made from ground, aerial, and spaceborne perspectives of sedimentary and meta-sedimentary geologic units in northeastern Death Valley National Park, California and both shortwave-infrared (SWIR) and LWIR hyperspectral measurements in an area of diverse Paleozoic and Tertiary geology in Oasis Valley, Nevada.

In Chapter 1, a brief overview of the dissertation is provided, including background on reflected and thermal-infrared mineral spectroscopy; remote sensing; the impacts of spatial and spectral resolution upon the ability to detect, identify, and map minerals using remote sensing image data; and the use of combined reflectance and emittance image data to better map minerals. In Chapter 2, ground-based SEBASS LWIR hyperspectral image data is analyzed in order to determine the utility of very high resolution remotely-sensed emittance measurements to delineate late-Proterozoic and Paleozoic sedimentary lithologies of an outcrop at Hell's Gate, Death Valley. In Chapter 3, airborne SEBASS image data over Boundary Canyon are analyzed in conjunction with moderate-scale geologic maps and laboratory measurements to map minerals associated with sedimentary and meta-sedimentary rocks and important in recognizing a detachment

fault structure, as well as metamorphic facies. In Chapter 4, ground-based and aerial SEBASS, aerial MASTER, and spaceborne ASTER emittance measurements are compared over two study sites to determine what repercussions viewing perspective and spatial, spectral, and radiometric resolutions have upon remote identification and mapping of minerals associated with the Boundary Canyon detachment fault. In Chapter 5, a comparison of reflectance and emittance hyperspectral measurements made over Oasis Valley is used to determine whether certain minerals are optimally detected, identified, and mapped within a certain wavelength range. In Chapter 6, the presented research is summarized, repercussions of the results are analyzed, and future research possibilities are suggested.

The research was successful in presenting: 1) new uses of imaging spectrometer data, 2) identifying mineralogic indicators of detachment faulting in the Boundary Canyon study area, 3) scale-based limitations upon detection of these mineral components associated with detachment faulting, and 4) limitations upon identifying particular minerals in specific wavelength segments, thereby constraining expectations of future VNIR/SWIR and LWIR image data mineral mapping surveys.

## Dedication

I want to dedicate this dissertation to my Grandpa, Zan Gene Aslett, who passed in the Spring of 2010 to cancer. He was as unique and likeable a character as I have met in my life (and others will say the same). A combination of impeccable class, undeniable charm, gut-wrenching humor, and roughneck sensibility, he spent his working life constructing many of the highways and roads found today throughout Idaho, Montana and Nevada. He loved flying his Cessna, restoring really awesome cars (ahem, 1940 Packard) and was probably the oldest guy out there riding a motorcycle. I left many games of quarters with emptier pockets, but they were well worth it to hear his play-by-play comments (“Well fellers, it looks like a crooked deal”, or “oh really?!”).

You are missed.

## Acknowledgements

I would like to thank Dr. James Taranik for his tremendous support, guidance, and “big picture” perspective throughout my time in the doctoral program. He was instrumental in focusing my efforts so that I could successfully gain from graduate school what I was looking for. Dr. Wendy Calvin’s tutelage helped me to develop a more proficient understanding of mineral spectroscopy and spectral remote sensing. Dr. Gary Oppliger invested a significant amount of his time teaching me the fundamentals and applications of geophysics, and I am grateful for that. I also thank Drs. Jim Carr, Don Sabol, and Paul Starrs for their respective help.

Thanks to Ingrid Ramos, Erika Waday, and Melodie Gander for making everything run smoothly for the graduate students, whether keeping supplies on hand, helping make field vehicles magically appear, or trading jokes. Dean Riley from The Aerospace Corporation was instrumental in coordinating and acquiring image data in my field area. Mark Landers and the SpecTIR Corporation also provided the ABLE laboratory with data sets and me with on-the-job learning experience. Mario Desilets took time out of his schedule to instruct me on XRD analysis. Your support has been much appreciated!

A big shout-out to ABLE lab and SpecTIR friends: AJ Markow, Andy Rael, George Yoshinaga, Chris Kratt, Shane Thompson, Jeff Shoffner, Laura Huebner, Jill Pocock, Niti Mankhemthong, and Todd Morken. Thanks guys and gals. It was fun... mostly. Ha!

Research funding for data acquisition, field surveys, and my stipend was provided by the Department of Energy. I sincerely appreciate this investment by DOE in my education and training, without which I would have not been able to complete the degree. Specific thanks to John DiBenedetto of the Special Technologies Laboratory and both Herb Fry and Kevin Mitchell at Los Alamos National Laboratory for providing learning experiences within their respective research groups.

A big thanks to Mary Conger for her encouragement and being an enthusiastic field assistant.

Lastly, thanks to my family for getting me to this point (the lives of gypsies aren't easy, but hey we're doing alright), general support (thanks for the cookies, Mom), and gentle reminders - "what the heck are you still doing in school?!"



## Table of Contents

<b>Chapter 1</b> .....	1
General Introduction .....	1
1.1 Overview of the dissertation .....	2
1.2 Thermal-infrared remote sensing in Boundary Canyon, Death Valley, California .....	2
1.3 Comparison of reflectance and emittance remote sensing in Oasis Valley, Nevada.....	4
1.4 Research questions.....	6
1.5 Conclusion .....	7
1.6 References.....	8
 <b>Chapter 2</b> .....	 12
Ground-based remote sensing of Precambrian-Cambrian lithologies at Hell’s Gate, Death Valley National Park, CA, USA, using SEBASS thermal-infrared hyperspectral image data .....	12
2.1 Abstract .....	13
2.2 Introduction.....	14
2.3 Background.....	15
2.4 Geologic background and area of study.....	18
2.5 Methods.....	21
2.6 Image data processing.....	27
2.7 Results.....	31
2.8 Discussion and summary .....	37
2.9 Conclusion .....	42
2.10 Acknowledgements.....	44
2.11 References.....	45
 <b>Chapter 3</b> .....	 74
Mapping rock-forming minerals at Boundary Canyon, Death Valley National Park, CA, USA using aerial SEBASS thermal-infrared hyperspectral image data.....	74
3.1 Abstract .....	75
3.2 Introduction.....	76
3.3 Background.....	78
3.4 Area of study.....	80
3.5 Methodology .....	82
3.6 Results.....	88
3.7 Discussion .....	94
3.8 Conclusion .....	100
3.9 Acknowledgements.....	102
3.10 References.....	104

<b>Chapter 4</b> .....	128
Multi-scale Comparison of Mineral Emittance Measurements using Ground, Aerial, and Spaceborne Image Data in Northeastern Death Valley National Park, California, USA .....	128
4.1 Abstract .....	129
4.2 Introduction .....	130
4.3 Background .....	132
4.4 Area of study .....	137
4.5 Methods .....	139
4.6 Image data acquisition and calibration .....	141
4.7 Results .....	146
4.7 Discussion and summary .....	152
4.9 Acknowledgements .....	158
4.10 References .....	159
<b>Chapter 5</b> .....	189
Multi-wavelength mineral mapping in Oasis Valley, Nevada using ProSpecTIR V-S reflectance and SEBASS emittance hyperspectral image data .....	189
5.1 Abstract .....	190
5.2 Introduction .....	191
5.3 Previous work .....	194
5.4 Data and instrumentation .....	196
5.5 Image data calibration .....	200
5.6 Data processing methodologies .....	201
5.7 SWIR image data results .....	204
5.8 LWIR image data results .....	207
5.9 Mapping small instances of minerals in a hot spring area .....	210
5.10 Discussion .....	211
5.11 Comparisons of SWIR and LWIR mineral map results .....	212
5.12 Resolving ambiguity in mineral spectra interpretation .....	219
5.13 Comprehensive mineral mapping .....	219
5.14 Conclusion .....	220
5.15 Acknowledgements .....	222
5.16 References .....	223
<b>Chapter 6</b> .....	251
Conclusions .....	251
6.1 Important aspects of the research .....	251
6.2 Brief review of case studies .....	253
6.3 Implications of research .....	258
6.4 Recommendations and conclusion .....	260
<b>Chapter 7</b> .....	263
Appendices .....	263

<b>Appendix I.</b> Mineral chemical formulas .....	264
<b>Appendix II.</b> Mineral spectra used from public spectral libraries .....	265
<b>Appendix III.</b> National Park Service work permit .....	266
<b>Appendix IV.</b> Image data and rock sample information: Hell’s Gate .....	267
<b>Appendix V.</b> Image data and rock sample information: schist outcrop.....	283
<b>Appendix VI.</b> Image data and rock sample information: Boundary Canyon .....	291
<b>Appendix VII.</b> Image data and rock sample information: Oasis Valley .....	306

## List of Tables

### Chapter 2

Table 1. Transect 1 rock descriptions and mineral constituents .....	54
Table 2. Transect 2 rock descriptions and mineral constituents .....	55
Table 3. Local area rock descriptions and mineral constituents .....	56
Table 4. Image data classification matrix .....	57

### Chapter 3

Table 1. Geological units with name, age, lithology, and description.....	111
Table 2. Minerals associated with local lithologies .....	112
Table 3. Rock samples gathered during field survey of scene one.....	113
Table 4. Rock samples gathered during field survey of scene two.....	114
Table 5. Rock samples gathered during field survey of scene three.....	115

### Chapter 4

Table 1. Instrument, sensor, and image data specifications.....	167
Table 2. Geologic units, associated ages, and descriptions .....	168
Table 3. Rock samples gathered in study site one .....	169
Table 4. Rock samples gathered in study site two .....	170
Table 5. Ground and aerial data quartz classification information.....	171

### Chapter 5

Table 1. Sensor specifications.....	231
Table 2. Data acquisition parameters.....	231
Table 3. Number of pixels classified for each mineral per segment.....	231

## List of Figures

### Chapter 2

Figure 1. Location map .....	58
Figure 2. Outcrop photograph.....	59
Figure 3. Rock photographs.....	60
Figure 4. Transect 1 photograph, map, ASD, and Nicolet measurements.....	61
Figure 5. Transect 2 photograph, map, ASD, and Nicolet measurements.....	62
Figure 6. Quartz emissivity spectra comparison.....	63
Figure 7. SEBASS image data endmember spectra.....	64
Figure 8. Temperature data histogram plot.....	65
Figure 9. Laboratory emissivity spectra analysis of argillite.....	66
Figure 10. Transect 1 photograph and DCS comparison.....	67
Figure 11. Transect 1 mineral classification map .....	68
Figure 12. Transect 2 photograph and DCS comparison.....	69
Figure 13. Transect 2 mineral classification map .....	70
Figure 14. SAM rule classification images for each mineral.....	71
Figure 15. Comprehensive mineral classification map for the outcrop .....	72
Figure 16. Minimum/average/maximum emissivity values for endmembers .....	73

### Chapter 3

Figure 1. Location map (state boundaries) .....	116
Figure 2. Location map (local area).....	117
Figure 3. Geology map .....	118
Figure 4. Laboratory-derived emissivity spectra of local rocks .....	119
Figure 5. Image data decorrelation stretch.....	120
Figure 6. SEBASS image data endmember spectra.....	121
Figure 7. Scene one image data classification .....	122
Figure 8. Scene two image data classification.....	123
Figure 9. Scene three image data classification .....	124
Figure 10. BCDF geology and image data map comparison.....	125
Figure 11. Transverse fault geology and image data map comparison.....	126
Figure 12. Death Valley Buttes geology and image data map comparison .....	127

### Chapter 4

Figure 1. Location map (state boundaries) .....	172
Figure 2. Location map (local area).....	173
Figure 3. Geology map .....	174
Figure 4. Ground instantaneous field of view comparison.....	175
Figure 5. Radiance and emissivity spectra comparison for multiple sensors .....	176
Figure 6. Variability of emissivity for pelitic schist .....	177

Figure 7. Resampling of hyperspectral emissivity spectra .....	179
Figure 8. Difference between ground and aerial radiance spectra.....	180
Figure 9. SAM quartz classification comparison: ground data.....	181
Figure 10. SAM quartz classification comparison: aerial data.....	182
Figure 11. Resampled spectra for each rock class .....	183
Figure 12. Multi-resolution image data classifications – site 1 .....	185
Figure 13. Multi-resolution image data classifications – site 2 .....	187
Figure 14. MASTER amphibolite map.....	189

## Chapter 5

Figure 1. Photograph of ProSpecTIR V-S and SEBASS sensors.....	232
Figure 2. Location map (local area).....	233
Figure 3. Geology map .....	234
Figure 4. Color band combination image: ProSpecTIR V-S .....	235
Figure 5. SWIR and LWIR image data endmember spectra .....	236
Figure 6. Comprehensive SWIR mineral map.....	237
Figure 7. Scene 1 mineral map .....	238
Figure 8. Scene 2 mineral map .....	239
Figure 9. Scene 3 mineral map .....	240
Figure 10. Scene 4 mineral map .....	241
Figure 11. Color band combination image: SEBASS.....	242
Figure 12. Comprehensive LWIR mineral map.....	243
Figure 13. SWIR and LWIR comparison: hot spring area.....	244
Figure 14. SWIR and LWIR comparison: evaporite area 1.....	246
Figure 15. SWIR and LWIR comparison: evaporite area 2.....	247
Figure 16. SWIR and LWIR comparison: evaporite area 3.....	248
Figure 17. LWIR mineral spectra ambiguity .....	249
Figure 18. Combined SWIR and LWIR mineral map results: alteration area.....	250

## Chapter 1. General Introduction

Remote sensing is the study or act of measuring and interpreting information that is derived from indirect contact with an object or material (Jensen, 1996). In this dissertation, remote sensing refers to the measurement of electromagnetic (EM) energy in the form of photons that are reflected or emitted by surface materials. Imaging spectrometers measure this energy in discrete wavelength bands to analyze wavelength-dependent variations diagnostic of particular materials throughout the EM spectrum, from approximately 0.4 - 14  $\mu\text{m}$ . These variations in EM radiation can be related to specific mineral constituents of rocks, soils, and other cover types, thereby facilitating remote detection and potential mapping of surfaces (Clark, 1999).

EM energy is radiated by the sun in a wavelength range and intensity modeled by a 6000 K blackbody curve. Within certain atmospheric transmission windows, including: the shorter visible (VIS) from 350 - 750 nm, near-infrared (NIR) from 750 - 1400 nm, and shortwave-infrared (SWIR) from 1400 - 2500 nm, this energy is partially absorbed. These absorptions activate particular electronic and vibrational molecular processes and lead to the emission of photons in a wavelength range and intensity modeled by the blackbody curve of an approximately-300 K earth surface. These measurable regions include the midwave-infrared (MWIR) from 3 - 5  $\mu\text{m}$ , and the longwave-infrared (LWIR) from 7 - 14  $\mu\text{m}$  (Elachi, 1987). This dissertation focuses on the analysis of measured variation in reflectance and emittance spectra to infer the surficial presence of minerals. Once unique mineral-related spectra have been detected and identified during analysis of imaging spectrometer data, the distribution of surficial mineralogy can be mapped.

## **1.1 Overview of the dissertation**

The dissertation is formatted using the manuscript option, which entails the compilation and submission of research papers to peer-reviewed journals. The doctoral research was conducted in a sequential manner such that each of four studies would comprise individual chapters of the dissertation.

The presented research initially focuses on the use of TIR hyperspectral image data to map sedimentary and meta-sedimentary lithologies in the northeastern Death Valley National Park, California, USA. These data were acquired from ground, aerial, and spaceborne perspectives and used in three separate case studies to investigate the surficial mineralogy of a small study area within Boundary Canyon.

In the final case study, reflectance and emittance image data collected over Oasis Valley, Nevada are compared to determine optimal wavelength ranges with which to detect, identify, and map silicate, clay, carbonate, and sulfate minerals.

## **1.2 Thermal-infrared remote sensing in Boundary Canyon, Death Valley, California**

The primary objective of the dissertation research was to focus on the mapping and interpretation of minerals associated with sedimentary and meta-sedimentary lithologies in the Boundary Canyon area of northeastern Death Valley using ground, aerial, and spaceborne LWIR hyperspectral image data measurements<sup>1</sup>. The dissertation research utilizes older Spatially Enhanced Broadband Array Spectrograph (SEBASS) (Hackwell et al., 1995) image data provided by The Aerospace Corporation. These

---

<sup>1</sup> Field work in Death Valley was conducted with permission from the National Park Service via research permit DEVA-00207.



included ground-based image data measurements acquired in northeastern Death Valley during the spring of 1998 that had not yet been researched for geologic applications. Newer aerial SEBASS image data were then collected in the summer of 2007 that coincided with the location of these previous ground data, and allowed direct comparison of respective measurements to be made.

The research began with analysis of these ground-scanned image data to map minerals associated with sedimentary and meta-sedimentary lithologies in Boundary Canyon, and continued with analysis of aerial data covering the area at high spatial resolution. Image data measurements synthesized from additional emittance-measuring instruments, MODIS/ASTER Airborne Simulator (MASTER) (Hook et al., 2001) and Advanced Spaceborne Thermal Emission and Reflection Radiometer (ASTER) (Abrams et al., 1999), helped determine what repercussions lower spatial, spectral, and radiometric resolutions held for mapping minerals in this particular geological environment. Characteristics of these imaging systems can be found in Appendix 1.

The Death Valley National Park region is representative of Basin and Range geologic structure (NPS, 2010). Boundary Canyon, which dissects the Grapevine and Funeral Mountain ranges of northeastern Death Valley, was chosen as an area of study due to its high diversity of sedimentary and meta-sedimentary rock exposures within a small area (Hoisch and Simpson, 1993). Such rocks are found to either side of the Boundary Canyon detachment fault (BCDF), a low-angle normal fault that has exposed the metamorphic core complex of the Funeral Mountains (Applegate et al., 1992). Previous geological and geochemical studies of the BCDF have resulted in a thorough understanding of the mineralogical composition of the exposed rocks here, as well as the

relationship between particular metamorphic mineral constituents of rocks and depth of formation (Labotka et al., 1980; Reynolds et al., 1986; Hoisch and Simpson, 1993).

Extensive geologic mapping has been conducted throughout the study area, including 1:96,000 (Hunt and Mabey, 1966); 1:48,000 (Wright and Troxel, 1993); and 1:250,000 scales (Workman et al., 2002), thereby providing contextual information with which to interpret remote sensing data results.

### **1.3 Comparison of reflectance and emittance remote sensing in Oasis Valley, Nevada**

The secondary objective of the research was to examine simultaneously-acquired VNIR/SWIR and LWIR hyperspectral image data to remotely detect, identify, and map specific minerals in Oasis Valley, Nevada. Oasis Valley is a fault-controlled basin in southern Nevada that features a diverse geological environment dominated by Tertiary volcanics, Mesozoic acid-sulfate alteration, and Paleozoic sedimentary units (Carr et al., 1996; Workman et al., 2002; Mankinen et al., 2003; Fridrich et al., 2007). The fault-bounded valley results in structural control and redistribution of meteoric waters, which yield more than 80 hot springs in the local area (Reiner et al., 2002). The area also hosts numerous inactive precious metal mines that have exploited epithermal mineralization and sulfide ore deposits (Eng et al., 1996). As a result, a wide variety of silicate, sulfate, carbonate, and secondary clay minerals are surficially expressed in the area, making it an ideal location for comparisons between remotely-sensed reflectance and emittance measurements.

SEBASS and ProSpecTIR VS (SpecTIR LLC, 2009) sensors were used as sources of image data for the research. The topic of optimal wavelength range for remote mineral detection and mapping has been presented in previous literature (Clark, 1999; Cudahy et al., 2001; Kruse, 2002; Vaughan et al., 2005; Chen et al., 2007; Kirkland et al., 2007). However, research in this topic area has been limited due to a scarcity of simultaneously-acquired reflectance and emittance data with similar ground instantaneous field of view (GIFOV) and high spectral resolution. Simultaneous acquisition of image data is important because differences in atmospheric or environmental conditions (e.g., surface moisture) between times of separate collections can limit the efficacy of directly compared image data measurements. As both high spatial and spectral resolution reflectance and emittance remote sensing data sets become more available to the scientific community, it will become increasingly important to know what type of data set is optimal for mapping specific minerals.

## 1.4 Research questions

Research questions for the first three case studies were formulated to meet two goals: 1) establishing surficial mineralogy for each area of study, and 2) exploring the geologic importance of the determined mineral distributions. For the final case study, the over-arching goal was to enhance knowledge of the comparative capabilities and optimal uses of both reflectance and emittance image data. Specific research questions for each of the four case studies comprising the dissertation are presented below:

Case Study 1. Identification of sedimentary lithologies of the Wood Canyon and Stirling Quartzite formations at Hell's Gate, Death Valley National Park using ground-based remote sensing data:

What minerals can be remotely identified and mapped at close distance to a Precambrian-Cambrian outcrop, and of what lithologies are these minerals representative? Are certain lithologies more difficult to delineate than others? What effect does background sky in the field of view have upon emissivity spectra?

Case Study 2. Characterization of sedimentary and meta-sedimentary lithologies in the Boundary Canyon detachment fault zone of Death Valley National Park:

What minerals are expressed in the unmetamorphosed miogeoclinal and metamorphic core complex contact zone of the Grapevine and Funeral Mountains? With what lithologies are these minerals associated? Can sedimentary and meta-sedimentary counterparts be mineralogically and remotely distinguished?

Can minerals associated with meta-sedimentary lithologies be identified and mapped in order to remotely establish metamorphic facies?

Case Study 3. Multi-scale comparison of emittance image data measurements of rocks in Boundary Canyon:

What minerals can be detected and mapped using multispectral emittance image data of lower spatial, spectral, and radiometric resolutions? Can mineralogic indicators of the BCDF contact zone be identified? What differences in emittance measurements are observed between ground and aerial hyperspectral image, and what are the spatial and spectral repercussions for these distinct imaging perspectives for mineral mapping?

Case Study 4: Comparison of reflectance and emittance measurements over Oasis Valley, Nevada:

What minerals are detectable in both the SWIR and LWIR wavelength ranges in Oasis Valley? Which wavelength ranges are better suited for identification of clay, sulfate, carbonate, and silicate minerals in the study area? Are the SWIR and LWIR complementary for mineral mapping?

## **1.5 Conclusion**

The dissertation is concluded in Chapter 6 and provides a summary of the research questions, methods, and results; comprehensive synthesis of the conclusions for the respective case studies; and recommendations for potential future research prospects.

## 1.6 References

- Abrams, M.J. (2000). The Advanced Spaceborne Thermal Emission and Reflection Radiometer (ASTER): Data Products for the High Resolution Imager on NASA's Terra Platform. *International Journal of Remote Sensing*, 21 (5), pp. 847-859.
- Applegate, J.D.R., Walker, J.D., and Hodges, K.V. (1992). Late Cretaceous extensional unroofing in the Funeral Mountains metamorphic core complex, California. *Geology*, 20 (6), pp. 519-522.
- Carr, M.D., Sawyer, D.A., Nimz, K., Maldonado, F., and Swadley, W.C. (1996). Digital Bedrock Geologic Map Database of the Beatty 30 X 60-Minute Quadrangle, Nevada and California: U.S. Geological Survey Open-File Report 96-291.
- Chen, X., Warner, T.A., and Campagna, D.J. (2007). Integrating visible, near-infrared and short-wave infrared hyperspectral and multispectral thermal imagery for geological mapping at Cuprite, Nevada. *Remote Sensing of Environment* 110 (3), pp. 344-356.
- Clark, R.N. (1999). Spectroscopy and Principles of Spectroscopy, *Manual of Remote Sensing*, A. Rencz, Editor, John Wiley and Sons, Inc.
- Cudahy, T.J., Wilson, J., Hewson, R.D., Okada, K., Linton, P., Harris, P., Sears, M., and Hackwell, J.A. (2001). Mapping variations in plagioclase feldspar mineralogy using airborne hyperspectral VNIR-SWIR-TIR imaging data. In: *Proceedings of Geoscience and Remote Sensing Symposium*. IEEE 2001 International Conference on Geoscience and Remote Sensing, Sydney, Australia.
- Elachi, C. (1987). *Introduction to the physics and techniques of remote sensing*. Wiley,

New York, pp. 413.

- Eng, T., Boden, D.R., Reischman, M.R., and Biggs, J.O. (1996). Geology and mineralization of the Bullfrog Mine and vicinity, Nye County, Nevada. In: *Geology and Ore deposits of the American Cordillera: Geological Society of Nevada Symposium Proceedings*, A.R. Coyner, and P.L. Fahey, editors, pp. 353-402.
- Fridrich, C.J., Minor, S.A., Slate, J.L, and Mankinen, E.A. (1999). Geologic evaluation of the Oasis Valley basin, Nye County, Nevada. *United States Geological Survey Open-File Report 99-533-A*.
- National Park Service (2010). Geologic formations of Death Valley National Park, *United States National Park Service web site*.  
<http://www.nps.gov/deva/naturescience/geologicformations.htm>.
- Hackwell, J.A., Warren, D.W., Bongiovi, R.P., Hansel, S.J., Hayhurst, T.L., Mabry, D.J., Sivjee, M.G., and Skinner, J.W. (1996). LWIR/MWIR imaging hyperspectral sensor for airborne and ground-based remote sensing, *The International Society for Optical Engineering (SPIE)*, 2819, pp. 102-107.
- Hoisch, T.D. and Simpson, C. (1993). Rise and tilt of metamorphic rocks in the lower plate of a detachment fault in the Funeral Mountains, Death Valley, California. *Journal of Geophysical Research*, 98, pp. 6805-6827.
- Hook, S.J., Myers, J.J., Thome, K.J., Fitzgerald, M., and Kahle, A.B. (2001). The MODIS/ASTER airborne simulator (MASTER) – a new instrument for earth science studies. *Remote Sensing of Environment*, 76, pp. 93-102.
- Hunt, C.B., and Mabey, D.R. (1966). General geology of Death Valley, California. *United States Geological Survey Professional Paper 494-A*.

- Jensen, J.R. (1996). *Introductory Digital Image Processing: A Remote Sensing Perspective*. 2<sup>nd</sup> edition, Prentice-Hall, New York, 318 pp.
- Kirkland, L.E., Herr, K.C., and Adams, P.M. (2007). Straightforward results from a Mars analog site (Alunite, Nevada): Learning to combine near- and thermal-infrared spectral interpretations for Mars. *Proceedings of the 38th Lunar and Planetary Science Conference*, 2232, pp. 2.
- Kruse, F. A. (2002). Combined SWIR and LWIR Mineral Mapping Using MASTER/ASTER. In: *Proceedings of Geoscience and Remote Sensing Symposium*. IEEE 2002 International Conference on Geoscience and Remote Sensing, Toronto, Canada, pp. 3.
- Labotka, T.C. (1980). Petrology of a medium-pressure regional metamorphic terrane, Funeral Mountains, California. *American Mineralogist*, 65 (7-8), pp. 670-689.
- Mankinen, E.A., Hildenbrand, T.G., McKee, E.H., and Schenkel, C.J. (2003). Geophysical setting of the Pahute Mesa-Oasis Valley region of southern Nevada. *Nevada Bureau of Mines and Geology*, Report 50, pp. 45.
- Reiner, S.R., Lacznik, R.J., Demeo, G.A., Smith, J.L., Elliott, P.E., Nylund, W.E., and Fridrich, C.J. (2002). Ground-water Discharge Determined from Measurements of Evapotranspiration, Other Available Hydrologic Components, and Shallow Water-Level Changes, Oasis Valley, Nye County, Nevada. *USGS Water-Resources Investigations Report* 01-4239.
- Reynolds, M.W., Wright, L.A., and Troxel, B.W. (1986). Geology and chronology of late Cenozoic detachment faulting, Funeral and Grapevine Mountains, Death Valley, California. *Geological Society of America abstracts with Programs*, 18 (2), p. 175.



- Vaughan, R.G., Hook, S.J., Calvin, W.M., and Taranik, J.V. (2005). Surface mineral mapping at Steamboat Springs, Nevada, USA, with multi-wavelength thermal infrared images. *Remote Sensing of Environment*, 99, pp. 140-158.
- Workman, J.B., Menges, C.M., Page, W.R., Taylor, E.M., Ekren, E.B., Rowley, P.D., Dixon, G.L., Thompson, R.A., and Wright, L.A. (2002). Geologic Map of the Death Valley Ground-Water Model Area, Nevada and California. *USGS Misc. Field Studies Map MF-2381-A*.
- Wright, L.A., and Troxel, B.W., (1993). Geologic map of the central and northern Funeral Mountains and adjacent areas, Death Valley region, southern California. *US Geological Survey Misc. Invest. Series Map I-2305*.

## Chapter 2

### **Ground-based remote sensing of Precambrian-Cambrian lithologies at Hell's Gate, Death Valley National Park, CA, USA, using SEBASS thermal-infrared hyperspectral image data**

Zan Aslett

Mackay School of Earth Sciences and Engineering, University of Nevada, Reno

\* Based on a manuscript to be submitted to Remote Sensing of Environment

## 2.1 Abstract

Hyperspectral image data collected from The Aerospace Corporation's ground-based Spatially Enhanced Broadband Array Spectrograph System (SEBASS) were investigated to remotely identify the mineralogy of lightly metamorphosed sedimentary lithologies. SEBASS is an imaging spectrometer that measures electromagnetic energy in two wavelength regions ranging from approximately 2.5- to 5.5-  $\mu\text{m}$  in the midwave infrared (MWIR) and 7.5- to 13.5-  $\mu\text{m}$  in the longwave infrared (LWIR) segments of the electromagnetic spectrum. Three individual image data scans were acquired at a ground instantaneous field of view (GIFOV) ranging from an estimated 0.16 – 2 m at Hell's Gate, Death Valley National Park, an outcropping sequence of folded quartzite, argillite, and dolomite beds that transition from the late Precambrian upper Stirling Quartzite to the Cambrian lower Wood Canyon formation. LWIR image data are sensitive to vibrational emission minima diagnostic of silicate, phyllosilicate and carbonate minerals, which comprise the bulk mineralogy of the lithologies found in the study area. The radiance image data were atmospherically-corrected using an in-scene atmospheric correction (ISAC) routine, however remnant ozone ( $\text{O}_3$ ) were observed in some image data spectra. Temperature-emissivity separation (T $\epsilon$ S) was used to produce emissivity image data that were then continuum removed to yield spectra comparable to that of laboratory measurements. Two transects were made across the outcrop in order to sample and characterize the respective lithologies. Reflectance and emissivity measurements of these samples were then made in the laboratory in order to validate the image data spectra. Hyperspectral data processing included dimensionality reduction, identification of statistically unique endmembers, and mineral mapping using spectral classification

algorithms. Classification of the image data resulted in mapping of four lithologies based upon their respective dominant mineralogy. Low mineral spectral contrast resulting from shadowing, unconsolidated surface cover, vegetative cover and sub-pixel bed sizes prevented mineral identification of every scene pixel. Spectral uniqueness of rocks, adequate exposure of rock in relation to the sensor-to-target geometry, and bed thickness equal to or larger than the data GIFOV generally resulted in high confidence identification of mineral spectra. Ground-based mapping of minerals associated with sedimentary lithologies was shown to be successful using SEBASS image data.

## **2.2 Introduction**

Ground-based imaging spectrometers have seen limited use in mineral identification studies compared to airborne and spaceborne remote sensing surveys. The differences in scale and spatial extent between these distinct modes of observation often preclude the former due to the increased time or cost involved for an effectively smaller surface area of measurement (Jensen, 2007). Instead, discrete field-based in-situ radiometric measurements and ancillary analyses are commonly used for comparison and corroboration of air- or space-borne remotely sensed measurements (Milton et al., 2009). However, limitations imposed upon traditional remote sensing data in terms of the spatial, spectral and radiometric resolution suggest that ground-based image data may have utility when high spatial resolution is required for particular geologic applications (Kruse, 2000).

There exist notable examples of practical geological studies that utilize ground-based imaging spectroscopy. These include measurement of the Martian surface using the miniature thermal emission spectrometer (Christensen et al., 2003); enhanced interpretation of paleoseismic exposures within trench emplacements using visible, near infrared (VNIR) and shortwave infrared (SWIR) reflectance image data (Ragona et al., 2006); mineralogical and structural interpretation of an outcrop using coupled light detection and ranging (LiDAR) and reflectance image data (Buckley et al., 2007); and use of reflectance image data to detect and monitor slope failure in an open pit mine setting (McHugh et al., 2000).

## **2.3 Background**

### 2.3.1 Thermal infrared spectra

The thermal infrared (TIR) region of the electromagnetic spectrum has been used to characterize the crystalline nature of pure mineral samples since the 1950s. The characteristics of fundamental and overtone vibrational-induced emission spectra for most common minerals have been established by numerous laboratory measurements (Hunt and Salisbury, 1970; Farmer, 1974; Salisbury and D'Aria, 1992; Salisbury and Wald, 1992, Christensen et al., 2000). Following the spectral characterization of pure minerals, research focused on the effects of mineral mixtures (Thomson and Salisbury, 1993). This benefited the interpretation of radiometric measurements made in field and remote mineral identification studies (Horton et al., 1998; Johnson, 1998).

Fundamental vibrational bending and stretching modes of molecules occur in the TIR portion of the electromagnetic spectrum, which produce emission minima (Lyon and Green, 1975). Diagnostic reststrahlen bands within the range of measured emission spectra facilitate the identification of particular minerals. These emission minima are related to mineral crystal structure, and result in diagnostic spectra for mineral groups such as silicates ( $\text{SiO}_4$ ), and carbonates ( $\text{CO}_3$ ). Collectively these minerals form a large proportion of rocks observable at the surface of the earth. Image data that can resolve emission spectra in the LWIR wavelength range are thus applicable for mapping major rock types. SEBASS is a sensor that remotely measures both MWIR and LWIR thermal emission spectra. The LWIR image data were analyzed in order to identify mineral signatures emitted from a studied outcrop.

### 2.3.2 Remote sensing measurements and applications

Multi-band TIR scanning with the Thermal Infrared Multispectral Scanner (TIMS) sensor provided the first widely utilized TIR data sets for analysis (Kahle and Goetz, 1983). SEBASS (Hackwell et al., 1996) and the Airborne Hyperspectral Imager (AHI) (Lucey et al., 1998) collectively formed the first generation of hyperspectral TIR sensors capable of making measurements across 100 or more discrete bands. Fourier transform infrared (FTIR) instruments were developed to facilitate field-based TIR measurements and to corroborate image data measurements (Korb et al., 1996). The MODIS/ASTER airborne simulator (MASTER), a multispectral sensor, was developed to make both reflectance and emittance measurements, as well as validate the Advanced Spaceborne Thermal Emission and Reflection Radiometer (ASTER) spaceborne

instrument (Hook et al., 2001). Recently developed TIR imaging spectrometers including the Field-portable Imaging Radiometric Spectrometer Technology (FIRST) sensor (Chamberland et al., 2005; Balick et al., 2009) have increasingly higher radiometric and spectral resolutions in smaller sensor formats.

Geological research utilizing aerial multi- and hyper-spectral TIR image data has facilitated an enhanced understanding of both the capabilities and constraints of remote mineral identification. Multispectral TIRS image data have been shown to be useful for multiple applications. These data were used to delineate alluvial fan units in the Death Valley region based upon variations in measured broadband emissivity (Gillespie et al., 1984), while Crowley and Hook (1996) used these data to identify and map the presence and distribution of evaporite minerals in Death Valley. Kahle et al. (1988) used TIRS data to differentiate the age of lava flows in Hawaii based upon variation of emissivity attributed to development of silica rinds.

Hyperspectral instruments have been used to remotely target more specific surface expression of mineralogic constituents. Aerial SEBASS image data were used by Cudahy et al. (2000) to identify and map the distribution of feldspar, pyroxene, and garnet solid solution series minerals in Yerington, Nevada. SEBASS image data were used in Virginia City, Nevada to map minerals associated with hydrothermal alteration and mine waste (Vaughan et al., 2003), while a study to map minerals indicative of geothermal potential was conducted Steamboat Springs, Nevada (Vaughan et al., 2005).

More recent research has focused on the effects of imaging geometry (Horton et al., 2002; Balick et al., 2008), near-surface atmospheric turbulence (Balick et al., 2006)

and anisothermal pixel endmember mixtures (McCabe et al., 2008) upon the resultant measurement of emissivity of various rock types.

## **2.4 Geologic background and area of study**

### 2.4.1 Regional geology

Death Valley, California is a range-bounded basin located approximately 150 km west-northwest of Las Vegas, Nevada, USA. Spanning an area nearly 7800 km<sup>2</sup>, it is characterized by an extremely arid climate and displays preserved rock exposures, up to 1800 million years old, in a geological environment characteristic of basin and range structure. Twenty-three distinct geological formations and two unconformity events have been classified within Death Valley (Hunt and Mabey, 1966). Active extensional and block-rotation tectonics, in addition to historic compressional forces, have resulted in a complex structural environment that exhibits a prevalence of normal- and thrust-faulted rock throughout the area.

The northeastern perimeter of Death Valley is formed by the northwest-trending Grapevine and Funeral Mountains. The Keane-Wonder fault bounds the south-facing skirt of both ranges and dips approximately 25 degrees to the west. Both ranges are comprised of meta-sedimentary basements overlain by miogeoclinal Precambrian and Cambrian sedimentary rock sequences. Boundary Canyon features an alluvial flood plain that feeds the Hell's Gate fan system. The Boundary Canyon detachment fault is a low-angle normal fault which dissects the ranges and in which late Cretaceous extensional unroofing has exposed the metamorphic core complex of the Funeral Mountains (Applegate et al., 1992). This unroofed early Cretaceous metamorphic overprint is



observed culminating in amphibolite-grade rocks at the northwestern termination of the range (Labotka, 1980). In contrast, the Grapevine Mountains are characterized by non- or lightly-metamorphosed sedimentary rock units.

#### 2.4.2 Local geology

The local geology of the studied area consists of two distinct sedimentary formations, the Precambrian Stirling Quartzite and the Cambrian Wood Canyon (Wright and Troxel, 1993). The transition between the two formations can be lithologically indistinct, as both display similar types of bedding at different ages of deposition. The two can be distinguished by a proliferation of fossils in the latter. The Stirling Quartzite formation is comprised primarily of quartzite, ranging to 540 million years old, which was lightly metamorphosed from crossbedded sandstone deposited in a near-shore environment (Wertz, 1983). In addition, beds of conglomerate and fine- to medium-grained feldspathic sandstone, siltstone and shale are also interlayered. The Stirling Quartzite is divided into five informal units - A (oldest) through E (youngest), which are comprised of varying combinations of the aforementioned lithologies. The Wood Canyon formation is of late Precambrian to Cambrian age and is divided into three informal members: lower, middle, and upper, listed sequentially from oldest to youngest; a range of siliceous sandy dolomite, fine-to-medium grained feldspathic and micaceous sandstone, and thin platy siltstone comprise the bulk of the beds within the formation (Stewart, 1970; Diehl, 1979).

### 2.4.3 Area of study

The area of study is found at the southern terminus of Boundary Canyon, which served as an early transportation corridor between the mining community of Beatty, Nevada and Death Valley, California. Hell's Gate was the name given to the mouth of the canyon by settlers and miners who first entered Death Valley. The studied outcrop is a folded and faulted stratigraphic assemblage located at  $36^{\circ} 43' 27''$ ,  $116^{\circ} 58' 36''$ , to the eastern margin of Daylight Pass Road (figure 1). The imaged portion of the outcrop measures approximately 160 meters in width, 80 meters in height, and the unit strikes N50W and dips 60SW (figure 2). The outcrop is comprised of a sequence of quartzite, dolomite, and argillite beds ranging in age from upper Stirling Quartzite unit D to lower Wood Canyon (figure 3).

Interbedded quartzites and argillite form the bulk of the lower half of the outcrop, while grading from sparse argillite to dolomite-dominated beds in the upper half. The quartzite displays intermittent cross-bedding structure, and is the most resistant unit in the outcrop. Minor iron oxidation on the face of the quartzite was observed. The dolomite beds are moderately resistant, display prevalent reddish-brownish iron oxidation, feature roughly-textured surfaces in which intermittent patches of desert varnish have formed, and the rock exhibits both massive and low-percentage quartz sand composition. The argillite varies in structure from massive to laminated and these are the least resistant lithology in the outcrop, resulting in prominent bedding cavities between the more resistant adjacent lithologies. Correspondingly, piles of unconsolidated clayey material are found accumulated upon ledges or surfaces below recesses. Fossils or related biogenic structures were not observed during field sampling of the study area.

The outcrop displays symmetric folding resulting from compressional tectonic forces. Faulting has occurred along an approximately vertical orientation upon the left-most segment of the image data boundary, and associated fault gouge was observed during field study. However, the sensor-to-outcrop geometry was not oriented to allow direct observation of this material in the image data.

Sparse instances of vegetative species common to the peripheral basin environment of the Death Valley area were observed within the boundaries of the image data (Hunt, 1966). Beavertail cactus, creosote bush and mesquite grow from the alluvial material within the foreground of the outcrop, partially obscuring the view of the outcrop. Brittlebrush stands were more frequently observed growing on the surface of resistant beds where clayey material and eroded gravel had accumulated.

## **2.5 Methods**

### 2.5.1 Introduction

Field-collected SEBASS image data were investigated to remotely map minerals and delineate a sequence of thin meta-sedimentary beds of an outcrop at Hell's Gate. The SEBASS is an imaging spectrometer operated by The Aerospace Corporation that measures at-sensor radiance across two infrared ranges in 12-bit radiometric resolution. MWIR data is measured from 2.5- to 5.5- $\mu\text{m}$ , while LWIR data is measured from 7.5- to 13.5- $\mu\text{m}$ . Both the midwave and longwave data sets measure radiance in 128 spectral channels across 128 spatial pixels. Hot and cold blackbodies are used to establish floor and ceiling temperature reference measurements at the conclusion of a data scans. The

vendor-provided radiance product incorporates these temperature data ( $NE\Delta T = 0.02$  in the MWIR and  $0.032$  K in the LWIR) to yield accurate calibrated spectral measurements. Due to the complexity of separating reflectance and emittance components of measured at-sensor radiance in the MWIR wavelength range during daytime data acquisition, only the LWIR data were utilized for our research.

Field surveys were used to locate the imaged outcrop, find the dimensions of the scanned area, and make general observations about the study area. Photographs were taken of the outcrop to reference during image data analysis. Rock samples representative of the scene were collected to identify minerals observable with a hand lens, as well as reflectance and TIR laboratory measurements. Two transects were made in separate portions of the outcrop to sample each individual bed along the length of the respective transect. The ENVI Hourglass hyperspectral data analysis methodology was then used to reduce dimensionality, identify mineral endmembers, and use statistical methods to map minerals with the image data. Lastly, image data results for each scan were mosaiced together to provide more synoptic mineral map coverage of the outcrop.

### 2.5.2 Field collection of SEBASS image data

Ground-based SEBASS image data were collected in the Death Valley area on April 10<sup>th</sup>, 1998. Three separate scans were acquired during the day at different elevation angles and recorded in band-interleaved-by-pixel (BIP) format. The collection vehicle was oriented parallel to the face of the outcrop at a distance of approximately 120 meters. The dimensions of each image data scan were  $128 \times 1000$  pixels, and the resulting GIFOV was estimated to range from  $0.16 - 2$  m, based upon the distance from surface

area to measured pixel. Specific environmental conditions present during the time of collection were not recorded.

In ground acquisition mode the sensor is vehicle-mounted and uses a scanning mirror to horizontally collect line-by-line spectral measurements. Scan frequency can be adjusted to increase dwell time and subsequently increase the intensity of measured TIR radiance. Each line scan of the data set was acquired over a period of approximately 10 seconds. At the conclusion of a scan, the elevation angle of the sensor was adjusted to collect new data at a higher angle in manner that provided slight overlap (less than 20%). Thus, the individual image data sets could be combined into a vertical panoramic image mosaic.

### 2.5.3 Calibration of image data

Measured at-sensor radiance ( $L_\lambda$ ) is comprised of upwelling surface ( $\varepsilon_\lambda L_{bb\lambda}(T)$ ) and atmospheric ( $L_{atm\lambda}$ ) components; a reflected downwelling atmospheric radiance component ( $L_{sky\lambda}$ ); each of which is constrained by transmissivity of the atmosphere ( $\tau_\lambda$ ). Measurement of TIR radiance is limited by the range of wavelengths radiated by a blackbody at a certain temperature, and further restricted by atmospheric transmissivity, effectively bounding remote measurement of emittance to the 7 – 14  $\mu\text{m}$  wavelength range (equation 1). An in-scene atmospheric correction (ISAC) routine in the ENVI V. 4.6 software was applied to the ground-based radiance image data to mitigate the impact of atmospheric effects upon identifying mineral features in image data spectra (Johnson, 1998; Young et al., 2002; and as reviewed in Vaughan et al., 2003). The ISAC algorithm

relies upon the presence of an approximated blackbody in the data scene of which graybody objects, represented by water or vegetation, are likely sources.

TIR radiance emitted from a surface is comprised of distinct temperature and emissivity components. A temperature-emissivity separation (TeS) algorithm is applied to resolve unknown information for radiance measurements ( $n$  emissivity bands + 1 temperature), based upon the best-estimate of temperature (Realmutu, 1990). Empirical methods are employed to best estimate temperature via collection of reference hot and cold blackbody temperatures at the completion of SEBASS image data scans. This allows an accurate ( $NE\Delta T = 0.032$  K) measurement of apparent kinetic temperature to be made. The identification of the brightest radiance band value per pixel is used to best estimate the location of unity to a Planck curve for a corresponding temperature. Per band radiance values are then divided by the value of the Planck curve at corresponding wavelengths to derive emissivity spectra. ENVI V. 4.6 software was used to normalize the radiance data to emissivity using a method described by Hook et al., 1992. Validation of the results was accomplished by comparing quartz emissivity spectra from: (a) atmospherically-uncorrected image data, (b) ISAC atmospherically-corrected image data, (c) field-based Designs & Prototypes FTIR, (d) laboratory Nicolet FTIR, and (e) ASU library spectra (figure 6).

#### 2.5.4 Other field measurements

Digital photographs were taken of the outcrop at close range to maximize resolution of the surface features. These images were then mosaiced to create a more synoptic view of study area. Tape measurement of the base width and height of the

imaged area were used to establish the image area dimensions. Rock sampling of the outcrop and the alluvium within foreground of the image data scene were used to better understand the types of rock found in the studied scene. Unique rocks were initially characterized based upon grain size and mineral content features identified in hand sample analysis.

Transect sampling of two separate locations of the outcrop was performed to gather rocks in order of bed sequence. This would facilitate later comparison of laboratory emissivity spectra of these rocks to image spectra corresponding to these surface areas (figure 2). These transects were chosen in areas where continuity of lateral bedding plane thickness was observed. In contrast, the majority of the outcrop exhibited folded and faulted beds that were often pinched or terminated, rendering lateral bed continuity difficult to follow in the image data. Each transect consisted of an established base and termination, termed T1 and T1' and T2 and T2', respectively (figures 4 and 5). Each bed that intersected the transect vector was recorded if thickness measured at least 0.16 meter, or roughly the size of the minimum estimated GIFOV. Characteristics relevant to the spectral analysis of each bed in transects 1 and 2 were recorded in tables 1 and 2, respectively, including transect number, bed number, bed thickness, visual observations of the rock constituting the bed, and the dominant minerals comprising the collected samples as determined by laboratory FTIR and XRD analysis.

#### 2.5.5 Laboratory measurements

A Nicolet 6700 series FTIR spectrometer in the Arthur Brant Laboratory was used to make laboratory measurements of rock samples gathered during field investigation.

This information was to be used as an accurate reference for image data emissivity spectra. The FTIR measures bidirectional reflectance in wavelengths ranging from 2.5 to 25  $\mu\text{m}$  and incorporates a specular-reflecting gold background target for calibration purposes. General laboratory measurement procedure involved measurement of rock chip samples approximately 1 x 1 x 0.5 cm in size that best preserved surficial expression with regard to the viewing geometry of the SEBASS sensor. Crushed rock samples of varying grain size were also measured for comparison to bulk samples. Seventy-four total samples were measured in reflectance, and subsequently converted to approximate emissivity using Kirchhoff's  $E=1-R$  relationship between reflectance and emissivity.

An Applied Spectral Devices (ASD) FieldSpec Pro instrument was used to make laboratory measurements of reflected electromagnetic energy from 350 to 2500 nm. These measurements were taken to corroborate FTIR findings and increase overall information about mineralogical constituents of samples. The spectral sampling of the instrument is 1.4 nm from 350 to 1050 nm and 2 nm from 1000 to 2500 nm. The spectral resolution is 3 nm at 700 nm, 10 nm at 1400 nm and 12 nm at 2100 nm. The instrument measurements were calibrated by using a spectralon reference panel to convert to reflectance units.

X-ray diffraction (XRD) analysis was performed to further corroborate mineralogy of rocks yielding unique spectral measurements. The Nevada Bureau of Mines and Geology (NBMG) Philips Electronics PW2273/20 instrument was used. XRD measurements were analyzed to determine the absolute presence of mixed minerals in rock samples. Material Data, Inc. (MDI) Datascan V. 4 software was used to process the



samples and MDI Jade V. 6.5 software was used to analyze the measurements using the International Centre for Diffraction Data (ICDD) PDF-2 database.

## **2.6 Image data processing**

### 2.6.1 Overview

The emissivity image data were processed following methodologies originally developed to analyze reflectance hyperspectral image data. Pixels constituting the outlying column ( $i_{1,*}$  and  $i_{128,*}$ ) and row ( $j_{1,*}$  and  $j_{1000,*}$ ) edges of the image data were removed from subsequent processing consideration due to anomalous data artifacts. Pixels that consisted of background sky in the top-left corner of the image data were masked. A decorrelation stretch was utilized to enhance visual delineation between pixels dominated by quartz, muscovite, and dolomite. The ENVI Hourglass routine was utilized in order to reduce the dimensionality of the data, identify pure pixel endmembers, and map the spatial occurrences of the mineral endmembers by use of established classification algorithms (Kruse et al., 1993; ITT Visual Solutions, 2008). The validity of these processes, as applied to LWIR hyperspectral image data analysis, was previously established in Vaughan et al., 2003. Following mapping, individual scans were mosaiced together to form more synoptic mineral maps. The following section will briefly summarize the steps used, in addition to noting deviations from previously established methodologies.

### 2.6.2 Decorrelation stretch images

Decorrelation stretching (DCS) is a statistical method introduced in Gillespie et al. (1986) to visually enhance 3-band images so that contrast between image components

is increased. These images were used to help guide initial steps to identify basic mineralogy of imaged rocks within the scene. The bands chosen were 71 (11.24  $\mu\text{m}$ ), 27 (9.01  $\mu\text{m}$ ), and 20 (8.6  $\mu\text{m}$ ), and corresponded to emission features of quartz, muscovite, and dolomite. The process involves first applying a principle components transform to input 3-band image data. Next, pixel values for each band are rescaled using a Gaussian stretch to maximize use of the radiometric resolution of the data. An inverse principle components transform is used to complete the process and revert to original image data space. This effectively provides visual separation between image data components in the DCS image that may be subtle or not otherwise readily observed in the original RGB image.

### 2.6.3 Dimensionality reduction

The Minimum Noise Fraction (MNF) algorithm is a cascading principal components transform that is used to statistically order data according to decreasing variance and thus establish a threshold upon which to separate data representing noise (Boardman and Kruse, 1994). Each of the 128 measured bands was included for processing in the MNF function. This differs from the input previously defined by Vaughan and Cudahy for aerially-acquired SEBASS image data, in which the respective studies utilized approximately 82 bands limited to the 8 - 12  $\mu\text{m}$  wavelength range. Inclusion of all bands was based upon spatial coherence of each band image, in addition to observation of high-quality emissivity spectra features in the 7.5 - 8 and 12 - 13.5  $\mu\text{m}$  ranges representative of particular minerals such as quartz, as opposed to image incoherence and noise in emissivity spectra observed in these same ranges in aerial

SEBASS image data. The routine was applied to the emissivity data to produce band-ordered MNF data that represented the bulk variance of the emissivity data. The resulting MNF bands were each visually inspected and those displaying incoherence, striping, or other significant spatial data artifacts were removed from further inclusion. Nine MNF bands were selected based upon a lack of significant noise or artifact components.

#### 2.6.4 Pure pixel identification

The Pure Pixel Index (PPI) algorithm (Boardman and Kruse, 1994) was used to identify spectra representing statistically unique spectral endmembers in the previously selected bands of the MNF image data. The parameters of the routine utilized 15,000 iterations and a conservative threshold factor of 2.5. The resulting pure pixel image was linked to the spectral image data and visually inspected to manually determine uniqueness of the identified pure pixels. A histogram stretch was applied to the pure pixel image to increase contrast between unique and non-unique pixels. Redundant spectra were removed from consideration and the remaining spectra were used to create a spectral library comprised of five endmembers (vegetation, quartz, muscovite, dolomite, and calcite); one additional endmember was added during expert analysis of the image data (gypsum) (figure 7).

#### 2.6.5 SAM spectral mapping

Spectral Angle Mapper (SAM) and match filtering classification algorithms were evaluated based upon their respective ability to map the distribution of image data endmembers. SAM creates a specified angle with axes based upon the  $n$ -dimensional character of the input endmember and image data spectra. The angle can be adjusted to

either narrow or broaden, resulting in a more strict or loose match to the input spectra, respectively. An identified benefit of the algorithm is that matches can be made in spite of varying magnitude or strength of a feature, thereby decreasing the impact of topographic and shadowing variability (Yuhus et al., 1992). The match filter uses a measure of feasibility relative to the input spectra; matches are scored using this factor (Harsanyi and Chang, 1994). Both algorithms were applied to the emissivity data set using the previously created spectral library as input. The classification results were evaluated by linking to the image data and inspecting the emissivity spectra in order to determine 1) how successful the classification was in mapping particular endmembers, and 2) whether a particular algorithm was better suited to the application. The match filter classification results were generally less satisfactory, thus SAM classifications were retained for image data analysis and mineral mapping.

#### 2.6.6 Mosaicing and georectification

A series of high-resolution photographs taken of the study site from the approximate location and elevation of the SEBASS sensor were used as a background upon which to georectify the image data. Overlapping pixels of the three individual SEBASS image data sets were used as initial spatial references in which to manually create a mosaic of the data. Twenty-three ground control points (GCP) were established to perform a nearest neighbor-based georectification of the data to the digital photograph background. Although differences in the geometries between each data scan made at progressively higher angles and the photographs were inevitable and only partially

correctable for limiting georectification error, the results were deemed acceptable within the context of the research objectives.

## **2.7 Results**

### **2.7.1 Synopsis**

Hand-sample, transect mapping, laboratory measurement, and image data analyses resulted in the identification of minerals associated with particular lithologies found in the imaged outcrop. Image data emissivity spectra were validated by comparison of quartz-dominated pixel spectra to that of library and laboratory pure quartz spectra. Mapping of two transects yielded the identification of rock types constituting a sequence of beds, as well as further rock characteristics and bed thickness. Laboratory TIR measurements were useful in identifying bulk and minor mineralogical constituents of each rock type. VNIR/SWIR reflectance measurements introduced identification of iron-oxide minerals, as well as better identifying clay minerals. SAM-derived mineral maps produced good matches to quartzite, dolomite, and argillite beds, as well as identifying subtle mineralogical variations within the outcrop.

### **2.7.2 Validation of temperature/emissivity image data calibration**

Emissivity and temperature image data resulting from the ENVI T&S routine were evaluated to determine feasibility of the spectra for remote mineral mapping. The temperature data were first examined, and these values ranged from 285.56 to 317.65 (min/max). These values were reasonable in context of normal expected surface temperature range for Death Valley on the date of data acquisition. The emissivity spectra of quartz-dominated pixels corresponding to quartzite were plotted for comparison

against laboratory FTIR and USGS and ASTER library quartz spectra for the 7.5 – 13.5  $\mu\text{m}$  wavelength range. The image data seemed to replicate the prominent emission minima doublet feature well in this range, and the overall slope and shape of spectra indicated a reasonable calibration effort.

### 2.7.3 Transect mapping

Transect mapping across two different portions of the outcrop resulted in the identification and general characterization of the rock sequences here. Transect one was set in the bottom half of the outcrop, which was dominated by quartzite and argillite. The quartzite appeared well sutured and massive, however some of these beds exhibited cross-bedding. Oxidized grains of feldspar were found infrequently on the weathered surface of these rocks. The argillite was of mixed composition, exhibiting varying percentages of clay, silt, and sand grains. These beds alternated randomly between massive and laminated structure. Rocks mapped in transect two, located toward the upper half of the outcrop, were predominantly comprised of dolomite beds, with thin argillite beds interspersed between them. The dolomite exhibited a uniformly increased iron oxidation and more rough, textured surfaces. Fresh exposure of these rocks exhibited dark, nearly massive dolomite with small percentage of quartz sand grains. Within the two transects, small conglomerate beds were noted, however these were not prominently exposed, with respect to the imaging sensor, and thus were not represented in image data measurements.

#### 2.7.4 Laboratory analyses of transect samples

Laboratory reflectance and TIR measurements were made of samples from beds intersecting transects 1 and 2 to determine mineral constituents and for reference to image data emissivity spectra (figures 4 and 5). In transect 1 quartzite and argillite samples were both identified during field study (figure 4). Reflectance spectra measurements of iron-oxide on the quartzite identified goethite in each sample, as characterized by absorptions at 650 and 915 nm, resulting in a peak at 765 nm in the visible/near-infrared (VNIR) spectrum. In the shortwave-infrared (SWIR) spectrum, muscovite was identified in samples T1-01, 04, 05, 06, 07, 10, and 11 by a large absorption feature at 2200 nm and a minor absorption at 2350 nm. Kaolinite was identified by an absorption doublet feature centered at 2220 nm in T1-03. Kaosmectite, a term for the mixture of kaolinite and smectite, was characterized in T1-02, 07, and 10 by a similar absorption at 2200 nm that lacked a well-defined doublet absorption. In the FTIR measurements spanning 7.5 to 13.5  $\mu\text{m}$ , quartz was identified by the diagnostic doublet emission minima centered at 8.4 and 9  $\mu\text{m}$  in samples T1-01, 03, 04, 08, 10 and 11. The presence of clay upon quartz was indicated by the 9  $\mu\text{m}$  minima being split further into another weak doublet. Muscovite was identified in the LWIR spectra via broad minimas peaking at 8.81 and 9.58  $\mu\text{m}$ . The presence of clay again split the muscovite minima into a weak doublet centered at 9  $\mu\text{m}$ . Samples T1-02, 05, 06, 07, and 09 each exhibited the presence of muscovite.

In transect 2 the VNIR reflectance measurements were used to identify oxidation on each sample as goethite (figure 5). In the SWIR, muscovite was detected in samples T2-05 through T2-12. Kaosmectite was measured in T2-01 through T2-03. Dolomite was

detected in approximately half of the samples: T2-04, T2-06, T2-07, T2-08, T2-11, and T2-12; however establishing the absorption feature center at 2315 nm was difficult as this region was noisy in laboratory measurements. The LWIR FTIR spectra showed quartz as a component of each sample in the T2 transect, to varying degrees. Clays were again indicated by the weak doublet of the 9  $\mu\text{m}$  emission minima in quartz- and muscovite-rich samples. The presence of muscovite, feldspar, and quartz was identified in the argillite rocks (T2-05 and 09) by distinct narrow emission minima centered at 8.16  $\mu\text{m}$  (quartz), 8.54  $\mu\text{m}$  (orthoclase/albite), 8.78  $\mu\text{m}$  (kaosmectite/muscovite), 9.1  $\mu\text{m}$  (kaosmectite/muscovite), 9.5  $\mu\text{m}$  (orthoclase/albite), and 11.28  $\mu\text{m}$  (muscovite) (figure 10). Dolomite was identified via narrow emission minima centered at 11.15  $\mu\text{m}$  and calcite was characterized by a similar feature shifted to longer wavelengths centered at 11.33  $\mu\text{m}$ .

#### 2.7.5 Image data analysis of transect areas

SEBASS image data coinciding with the two transects were examined first. The sedimentary rock column map and laboratory reflectance and TIR measurements were used to interpret the corresponding image data spectra and resulting mineral maps. Specific beds mapped in the transects corresponded well with image data-derived DCS images and SAM mineral maps (figures 11 - 14). The image data spectra were less detailed than the laboratory spectra, as expected due to decreased spectral resolution, signal-to-noise ratio, pixel mixtures, and atmospheric effects. An emission minima feature at approximately 10  $\mu\text{m}$  was noted that could have been due to a clay mineral coating, however it was observed ubiquitously throughout the image data, and may have



been a data artifact attributable to a shortcoming in the atmospheric correction. The presence of clays within the scene was not immediately identifiable, as an emission minima doublet indicative of kaolinite or kaolinite was not observed centered at 9  $\mu\text{m}$  in the emissivity spectra. A secondary quartz doublet, however, was well resolved at 12.46 and 12.76  $\mu\text{m}$ . Mixed quartz, muscovite, and feldspar emissivity spectra were able to be differentiated from more pure quartz spectra; however these mixed spectra exhibited less pronounced minima. In general, fewer pixels exhibited these spectral mixtures in comparison to the more frequently observed pure quartz. Mixed quartz + dolomite, and quartz + calcite, were able to be separated from these other unique spectra, as the 11.2 and 11.3  $\mu\text{m}$  minimas attributed to these rocks contrasted with other mineral endmembers, and were generally limited to certain areas in the top half of the outcrop.

#### 2.7.6 Mineral mapping of the outcrop

PPI analysis of the MNF data resulted in the identification of six unique LWIR emissivity spectra endmembers representing single or mixed minerals; expert analysis of the image data spectra resulted in the identification of an additional mineral endmember. Quartz, gypsum, dolomite + quartz, calcite + quartz, and muscovite + quartz + feldspar mineral endmembers were each validated by being matched to spectral library measurements of corresponding pure mineral samples. Next, SAM was applied to the image data to generate classification and rule image data using these endmember spectra. The image data bands used as input for each endmember varied according to the respective diagnostic emissivity features. Input bands spanned the shoulders and trough of emission minima features. For quartz, bands 1 through 40 (7.3 to 9.71  $\mu\text{m}$ ) were used.

Dolomite was mapped using bands 57 through 76 (10.57 to 11.45  $\mu\text{m}$ ) and calcite was mapped using bands 65 through 80 (10.95 to 11.63  $\mu\text{m}$ ). Muscovite-dominated pixels were mapped using bands 15 through 42 (8.28 to 9.86  $\mu\text{m}$ ). Gypsum was mapped using bands 1 through 36 (7.36 to 9.51  $\mu\text{m}$ ). Lastly vegetation was mapped using bands 1 through 128 (7.36 to 13.41  $\mu\text{m}$ ). The resulting classification images were individually examined and conservatively thresholded to produce reasonable mineral matches (figure 15). Specific threshold levels were determined by linking emissivity image data with rule images. The thresholds were then modified while manually observing emissivity spectra in real-time. A comprehensive class image was created which combined all map results together (figure 16).

The pixel classification results are summarized in table 4. Quartz was the most commonly mapped mineral in the image data (11.81%), while dolomite (2.81%), muscovite (2.25%), calcite (0.27%) and gypsum (0.004%) comprised the rest of the minerals identified in the scene. The bulk of image data pixels were not mapped or associated with minerals: unclassified (69.48%), background sky (5.01%), shadow (4.75%), and vegetation (3.58%).

The average emissivity values of mapped pixels for respective mineral classes were compared to determine differences in strength of diagnostic features (figure 17). The quartz doublet exhibited the deepest diagnostic emission minima of the mineral endmembers, with an average emissivity of .87117 at band 29 (9.12  $\mu\text{m}$ ). The secondary quartz exhibited the next deepest emission minima, with an average emissivity of .92905 at band 108 (12.8  $\mu\text{m}$ ). Calcite had an average of .96489 emissivity at band 73 (11.33  $\mu\text{m}$ ), while muscovite and dolomite exhibited similar average emissivity: .97592 at band

29 (9.12  $\mu\text{m}$ ), and .97764 at band 69 (11.15  $\mu\text{m}$ ), respectively. Vegetation exhibited general variability of emissivity of under 0.002 at band 23 (8.77  $\mu\text{m}$ ).

## **2.8 Discussion and summary**

### **2.8.1 Lithologic delineation**

The dominant lithologies identified during field study were quartzite, dolomite, and argillite. The lower half of the outcrop was comprised of quartzite and argillite (table 1); the upper half was comprised primarily of dolomite, thin, sparse argillite beds, and two conglomerate beds, however these were not exposed enough to be viewed from the perspective of the sensor (table 2). In the scene foreground, the alluvial wash was dominated by quartzite pebbles; in addition, varnished dolomite, opaline silica, and muscovite schist were scattered infrequently here (table 3). Nearly all rocks were oxidized or clay-coated, to some degree, and desert varnish commonly occurred on smoother surfaces of the dolomite, and infrequently upon the quartzite. Beds were mapped along the two transects when larger than the GIFOV of the SEBASS image data and these ranged in thickness from .2 to 1.14 m. Separate classification images of quartz, dolomite, calcite, gypsum, and muscovite were generated and then combined to create a comprehensive mineral classification image. Direct comparison of image data classification results and transect maps reveal good matches between the two. The presence of dolomite, calcite, and muscovite were mutually exclusive to a particular lithology, while quartz was identified as a constituent of each lithology, to varying degrees.

Relatively pure quartz-dominated pixels were found to most closely match quartzite beds and pebbles constituting the wash found within the foreground of the scene. The strong emission of quartz contrasted with surrounding lithologies. In addition, quartz was a component detected in spectral mixtures indicative of argillite, dolomite, and possible marbleization. Mapped dolomite pixels clearly delineated dolomite beds, as well as talus at the base of the outcrop that had originated from dolomite beds immediately above the sensor's field of view. Transect 2 passed near an area of mapped calcite however this area was not noted as visually distinct from dolomite in the field surveys. Rock samples from this area did display calcite veining within fractures of dolomite, however these were generally small-scale features. In contrast, calcite was mapped in areas wide enough to constitute partial beds which graded from dolomite; this may be evidence of marbleization.

The dominant minerals identified in the argillite samples were muscovite, quartz and either orthoclase or albite. Muscovite was mapped as the primary component of this lithology as well as for desert varnish, which led to some ambiguity. In general, the presence of desert varnish was deemed likely when muscovite-dominated pixels were mapped within the lateral extent of dolomite-mapped pixels, representing dolomite beds. This was interpreted as desert varnish coatings that had formed at certain locations along the face of some dolomite beds. In addition, a small number of pixels mapped as muscovite upon dolomite beds exhibited a prominent emission doublet feature; these peaks were located at 9.45 and 9.67  $\mu\text{m}$ , and likely indicative of ozone gas ( $\text{O}_3$ ). This was also observed in some vegetation-dominated pixels. This spectral was interpreted as either measurement of reflected downwelling radiance by specular surfaces incident to

the sensor aperture, or simply inadequate atmospheric correction of the image data provided by the ENVI-based ISAC routine.

A high number of unclassified pixels may be explained by conservative rule image thresholding; varying strength of diagnostic emission minima from particular lithologies; and different levels of surface exposure for the respective lithologies. The quartzite beds exhibited high levels of emission, and subsequently were mapped well; while the argillite, dolomite, and marbleized dolomite beds exhibited lower overall diagnostic feature emissivities. However, the dolomite and marbleized beds were clearly delineated while the argillite beds were not as successfully mapped. This may be attributable to a few different factors.

Dolomite and calcite have single narrow diagnostic features at 11.2 and 11.3  $\mu\text{m}$ , respectively, while no other mineral found in the study area exhibited emissivity features that coincided with these minima. In contrast, argillite was comprised of a mixture of muscovite, quartz, and feldspar, which each exhibit diagnostic features in the 8 to 10  $\mu\text{m}$  range. In addition, pure quartz tends to dominate these weaker spectral features of mineral mixtures. Next, physical characteristics of the outcrop were unfavorable for mapping the argillite more extensively. This lithology is non-resistant, and consequently has been weathered from between the more resistant quartzite and dolomite beds, resulting in less prominent areas of surface exposure, and thus less absorption and subsequent re-emission of energy. Lastly, these beds were more frequently covered by dust or particle films that could decrease thermal inertia and cumulatively reduce the ability to remotely identify this lithology

### 2.8.2 Reflectance and thermal-infrared laboratory measurements

Reflectance and TIR measurements were complimentary in characterizing the transect rock samples. For example, goethite is identifiable in the visible/near-infrared (VNIR) spectrum due to absorptions attributable to electronic processes, however diagnostic features are not present in the LWIR; alternatively, quartz is identifiable in the LWIR spectrum due to Si-O stretching attributable to vibrational processes, but is opaque in the VNIR and SWIR spectrums. The vibrational absorption features of hydroxyl (OH) in the SWIR wavelength range produced more detail for identifying clay minerals than the LWIR, as vibrational emission minima features of clay observed in LWIR laboratory spectra consist of wide and more subtle emission minima that overlap diagnostic features of other mineral features such as the quartz minima at 9  $\mu\text{m}$ . Correctly identifying kaolinite, kaolinite and minor muscovite as clay films or coatings was difficult to accomplish in the LWIR, perhaps due to these instances of minerals being expressed as unconsolidated fine grains versus consolidated material, which better suits SWIR reflectance identification, in which fine grains result in higher reflectance. Muscovite was a prominent component of argillite spectra, and distinctive emissivity spectra resulted. Identifying dolomite in the SWIR measurements was more difficult to accomplish when mixed with muscovite, owing to overlapping absorption features at 2320 nm and overall lower albedo of the rock. The LWIR detection of dolomite and calcite, in contrast, were unambiguous as no other mineral encountered in this study exhibited such narrow and well-defined diagnostic features that overlapped the carbonate minimas.

These findings suggest that ideally both reflectance and emissivity measurements

should both be made in future studies, as more comprehensive mineral identification and higher confidence in results can be achieved. As observed by Clark et al. (1990) and Vaughan et al. (2003), VNIR/SWIR measurements may better resolve clays and are the best option for detecting oxides such as goethite in comparison to wavelength ranges measured by the SEBASS sensor. LWIR is the only option for identifying certain silicate minerals, such as quartz, while introduces the capability of identifying silicate mineral mixtures such as quartz, muscovite, and feldspar. It may be preferable to use LWIR measurements for identifying carbonates, rather than SWIR, due to unambiguity of narrow diagnostic features and absence of other common minerals which have overlapping features.

### 2.8.3 Comparison of laboratory and image data spectra

Differences in the image data and laboratory spectra were found to be minor, and primarily attributed to previously identified differences in spectra resolution, SNR, pixel mixtures, and atmospheric effects. Dissimilarity in slope in certain image data spectra were observed, and may be attributable to varying angles of emission in relation to the sensor, or multiple temperature elements within given pixels that were not compensated for. Ancillary range-finding image data that provides per-pixel information on distance from the sensor to the surface of the target, such as LiDAR, may enable a better understanding of this phenomenon and allow modeling and subsequent compensation.

Muscovite, kaolinite and kaolinite clay coatings upon transect samples were identified with SWIR reflectance measurements, however these were not as well represented in laboratory measurements, and were not mapped with confidence in the

LWIR image data. This may be a function of the small particulate nature of the coatings as opposed to a consolidated exposure of clay-rich rock in the outcrop. The presence of films and coatings are noteworthy due to their dynamic nature (Dorn, 1998), and thus in future studies, understanding and characterizing varying thicknesses of clay coatings will be critical for increasing the information derived from spectral identification of underlying rock-comprising minerals.

## **2.9 Conclusion**

The collection of image data with increasingly higher spectral and spatial resolution has resulted in the ability to detect smaller instances and more subtle mineralogic variation of rocks. The nadir look angle associated with spaceborne and aerial imagery has the benefit of providing a wide area of coverage. For materials that are vertically ordered or differentiated, however, this viewing perspective may not allow observation, as in the case of horizontally bedded columns of sedimentary strata. The research presented here demonstrates a basic application of ground-based LWIR hyperspectral image data to remotely identify the dominant mineralogy of Precambrian-Cambrian sedimentary lithologies in the Death Valley area.

Remote identification of quartz, dolomite, calcite, muscovite, and feldspar were linked to matching lithologies of quartzite, dolomite, marbleized dolomite, and argillite using statistical mapping methods, such as SAM, as well as manual inspection of image spectra to subsequently refine mineral maps. An extremely small instance of gypsum was also remotely identified and mapped with high confidence. The presence of muscovite in both argillite and desert varnish resulted in initial confusion; this was able to be resolved



using contextual information provided by photographic interpretation to indicate that these pixels were mapped upon dolomite beds. Spectral measurement of the outcrop was successful for mineral mapping due to sufficient strength of emission and spectral contrast of mineral constituents representative of each lithology. Quartzite beds were most successfully mapped; dolomite beds and marbleized rock were next best mapped; and argillite showed only limited success.

Short pathlength from sensor-to-target decreased the role of atmospheric effects in emittance measurements; this effectively increased prominence of the surface mineralogy component of radiance measured by ground-based SEBASS. This was shown to result in usable data in the 7.5 to 8 and 12 to 13.5  $\mu\text{m}$  wavelength ranges, which were not used in previous studies involving aerial SEBASS image data.  $\text{O}_3$  emission attributed to reflected downwelling radiance was possibly observed in certain pixels, representative of desert varnish and vegetation, within the outcrop scene. This may instead indicate the need for an ISAC algorithm more directly tailored toward ground-based TIR measurements. In particular, accounting for adjacency effects of ground material emission along the pathlength of measurement, as well as addressing only partial integration of hemispherical down-welling radiance should be addressed.

The use of coupled high-resolution digital photographs during TIR hyperspectral measurements enables a background image to be generated, which is beneficial for the visual inspection of sub-pixel components. The presence of shadowing, indicative of recession of weathered beds, is important in recognizing high-contrast thermal components within the scene. Geometrically co-registered LiDAR image data may also

play an important role in measuring per pixel GIFOV. Thus angular variation of emission from an imaged outcrop could be modeled and integrated into future studies.

### **2.10 Acknowledgements**

We would like to thank the respective manuscript reviewers for their helpful suggestions and contributions. The Aerospace Corporation kindly supplied the SEBASS image data and supporting documentation. The National Park Service granted permit # DEVA-2008-SCI-0037 that allowed field work in the study area. Mary Conger provided much-appreciated field assistance during transect sampling. This research was supported by a Department of Energy grant.

## 2.11 References

- Applegate, J.D.R., Walker, J.D., and Hodges, K.V. (1992). Late Cretaceous extensional unroofing in the Funeral Mountains metamorphic core complex, California. *Geology*, 20 (6), pp. 519-522.
- Balick, L., Gillespie, A., French, A., Danilina, I., Allard, J., and Mushkin, A. (2009). Longwave thermal infrared spectral variability in individual rocks. *IEEE Geoscience and Remote Sensing Letters*, 6 (1), pp. 52-56.
- Balick, L.K., Jeffery, C., and McCabe, M.F. (2006). Understanding thermal variability using a new dynamical model of the surface skin temperature and turbulent near atmosphere. *American Geophysical Union Fall Meeting*.
- Boardman J. W., and Kruse, F. A. (1994). Automated spectral analysis: A geologic example using AVIRIS data, north Grapevine Mountains, Nevada. *Proceedings of the Tenth Thematic Conference on Geologic Remote Sensing*, Environmental Research Institute of Michigan, Ann Arbor, MI, pp. I-407-I-418.
- Buckley, S., Howell, J., Enge, H., Leren, B., and Kurz, T. (2006). Integration of terrestrial laser scanning, digital photogrammetry and geostatistical methods for high-resolution modeling of geological outcrops. *Proceedings of the ISPRS Commission V Symposium*, Dresden, Germany.
- Christensen, P.R., Bandfield, J.L., Hamilton, V.E., Howard, D.A., Lane, M.D., Piatek, J.L., Ruff, S.W., and Stefanov, W.L. (2000). A thermal emission spectral library of rock-forming minerals. *Journal of Geophysical Research*, 105 (E4), pp. 9735-9739.
- Chamberland, M., Farley, V., Vallieres, A., Villemaire, A., Belhumeur, L., Giroux, J., and Legault, J.F. (2005). High-performance field-portable imaging radiometric

spectrometer technology for hyperspectral imaging applications. *Proceedings of SPIE, The International Society for Optical Engineering*, 5994, 59940N.

- Christensen, P.R., Mehall, P.R., Silverman, S.H., Anwar, S., Cannon, G., Gorelick, N., Kheen, R., Tourville, T., Bates, D., Ferry, S., Fortuna, T., Jeffryes, J., O'Donnell, W., Peralta, R., Wolverton, T., Blaney, D., Denise, R., Rademacher, J., Morris R.V. and Squyres, S.W. (2003). Miniature thermal emission spectrometer for the Mars Exploration Rovers, *Journal of Geophysical Research*, 108 (E12), 8064.
- Clark, R.N., King, T.V.V., Klejwa, M. and Swayze, G.A. (1990). High spectral resolution reflectance spectroscopy of minerals. *Journal of Geophysical Research*, 95 (B8), pp. 12653-12680.
- Crowley, J.K., and Hook, S.J. (1996). Mapping playa evaporite minerals and associated sediments in Death Valley, California, with multispectral thermal infrared images. *Journal of Geophysical Research*, 101, pp. 643-660.
- Cudahy, T.J., Okada, K., Yamato, Y., Maekawa, M., Hackwell, J.A., and Huntington, J.F. (2000). Mapping skarn and porphyry alteration mineralogy at Yerington, Nevada, using airborne hyperspectral TIR SEBASS Data, *CSIRO exploration and mining report 734R*, CSIRO Exploration and Mining Co, Floreat Park, WA, Australia.
- Diehl, P.E. (1979). The stratigraphy, depositional environments, and quantitative petrography of the Precambrian-Cambrian Wood Canyon Formation, Death Valley. *Ph.D. thesis*, Pennsylvania State University.
- Dorn, R.I. (1998). *Developments in Earth Surface Processes 6: Rock Coatings*. Elsevier Science B.V.

- Farmer, V.C., Editor (1974). *The infrared spectra of minerals*. Mineralogical Society Monograph vol. 4, Mineralogical Society, London.
- Gillespie, A.R., Kahle, A.B. and Walker, R.E. (1986). Color enhancement of highly correlated images: I. Decorrelation and HIS contrast stretches. *Remote Sensing of Environment*, 20, pp. 209-235.
- Gillespie, A.R., Kahle, A.B., and Palluconi, F.D. (1984). Mapping alluvial fans in Death Valley, California, using multi channel thermal infrared images. *Geophysical Research Letters*, 11, pp. 1153-1156.
- Hackwell, J.A., Warren, D.W., Bongiovi, R.P., Hansel, S.J., Hayhurst, T.L., Mabry, D.J., Sivjee, M.G., and Skinner, J.W. (1996). LWIR/MWIR imaging hyperspectral sensor for airborne and ground-based remote sensing, *The International Society for Optical Engineering*, 2819, pp. 102-107.
- Harsanyi, J.C., and Chang, C.I. (1994). Hyperspectral image classification and dimensionality reduction: an orthogonal subspace projection approach. *IEEE Transactions on Geoscience and Remote Sensing*, 32, pp. 779-785.
- Hook, S. J., Myers, J. J., Thome, K. J., Fitzgerald, M., and Kahle, A. B. (2001). The MODIS/ASTER airborne simulator (MASTER) – a new instrument for earth science studies. *Remote Sensing of Environment*, 76, pp. 93-102.
- Hook, S.J., Gabell, A.R., Green, A.A., and Kealy, P.S. (1992). A comparison of techniques for extracting emissivity information from thermal infrared data for geologic studies. *Remote Sensing of Environment*, 42, pp. 123-135.
- Horton, K.A., Moersch, J.E., Lucey, P.G., and Ruff, S.W. (2002). A rover's-eye view in the thermal infrared: spectral adjacency effects. Proceedings from the 33<sup>rd</sup> Lunar and

- Planetary Science Conference, 1808. 2 pp.
- Horton, K.A., Johnson, J.R., and Lucey, P.G. (1998). Infrared measurement of pristine and disturbed soils: environmental effects and field data reduction. *Remote Sensing of Environment*, 64, pp. 47-52.
- Hunt, C.B. (1966). Plant ecology of Death Valley, California, U.S. Department of Interior, *Geological Survey Professional Paper*, 509.
- Hunt, C.B., and Mabey, D.R. (1966). General geology of Death Valley, California. *United States Geological Survey Professional Paper*, 494-A.
- Hunt, G. R. and Salisbury, J. W. (1970). Visible and near-infrared spectra of minerals and rocks – I. *Silicate Minerals: Modern Geology*, 1, pp. 283-300.
- ITT Visual Solutions (2008). ENVI User's Guide, Version 4.3. ITT Visual Solutions, Boulder, Colorado.
- Jensen, J.R. (2007). Remote Sensing of the Environment: an Earth Resource Perspective, 2<sup>nd</sup> ed., Prentice-Hall. ISBN 0-13-188950-8, 544 pp.
- Johnson, B.R. (1998). In-scene atmospheric compensation: application to the SEBASS data collected at the ARM site, Part I. *Aerospace Corporation Report*, (ATR-99(8407), Part I).
- Johnson, J.R., Lucey, P.G., Horton, K.A., and Winter, E.M. (1998). Infrared measurements of pristine and disturbed soils 1. Spectral contrast differences between field and laboratory data. *Remote Sensing of Environment*, 64, pp. 34-46.
- Kahle, A.B., Gillespie, A.R., Abbott, E.A., Abrams, M.J., Walker, R.E., Hoover, G., and Lockwood, J.P. (1988). Relative dating of Hawaiian lava flows using multispectral

- thermal infrared images: A new tool for geologic mapping of young volcanic terranes. *Journal of Geophysical Research*, 93 (B12), pp. 15,239-15,251.
- Kahle, A.B. and Goetz, A.F.H. (1983). Mineralogic information from a new thermal infrared multispectral scanner, *Science*, 222, pp. 24–27.
- Kirkland, L.E., Herr, K.C., Keim, E., Adams, P.M., Salisbury, J., Hackwell, J., and Treiman, A. (2002). First use of an airborne thermal infrared hyperspectral scanner for compositional mapping. *Remote Sensing of Environment*, 80, pp. 447-459.
- Kirkland, L.E., Herr, K.C., Adams, P.M., McAfee, J., and Salisbury, J. (2002). Thermal infrared hyperspectral imaging from vehicle-carried instrumentation. Imaging Spectrometry VIII., *Proceedings of the SPIE*, S.S. Shen, editor, 4816, pp. 415-425.
- Korb, A.R., Dybwad, P., Wadsworth, W., and Salisbury, J.W. (1996). Portable Fourier transform infrared spectrometer for field measurements of radiance and emissivity, *Applied Optics*, 35, pp. 1679-1692.
- Kruse, F. A. (2000). The effects of spatial resolution, spectral resolution, and signal-to-noise ratio on geologic mapping using hyperspectral data, Northern Grapevine Mountains, Nevada, *Proceedings of the 9th JPL Airborne Earth Science Workshop*, Jet Propulsion Laboratory Publication 00-18, pp. 261-269.
- Kruse, F.A., Lefkoff, A.B., and Dietz, J.B. (1993). Expert system-based mineral mapping in Northern Death Valley, California/Nevada, using the Airborne Visible/Infrared Imaging Spectrometer (AVIRIS). *Remote Sensing of Environment* 44, pp. 309-336.
- Labotka, T.C. (1980). Petrology of a medium-pressure regional metamorphic terrane, Funeral Mountains, California. *American Mineralogist*, 65, (7-8), pp. 670-689.
- Lucey, P.G., Williams, T., Mignard, M., Julian, J., Kokobun, D., Allen, G., Hampton, D.,

- Schaff, W., Schlangen, M., Winter, E.M., Kendall, W., Stocker, A., Horton, K., and Bowman, A.P. (1998). AHI: an airborne long wave infrared hyperspectral imager. *Proceedings of the SPIE Conference on Airborne Reconnaissance*, San Diego, CA, pp. 36-43.
- Lyon, R. J. P., and Green, A. A. (1975). Reflectance and emittance of terrain in the mid-infrared (6 – 25  $\mu\text{m}$ ) region. Ch 7 in: *Infrared and Raman Spectroscopy of Lunar and Terrestrial Minerals*, Academic Press, Inc., pp. 164-194.
- McCabe, M.F., Balick, L.K., Theiler, J.P., Gillespie, A.R., and Mushkin, A. (2008). Forward modeling of linear mixing in thermal IR temperature retrieval. *International Journal of Remote Sensing*, 29 (17), pp. 5047-5061.
- McHugh, E.L., Girard, J.M., Denes, L.J., Metes, P., and Sabine, C. (2000). Current research on slope movement in mines: use of hyperspectral imagery. *Proceedings of the 14<sup>th</sup> International Conference on Applied Geologic Remote Sensing*, Las Vegas, NV, pp. 1-8.
- Michalski, J.R., Kraft, M.D., Diedrich, T., Sharp, T.G., and Christensen, P.R. (2003). Thermal emission spectroscopy of the silica polymorphs and considerations for remote sensing of mars. *Geophysical Research Letters* 30 (19).
- Milton, E.J., Schaepman, M.E., Anderson, K., Kneubuhler, M., and Fox, N. (2009). Progress in field spectroscopy. *Remote Sensing of Environment*, 113, Supplement 1, pp. S92-S109.
- Ragona, D., Minster, B., Rockwell, T., and Jussila, J. (2006). Field imaging spectroscopy: a new methodology to assist the description, interpretation, and archiving of



- paleoseismological information from faulted exposures. *Journal of Geophysical Research*, 111, B10309.
- Realmuto, V.J. (1990). Separating the effects of temperature and emissivity: emissivity spectrum normalization. *Proceedings of the 2<sup>nd</sup> TIMS Workshop*, JPL Publication 90-55, pp. 31-35.
- Salisbury, J.W., and D'Aria, D.M. (1992). Emissivity of terrestrial materials in the 8-14  $\mu\text{m}$  atmospheric window. *Remote Sensing of Environment*, 42, pp. 83-106.
- Salisbury, J.W., and Wald, A. (1992). The role of volume scattering in reducing spectral contrast of reststrahlen bands in spectra of powdered minerals. *Icarus*, 96, pp. 121-128.
- Stewart, J.H. (1970). Upper Precambrian and lower Cambrian strata in the southern Great Basin, California and Nevada, *USGS Professional Paper 620*, 206 pp.
- Thomson, J.L., and Salisbury, J.W. (1993). The mid-infrared reflectance of mineral mixtures (7-14  $\mu\text{m}$ ). *Remote Sensing of Environment*, 45, pp. 1-13.
- Vaughan, R. G., Calvin, W. M., and Taranik, J. V. (2003). SEBASS hyperspectral thermal infrared data: surface emissivity measurement and mineral mapping. *Remote Sensing of Environment*, 85, pp. 48-63.
- Vaughan, R.G., Hook, S.J., Calvin, W.M., and Taranik, J.V. (2005). Surface mineral mapping at Steamboat Springs, Nevada, USA, with multi-wavelength thermal infrared images. *Remote Sensing of Environment*, 99, pp. 140-158.
- Wertz, W.E. (1983). The depositional environments and petrography of the Stirling Quartzite, Death Valley Region, California and Nevada. *Ph.D. Thesis*, Pennsylvania State University.
- Wright, L.A., and Troxel, B.W. (1993). Geologic map of the central and northern Funeral

Mountains and adjacent areas, Death Valley region, southern California. *US Geological Survey Misc. Invest. Series Map I-2305*.

Young, S. J., Johnson, B. R., and Hackwell, J. A. (2002). An in-scene method for atmospheric compensation of thermal hyperspectral data. *Journal of Geophysical Research*, 107 (D24), 4774.

Yuhas, R.H., Goetz, A.F.H., and Boardman, J.W. (1992). Discrimination among semi-arid landscape endmembers using the Spectral Angle Mapper (SAM) algorithm. *Summaries of the 4<sup>th</sup> Airborne Earth Science Workshop, JPL publication 92-41*, pp. 147-149.

## Equations

Equation 1.

Radiance equation for aerial thermal-infrared imaging of ground targets

$$L_{\lambda} = [\varepsilon_{\lambda} L_{bb\lambda}(T) + (1 - \varepsilon_{\lambda}) L_{sky\lambda}] \tau_{\lambda} + L_{atm\lambda} \#$$

Where:

$L_{\lambda}$  = at-sensor radiance;

$\varepsilon_{\lambda}$  = surface emissivity at wavelength  $\lambda$ ;

$\varepsilon_{\lambda} L_{bb\lambda}(T)$  = spectral radiance from a blackbody at surface temperature T;

$L_{sky\lambda}$  = reflected downwelling atmospheric radiance;

$\tau_{\lambda}$  = spectral atmospheric transmission;

$L_{atm\lambda}$  = upwelling spectral radiance;

## Tables

Table 1.

### Transect 1 rock sample descriptions and measured mineral constituents

Sample	Bed thickness (m)	Visual description	ASD	TIR	XRD
T1-01	0.43	quartzite	goethite, muscovite	quartz, kaolinite	quartz
T1-02	0.25	silty stratified micaceous argillite	goethite, muscovite, kaosmectite	muscovite, quartz, microcline	kaolinite, muscovite, quartz, microcline
T1-03	0.41	quartzite with slight oxidized clay surface	goethite, kaolinite	quartz	quartz
T1-04	0.2	quartzite	goethite, muscovite	quartz	-
T1-05	0.43	silty stratified micaceous argillite	goethite, muscovite	muscovite, quartz, microcline	goethite, kaolinite, quartz, muscovite, microcline
T1-06	0.28	silty massive argillite	muscovite	muscovite, microcline, quartz	kaolinite, muscovite, quartz, microcline
T1-07	0.61	argillite	goethite, muscovite, kaosmectite	muscovite, quartz, microcline	-
T1-08	0.41	quartzite	goethite	quartz, kaolinite	-
T1-09	0.66	silty stratified argillite	goethite, muscovite	muscovite, quartz, microcline	-
T1-10	0.56	quartzite	goethite, kaosmectite, dolomite	quartz, kaolinite	-
T1-11	1.14	quartzite with slight oxidized clay surface	goethite, muscovite	quartz, muscovite	-

Table 2.

Transect 2 rock sample descriptions and measured mineral constituents.

Sample	Bed thickness (m)	Visual description	ASD	TIR	XRD
T2-01	0.66	fractured quartzite with oxidized clay surface	goethite, muscovite	quartz, muscovite	quartz, muscovite
T2-02	0.33	quartzite with oxidized clay surface	goethite, muscovite, dolomite	dolomite, quartz	quartz, calcite, dolomite
T2-03	0.28	dolomite with quartz sand grains; oxidized clayey surface	goethite, muscovite, dolomite	dolomite, quartz, muscovite	muscovite, quartz, paragonite, dolomite
T2-04	0.58	quartzite	goethite, dolomite	quartz	-
T2-05	0.38	fissile silty argillite	goethite, muscovite	muscovite, quartz	muscovite, kaolinite, quartz
T2-06	0.76	dolomite with quartz sand grains; oxidized clayey surface	goethite, muscovite, dolomite	dolomite, quartz, muscovite	-
T2-07	0.56	dolomite with quartz sand grains; oxidized clayey surface	goethite, muscovite, dolomite	dolomite, quartz	kaolinite, muscovite, quartz, microcline, dolomite
T2-08	0.89	dolomite with quartz sand grains; oxidized clayey surface	goethite, calcite	dolomite, quartz	-
T2-09	0.64	oxidized argillite	goethite, muscovite	muscovite	muscovite, kaolinite, quartz, orthoclase
T2-10	0.53	fractured quartzite with oxidized clay surface	goethite, muscovite	quartz, muscovite	-
T2-11	0.48	fissile silty argillite	goethite, muscovite, dolomite	muscovite, dolomite	muscovite, kaolinite, quartz, orthoclase, dolomite
T2-12	0.56	dolomite with quartz sand grains; low oxidation	goethite, dolomite, muscovite	dolomite, quartz	quartz, dolomite, muscovite

Table 3.

Local area rock sample descriptions and measured mineral constituents.

Sample	Visual description	TIR	XRD
1	volcanic glass	opal	opal
2	pelitic schist	muscovite	muscovite, quartz, chlorite
3	heavy desert varnish (on oxidized dolomite)	goethite, muscovite, dolomite	muscovite, dolomite

Table 4.

## Image data classification matrix

Endmember	Color	Classified pixels	Bands input to SAM	Percent of total pixels
Quartz 1	yellow	31,536	1-40	0.11811
Quartz 2*	n/a	30,261	95-120	0.11333
Dolomite	magenta	7,526	57-76	0.02818
Calcite	red	734	65-80	0.00274
Muscovite	cyan	6,009	15-42	0.02250
Gypsum	green	12	1-36	0.00004
Vegetation	black	9,572	1-128	0.03585
Shadow	black	12,705	-	0.04758
Sky	black	13,398	-	0.05017
Unclassified	black	206,254	-	0.69483

**Figures**

Figure 1.

The location of the Hell's Gate area of study, Death Valley National Park, California, USA is shown below. A map of the local geology (modified from Wright & Troxel, 1993) emphasizes the sedimentary Wood Canyon and Stirling Quartzite geologic units. The red boundary box indicates the approximate location and width of image data scans. The black arrow indicates the direction that the sensor was oriented for scanning.

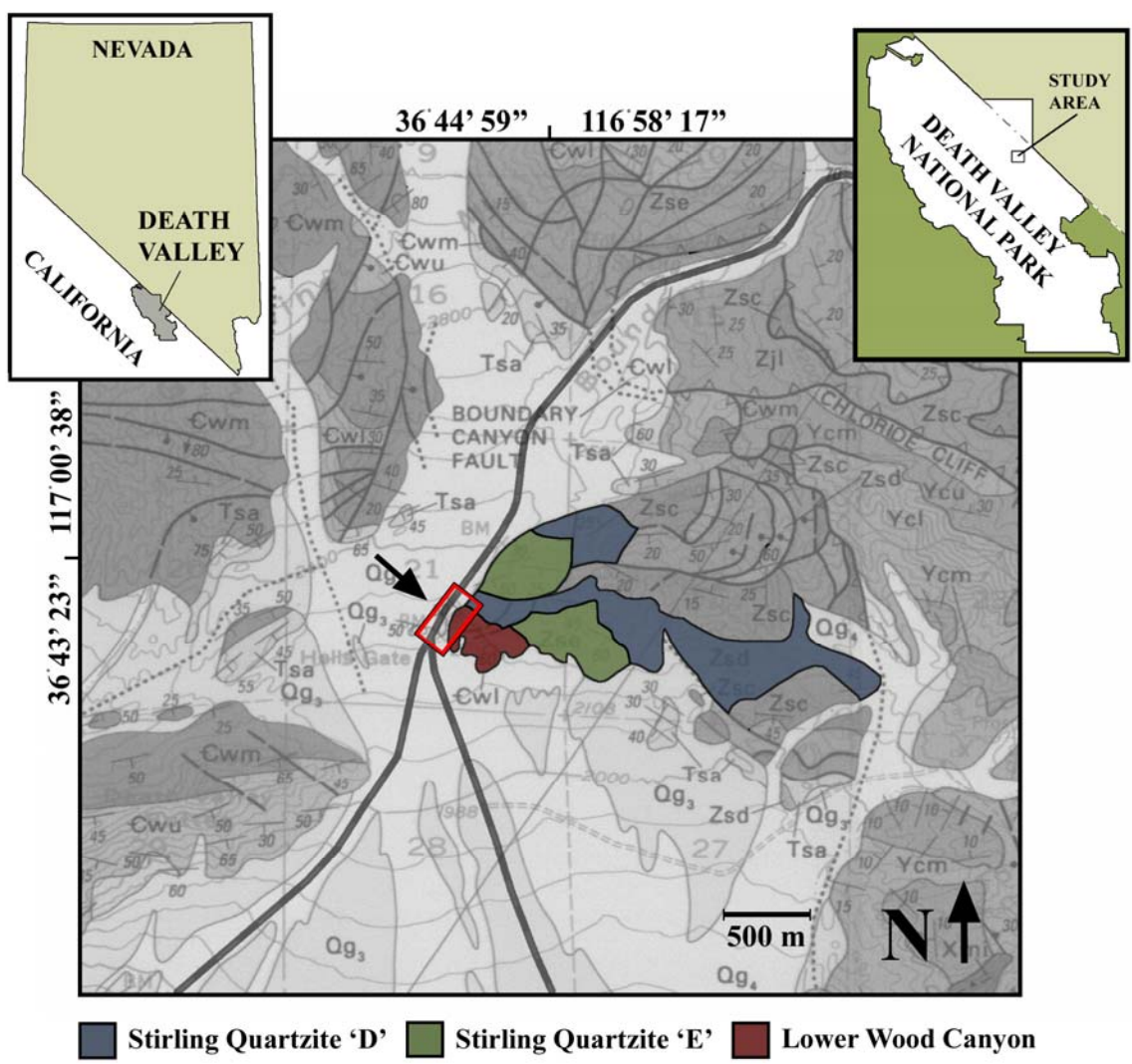




Figure 2.

A digital photograph of the measured outcrop is shown below. The boundaries of the mosaiced SEBASS image data sets are indicated by the boxed area. Two sampling transects were established within the measured area, indicated as "T1" and "T2". Rock samples were collected from each bed larger than 0.16 m that intersected the respective transect.

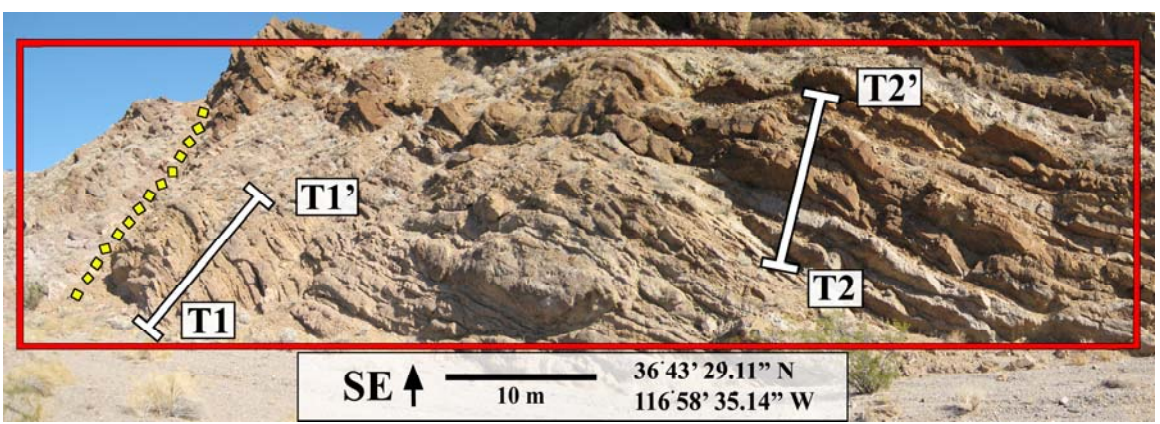


Figure 3.

Digital photographs of the most common mapped bed lithologies within the area of study are shown in sub-figures A through D: quartzite (A), argillite (B), dolomite (C), and calcite veining within dolomite (marbleization?) (D). Other unique rock types found within the immediate vicinity included: clayey fault gouge (E), desert varnish (F), muscovite schist (G) and volcanic glass (H).

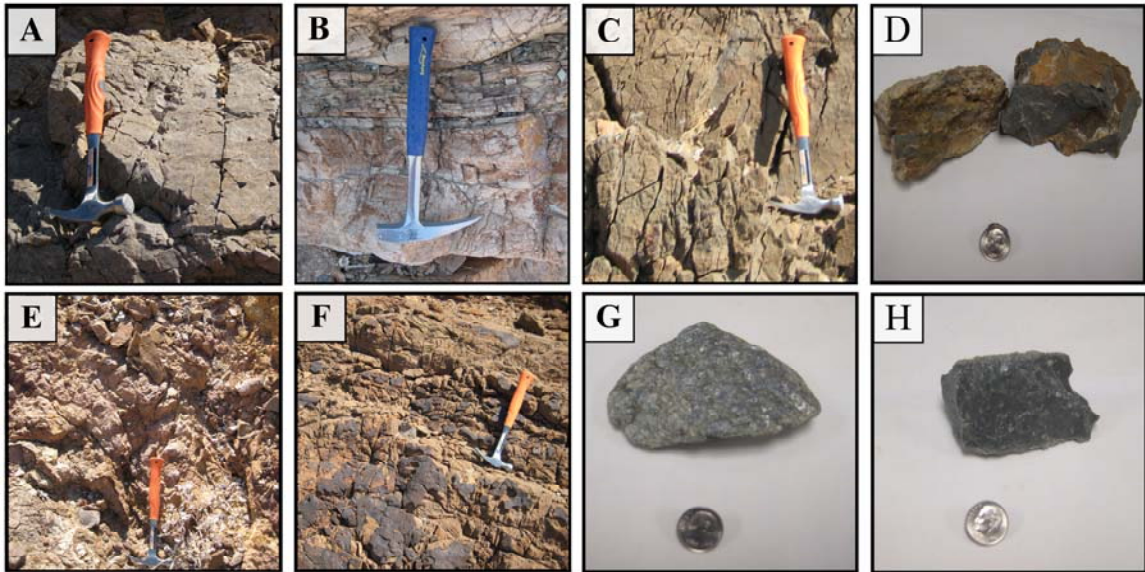


Figure 4.

A photograph of transect T1 established along the lower half of the outcrop is shown (A). The major lithologies mapped are indicated in the stratigraphic column map below, and include: quartzite and argillite (B). Laboratory measurements of rock samples from the corresponding bed area are shown in C and D. VNIR and SWIR reflectance spectra are shown for the same samples (C). Thermal infrared measurements spanning the wavelength range of SEBASS are shown (D).

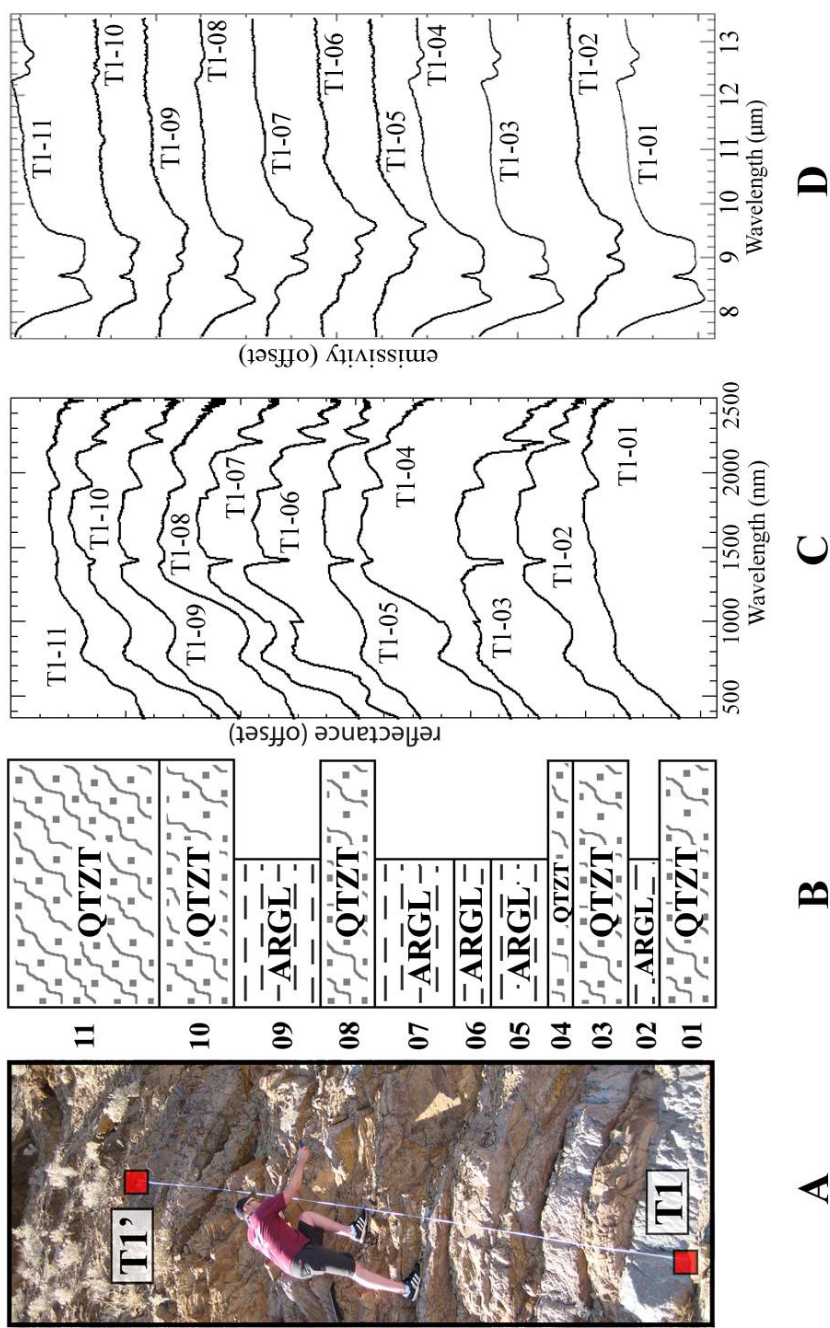


Figure 5.

A photograph of transect T2 established along the upper half of the outcrop is shown (A). The major lithologies mapped are indicated in the stratigraphic column map below, and include: quartzite, argillite, dolomite, and conglomerate (not exposed sufficiently for imaging) (B). Laboratory measurements of rock samples from the corresponding bed area are shown in C and D. VNIR and SWIR reflectance spectra are shown for the same samples (C). Thermal infrared measurements spanning the wavelength range of SEBASS are shown (D).

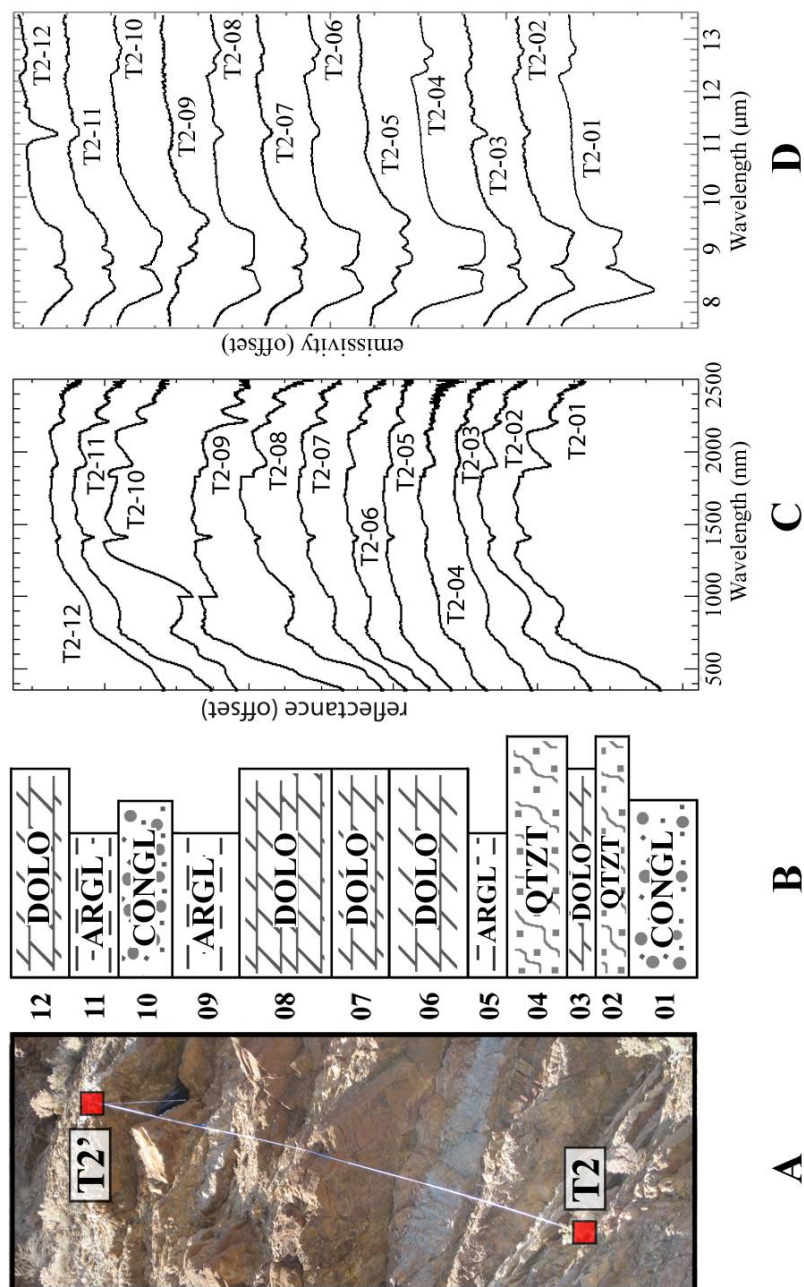


Figure 6.

Emissivity spectra of quartz are plotted below from (A) atmospherically-uncorrected SEBASS image data, (B) ISAC atmospherically-corrected SEBASS image data, (C) field-based Designs & Prototypes FTIR, (D) Nicolet laboratory FTIR measurement, and (E) ASU library spectra.

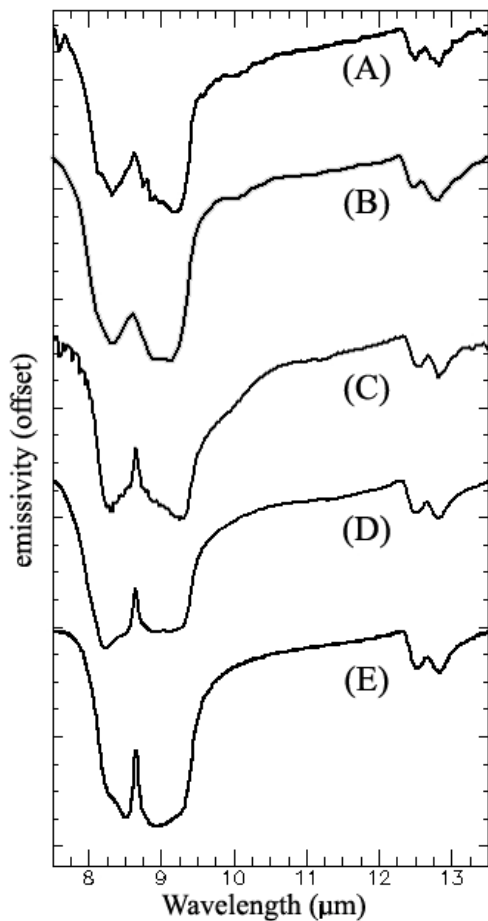


Figure 7.

SEBASS image data endmember emissivity spectra identified by the pure pixel index routine and/or expert analysis are plotted below. Unique spectra include vegetation (A), gypsum (B), calcite (C), dolomite (D), quartz + muscovite + feldspar (E), and quartz (F). Ozone ( $O_3$ ) can also be identified in these spectra via emission peaks at 9.45 and 9.67  $\mu\text{m}$ , indicating atmospheric correction was not completely successful. (E) and (F) exhibit bowl-shaped spectral curves that may be due to a range of temperatures within a pixel measurement, where radiance measurements are converted to emissivity assuming a single temperature.

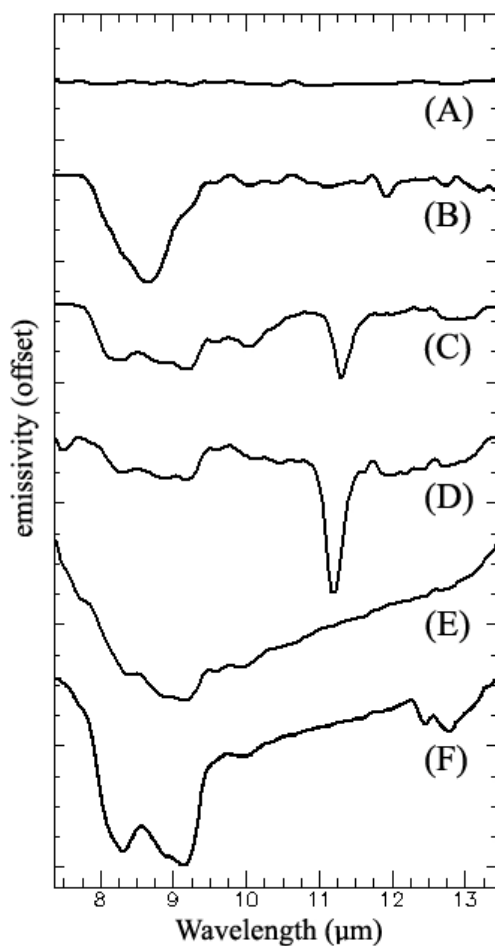


Figure 8. A histogram of the apparent temperature values for each pixel representing a mapped surface in the image data. These data were derived from an ENVI-based temperature-emissivity separation (T&S) process. The minimum value represented for surfaces in the scene was 285.56 K, mean was 297.67 K, and maximum was 317.65 K. These values are a reasonable range in the context of the data collection date.

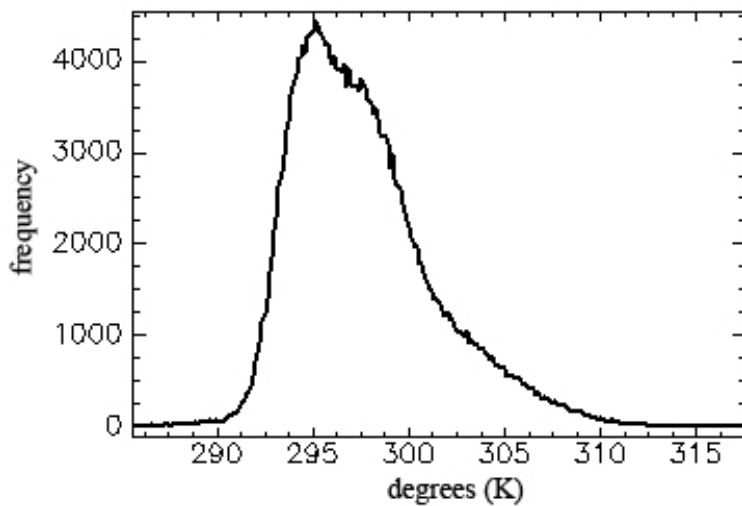


Figure 9. Laboratory FTIR measurement of argillite, sample T2-05. The presence of multiple silicate minerals in the sample is indicated by narrow emission minima features. The wavelength location of each trough feature was noted and was used to match library spectra. XRD measurements were used to corroborate the presence of these minerals. The narrow feature at 8.16  $\mu\text{m}$  was attributed to quartz; the 8.54  $\mu\text{m}$  feature is indicative of feldspar (either orthoclase or albite) and quartz; 8.78 and 9.1  $\mu\text{m}$  are a doublet feature attributed to either kaolinite or kaolinsmectite, which overlap a broad quartz lobe; 9.5  $\mu\text{m}$  is another feldspar feature; and 11.28  $\mu\text{m}$  indicates a carbonate mineral, likely calcite.

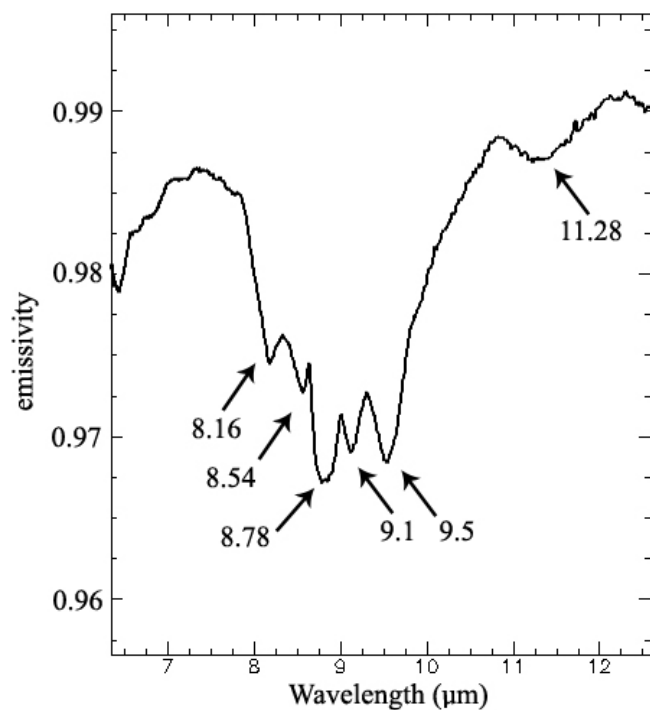


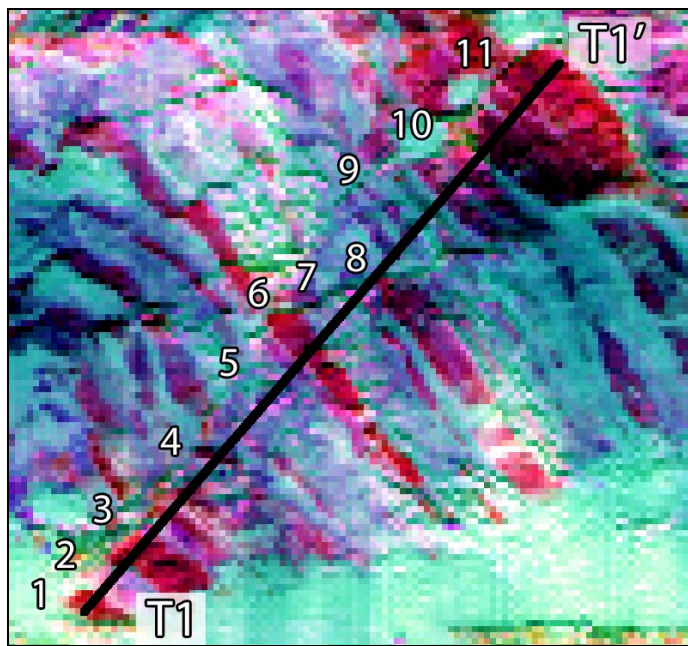


Figure 10.

A photograph of transect 1 is shown with interpreted lithologic boundaries (dashed lines). Beds are numbered according to sampled location (A). A DCS image of SEBASS data (RGB bands 71 (11.24  $\mu\text{m}$ ), 27 (9.01  $\mu\text{m}$ ), 20 (8.6  $\mu\text{m}$ ) with location of transect and samples is shown (B).



(A)



(B)

Figure 11.

A subset of the SEBASS DCS image (RGB bands 71 (11.24  $\mu\text{m}$ ), 27 (9.01  $\mu\text{m}$ ), 20 (8.6  $\mu\text{m}$ ) limited to transect area 1 is shown (A). A SAM rule classification image of the transect is shown, where yellow is quartz, magenta is dolomite, red is calcite, cyan is muscovite, and unclassified pixels are black (B). Emissivity spectra extracted from the SEBASS image data pixels overlapping the transect sample areas are shown (C).

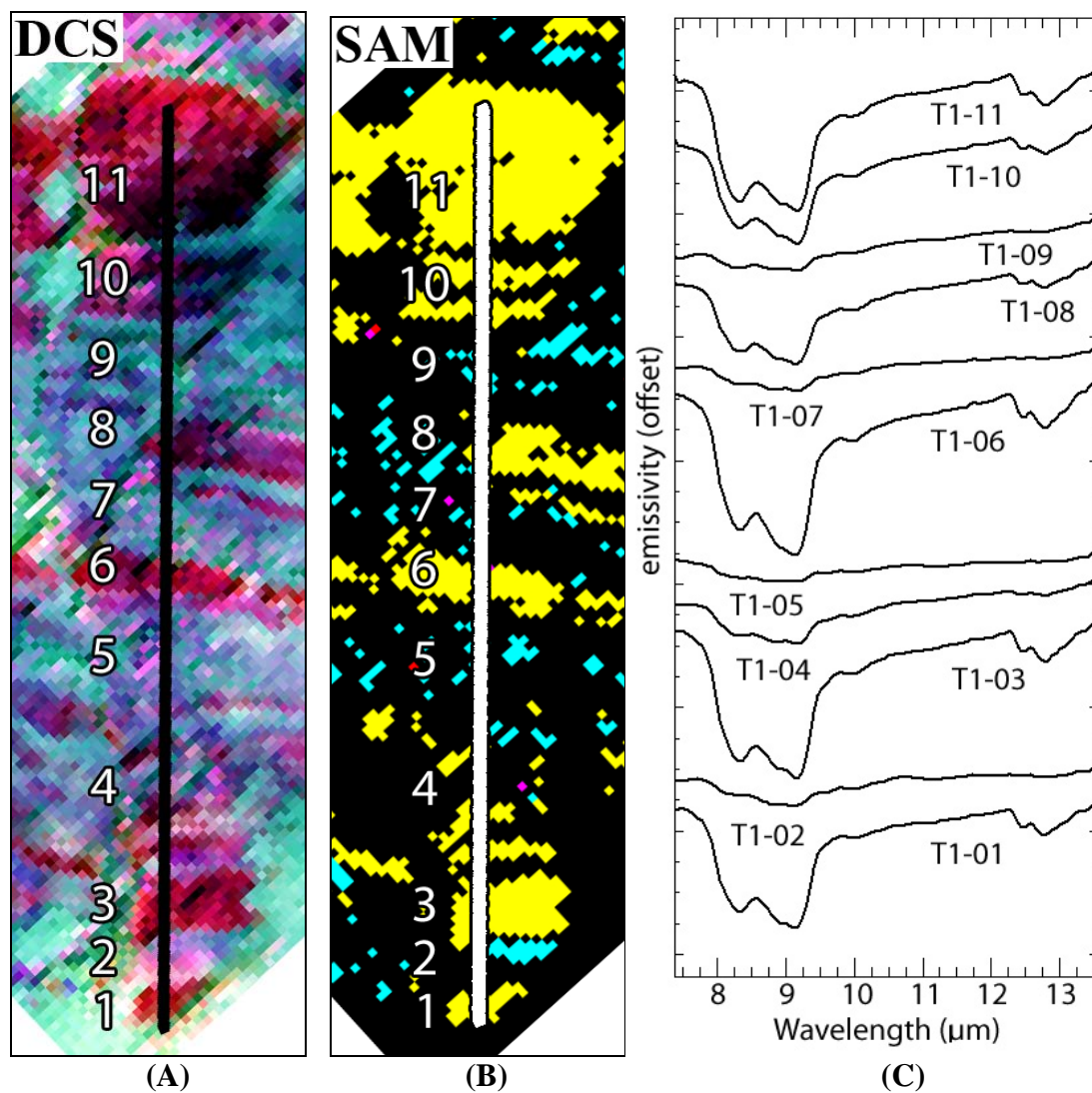
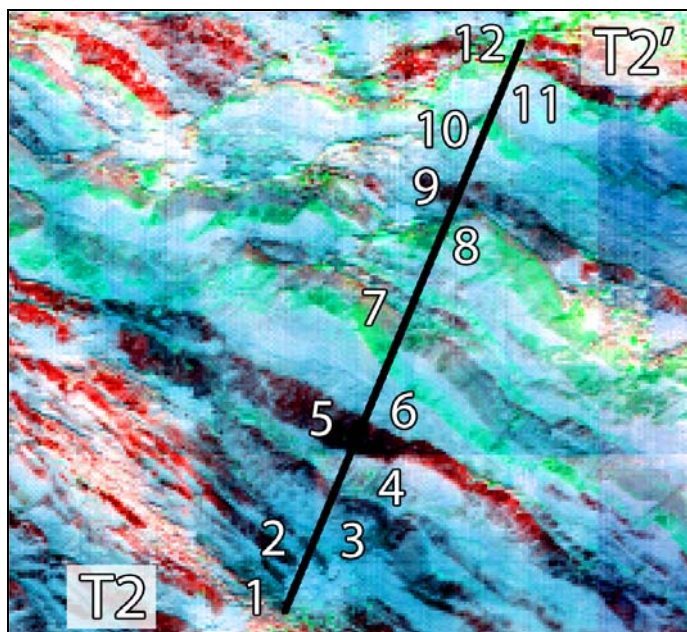


Figure 12.

A photograph of transect 2 is shown below with interpreted lithologic boundaries (dashed lines). Beds are numbered according to sampled location (A). A DCS image of SEBASS data (RGB bands 71 (11.24  $\mu\text{m}$ ), 27 (9.01  $\mu\text{m}$ ), 20 (8.6  $\mu\text{m}$ ) with location of transect and samples is shown (B).



(A)



(B)

Figure 13.

A subset of the SEBASS DCS image limited to transect area 2 is shown (RGB bands 71 (11.24  $\mu\text{m}$ ), 27 (9.01  $\mu\text{m}$ ), 20 (8.6  $\mu\text{m}$ ) (A). A SAM rule classification image of the transect is shown, where yellow is quartz, magenta is dolomite, red is calcite, cyan is muscovite, and unclassified pixels are black (B). Emissivity spectra extracted from the SEBASS image data pixels overlapping the transect sample areas are shown (C).

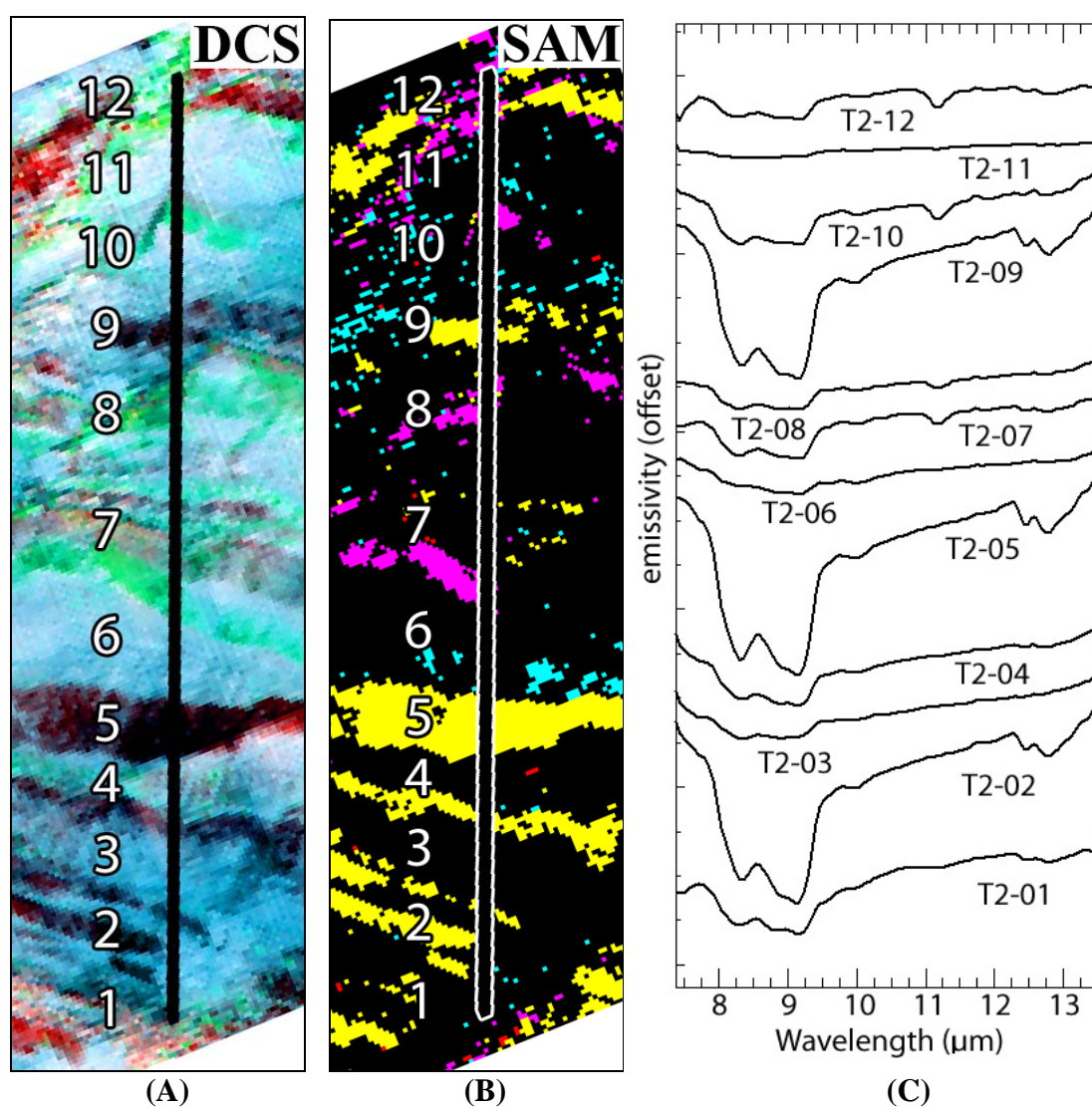


Figure 14.

SAM rule classification images for minerals corresponding to outcrop lithologies. White indicates a match to input spectra and black indicates no match. (A) quartz resulting from input of bands 1 through 40 (7.36 to 9.72  $\mu\text{m}$ ); (B) dolomite from input of bands 57 through 76 (10.58 to 11.46  $\mu\text{m}$ ); (C) muscovite from input of bands 15 through 42 (8.29 to 9.83  $\mu\text{m}$ ); (D) calcite from input of bands 65 through 80 (10.56 - 11.64  $\mu\text{m}$ ); (E) gypsum from input of bands 1 through 36 (7.36 - 9.51  $\mu\text{m}$ ).

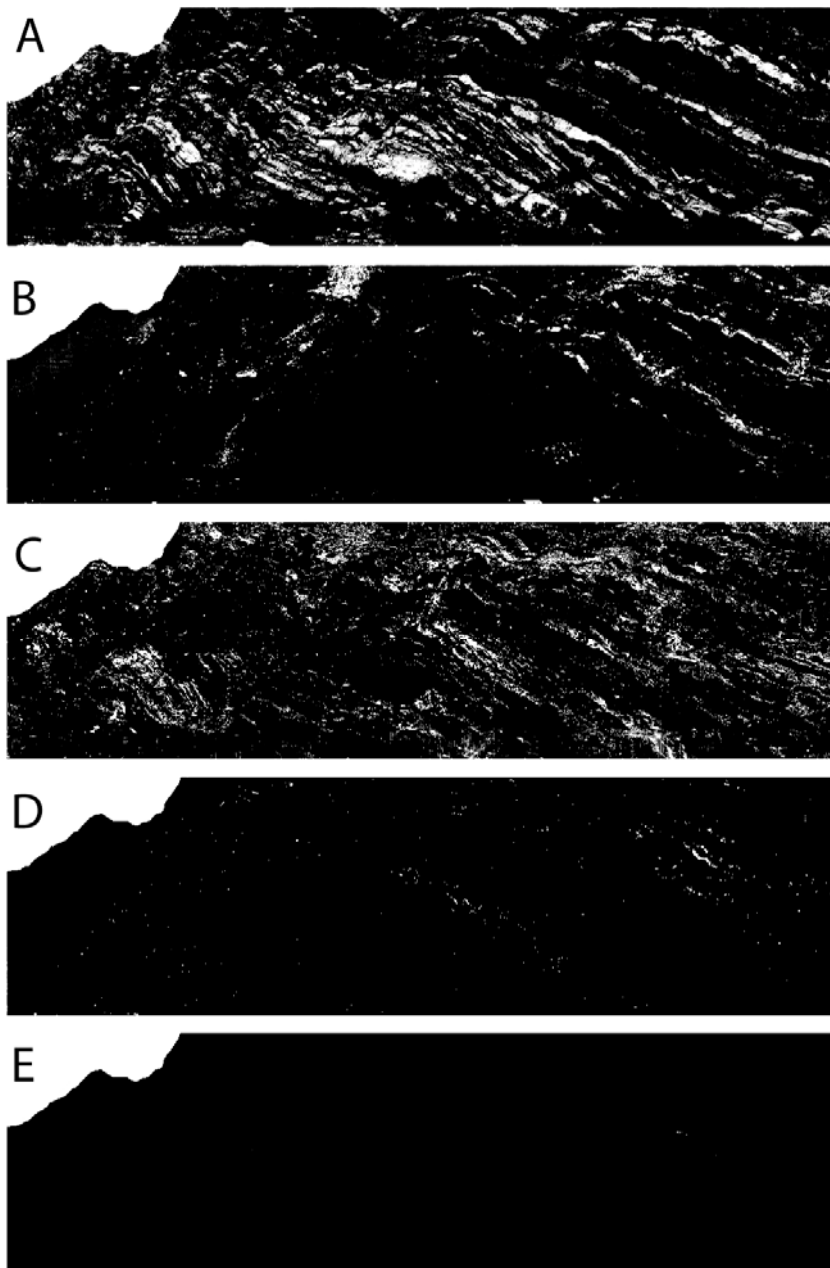


Figure 15.

Comprehensive classification image generated with the Spectral Angle Mapper algorithm. The mineral map indicates pixels which best represent the presence of quartz (yellow), dolomite (magenta), calcite (red), muscovite (cyan), and gypsum (green), as opposed to a mixture analysis map. Vegetation, sky, shadow, and unclassified pixels were masked from the map. These pixels are represented in black.

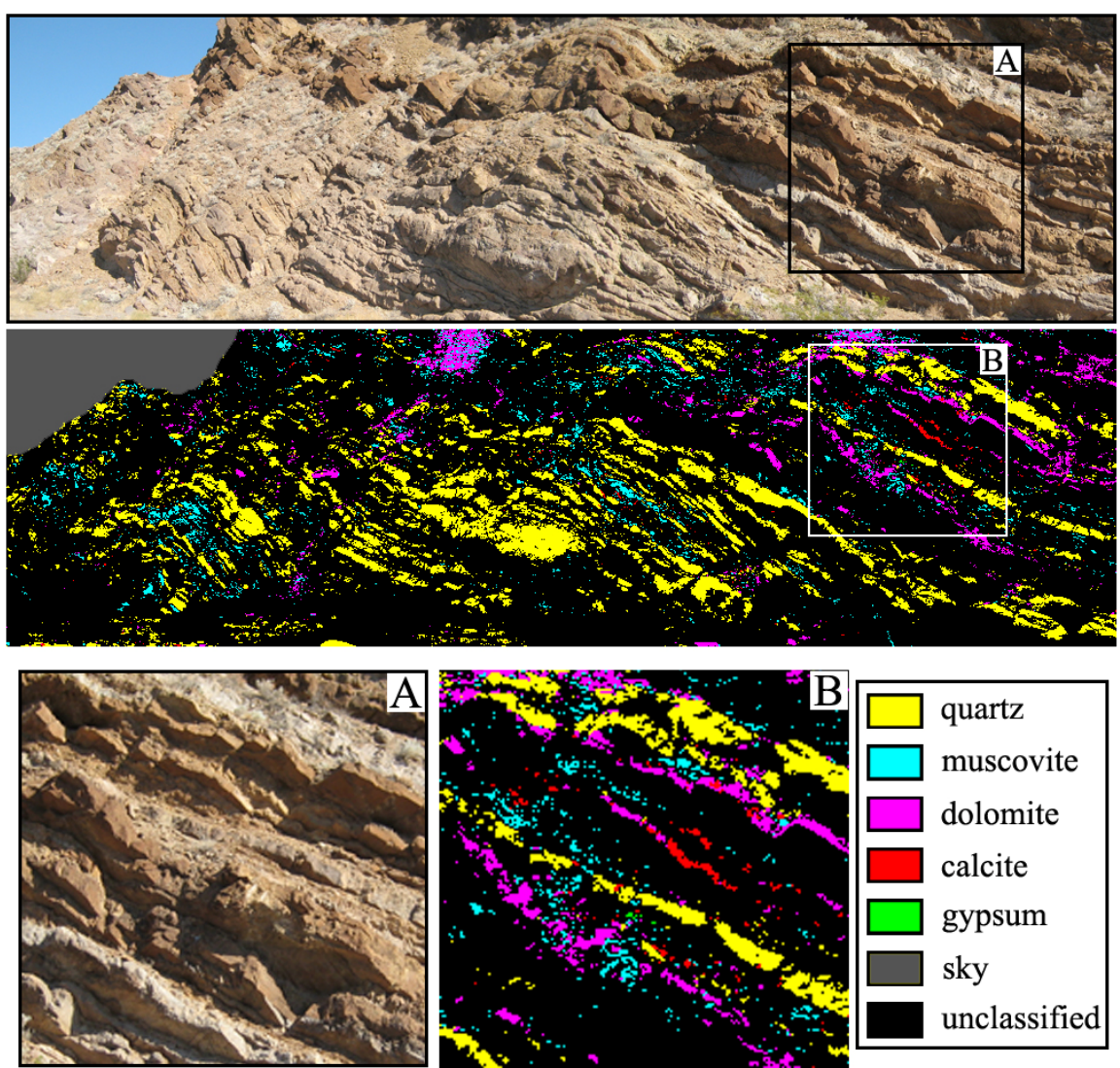
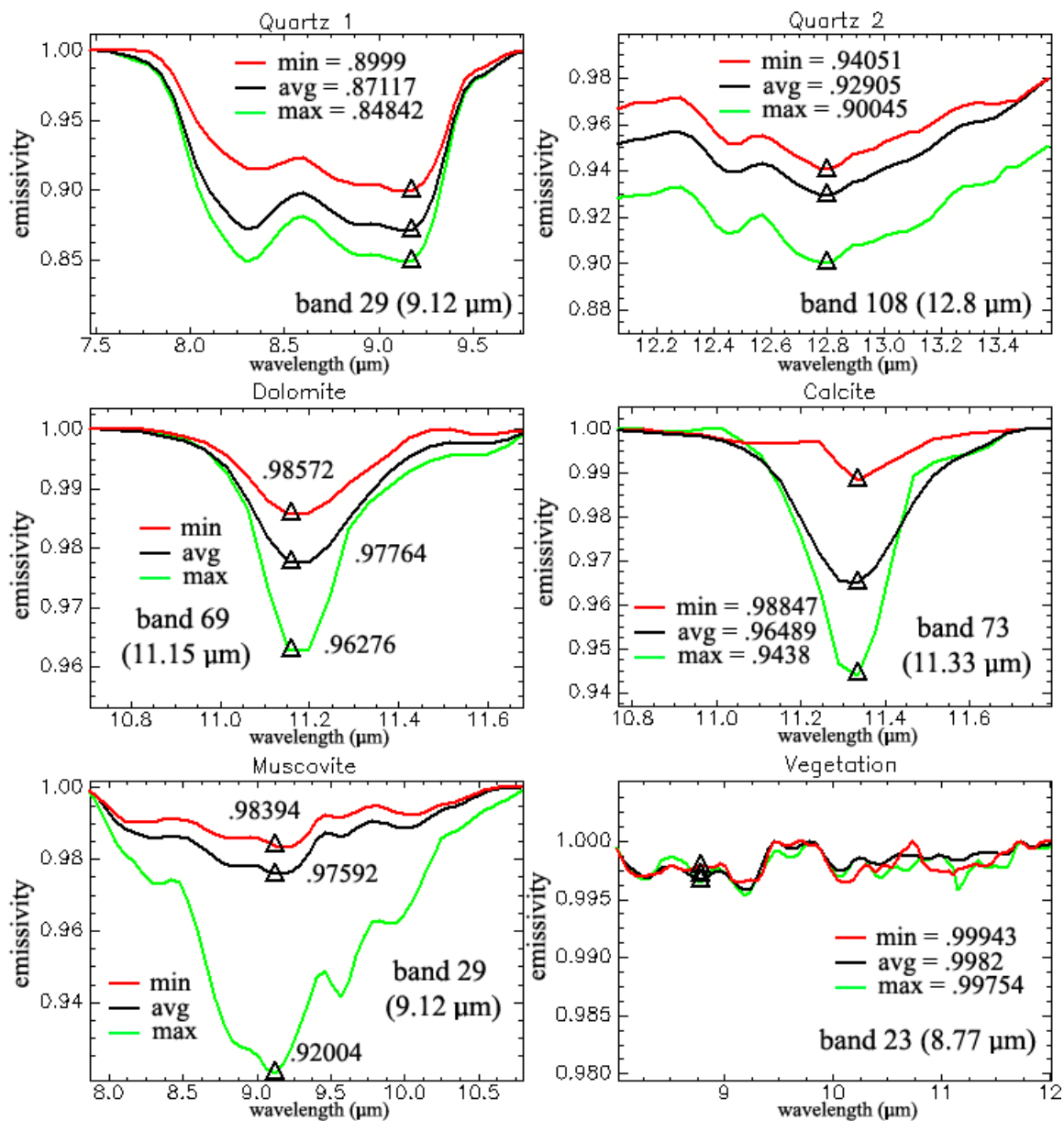


Figure 16. Minimum, average, and maximum emissivity values for mapped minerals corresponding to particular lithologies. The emissivity values indicated are drawn from the center band location of emission minima diagnostic features, denoted by black triangles.



### Chapter 3

## **Mapping rock-forming minerals at Boundary Canyon, Death Valley National Park, California, using aerial SEBASS thermal-infrared hyperspectral image data**

Zan Aslett

Mackay School of Earth Sciences and Engineering, University of Nevada, Reno

\* Based on a manuscript to be submitted to International Journal of Remote Sensing



### 3.1 Abstract

Aerial remotely-sensed spatially enhanced broadband array spectrograph system (SEBASS) longwave-infrared (LWIR) hyperspectral image data were used to map the distribution of rock-forming minerals indicative of sedimentary and meta-sedimentary lithologies around Boundary Canyon, Death Valley, California, USA. Collection of image data over the Boundary Canyon detachment fault (BCDF), which represents a contact between the relatively unmetamorphosed Grapevine Mountains allochthon and the metamorphosed core complex of the Funeral Mountains autochthon, facilitated measurement of numerous lithologies. These included quartz-rich sandstone, quartzite, conglomerate, and alluvium; muscovite-rich schist, siltstone, and slate; and carbonate-rich dolomite, limestone, and marble, ranging in age from late Precambrian to Quaternary. Hyperspectral data processing methodologies were used to reduce data dimensionality and statistically identify and map unique emissivity spectra endmembers. Some minerals (e.g., quartz and muscovite) dominate multiple lithologies, resulting in a limited ability to differentiate them. Abrupt variations in image data emissivity amongst pelitic schists corresponded to and were mapped as amphibolite; these rocks represent gradation from greenschist- to amphibolite-metamorphic facies lithologies. Petrographic analyses of pelitic schists from this area conducted in a previous study identified the presence of low-percentage minerals that are related to degree of metamorphism. However, both laboratory and image data spectral measurements of rocks sampled here revealed no diagnostic spectral features attributed to the presence of these indicator minerals, suggesting remote identification may be limited for this purpose. Although the full potential of LWIR hyperspectral image data may not be fully utilized within this

study area due to lack of measurable spectral distinction between rocks of similar bulk mineralogy, the high spectral resolution of the image data was useful in characterizing silicate- and carbonate-based sedimentary and meta-sedimentary rocks in proximity to fault contacts, as well as for interpreting some mineral mixtures.

### **3.2 Introduction**

This study focuses on analysis of aerially-collected longwave-infrared (LWIR) hyperspectral image data to map rock-forming minerals in a small area within northeastern Death Valley National Park, California, USA (figure 1). Image data were collected over a range of late Precambrian, Cambrian, Tertiary, and Quaternary rock units throughout Boundary Canyon, including a portion of the Boundary Canyon detachment fault (BCDF) and uplifted sedimentary rocks in the northeastern portion of the study area (Workman et al., 2002). The BCDF represents a contact between the generally unmetamorphosed Grapevine Mountains allochthon and the Funeral Mountains autochthon, which was unroofed in the late Cretaceous, thereby exposing a metamorphic core complex (Applegate et al., 1992). As a result, a variety of sedimentary and meta-sedimentary lithologies are exhibited and can be sampled within a small area. Electromagnetic energy emitted from these surfaces can be remotely measured in discrete wavelength ranges and used to identify and map mineralogy based upon variation in emissivity.

The analysis of early remotely-sensed multispectral thermal-infrared (TIR) data highlighted the interpretative utility of airborne emittance measurements to delineate broad lithologies based upon mineralogic variations of emissivity (Kahle et al., 1976;

Kahle and Goetz, 1983; Gillespie et al., 1984; Kahle, 1987; Collins, 1991; Crowley and Hook, 1996). LWIR hyperspectral image data sets collected with sensors such as the Spatially Enhanced Broadband Array Spectrograph System (SEBASS) have expanded the applicability of remote sensing data for geologic applications. Though limited in availability, these data enable detailed identification of subtle differences in surficial mineralogy (Cudahy et al., 2000; Kirkland et al., 2002; Vaughan et al., 2003; Vaughan et al., 2005; Shoffner and Calvin, 2009).

The presented research was concerned with two primary objectives. The first was to determine what minerals could be identified within the study area, whether these were indicative of a) relatively unmetamorphosed sedimentary rock units or b) metamorphosed rock units unroofed by detachment faulting, and if spectral delineation of these rocks was likely. Price (1994) cautions that although hyperspectral measurements are capable of remotely discriminating between common minerals associated with sedimentary rocks, this does not imply that they will be accurate enough to replicate at the same level commonly used by geologists.

The second objective of the study was to investigate and interpret the distribution of these minerals, in context of mapped geology, to determine if image data-derived mineral maps indicated lithologic boundaries associated with the detachment fault structure or alternatively, if the data indicated that this area was mineralogically non-descript. Labotka (1980) conducted petrographic analyses of metamorphic rocks in this area. Biotite-staurolite as well as kyanite-biotite-garnet assemblages in pelitic schists were noted as mineral indicators of particular degrees of metamorphism. Remotely identifying minerals that correspond to certain types of metamorphic rocks within the

exposed core complex could assist in better understanding the distribution of these visually-similar rocks.

Sedimentary rocks comprise a large portion of the Earth's surface; thus many laboratory and remote sensing studies concern mineral mapping of these lithologies. Hunt and Salisbury (1975) established the emissivity characteristics of various sedimentary rocks using laboratory reflectance measurements. Lang et al. (1987) utilized Thermal Infrared Multispectral Scanner (TIMS) image data to identify and associate remotely-mapped silicate, carbonate, and sulfate minerals with sedimentary lithologies in central Wyoming. These measurements were then added to Airborne Imaging Spectrometer (AIS) and Landsat Thematic Mapper (TM) image data classification results to more comprehensively understand the mineral distribution in this area. Evans (1988) evaluated the individual and combined use of TIMS emittance, Landsat TM reflectance, and Synthetic Aperture Radar (SAR) image data to assist in mapping sedimentary lithologies in the Wind River Basin, Wyoming. Bartholomew et al. (1989) used field and laboratory FTIR measurements to characterize common sedimentary rocks, and thereby better understand remotely-sensed measurements of emittance for these types of rocks. Bihong and Xiaowei (1998) demonstrated the use of TIMS image data to delineate sedimentary rocks at the Kalpin Uplift, China based upon bulk mineralogical differences in silica-, carbonate-, and clay-rich lithologies.

### **3.3 Background**

#### 3.3.1 TIR mineral spectroscopy

Laboratory studies using infrared spectroscopy to characterize minerals have resulted in a conceptual understanding of the relationships between molecular crystal structure, interaction of incident radiation, and subsequent molecular vibrational modes (Farmer, 1974; Lyon and Green, 1975; Salisbury and D'Aria, 1992; Thomson and Salisbury, 1993). Consequently numerous spectral libraries have been compiled and are publicly available for research application (Christensen et al., 2000; Clark et al., 2007; Baldridge et al., 2009).

Minerals exhibit vibrational emission features that are diagnostic of crystal lattice structure. Absorption of energy at shorter wavelengths in the reflectance spectrum activates bending and stretching modes of Si-O molecular bonds, thus producing diagnostic emission minima features according to isolation of SiO<sub>4</sub> tetrahedra (Farmer, 1974). Framework silicates exhibit features at shorter wavelengths around 9 μm, sheet silicate minerals between 9 - 10 μm, and chain silicates exhibit features at longer wavelengths between 10 - 11 μm.

Carbonate (CO<sub>3</sub>) crystal structure produces LWIR emission minima in the 11.1 - 11.4 μm region, owing to an asymmetric stretching vibration mode (Lane and Christensen, 1997). Although many minerals exhibit emission features that overlap and can introduce ambiguity, mineral mixtures (e.g., framework silicate, chain silicate, and carbonate mineral mixtures) can produce a combination of features throughout the 8 - 12 μm range. These can potentially be individually identified in hyperspectral image data emissivity spectra and validated using linear mixture models (Vaughan et al., 2003).

### 3.3.2 TIR remote sensing

LWIR spectrometers are suited for identification of crystal structure in rock-forming silicate minerals such as quartz, feldspars, micas, pyroxenes, and garnets, as well as other mineral groups such as carbonates and sulfates, due to their respective diagnostic fundamental vibrational properties. In comparison, diagnostic vibrational, overtone, and combination spectral features indicative of silicates may not be as prominent or even present for these same minerals in the reflected infrared wavelength range.

Remotely-sensed emittance of surface materials varies according to factors such as purity of mineralogical composition; grain size; surface roughness; surface temperature; thermal inertia; and geometric relationship of surfaces to the overhead sensor (Salisbury and D'Aria, 1992). Radiant energy emitted by surfaces exhibits temperature and emissivity components that can be statistically estimated and separated (Realmuto, 1990) using empirical methods (Hook et al., 1992). However, the wavelength-dependent transmissivity of the atmosphere effectively restricts field and remote LWIR measurements of emitted energy to the 7 - 14  $\mu\text{m}$  range. Even within this window of transmission atmospheric absorption and emission (e.g.,  $\text{O}_3$ ,  $\text{H}_2\text{O}$ ), can degrade measurements of surface emittance.

## **3.4 Area of study**

### 3.4.1 Overview

The study area is centered at latitude  $36^{\circ} 47'3''\text{N}$ , longitude  $116^{\circ} 48'24''\text{W}$  along Daylight Pass Road, between the Grapevine and Funeral Mountains of Nevada and California; these ranges together form the northeastern perimeter of Death Valley (figure

2). The study boundaries are based on coverage by a single SEBASS image data flightline extending approximately 14.5 km from the Death Valley Buttes in the southwest to an area near the California/Nevada border and due east of Daylight Pass. The image data intersects seven distinct geologic units as mapped by Workman, et al., 2002. The local environment is extremely arid and only sparse vegetation is observed, minimizing the attenuation of emittance from rock surfaces that can occur at levels as low as 5% (Gillespie and Abbott, 1984). Extensive outcrops of Precambrian, Cambrian, and Tertiary lithologies here provide excellent exposure from which to make remote sensing measurements.

#### 3.4.2 Regional geology

Death Valley is a range-bounded basin located approximately 150 km west-northwest of Las Vegas, Nevada, USA. The basin spans an area measuring nearly 7800 km<sup>2</sup>, and rock units up to 1800 million years old are exposed in a geological environment typical of basin and range configuration. Down-warping of the late Precambrian land surface resulted in regional subsidence (Wright, 1953). A miogeosyncline subsequently developed, and deposition of sediment throughout the Cambrian resulted in diagenesis of sedimentary and meta-sedimentary lithologies exposed today (Norris and Webb, 1976). Twenty-three distinct sedimentary geological formations and two unconformity events have been classified within Death Valley (Hunt and Mabey, 1966). Mesozoic compressional forces and Cenozoic extensional and block-rotation tectonics have resulted in a structurally complex geological environment exhibiting folded normal- and thrust-faulted rock throughout the area.

### 3.4.3 Local geology

This study focuses on the sedimentary and meta-sedimentary rocks comprising the Grapevine Mountains and Funeral Mountains. Unmetamorphosed miogeoclinal strata younger than late Proterozoic Stirling Quartzite form the bulk of rock sequences in the Grapevines, while metamorphosed Proterozoic basement rocks, Pahrump Group, and Johnnie Formation units form the metamorphic core complex representative of the Funeral Mountains (Wright and Troxel, 1993). The BCDF, a late Cretaceous low-angle extensional structure, denotes a structural contact between the ranges (Reynolds et al., 1986; Applegate et al., 1992) (figure 3). The Grapevine Mountains allochthon dips gently at N60W away from the Funeral Mountains autochthon. Extension of the upper plate has been estimated to be between 25 - 30 km (Snow and Wernicke, 1989; Hoisch and Simpson, 1993) based upon correlation of the Grapevine hanging wall at the detachment with the footwall exposed near the Winter's Peak anticline (Snow and Wernicke, 1989). The detachment unroofed low- to medium-grade metamorphic rocks in the Funeral Mountains, yielding greenschist- to amphibolite-facies (Labotka, 1980). A staurolite + biotite isograd for pelitic schist was mapped in proximity to the BCDF contact (Labotka, 1980). Boundary Canyon exhibits a composition of poorly-sorted and well-rounded gravel, represented primarily by weathered quartzite and, to a lesser extent, dolomite and schist.

## **3.5 Methodology**

### 3.5.1 Synopsis



Field surveys were conducted to collect rock samples throughout the area of study to be used as references during image data analysis. Laboratory reflectance measurements in the LWIR wavelength range were made of these samples to produce high quality emissivity spectra and to better interpret image data emissivity spectra. Ancillary laboratory measurements were made using a visible, near-infrared (VNIR), and shortwave-infrared (SWIR) spectrometer, as well as x-ray diffraction (XRD) instrumentation to further corroborate the presence of minerals in certain rocks. Radiometrically-calibrated SEBASS apparent emissivity image data provided by the vendor were then validated against laboratory and library spectra of common minerals. A decorrelation stretch (DCS) image was used for preliminary mineralogical analysis of the image data. The ENVI Hourglass methodology was next used to perform statistical mapping. Manual interpretation of emissivity spectra (expert analysis) was used to further improve mineral map results.

### 3.5.2 Field sample collection

Rock samples were collected throughout an area corresponding to the boundaries of the image data. Samples were chosen based upon their representation of lithologies belonging to a particular geologic unit, as previously mapped (Wright and Troxel, 1993; Workman et al., 2002), or when an otherwise unique outcrop was noted. A total of 103 samples were collected. Eight measurements were made in the field using a Designs & Prototypes micro-FTIR ( $\mu$ FTIR) instrument (Korb et al., 1996; Hook and Kahle, 1996). These were limited due to time constraints, as well as difficulty in transporting the instrument over long distances by foot in variable topography. The sedimentary

lithologies found in the study area were not necessarily exclusive to particular geologic units. Tables 2 - 4 list selected samples collected within the study area with corresponding rock description and minerals identified.

### 3.5.3 Laboratory measurements

A Nicolet 6700 series Fourier transform infrared (FTIR) spectrometer was used to make laboratory measurements of rock samples gathered during field surveys. The FTIR measures bidirectional reflectance and incorporates a gold specular reflector reference panel for calibration purposes. General laboratory measurement procedure involved identifying bulk rock chip samples approximately 1 x 1 x 0.5 cm in size that best preserved surficial expression with regard to the viewing geometry of the overhead sensor. XRD analysis was performed to corroborate select samples in which mineral identity was not satisfactorily determined following spectral measurements. A Philips Electronics PW2273/20 instrument was used to perform these measurements.

### 3.5.4 SEBASS data acquisition and calibration

SEBASS data were acquired over the Boundary Canyon area on July 16, 2007 at 9:15 AM PST. The instrument was flown at approximately 3.7 km above mean ground level. The data dimensions were 128 samples and 4000 line pixels, and resultant ground instantaneous field of view (GIFOV) was approximately 3.7 m. The area of data coverage measured approximately 474 m in width and 14.5 km in length and was oriented approximately SW to NE, extending from the Death Valley Buttes in the southwest, through Boundary Canyon, and terminating in the northeast near Daylight Pass.

SEBASS is a 12-bit pushbroom hyperspectral sensor operated by The Aerospace Corporation that measures emitted TIR energy in 128 channels for each the midwave-infrared (MWIR) range, from 2.0 - 5.2  $\mu\text{m}$ , and LWIR range, from 7.6 - 13.5  $\mu\text{m}$  (Hackwell et al., 1996). Only the LWIR data were investigated in this research due to complexity in separating the mixed reflectance and emittance components of MWIR measurements during daytime collection.

SEBASS data were delivered by the vendor in the form of calibrated radiance, apparent emissivity, and apparent temperature. The apparent emissivity image data were generated using their proprietary in-scene atmospheric correction (ISAC) routine presented in Johnson (1998) and Young et al., (2002), and as reviewed in Vaughan et al. (2003). This procedure results in partial removal of atmospheric effects (only upwelling and transmission are addressed) from radiance measurements and subsequently produces emissivity data using a temperature-emissivity separation (T&S) routine. ENVI 4.6 software was also used to produce a separate calibrated emissivity dataset using the software's atmospheric correction and T&S algorithms (ITT Visual Solutions, 2008). The emissivity data generated with ENVI were first atmospherically corrected using an algorithm similar to that employed by Johnson (1998) and Young et al. (2002). Next, radiance image data were separated into temperature and emissivity image data components using a T&S routine provided in ENVI and based on methods presented in Hook et al. (1992) and Gillespie et al. (1998). The vendor-provided apparent emissivity spectra were then compared to emissivity spectra generated using ENVI. The Aerospace Corporation data were determined to be of higher quality and were retained for mineral mapping, as these image data emissivity spectra more consistently agreed with library

and laboratory mineral spectra than did the ENVI-generated emissivity image data spectra, which exhibited greater variability in mineral features.

### 3.5.5 Image data analysis

Decorrelation stretching was used as the initial method to investigate the emissivity image data. DCS images are generated by applying a principle components transformation to a red, green, blue (RGB) 3-band combination. Color values are then rescaled across the complete range of digital number (DN) values according to the radiometric resolution of the image data. As a result, visual separation of scene components with unique spectral features is enhanced for image data that may otherwise be subdued (Gillespie et al., 1986). A DCS image was generated using RGB bands 70, 40, 29 (11.26  $\mu\text{m}$ , 9.86  $\mu\text{m}$ , 9.29  $\mu\text{m}$ ) to emphasize bulk mineralogical differences of siliceous, micaceous, and carbonate geologic units. The chosen bands corresponded to wavelengths in which quartz, muscovite, and calcite emission minima features occurred.

Statistical mapping was conducted using the ENVI Hourglass methodology to perform more detailed image data analysis. This series of processing steps was originally used to analyze reflectance image data, however the methodology has been previously demonstrated for use in analyzing LWIR hyperspectral image data to map minerals (Vaughan et al., 2003). The supervised ENVI hourglass sequentially performs dimensionality reduction, identification of image data endmembers related to minerals, and mapping of these endmembers using spectral classification algorithms (Boardman and Kruse, 1994).

The data were first processed using the minimum noise fraction (MNF) statistical data reduction procedure. MNF performs noise whitening and then separates noise and coherent information exhibiting the bulk of variance by use of two cascading principal components transforms. Bands used as input for spectral processes were limited to 7 through 88 (8.03  $\mu\text{m}$  - 12.02  $\mu\text{m}$ ) because of noise attributed to atmospheric components below 8  $\mu\text{m}$  and above 12  $\mu\text{m}$ , as in Cudahy (2000), and Vaughan (2003). MNF image data were produced in 15 user-specified bands. Bands 1, 2, 4 and 9 exhibited systematic noise or striping, while bands 3, 5, 6, 7, 8, and 10 produced coherent images. MNF bands above 10 produced speckled or incoherent images.

The coherent MNF bands were used as input for the Pure Pixel Index (PPI) program and processed using default parameters of 10,000 iterations and a threshold factor of 2.5. PPI resulted in the identification of 4454 pixels representative of unique spectra. The N-dimensional Visualizer routine was used to group and average the spectra of these pixels, thus delineating “pure” image data spectra endmembers. These emissivity spectra were then manually inspected, and examples that exhibited similar features were deemed redundant and removed from further consideration. A total of ten PPI-derived mineral endmember spectra were determined to be unique and used to create a spectral library.

The Spectral Angle Mapper (SAM) algorithm was utilized to match PPI-identified endmember spectra against image data spectra (Kruse et al., 1993). SAM has been shown in previous literature to be of particular use in areas where shadowing or topographical variability is present (Yuhua et al., 1992). For the purpose of TIR spectral image data processing, the effects of shadow upon reflectance image data spectra may be analogous

to those of temperature upon emissivity spectra. Region of interest (ROI) pixels were generated for each endmember class and combined to produce comprehensive final mineral maps.

Expert analysis was used as a final method to manually inspect emissivity spectra of select areas of interest identified by either DCS image or SAM mineral maps. Image data emissivity spectra were compared to laboratory FTIR, and library emissivity spectra (Clark et al., 2007 and Christensen et al., 2000 and Baldridge et al., 2009). Context provided by geology maps was used to corroborate and yield better interpretation of image data spectra.

### **3.6 Results**

#### **3.6.1 Interpretation of laboratory FTIR measurements**

Emissivity spectra produced from laboratory FTIR measurements of rock samples collected during field surveys were plotted to determine their mineralogical constituents (figure 4 and table 2). Siliceous rocks were examined first. Quartzite exhibited a relatively pure quartz ( $\text{SiO}_2$ ) signature identified by a prominent doublet with emission minima centered at 8.35 and 9  $\mu\text{m}$  (figure 4a). Fresh surfaces were distinguished by the addition of a sharp minima at 8.18  $\mu\text{m}$  that may be due to increased crystallinity resulting from a high silica percentage (Clark et al., 2007). Sandstone exhibited a quartz-dominated spectra mixed with either albite ( $\text{NaAlSi}_3\text{O}_8$ ), or microcline ( $\text{KAlSi}_3\text{O}_8$ ), as well as muscovite ( $\text{KAl}_2(\text{AlSi}_3\text{O}_{10})(\text{F},\text{OH})_2$ ) (figure 4b). Feldspars were characterized by narrow emission minima centered near 9.17, 9.6, and 10  $\mu\text{m}$  while muscovite exhibited a broad emission minima feature with shoulders spanning from 8.35 - 10.6  $\mu\text{m}$  punctuated

by a broad lobe centered at 9  $\mu\text{m}$  and a narrow minima at 9.6  $\mu\text{m}$ . Conglomerate samples varied in emissivity depending upon clast (usually quartzite pebbles or gravel) and matrix composition. Silicic matrices were most often observed during field surveys, and these resulted in quartz-dominated emissivity spectra (figure 4c).

Carbonate lithologies were next investigated. Conglomerates with carbonate matrices were observed in more limited instances that exhibited mixed quartz-calcite ( $\text{CaCO}_3$ ) (figure 4d) or quartz-dolomite ( $\text{CaMg}(\text{CO}_3)_2$ ) (figure 4e) emissivity spectra. Calcite was identified via a narrow emission minima centered at 11.3  $\mu\text{m}$ , while dolomite was characterized by similar emission minima shifted to a lower wavelength of 11.2  $\mu\text{m}$ . Oxidized dolomite with generally rough surface texture exhibited mixed dolomite and subtle quartz emissivity spectra (figure 4f). Oxidized limestone was identified as mixed calcite and minor quartz (figure 4g). Marble was somewhat distinct from dolomite and limestone due to a slightly wider and asymmetric emission minima feature located near 11.25  $\mu\text{m}$  (figure 4h).

Micaceous lithologies were next examined. Siltstone exhibited a muscovite-dominated mixture with a minor contribution by quartz, but presence of feldspar was not indicated (figure 4i). Metamorphosed sedimentary rocks largely exhibited muscovite as well. Chloritized siltstone featured muscovite-dominated spectra mixed with a chlorite component (figure 4j). The presence of chlorite ( $(\text{Fe,Mg,Al})_6(\text{Si,Al})_4\text{O}_{10}(\text{OH})_8$ ) was indicated by a moderate emission minima near 9.65  $\mu\text{m}$  and a narrow subtle feature at 10.4  $\mu\text{m}$ . Slate exhibited very similar spectra dominated by mixed muscovite and chlorite (figure 4k). Pelitic schists produced emissivity spectra with features that varied according to the proportion of muscovite, quartz, feldspar, and chlorite apparent at a particular

surface area of a sample (figures 4l, 4m, and 4n). Schists with notable porphyroblasts produced mixed emissivity spectra of muscovite, quartz, and chlorite. These porphyroblasts were muscovite-dominated, which may be attributed to retrograde metamorphism (Labotka, 1980). Greenish sandstone was dominated by chlorite, with only minor observable contributions by muscovite and quartz (figure 4o). Emissivity spectra of this sample exhibited moderately broad emission minima centered at 9.6  $\mu\text{m}$ .

Measurements of amphibolite produced emissivity spectra dominated by hornblende, as identified by a broad emission minima from 8.6 - 11  $\mu\text{m}$  and punctuated by narrower minima at 8.9, 9.6, and 10.15  $\mu\text{m}$  (figure 4p). The narrow emission minima features of this rock type were muted at some angles of measurement, and the overall shape of the spectra in the 8.6 - 11  $\mu\text{m}$  range somewhat resembled library spectra of both spessartine ( $(\text{Mn(II)}_3)\text{Al}_2(\text{SiO}_4)_3$ ) and hematite ( $\text{Fe}_2\text{O}_3$ ), each of which are characterized by a broad trough centered at 10.16  $\mu\text{m}$ . This ambiguity was addressed and resolved through additional laboratory measurements.

### 3.6.2 Ancillary VNIR/SWIR and XRD laboratory measurements

Additional laboratory measurements were made of rock samples in which mineral constituents could not be satisfactorily identified by FTIR-derived spectra alone. VNIR/SWIR measurements of schist samples resulted in the identification of chlorite, muscovite, and goethite in each. Goethite features dominated the visible and near-infrared (VIS/NIR) wavelength ranges, and was characterized by absorptions at approximately 485, 625, and 924 nm, resulting in a prominent peak at 765 nm. Spectral features in the SWIR for these samples included a sharp absorption at approximately



2200 nm attributed to muscovite. A moderate absorption at 2335 nm, as well as a minor absorption at 2250 nm were both attributed to chlorite. The green sandstone was comprised of goethite and chlorite. An asymmetric doublet absorption feature identified in the SWIR at 2335 and 2250 nm was attributed to the strong presence of chlorite; muscovite was not detected. The amphibolite sample yielded chlorite-dominated spectra similar to the greenish sandstone.

XRD measurements were made for the green sandstone, pelitic schists, and amphibolite. Chlorite, clinocllore, quartz, and albite were identified in the sandstone sample. Measurement of the schists yielded presence of muscovite, quartz, and chlorite. The amphibolite sample was found to be comprised of magnesio-hornblende, quartz, and chlorite.

### 3.6.3 Mineral mapping

#### 3.6.3.1 DCS image

The DCS image generated using bands that coinciding with emission minima features of siliceous, micaceous, and carbonate minerals was analyzed first. RGB bands 70, 40, 29 (11.26  $\mu\text{m}$ , 9.86  $\mu\text{m}$ , 9.29  $\mu\text{m}$ ) were used to visually emphasize bulk mineralogical differences in the study area (figure 5). Siliceous units were displayed in yellow, micaceous units were magenta, and carbonate units were cyan. Comparison of image data emissivity spectra to DCS color regions showed that yellow areas corresponded to prominent quartz spectra; magenta area exhibited muscovite-dominated spectra; and cyan colors represented either dolomite or calcite spectra. Abrupt changes in color were observed that indicated contacts between some geologic units (e.g., Johnnie

Formation, Stirling Quartzite, and Wood Canyon Formation) or surface types (e.g. alluvium and outcrop), while other units more subtly graded between colors. Areas of pronounced color contrast between units and intermediate colors (conveying variation of mineralogy possibly outside the scope of the targeted groups) were investigated in more detail by manual inspection of image data spectra and during statistical mapping.

### 3.6.3.2 Statistical mapping

The PPI endmember identification routine resulted in the identification of ten spectrally distinct image data endmembers. Mineral endmember classes included: quartz 1; quartz 2; muscovite + quartz 1; muscovite + quartz 2; calcite; dolomite; hornblende; montmorillonite; and quartz + feldspar + muscovite  $\pm$  chlorite (figure 6). The quartz 1 and quartz 2 classes were distinguished by an overall difference in emissivity values for the diagnostic doublet feature. At band 26 (9.13  $\mu\text{m}$ ) quartz exhibits the lowest emissivity value for the doublet; the average emissivity value of quartz 1 here was 0.85, and quartz 2 produced an average value of 0.72. Muscovite + quartz 1 represented a mixture dominated by muscovite, while the muscovite + quartz 2 mixture was dominated by quartz. Statistical mapping was performed by matching selected mineral endmember emissivity spectra to the image data using SAM. Analysis was first performed upon the entire data set, and then more detailed mapping was conducted upon smaller areas indicated in figure 2.

Scene one represented the southwestern portion of the image data coverage, which coincided with the Death Valley Buttes. The geologic units mapped within the boundaries of the image data here belonged to the late Proterozoic and lower Cambrian

Wood Canyon formation (€Zw), as well as Miocene and Eocene sedimentary rocks (Tso), and young Quaternary alluvium (Qay) (figure 7). SAM identified and mapped calcite (red), dolomite (magenta), and quartz 1 (green) within the boundaries of the €Zw unit. The muscovite and quartz 1 class (cyan) was mapped in an area corresponding to the Tso unit. The Qay unit was mapped as quartz 2 (yellow). Further description of rock samples collected in this area are listed in table 3.

Scene two is located further along the flightline toward the junction of Daylight Pass and Beatty Roads. The image data here intersected six different geologic units: late and middle Proterozoic Pahrump Group (ZYp); late Proterozoic Johnnie and Wyman formations (Zj); late Proterozoic Stirling Quartzite and Reed Dolomite formations (Zs); a limited exposure of €Zw; Pliocene and Miocene sedimentary rocks (Ts4); and Qay (figure 8). Mixed muscovite and quartz 1 (cyan) and calcite (red) pixels were mapped within the ZYp unit. Mixed muscovite and quartz 1 (cyan), in addition to small clusters of pixels representing hornblende (orange) was mapped in the Zj unit. The €Zw unit was mapped as quartz 1 (green), and dolomite (magenta), while the Ts4 unit was mapped as quartz 1 (green). Qay was mapped as quartz 2 (yellow) and mixed muscovite and quartz 2 (purple). Further description of rock samples collected in this area is listed in table 4.

The Zs, Tso, Ts4, Qay, and Qtau units were covered by image data in scene three (figure 9). Mixed muscovite and quartz 1 (cyan) and hornblende (orange) were mapped within boundaries of the Zs unit. Surface areas in the Tso unit were mapped as quartz 1 (green), mixed quartz, muscovite, and feldspar (brown), and montmorillonite (blue). Ts4 was mapped as quartz 1 (green), mixed quartz, muscovite, and feldspar (brown), and

dolomite (magenta). Qtau and Qay were mapped as quartz 1 (green). Further description of rock samples collected in this area are listed in table 5.

### 3.6.3.3 Expert analysis

Image data emissivity spectra were manually inspected in further detail within small areas of interest that were noted during analysis of DCS image and SAM mineral maps. This time-intensive process involved making comparisons between image data, laboratory, and library spectra to interpret subtle emission features within mineral mixtures, and thereby maximize the utility of the image data. For example, image data emissivity spectra of sandstone in scene three exhibited multiple minima features in the 8.1 - 10.5  $\mu\text{m}$  wavelength range. By matching library spectra of pure minerals with these spectra, a mixture comprised of framework (quartz and feldspar) and phyllosilicate (muscovite) minerals was identified.

A small number of pixels were found that displayed a unique emission minima at approximately 9.3  $\mu\text{m}$  that matched montmorillonite. This spectra was associated with altered argillite that had been overlooked during the PPI process. Manual inspection of the image data spectra also helped to extend the number of mapped pixels for the hornblende class that corresponded to outcrops of amphibolite, which had not been mapped during the statistical mapping process.

## **3.7 Discussion**

### 3.7.1 General observations

The LWIR image data were useful for detecting, identifying, and mapping quartz, muscovite, feldspar, montmorillonite, hornblende, calcite, dolomite, chlorite, and

mixtures of these in some pixels. Multiple lithologies were dominated by either quartz or muscovite. Sandstone, quartzite, siliceous conglomerate, and the majority of alluvium each exhibited strong quartz emissivity spectra. However, spectral separation of lithologies based upon the depth of quartz emission minima was not successful, as ranges in depth value of the quartz feature were found to be associated less with differences between particular lithologies and instead related to whether outcrops or unconsolidated material comprised the measured surfaces, with development of consolidated material generally resulting in decreased strength.

Outcropping sandstone in scene three were comprised of quartz, muscovite, and feldspar. In certain image data pixels the emissivity spectra yielded a broad emission minima ranging from 8.1 - 10.5  $\mu\text{m}$ , centered near 9  $\mu\text{m}$ , that was originally interpreted as a single unidentified mineral. In this example the combined emission minima features of quartz, feldspar, and muscovite had become indistinguishable, similar to what would be expected of a multispectral measurement of this surface. Manual inspection of adjacent pixels helped to examine variability of this spectra and emphasize the different constituents.

Quartzite features a sharp emission minima trough at approximately 8.4  $\mu\text{m}$  that is detected in laboratory FTIR measurements of fresh surfaces. However, emissivity spectra derived from image data covering quartzite exposures were not able to resolve this feature, likely due to a lack of sufficient fresh exposure, the presence of clay or oxide coatings attenuating the feature, or a limit of mineral-related spectral values in the 7.5 - 8.5  $\mu\text{m}$  range, where both transmissivity associated with water vapor and detector sensitivity decrease. Spectrally determining the presence of clay coatings upon rocks in

the study area was not able to be accomplished using the image data, whereas variability in emissivity associated with clays such as kaolinite and kaolinite, while still limited in comparison to SWIR reflectance measurements, were better observed in laboratory FTIR measurements.

For micaceous lithologies, including siltstone, schist, and slate, each was dominated by muscovite. Comparison of emissivity spectra derived from laboratory measurements of these rocks indicated that, with exception of chloritized siltstone and slate, spectral delineation should be possible. However, analysis of the image data did not support this observation. Image data spectra corresponding to pelitic schist did exhibit variation in subtle features related to quartz, feldspar, and chlorite, but this lithology was not able to be spectrally delineated from the other micaceous rocks based upon presence or lack of these accessory mineral features elsewhere using statistical mapping methods. A limited diversity of mappable muscovite-dominated rocks may be due in part to a lack of large outcrops and corresponding limitations of spatial resolution imposed by 4 m GIFOV image data.

Carbonate rocks were able to be successfully mapped with the image data as either dolomite- or calcite-based because of a distinctive shift in emission minima of  $0.08 \epsilon$  between the two minerals. However subtle differences between dolomite, calcite, and marble that were observed in laboratory FTIR spectra were not replicated in the image data. As a result, calcite marble was grouped with other calcite-rich rocks such as limestone and carbonate conglomerate, and a general calcite class was mapped. The spectral resolution of the SEBASS data should be sufficient to spectrally delineate the dolomite, calcite, and marble rocks; it is possible that the particular marble samples

characterized in the laboratory were unique however not entirely representative of the marble unit.

Hornblende was originally misidentified as a garnet mineral due to a similar broad emission minima features centered at 10.15  $\mu\text{m}$ . Amphibolite outcrops are relatively limited within the study area, however pelitic schists that feature a garnet component are more extensive (Labotka, 1980). As a result these rocks were initially characterized as garnetiferous mica schist. Further laboratory measurements helped to mineralogically identify the bulk constituent of this rock, magnesio-hornblende, and then accurately produce an image data pixel map.

### 3.7.2 Geological interpretation of mineral maps

#### 3.7.2.1 BCDF zone

Image data analysis and field checking of map results indicated that calcite and dolomite were well differentiated. This was useful at a practical level because oxidized limestone, dolomite, and marble were visually similar in most places within the study area; some carbonate rock exposures appeared banded and folded, indicating likely marbleization, however elsewhere marble was indistinguishable from lightly or relatively unmetamorphosed dolomite. As related to structure in the BCDF area, image data-delineated calcite and dolomite rocks indicated a distinct contact between metamorphosed calcite marble belonging to the mid- to late- Proterozoic Pahrump Group unit, and unmetamorphosed dolomite belonging to the Precambrian/Cambrian Wood Canyon Formation (figure 10). Because no other minerals found in the study area exhibit diagnostic spectral features that overlap the emission minima of these minerals, the

mapped pixels for these classes were mapped accurately. Field checks in these areas helped to corroborate the map results.

Remotely-identified and mapped muscovite was associated with greenschist-facies pelitic schist belonging to the Johnnie Formation. A biotite-staurolite isograd for schist in this unit was plotted from a previous geochemical study conducted in the area (Labotka, 1980). Analysis of image data emissivity spectra in this area did not result in successful detection of these indicator minerals, likely due to very small percentage of these to total rock composition. Hornblende associated with amphibolite was mapped amongst the predominant schist within the unit. This lithology is associated with medium-grade metamorphism of amphibolite facies; consequently, this is also the highest grade found within the Funeral Mountains metamorphic core complex (Labotka, 1980; Troxel and Wright, 1993). These rocks can be followed nearly at topographical contour here to outcrops on the floor of the opposite side of the canyon, and may indicate a transition point from medium-grade amphibolite facies to lower-grade greenschist facies, as well as provide a reliable mineralogic marker for the BCDF zone.

Muscovite, hornblende, dolomite, and calcite were each indicative of an aspect of the BCDF zone in this area, and each was found to be successfully mapped using the SEBASS image data. However, muscovite was also comprised many other rock types in the study area, and was not entirely unique to the fault zone. Calcite associated with marble was helpful in providing a mineralogic contrast with the relatively unmetamorphosed adjacent dolomite rock unit. However, other locations in the study scene also were comprised of calcite, namely limestone near the Death Valley Buttes.



Amphibolite was to be the most unique mineral that can be remotely mapped and is unequivocally related to the detachment fault structure.

### 3.7.2.2 Tertiary sedimentary rocks

A lithologic boundary in scene three was characterized by mineralogical contrast between gravels, uplifted sedimentary strata, and lightly-altered meta-sedimentary rocks (figure 11). Relatively unmetamorphosed sandstone and dolomite (Ts4), and altered argillite rocks (Tso) are juxtaposed against one another, where sandstone was identified and mapped as a mix of quartz, feldspar, and muscovite, and the argillite was spectrally dominated by montmorillonite, which was unique to the entire study area. Field observations of this area revealed that extensive alteration, including chloritization, had occurred near the boundary of these units. Past mining activity was noted by older piles of gangue material.

### 3.7.3 Refining geology maps with remote sensing data

Geology maps are created from observations made at discrete locations on the ground in order to interpolate lithologic information, thereby maximizing limited time in the field. Boundaries in remote sensing mineral maps between lithologies are not necessarily implied, especially as weathering products can converge or diverge from outcrops based on geomorphology (Siegal and Abrams, 1976), producing intimate mineral mixtures. One limitation of remote sensing data-derived mineral maps is that pixels mapped as a certain mineral in the sedimentary rock environment may not be easily constrained to a particular geologic unit due to some lithologies being present in multiple formations, such as quartzite and dolomite in both the Wood Canyon and

Stirling Quartzite formations (Diehl, 1979; Wertz, 1983). Differences between geology maps by Hunt and Mabey (1966); Wright and Troxel (1993); and Workman et al. (2002) and a mineral map derived from analysis of the SEBASS image data were compared.

The Death Valley Buttes area is used as an example to illustrate differences between information provided by respective data sources (figure 12). Mineral mapping indicated that the Buttes were comprised of siliceous (quartzite, conglomerate, and sandstone) and carbonate (limestone and dolomite) lithologies on the southeastern side of the grand Butte, while the northeastern flank was predominantly comprised of micaceous rocks (siltstone).

As a result, distinct mineralogical contacts could be used to provide further detail of likely rock units, and relate these to more specific geologic units. Hunt and Mabey mapped a single general Paleozoic unit in this area, but no further delineation of lithologic units is presented. The Workman map also did not delineate separate units in the grand Butte, though a fault is mapped that corresponds well to the location of the mineralogic boundary indicated by SEBASS image data. The Wright and Troxel map indicated further detail of the Grande Butte, but a small Tsa unit indicative of Tertiary siltstones and sandstones could be further extended to the northeastern corner of the Grande Butte, where two mapped Wood Canyon formation units could be withdrawn.

### **3.8 Conclusion**

SEBASS image data were used to remotely measure energy emitted from outcrops of numerous sedimentary and meta-sedimentary lithologies within the Boundary Canyon study area. Calibrated SEBASS image data were validated by comparison of

emissivity spectra to laboratory measurements of rock samples collected within areas of data coverage. The distributions of minerals mapped using the data within the study area were generally found to be in agreement with referenced geology maps. Broad groups of siliceous, micaceous, and carbonate lithologies were mapped with simple image processing techniques such as DCS. However, quartz- and muscovite-dominated pixels were not able to be mapped exclusively to particular sedimentary or meta-sedimentary lithologies. Instead quartz was mapped in pixels coinciding with exposed quartzite, sandstone, conglomerate, and certain alluvium units; muscovite was associated with schist, siltstone, slate, and an alluvial unit.

The image data complemented information provided by geologic maps by focusing attention to contacts between relatively unmetamorphosed dolomite and metamorphosed calcic marble and amphibolite; identifying small areas of unique mineral instances such as hornblende; and further defining lithologic boundaries. While multispectral image data may be appropriate for mapping lithologies comprised of simple bulk mineralogies, hyperspectral image data were shown to provide added benefit for identifying more narrow emission features indicative of framework and sheet silicates (e.g., feldspar and montmorillonite, respectively), and broad features specific to chain silicates, which is a powerful tool to assist in mapping rocks found in metamorphic core complex areas.

Data analysis can facilitate the extrapolation of mineralogically distinct yet visually similar rocks, reducing the time needed to identify the full diversity of rock types within an area and enabling efficient mineral mapping of areas that are difficult to travel to or work in. Conversely, field study is a requirement to understand the limitations and

overall usefulness of hyperspectral image data for answering research questions about geology. Geologic maps were crucial to reference during field surveys and image data analysis as they provided context and increased confidence in mapping minerals and lithologic boundaries.

The 4 m GIFOV of the collected SEBASS LWIR hyperspectral image data was found to be a good spatial resolution in which to accomplish the research objectives, because the data provided a good compromise between resolving small outcrops yet was able to differentiate between geologic unit contacts. A trade-off may occur with higher GIFOV data possibly enhancing the identification of mixture constituents that exhibit narrow emission features.

In conclusion, the image data were found to be an ideal tool with which to remotely identify minerals in the structurally complex sedimentary and meta-sedimentary rock environment of peripheral northeastern Death Valley. SEBASS image data collected along the length of the Funeral Mountains metamorphic core complex, from Daylight Pass Road to Winter's Peak, is recommended for future study. These data may assist in distinguishing and mapping the distribution of minerals associated with particular degrees of metamorphism, and thus better characterize the Funeral Mountains metamorphic core complex.

### **3.9 Acknowledgements**

This research was supported by a Department of Energy (DOE) / National Nuclear Security Administration (NNSA) NA-22 grant. We would like to thank Dean

Riley of The Aerospace Corporation for data acquisition and coordination. We also thank Todd Morken for helping with field surveys and  $\mu$ FTIR measurements.

### 3.10 References

- Applegate, J.D.R., Walker, J.D., and Hodges, K.V. (1992). Late Cretaceous extensional unroofing in the Funeral Mountains metamorphic core complex, California. *Geology*, 20, pp. 519-522.
- Abrams, M.J., Kahle, A.B., Palluconi, F.D., and Schieldge, J.P. (1984). Geologic mapping using thermal images. *Remote Sensing of Environment*, 16 (1), pp. 13-33.
- Baldrige, A. M., Hook, S. J., Grove, C. I. and Rivera, G. (2009). The ASTER Spectral Library V. 2.0., *In press, Remote Sensing of Environment*.
- Bartholomew, M.J., Kahle, A.B., and Hoover, G. (1989). Infrared spectroscopy (2-20  $\mu\text{m}$ ) for the geological interpretation of remotely-sensed multispectral thermal infrared data. *International Journal of Remote Sensing*, 10 (3), pp. 529-544.
- Bihong, Fu and Xiaowei, Chou (1998). Thermal infrared spectra and TIMS imagery features of sedimentary rocks in the Kalpin Uplift, Tarim Basin, China. *Geocarto International*, 13 (1). pp. 69-73.
- Boardman J. W., and Kruse, F. A. (1994). Automated spectral analysis: A geologic example using AVIRIS data, north Grapevine Mountains, Nevada. *Proceedings of the Tenth Thematic Conference on Geologic Remote Sensing*, Environmental Research Institute of Michigan, Ann Arbor, MI, pp. I-407-I-418.
- Christensen, P. R., Bandfield, J.L, Hamilton, V.E., Howard, D.A., Lane, M.D., Piatek, J.L., Ruff, S.W., and Stefanov, W.L. (2000). A thermal emission spectral library of rock-forming minerals, *Journal of Geophysical Research*, 105 (E4), pp. 9735-9739.

- Clark, R.N., Swayze, G.A., Wise, R., Livo, E., Hoefen, T., Kokaly, R., Sutley, S.J. (2007). USGS digital spectral library splib06a, *U.S. Geological Survey*, Digital Data Series 231.
- Collins, A.H. (1991). Thermal infrared spectra and images of altered volcanic rocks in the Virginia Range, Nevada, *International Journal of Remote Sensing*, 12 (7), pp. 1559-1574.
- Crowley, J.K. and Hook, S. J. (1996). Mapping Playa Evaporite Minerals and Associated Sediments in Death Valley, California, with Multispectral Thermal Infrared Images. *Journal of Geophysical Research*, 101, pp. 643-660.
- Cudahy, T.J., Okada, K., Yamato, Y., Maekawa, M., Hackwell, J.A., and Huntington, J.F. (2000). Mapping skarn and porphyry alteration mineralogy at Yerington, Nevada, using airborne hyperspectral TIR SEBASS Data, *CSIRO exploration and mining report 734R*, CSIRO Exploration and Mining Co, Floreat Park, WA, Australia.
- Diehl, P.E. (1979). The stratigraphy, depositional environments, and quantitative petrography of the Precambrian-Cambrian Wood Canyon Formation, Death Valley. *Ph.D. thesis*, Pennsylvania State University.
- Evans, D. (1988). Multisensor classification of sedimentary rocks. *Remote Sensing of Environment*, 25 (2), pp. 129-144.
- Farmer, V.C., Editor (1974). *The infrared spectra of minerals*. Mineralogical Society Monograph vol. 4, Mineralogical Society, London.
- Gillespie, A.R., Rokugawa, S., Matsunaga, J.S., Cothorn, S. and Kahle, A.B. (1998). Temperature and emissivity separation algorithm for Advanced Spaceborne Thermal Emission and Reflection Radiometer (ASTER) images, *IEEE Transactions on*

- Geoscience and Remote Sensing*, 36 (4), pp. 1113-1126.
- Gillespie, A.R., Kahle, A.B. and Walker, R.E. (1986). Color enhancement of highly correlated images: I. Decorrelation and HIS contrast stretches. *Remote Sensing of Environment*, 20, pp. 209-235.
- Gillespie, A.R., Kahle, A.B., and Palluconi, F.D. (1984). Mapping alluvial fans in Death Valley, California, using multi channel thermal infrared images. *Geophysical Research Letters*, 11, pp. 1153-1156.
- Gillespie, A.R., Abbott, E. (1984). Mapping compositional differences in silicate rocks with six-channel thermal images. *Proceedings of the 9<sup>th</sup> Canadian Symposium on Remote Sensing*, St. John's, Newfoundland, Canada, pp. 327-336.
- Hackwell, J.A., Warren, D.W., Bongiovi, R.P., Hansel, S.J., Hayhurst, T.L., Mabry, D.J., Sivjee, M.G., and Skinner, J.W. (1996). LWIR/MWIR imaging hyperspectral sensor for airborne and ground-based remote sensing, *The International Society for Optical Engineering*, 2819, pp. 102-107.
- Hoisch, T.D. and Simpson, C. (1993). Rise and tilt of metamorphic rocks in the lower plate of a detachment fault in the Funeral Mountains, Death Valley, California. *Journal of Geophysical Research*, 98, pp. 6805-6827.
- Hook, S.J. and Kahle, A.B. (1996). The Micro Fourier Transform Interferometer ( $\mu$ FTIR) - A New Field Spectrometer for Acquisition of Infrared Data of Natural Surfaces. *Remote Sensing of Environment*, 56, pp. 172-181.
- Hook, S.J., Gabell, A.R., Green, A.A., and Kealy, P.S. (1992). A comparison of techniques for extracting emissivity information from thermal infrared data for



- geologic studies. *Remote Sensing of Environment*, 42, pp. 123-135.
- Hunt, G.R. (1980). Electromagnetic radiation: The communication link in remote sensing. *Remote Sensing in Geology*, edited by B.S. Siegal and A.R. Gillespie. New York, Toronto: Wiley.
- Hunt, G.R., and Salisbury, J.W. (1975). Mid-Infrared Spectral Behavior of Sedimentary Rocks. *Air Force Cambridge Research Laboratories Report*, Number AFCRL-ERP-520, pp. 1-48.
- Hunt, C.B., and Mabey, D.R. (1966). General geology of Death Valley, California. *United States Geological Survey Professional Paper*, 494-A.
- ITT Visual Solutions (2008). ENVI User's Guide, Version 4.3. ITT Visual Solutions, Boulder, Colorado.
- Johnson, B.R. (1998). In-scene atmospheric compensation: application to the SEBASS data collected at the ARM site, Part I. *Aerospace Corporation Report*, (ATR-99(8407), Part I).
- Kahle, A.B. (1987). Surface emittance, temperature and thermal inertia derived from Thermal Infrared Multispectral Scanner (TIMS) data for Death Valley, California. *Geophysics*, 52 (7), pp. 858-874.
- Kahle, A.B. and Goetz, A.F.H. (1983). Mineralogic information from a new thermal infrared multispectral scanner, *Science*, 222, pp. 24-27.
- Kahle, A.B., Gillespie, A.R., Goetz, A.F.H. (1976). Thermal inertia imaging: a new geologic mapping tool. *Geophysical Research Letters*, 3 (1).
- Kirkland, L.E., Herr, K.C., Keim, E., Adams, P.M., Salisbury, J., Hackwell, J., Treiman, A. (2002). First use of an airborne thermal infrared hyperspectral scanner for

- compositional mapping. *Remote Sensing of Environment*, 80, pp. 447-459.
- Korb, A.R., Dybwad, P., Wadsworth, W., and Salisbury, J.W. (1996). Portable Fourier transform infrared spectrometer for field measurements of radiance and emissivity, *Applied Optics*, 35, pp. 1679-1692.
- Kruse, F.A., Lefkoff, A.B., and Dietz, J.B. (1993). Expert system-based mineral mapping in Northern Death Valley, California/Nevada, using the Airborne Visible/Infrared Imaging Spectrometer (AVIRIS). *Remote Sensing of Environment*, 44, pp. 309-336.
- Labotka, T.C. (1980). Petrology of a medium-pressure regional metamorphic terrane, Funeral Mountains, California. *American Mineralogist*, 65, (7-8), pp. 670-689.
- Lane, M.D. and Christensen, P.R. (1997). Thermal infrared emission spectroscopy of anhydrous carbonates. *Journal of Geophysical Research*, 102 (E11), pp. 25,581 - 25,592.
- Lang, H.R., Adams, S.L., Conel, J.E., McGuffie, B.A., Paylor, E.D., and Walker, R.E. (1987). Multispectral Remote Sensing as Stratigraphic and Structural Tool, Wind River Basin and Big Horn Basin Areas, Wyoming. *AAPG Bulletin*, 71 (4), pp. 389-402.
- Lyon, R. J. P., and Green, A. A. (1975). Reflectance and emittance of terrain in the mid-infrared (6 – 25  $\mu\text{m}$ ) region. Ch 7 in: *Infrared and Raman Spectroscopy of Lunar and Terrestrial Minerals*, Academic Press, Inc., pp. 164–194.
- Norris, R.M., and Webb, R.W. (1976). *Geology of California*. John Wiley & Sons, N.Y., pp. 91-122.
- Price, J.C. (1994). How unique are spectral signatures? *Remote Sensing of Environment*,

- 49 (3), pp. 181-186.
- Realmuto, V.J. (1990). Separating the effects of temperature and emissivity: emissivity spectrum normalization. *Proceedings of the 2<sup>nd</sup> TIMS Workshop*, JPL Publication 90-55, pp. 31-35.
- Reynolds, M.W., Wright, L.A., and Troxel, B.W. (1986). Geology and chronology of late Cenozoic detachment faulting, Funeral and Grapevine Mountains, Death Valley, California. *Geological Society of America Abstracts with Programs*, 18, p. 175.
- Salisbury, J.W., and D'Aria, D.M. (1992). Emissivity of terrestrial materials in the 8 - 14  $\mu\text{m}$  atmospheric window. *Remote Sensing of Environment*, 42, pp. 83-106.
- Siegal, B. and Abrams, M. (1976). Geologic Mapping using Landsat Data. *Photogrammetric Engineering & Remote Sensing*, 42, pp. 325-337.
- Shoffner, J.D. and Calvin, W.M. (2009). Application of Advanced Hyperspectral Thermal Data Analysis at Leviathan Mine, CA. *In review, Society of Exploration Geophysics*.
- Snow, J.K. and Wernicke, B. (1989). Uniqueness of geological correlations: An example from the Death Valley extended terrain. *Geological Society of America Bulletin*, 101, pp. 1351-1362, 7 figs.
- Thomson, J.L., Salisbury, J.W. (1993). The mid-infrared reflectance of mineral mixtures (7-14  $\mu\text{m}$ ). *Remote Sensing of Environment*, 45, pp. 1-13.
- Vaughan, R.G., Hook, S.J., Calvin, W.M., and Taranik, J.V. (2005). Surface mineral mapping at Steamboat Springs, Nevada, USA, with multi-wavelength thermal infrared images. *Remote Sensing of Environment*, 99, pp. 140-158.
- Vaughan, R. G., Calvin, W. M., and Taranik, J. V. (2003). SEBASS hyperspectral

- thermal infrared data: surface emissivity measurement and mineral mapping. *Remote Sensing of Environment*, 85, pp. 48-63.
- Wertz, W.E. (1983). The depositional environments and petrography of the Stirling Quartzite, Death Valley Region, California and Nevada. *Ph.D. Thesis*, Pennsylvania State University.
- Workman, J.B., Menges, C.M., Page, W.R., Taylor, E.M., Ekren, E.B., Rowley, P.D., Dixon, G.L., Thompson, R.A., Wright, L.A. (2002). Geologic map of the Death Valley ground-water model area, Nevada and California. *USGS Misc. Field Studies Map MF-2381-A*, scale 1:250,000.
- Wright, L.A., and Troxel, B.W. (1993). Geologic map of the central and northern Funeral Mountains and adjacent areas, Death Valley region, southern California. *US Geological Survey Misc. Invest. Series Map I-2305*.
- Wright, L.A. (1953). Mines and mineral deposits of San Bernardino County, *California*. *California Journal of Mines and Geology*, 49 (1-2), pp. 49-59; pp. 197-216.
- Yuhas, R.H., Goetz, A.F.H., and Boardman, J.W. (1992). Discrimination among semi-arid landscape endmembers using the Spectral Angle Mapper (SAM) algorithm. *Summaries of the 4<sup>th</sup> Airborne Earth Science Workshop*, JPL publication 92-41, pp. 147-149.
- Young, S. J., Johnson, B. R., and Hackwell, J. A. (2002). An in-scene method for atmospheric compensation of thermal hyperspectral data. *Journal of Geophysical Research*, 107 (D24), 4774.

## Tables

Table 1.

Geological units with name, age, lithology, and description (from Workman et al., 2002).

Name	Age	Lithologies	Description
Surficial deposits			
Qay *	Holocene to latest Pleistocene	young alluvium	medium- to coarse-grained alluvium; unconsolidated to poorly unconsolidated
Qayo	middle Holocene to latest Pleistocene	intermediate-age alluvium	mostly medium- to coarse-grained gravel and sand deposits; unconsolidated to poorly unconsolidated
Qau	Holocene to Pleistocene	undifferentiated alluvium	consists of various alluvial units
Qtau *	Holocene to latest Tertiary	undifferentiated older alluvium	complex suite of deposits of widely varying ages
Qao	late to middle Pleistocene	old alluvium	medium- to coarse-grained gravel and sand deposits
Bedrock units			
Tlt	middle Miocene	Lithic Ridge Tuff	rhyodacitic, rhyolitic, and comendite ash-flow tuff and lava flows
Ts4 *	Pliocene and Miocene	sedimentary rocks, unit 4	poorly to moderately consolidated, mostly fluvial sandstone, conglomerate, mudstone, limestone, and siltstone
Tso *	Miocene to Eocene?	older sedimentary rocks	moderately consolidated, fluvial and lacustrine sandstone, conglomerate, limestone, mudstone, and siltstone whose age is poorly constrained
Cnbc	lower to upper Cambrian	Nopah/Bonanza King/Carrara Formations	dolomite, limestone, sandstone, and shale
Cz	lower Cambrian	Zabriskie Quartzite	laminated to thick-bedded orthoquartzite
€Zw *	lower Cambrian and late Proterozoic	Wood Canyon Formation	quartzite, sandstone, siltstone, shale, and dolomite
Zs *	late Proterozoic	Stirling Quartzite Formation	quartzite and sandstone, conglomeratic quartzite, and micaceous siltstone
Zj *	late Proterozoic	Johnnie Formation	quartzite, conglomeratic quartzite, siltstone, shale, and limestone and dolomite
ZYp *	late and middle Proterozoic	Pahrump Group	pelitic schist, meta-conglomerate, calcite marble, amphibolite, micaceous quartzite
Xmi	early Proterozoic	metamorphic and igneous rocks	schist, meta-sedimentary rocks

\* denotes units that were covered by SEBASS image data measurements

Table 2.

Minerals associated with lithologies gathered during field surveys. Mineral associations are based on interpretation of laboratory FTIR measurements. 'X' denotes that the mineral is dominant for the particular lithology in the study area, while 'x' indicates that the mineral constitutes a minor proportion of a sample.

Lithologies	Minerals							
	quartz	muscovite	calcite	dolomite	hematite	feldspar	chlorite	hornblende
alluvium	X	x		x		x		
siltstone	x	X				x	x	
slate	x	X					x	
sandstone	X	x				x		
chloritized sandstone	x						X	
quartzite	X							
siliceous conglomerate	X	x	x	x				
carbonate conglomerate	x	x	X	x				
limestone	x		X					
dolostone	x	x		X				
marble			X					
pelitic schist	x	X			X	x	x	
amphibolite	x						x	X

Table 3.

Rock samples gathered during field survey of scene one (figure 7). Sample identification number, geologic unit that bounded the area (from Workman et al., 2002), rock description, and minerals identified by indicated laboratory instrument.

Sample	Unit	Visual description	Identified minerals
DVB-3	Єzw	dark folded siltstone	muscovite, quartz, feldspar, chloritoid
DVB-5	Єzw	thinly laminated siltstone	muscovite, hematite
DVB-6	Єzw	dark laminated siltstone	muscovite, quartz
DVB-10	Єzw	oxidized dolostone	dolomite
DVB-11	Єzw	slightly oxidized quartzite	quartz
DVB-12	Єzw	weathered quartzite	quartz
DVB-13d	Єzw	lightly oxidized limestone	calcite

Table 4.

Rock samples gathered during field survey of scene two (figure 8). Sample identification number, geologic unit that bounded the area (from Workman et al., 2002), rock description, and minerals identified by indicated laboratory instrument.

Sample	Unit	Visual description	ASD	FTIR	XRD
MC-66	Zj	massive greenish siltstone	chlorite, muscovite	quartz, muscovite, chlorite	chlorite, quartz, chlinoclore, albite
MC-68	ZYp	dark folded marble	goethite, calcite	calcite	n/a
MC-71	Zj	red-tinted pelitic schist	goethite, muscovite	muscovite	muscovite, quartz
MC-74	Zj	silver pelitic schist	goethite, muscovite	muscovite, chlorite	muscovite, chlorite, albite, quartz
MC-76	Zj	amphibolite	chlorite	hornblende	magnesio-hornblende, quartz, chlorite
MC-77	Zj	weathered pelitic schist	goethite, muscovite	muscovite, quartz	muscovite, quartz, chlinochlore



Table 5.

Rock samples gathered during field survey of scene three (figure 9). Sample identification number, geologic unit that bounded the area (from Workman et al., 2002), rock description, and minerals identified by indicated laboratory instrument.

Sample	Unit	Visual description	Identified minerals
DP-15	CZW	oxidized dolomite with mica grains	dolomite
DP-16	Zs	fractured quartzite	quartz
DP-17b	Zs	silicic conglomerate	quartz
DP-20	Tso	micaceous sandstone	muscovite, quartz
DP-21	Ts4	carbonate conglomerate	calcite, quartz
DP-29	CZW	dolostone with calcite veining	calcite, dolomite
DP-35b	Ts4	dark argillite or slate	muscovite, quartz, chlorite
DP-41	Ts4	greenish sandstone	muscovite, quartz, chlorite, albite
DP-42	Tso	varnished feldspathic sandstone	quartz, feldspar
DP-46	CZW	light-colored limestone	calcite
DP-47	Ts4	mixed quartzite pebbles from consolidated alluvium	quartz

**Figures**

Figure 1.

Location map of the study area in reference to the states of Nevada and California.

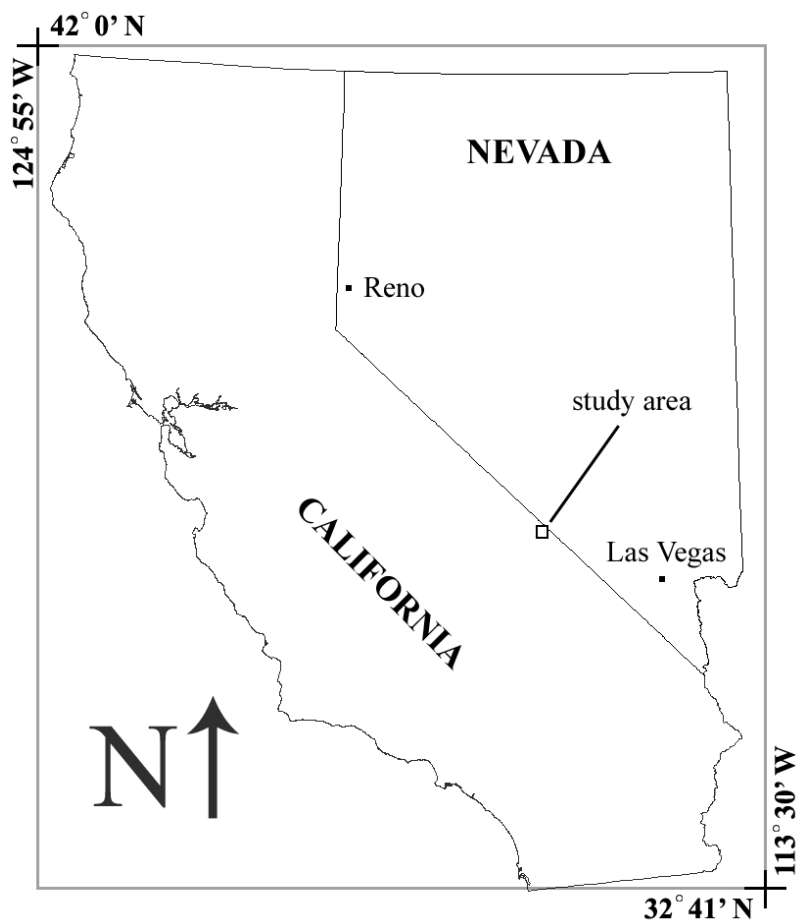


Figure 2.

Annotated study area map indicates the extent of SEBASS image data coverage (black box) in relation to local geographic features. Data coverage extends from the Death Valley Buttes to the border of California and Nevada. The SEBASS image data are analyzed and presented in subsets as indicated by scene number below.

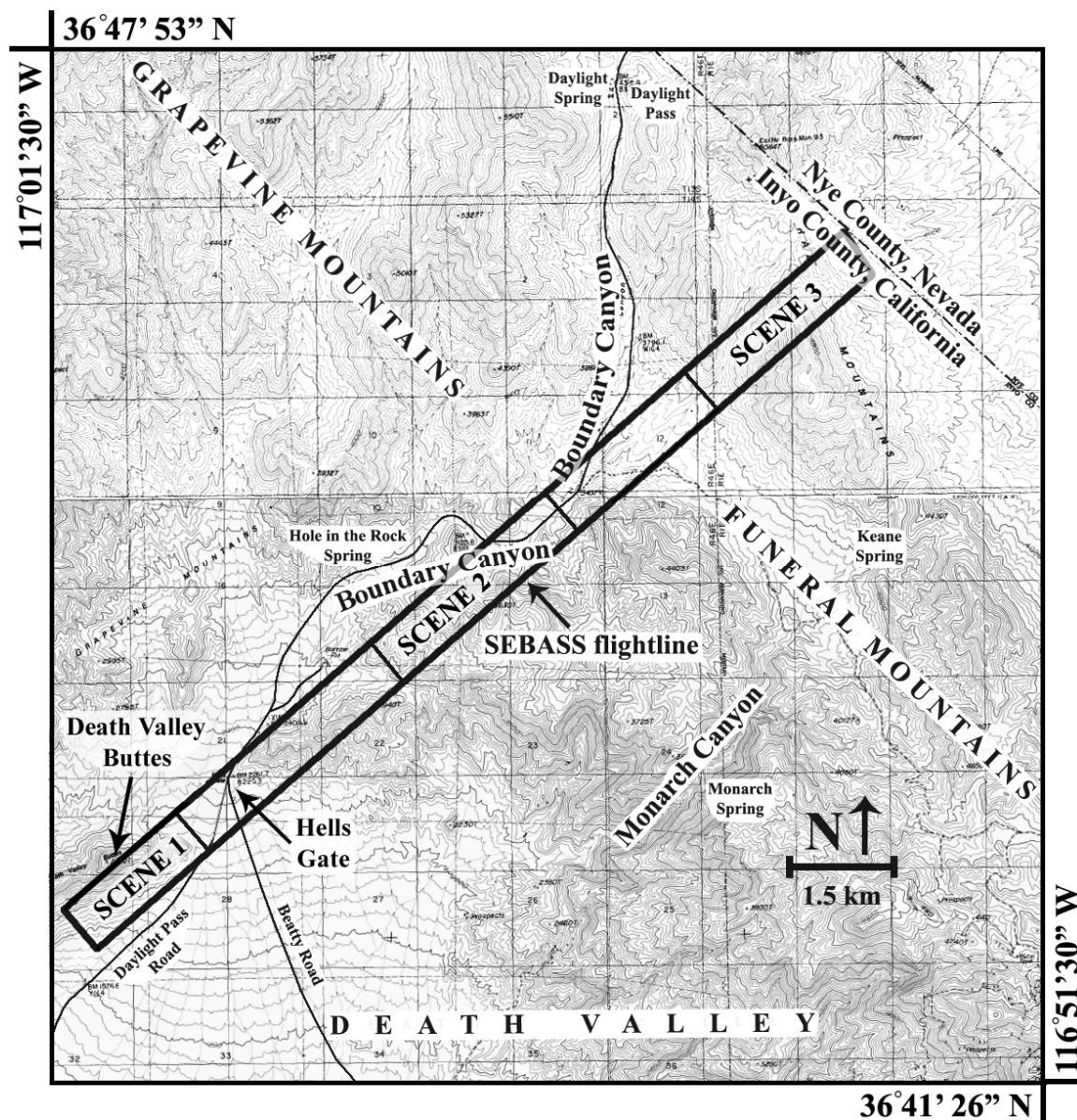


Figure 3.

Geology map of the study area (from Workman et al., 2002). Geologic units are explained in table 1. Geochemical isograd information is overlaid on geology map (from Labotka, 1980). The SEBASS image data flightline is denoted by the black box.

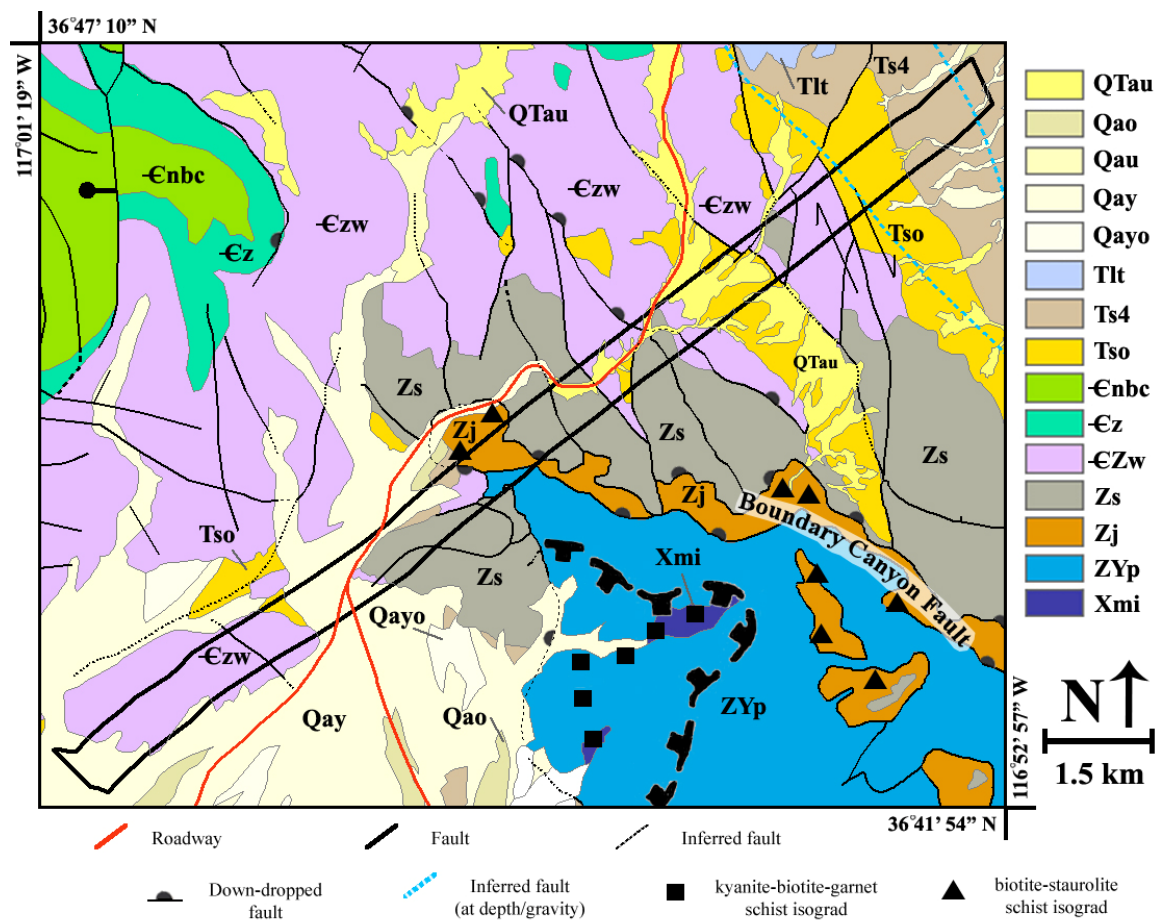


Figure 4.

Laboratory FTIR emissivity spectra in the 8 -12  $\mu\text{m}$  wavelength range produced from measurements of rocks collected within the study area. (Noisier spectra resulted from use of a bored sample tray holder).

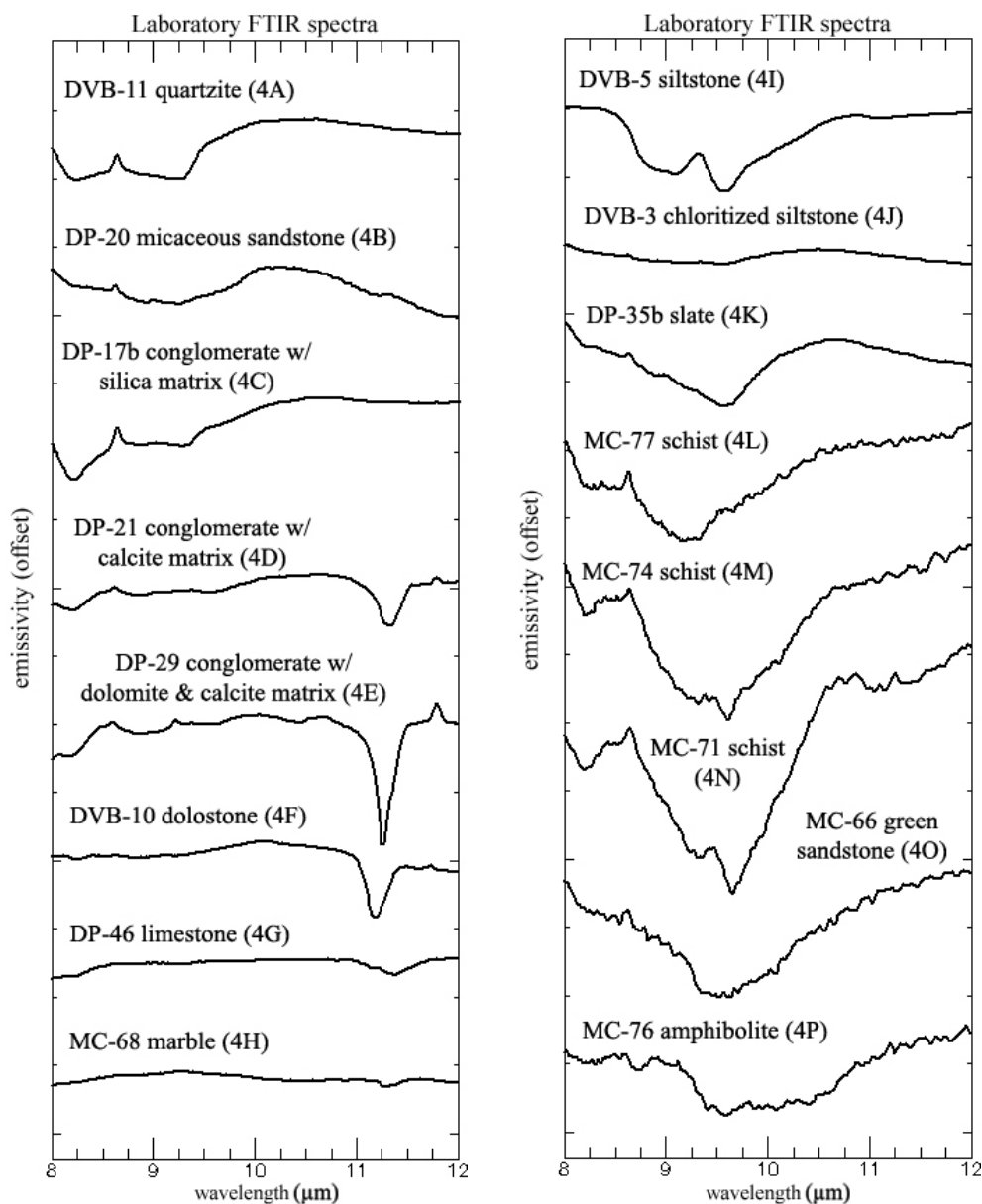


Figure 5.

A decorrelation stretch (DCS) was applied to non-georeferenced image data using SEBASS bands (RGB): 70, 40, 29 (11.26  $\mu\text{m}$ , 9.86  $\mu\text{m}$ , 9.29  $\mu\text{m}$ ). The resulting image results in magenta tones indicating areas of muscovite, cyan indicates carbonate, and yellow indicating quartz-rich rock.

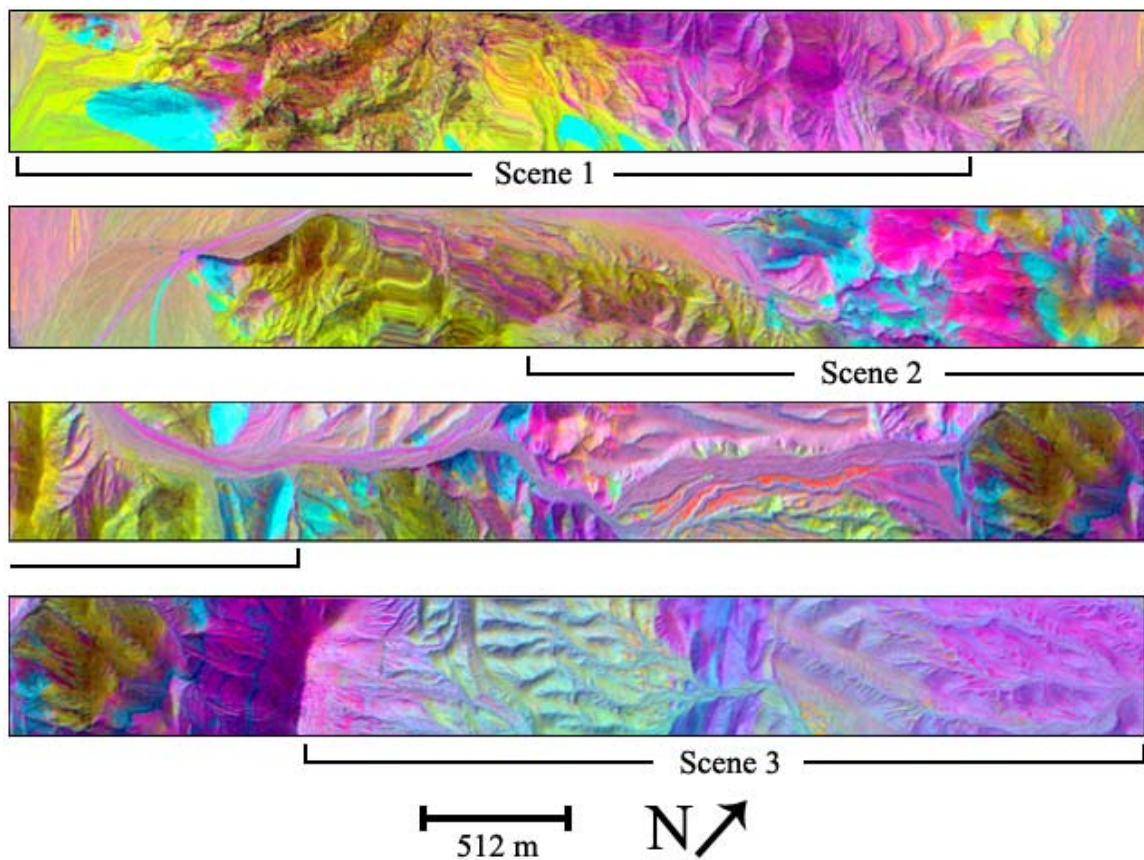


Figure 6.

SEBASS image data endmembers derived from the ENVI Hourglass process. Emissivity spectra are annotated according to interpreted dominant mineral or prominent mineral mixture components.

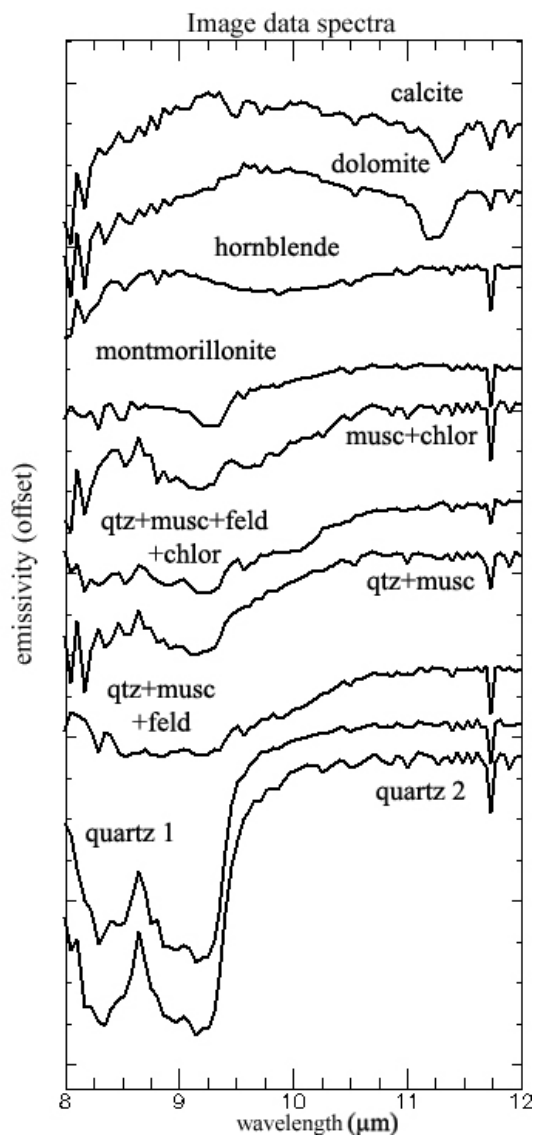


Figure 7.

Scene one, a subset portion of the SEBASS image data, is shown below. At left, a SAM-derived mineral map indicates pixels dominated by quartz-rich outcrop, quartz-rich alluvium, calcite, dolomite, and muscovite. At center, image data emissivity spectra for respective classes are plotted (colored) with laboratory FTIR-derived spectra for samples corresponding to the mapped surfaces (black). At right, ground photos corresponding to mineral map areas are shown.

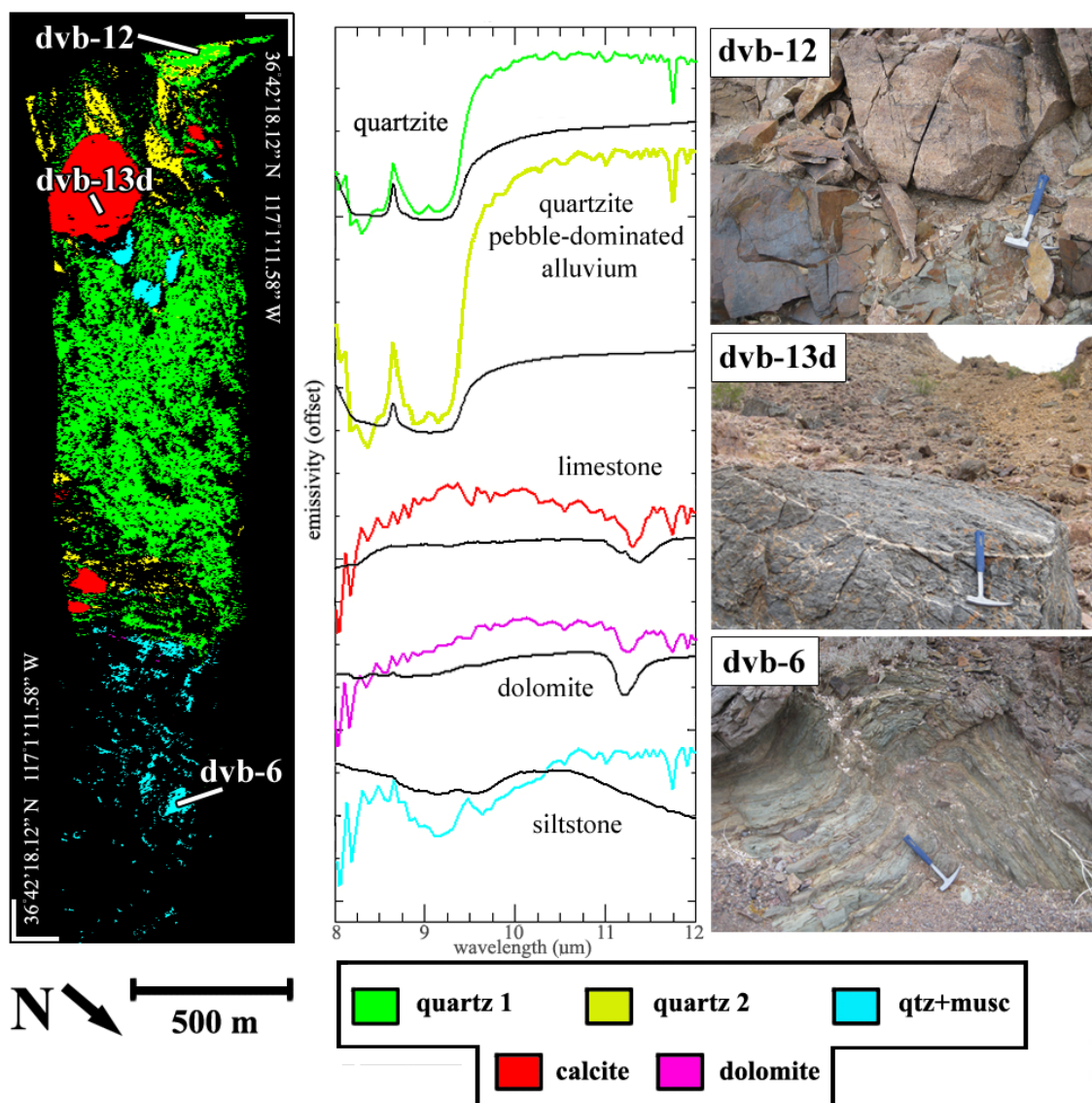




Figure 8.

Scene two of the SEBASS image data is shown below. At left, a SAM-derived mineral map indicates pixels dominated by quartz-rich outcrop, quartz-rich alluvium, muscovite-rich alluvium, marble, dolomite, pelitic schist, and amphibolite. At center, image data emissivity spectra for selected classes are plotted (colored) with laboratory FTIR-derived spectra for samples corresponding to the mapped surfaces (black). At right, ground photos corresponding to mineral map areas are shown.

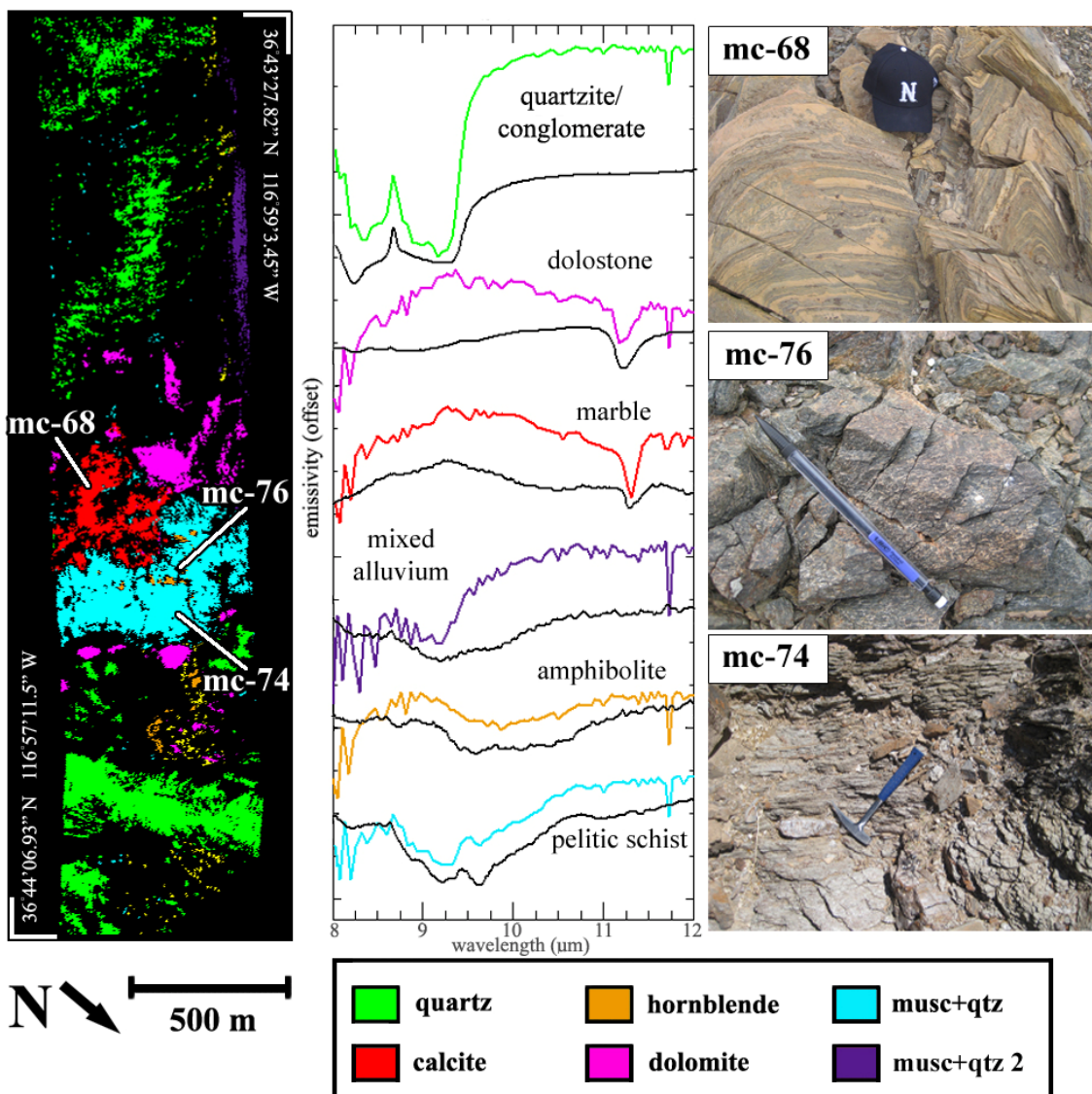


Figure 9.

Scene three of the SEBASS image data is shown below. At left, a SAM-derived mineral map indicates pixels dominated by quartz-rich consolidated gravel, altered argillite, dolomite, and sandstone. At center, image data emissivity spectra for respective classes are plotted (colored) with laboratory FTIR-derived spectra for samples corresponding to the mapped surfaces (black). At right, ground photos corresponding to mineral map areas are shown.

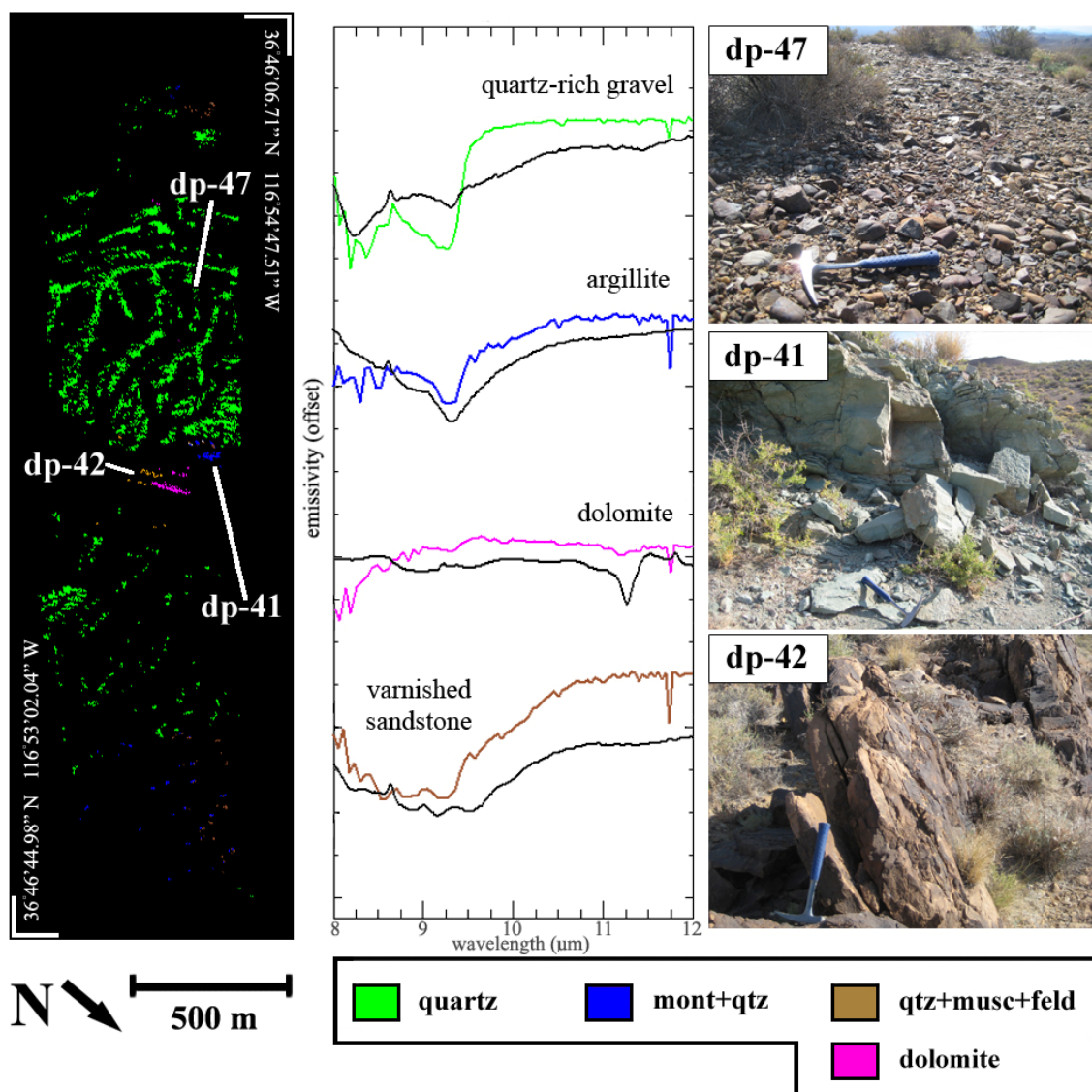


Figure 10.

Geologic map, at left, (from Workman et al., 2002) and SEBASS image data-derived mineral map, at right, of the BCDF zone (scene two) are compared. Inferred fault boundaries (dashed white lines) are interpreted from contacts between groups of minerals belonging to either sedimentary or meta-sedimentary geologic units, and are corroborated by location of faults indicated by the geologic map. Dolomite (magenta) and quartz (green) belong to the Stirling Quartzite and Wood Canyon sedimentary geologic units, while calcite (red), muscovite (cyan), and hornblende (orange) belong to the Pahump Group and Johnnie Formation meta-sedimentary units. The produced mineral map also indicates where geologic boundaries could be refined.

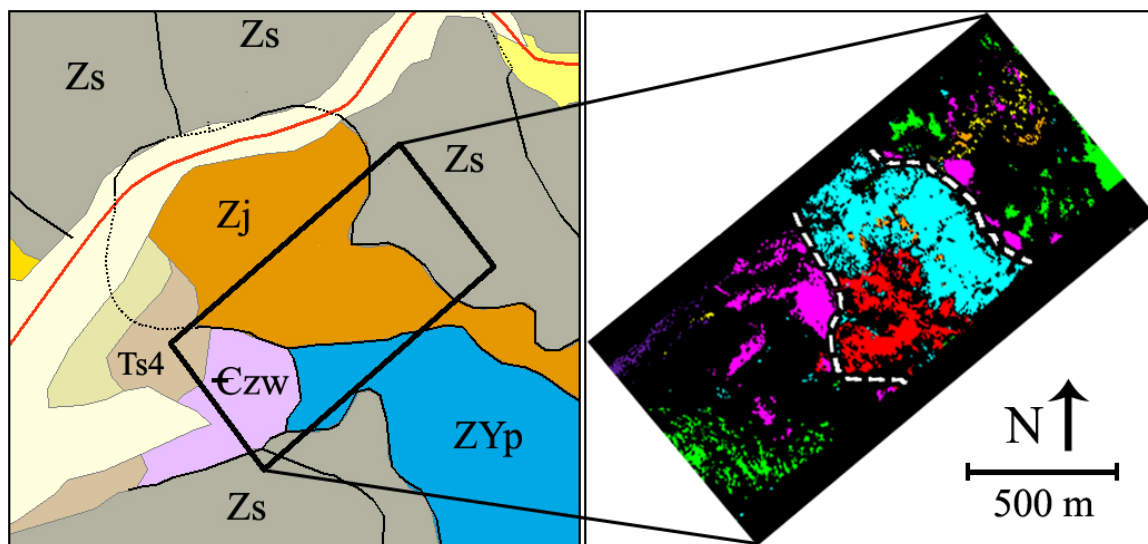


Figure 11.

Comparison of geologic map, at left, (from Workman et al., 2002) and SEBASS image data-derived mineral map, at right, at a lithologic boundary where sedimentary rocks have been uplifted (scene three). The boundary (dashed white lines) indicates contact between Tertiary sedimentary geologic units (Tso and Ts4). Quartz pixels are found in both units, while montmorillonite is found at the skirt of the gravel deposits, and dolomite and sandstone are found on the opposite side of the boundary.

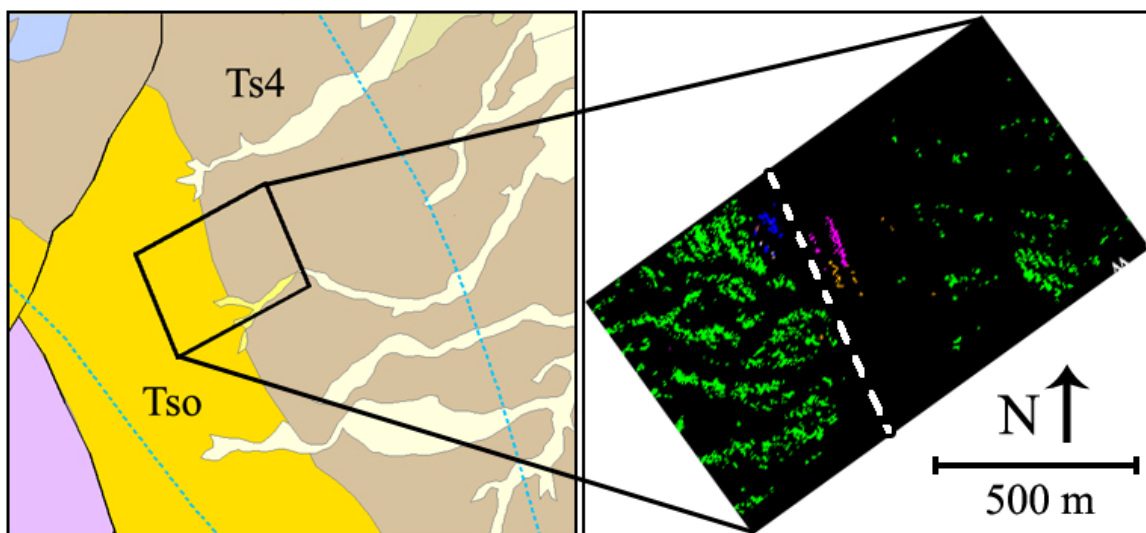
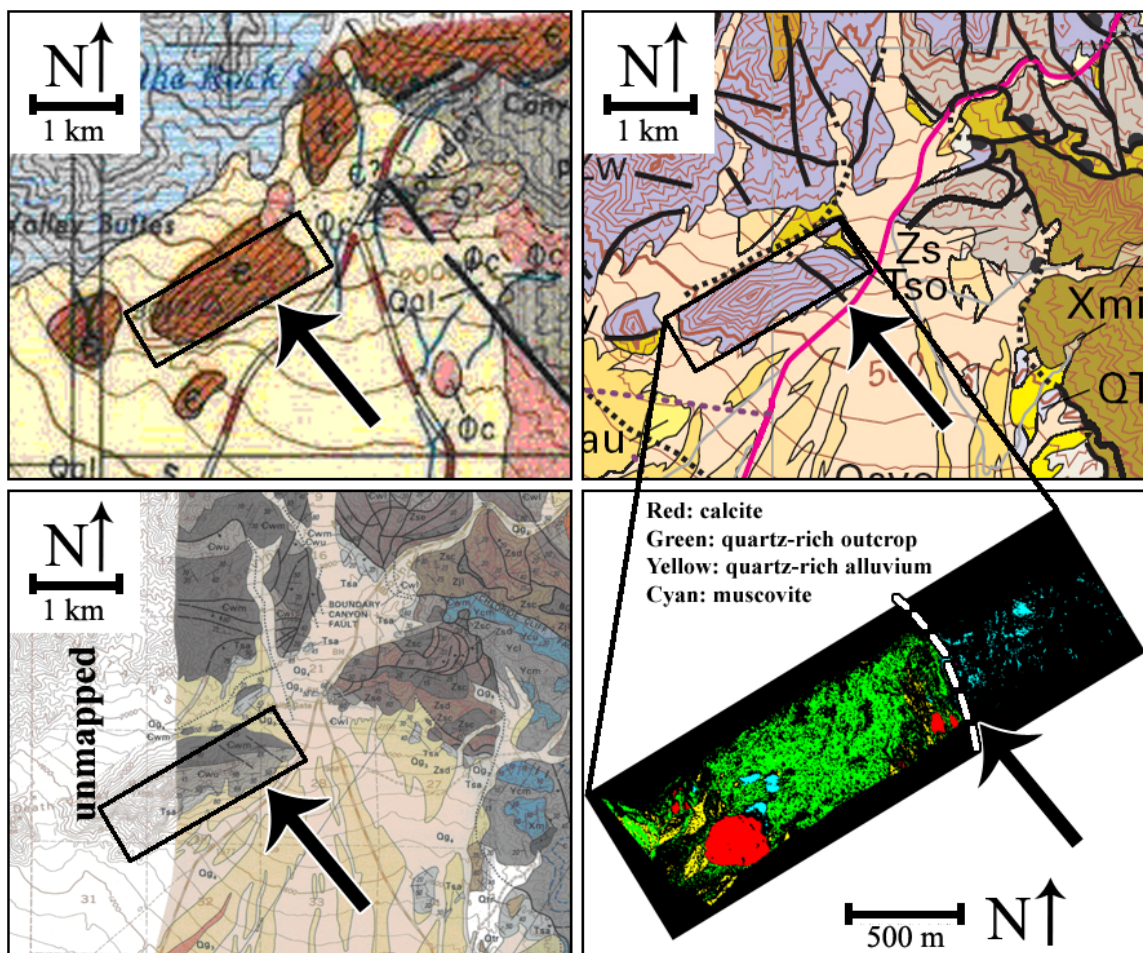


Figure 12.

Subset geology maps of the Death Valley Buttes area from Hunt and Mabey, 1966 (top left); Wright and Troxel, 1993 (bottom left); Workman et al., 2002 (top right), and SAM mineral classification map derived from statistical analysis of SEBASS image data (bottom right). The SAM mineral map indicates a mineralogical contact between siliceous rocks (green) and micaceous rocks (cyan). Arrows indicate the same location in each figure of a contact between lithologies inferred by the SEBASS image data (dashed white line). The geology maps by Wright and Troxel and Workman, et al. indicate a fault located at the contact; however unit delineation is not made.



## Chapter 4

### **Multi-scale Comparison of Mineral Emittance Measurements using Ground, Aerial, and Spaceborne Image Data in Northeastern Death Valley National Park, California, USA**

Zan Aslett

Mackay School of Earth Sciences and Engineering, University of Nevada, Reno

\* Based on a manuscript to be submitted to Journal of Applied Remote Sensing

#### 4.1 Abstract

Emittance measurements made with ground and aerial SEBASS, aerial MASTER, and spaceborne ASTER over Boundary Canyon, northeastern Death Valley National Park, California, USA were compared and used to produce maps of mineral constituents associated with sedimentary and meta-sedimentary rocks. Ground and aerial SEBASS image data were shown to differ in number of utilizable bands. For ground data, each band measured in the 7.6 - 13.5  $\mu\text{m}$  range exhibited mineral emissivity features. In contrast, the aerial data generally exhibited these features only in the 8 - 12  $\mu\text{m}$  range, while bands in the 7.6 - 8 and 12 - 13.5  $\mu\text{m}$  regions were dominated by an atmospheric water vapor component. As a result, the ground data demonstrated the ability to accurately map quartz based solely upon diagnostic spectral features at these extended ranges, whereas the aerial data did not. Next, unique emissivity spectra corresponding to quartzite, argillite, dolomite, marble, pelitic schist, and amphibolite were identified using hyperspectral data, resampled to match multispectral resolutions of MASTER and ASTER, and then mapped with respective image data sets. Certain mineralogic indicators of detachment faulting in Boundary Canyon (e.g., calcite, dolomite) were only able to be spectrally delineated with SEBASS data, while hornblende associated with amphibolite, the highest-grade metamorphic rock of the exposed Funeral Mountains core complex, was able to be detected and mapped with both SEBASS and MASTER data. These outcrops were not able to be mapped with ASTER however, suggesting that the 90 meter pixel size of these data limits remote detection or mapping of this class.

## 4.2 Introduction

Thermal-infrared (TIR) image data are a valuable tool with which to remotely assess surficial expression of rock-forming minerals such as silicates, carbonates, and sulfates, as well as secondary clay minerals. TIR remote sensing studies have been conducted for geological mapping in the Death Valley region in various capacities. Multispectral Thermal Infrared Multispectral Scanner (TIMS) data were first utilized for general mapping of major geologic units in the region (Kahle and Goetz, 1983). These data were later used to focus on spectral delineation of alluvial fans based upon compositional differences (Gillespie et al., 1984). Crowley and Hook (1996) used TIMS image data to distinguish between evaporative-rich crusts and sediments, while later use of MODIS/ASTER Simulator (MASTER) image data by Crowley facilitated more detailed mapping of mineral-related data endmembers within the basin (Crowley, 2000). More recently, MASTER and Advanced Spaceborne Thermal and Reflection Radiometer (ASTER) TIR image data were evaluated and used to map rock-forming minerals at a regional scale in the Grapevine Mountains (Kruse, 2002).

In comparison, higher spectral resolution TIR image data, as provided by the Spatially Enhanced Broadband Array Spectrograph (SEBASS), have been applied to more detailed mapping of surficial mineralogy in areas outside of Death Valley. Cudahy et al. (2000) demonstrated the utility of these data to map particular solid solution series minerals within the garnet, feldspar, and pyroxene mineral groups over the Yerington Mining District, Nevada. Vaughan et al. (2003) demonstrated the use of these data to map specific silicate, clay, sulfate, and carbonate minerals, as well as mixtures of these minerals in Virginia City, Nevada. These data were next used to remotely map minerals



indicative of an active geothermal system in Steamboat Springs, Nevada (Vaughan et al., 2005).

In this study, minerals comprising sedimentary and meta-sedimentary lithologies within the Boundary Canyon area of Death Valley National Park (DVNP), California, were remotely mapped at various scales using TIR image data with different spatial, spectral, and radiometric resolution characteristics (figures 1 and 2). Specific instrument and corresponding data collection parameters are summarized in table 1. Two different goals were incorporated into the research: 1) determine what utility for mineral mapping SEBASS data acquired from the ground-based horizontal perspective provided in comparison to data collected on an aerial platform from a nadir look angle. 2) Compare emissivity spectra of SEBASS image data with aerial MASTER and spaceborne ASTER measurements to determine if minerals indicative of the Boundary Canyon Detachment Fault (BCDF) can be detected and mapped with multispectral image data possessing lower spatial, spectral, and radiometric resolutions.

Boundary Canyon is located in northeastern DVNP, and is characterized by the BCDF structure, a low-angle normal fault that has extended to reveal the metamorphic core complex of the Funeral Mountains (Reynolds et al., 1986; Troxel, 1988) (figure 3). Prominent lithologies in this area include: quartzite, conglomerate, sandstone, argillite, dolomite, marble, pelitic schist, and amphibolite; these rocks are composed largely of common minerals that exhibit diagnostic emissivity spectral features attributed to fundamental vibrational modes of the respective crystal lattice (Hapke, 1993; Clark, 1999). In pure form, many of these minerals do not require high spectral resolution to identify (e.g., quartz, feldspar, chlorite) due to broad emission features (Salisbury and

D'Aria, 1992), while other minerals, such as calcite, exhibit more narrow emission features (Lane and Christensen, 1997). However, framework and sheet silicate minerals such as feldspar and chlorite, respectively, are usually minor constituents of many of these rocks. When mixed with dominant minerals such as quartz, these minerals instead exhibit more subtle emission features that may necessitate the use of higher spectral resolution data to identify in emissivity spectra (Collins, 1991; Vaughan et al., 2003).

### **4.3 Background**

#### **4.3.1 Previous mineral mapping in the study area**

In Chapter 3, surficial mineralogy within the BCDF study area was characterized using aerial SEBASS image data. Calcite, dolomite, muscovite, and hornblende were each noted as mineral indicators that were useful to determine the presence of particular rocks, and thereby characterize the fault contact between sedimentary units of the Grapevine Mountains and meta-sedimentary units associated with the Funeral Mountains. Calcite and dolomite were manifested in the form of dolomite and calcite marble of the Wood Canyon Formation (Czw) and Pahrump Group (ZYP), respectively. Muscovite was expressed in pelitic schists of the Johnnie Formation (Zj); these rocks corresponded to greenschist metamorphic facies of the exposed core complex. Hornblende, which was also remotely identified and mapped within the Zj unit, corresponded to amphibolite, an amphibolite facies lithology. In tandem these latter two minerals indicate a transition between low- to medium-grade metamorphic rocks in the study area (Labotka, 1980).

Dolomite- and calcite-dominated rocks were mapped in close proximity to one another, which indicated the fault contact between relatively unmetamorphosed lower Cambrian/late Proterozoic dolomite outcrops of the Grapevine allochthon and middle-late Proterozoic calcite marble of the unroofed Funeral Mountains autochthon. Although these minerals signified the fault contact within this part of the study area, elsewhere in the region this mineralogic relationship is likely not indicative of a similar structural feature. This is due to the presence of multiple geologic units found in NEDV that are composed of both limestone (dominated by calcite) and dolomite, but do not include calcite marble, and are much younger than the ZYp unit where marble is noted (e.g., Ts4 and Tso units from Workman et al., 2002); thus these rocks are unrelated to the targeted lithologies, and could be mistakenly interpreted with remote sensing data to be associated with the BCDF.

Late Proterozoic pelitic schist is associated with the unroofed metamorphic core complex, and pixels corresponding to these rocks exhibited emissivity spectra dominated by muscovite. These areas were investigated as further indicators of the fault boundary, however multiple lithologies found adjacent to the fault zone were also dominated by muscovite (e.g. siltstone, argillite, slate, and an alluvial unit). Thus remote mapping of muscovite over large areas in NEDV could also result in a mistaken association with non-schist lithologies, diminishing this mineral's overall reliability as a unique indicator for the fault contact.

Late Proterozoic amphibolite was observed in thinner, smaller exposures compared to the more extensive dolomite, marble, and schist units. Hornblende (comprising the bulk of amphibolite rocks) is unique within the NEDV region to the Zj

unit, and was thus deemed to be a potential unique mineral indicator of the fault zone. Comparison of hornblende and muscovite emissivity spectra helped determine that both feature broad diagnostic emission minima features which are sufficiently offset so that multispectral image data should be capable of delineating the two minerals. However, the task of detection and mapping of amphibolite becomes an issue of spatially resolving outcrops that are relatively limited in surficial expression, as noted during field surveys. This may dictate a minimum necessary spatial resolution of image data to resolve these rocks.

Hornblende was identified and mapped successfully with hyperspectral SEBASS data in Chapter 3, however these data were limited in coverage to a small study area. Multispectral data offers increased surface coverage at the expense of reduced spatial and spectral resolution (Kruse and Perry, 2010), hence MASTER and ASTER multispectral data were evaluated to determine whether amphibolite could be remotely identified and mapped. Hyperspectral emissivity spectra of hornblende, as well as other mineral endmembers, were resampled to respective multispectral instrument characteristics and applied to these data using spectral classification algorithms to expand mineral mapping, as in Cudahy et al. (2000) and Kruse and Perry (2010), where the procedure is referred to as "spectral modeling".

#### 4.3.2 Thermal-infrared mineral spectroscopy

The use of remotely-sensed TIR image data to create mineral maps is based upon the recognition of distinct variations of emission from exposed surface materials, such as rocks or soils. These variations in particular spectral bands were first observed for silicate

minerals, and found to be related to Si-O bond length (Lyon, 1965). The molecular lattice structure of minerals responds to energy absorbed at shorter wavelengths as vibrational processes (Farmer, 1974). For minerals such as silicates, vibration of  $\text{SiO}_4$  results in Reststrahlen band features diagnostic of crystal structure (Hapke, 1993). These features vary slightly dependent upon mineral composition, with emission minima occurring at longer wavelengths according to isolation of  $\text{SiO}_4$  tetrahedra; thus spectral characteristics can be generalized for some mineral groups (Lyon and Green, 1975). For instance, framework silicate minerals (e.g., quartz and feldspar) exhibit features at shorter wavelengths of the longwave-infrared spectrum (around 8 - 10  $\mu\text{m}$ ); sheet silicate minerals (e.g., kaolinite and muscovite) exhibit features at slightly longer wavelengths (around 9 - 10.5  $\mu\text{m}$ ); and single and double chain silicates (e.g., pyroxene and hornblende, respectively) exhibit features at yet longer wavelengths (10 - 11.5  $\mu\text{m}$ ). Silicate minerals exhibit broad emission minima features that can overlap, resulting in spectral mixing and potential for misinterpretation (Elachi, 1987).

Laboratory studies involving the emissivity characteristics of pure mineral samples have produced spectral libraries that are available to the public (e.g., ASTER: Baldridge et al., 2009 and USGS: Clark et al., 2009). These library spectra are useful for comparison and corroboration of image data emissivity measurements. With appropriate spectra, the repercussions of grain size for measured minerals upon spectral contrast of diagnostic features can be observed. Fine-grained mineral samples produce less prominent emission features due to multiple internal grain reflections and porosity, while coarse-grained materials exhibit increased spectral contrast (Salisbury and Eastes, 1985; Salisbury, and D'Aria, 1992).

### 4.3.3 Thermal-infrared remote sensing

Environmental conditions, physical surface characteristics, and image data parameters such as spatial, spectral, and radiometric resolution impose limitations upon the remote detection, identification, and mapping of minerals (Clark, 1999). Atmospheric transmissivity restricts the remote measurement of emitted energy to “windows” in the 3 - 5 and 7 - 14  $\mu\text{m}$  wavelength ranges; within these ranges the effects of atmospheric absorption and emission must also be corrected for to optimize interpretation of mineral-related spectral features. Atmospheric turbulence (e.g., wind) can cause non-surface material-related shifts in temperature, with respect to the rest of the image data scene, but are not usually accounted for in data calibration (Balick et al., 2003). Surface materials within anisothermal environments exhibit varying temperature, according to thermal inertia (Schieldge et al., 1980), causing pixel measurement of emittance to be dominated by hotter components and reducing the apparent contribution from colder components (McCabe et al., 2008).

Spatial resolution represents the relationship between a surface area and image data pixel measurement. Mixtures of varying minerals, non-mineral surface materials (e.g., vegetation or water), and shadow can each contribute to mixtures that effectively degrade the capability to interpret spectra and identify a specified mineral target. Thus, image data utilized in this study that measure varying surface areas will have different capabilities to resolve mineral features (figure 4). Spectral resolution concerns the range of wavelengths measured in a single channel, a high number of narrow channels facilitating spectral detail. Multispectral sensors commonly measure 4 - 50 channels

which allows the mapping of mineral composition. Hyperspectral instruments usually measure 100 or more channels and these data can be used to discriminate between specific minerals within a mineral group. Sufficiently high radiometric resolution enables image data measurements to better resolve subtle digital number (DN) differences between levels of measured emittance in each band, enhancing discrimination of surface materials.

#### **4.4 Area of study**

##### *4.4.1 Regional geology*

Death Valley is a range-bounded evaporative basin located in the western periphery of the Great Basin region, approximately 150 km west-northwest of Las Vegas, Nevada, USA. Structural extension has resulted in the thinning of crust in this area, creating alternating series of uplifted ranges and down-dropped basins in a region bounded by the Sierra Nevada and Cascade Mountains in the west, Wasatch Mountains in the east, the Snake River basalt plains in the north, and the Mojave Desert in the south. DVNP is found within the Great Basin and spans an area measuring nearly 13500 km<sup>2</sup>; rock units up to 1800 million years old are exposed in a geological environment typical of basin and range structural configuration.

Twenty-three distinct sedimentary geological formations and two unconformity events have been classified within the park (Hunt and Mabey, 1966). Mesozoic compressional forces and Cenozoic extensional and block-rotation tectonics have resulted in the prevalence of normal- and thrust-faulted rock noted throughout the area. Extensive outcrops of Proterozoic, Paleozoic, and Tertiary sedimentary and meta-sedimentary rocks

in the region provide excellent exposure and limited development of soils which benefits the remote measurement of emitted energy. The study area's geology has been previously mapped at medium scales of 1:96,000 by Hunt and Mabey (1966) and 1:48,000 by Wright and Troxel (1993), while a compilation of maps applied toward regional structure is available at 1:250,000 scale (Workman et al., 2002).

#### 4.4.2 Local geology

The area of study represents an abrupt transition between relatively unmetamorphosed lithologies belonging to the Grapevine Mountains and metamorphosed lithologies of the Funeral Mountains. The BCDF is a low-angle normal fault that marks this boundary. Late Cretaceous extension here resulted in unroofing of the metamorphic core complex of the Funeral Mountains, which has exposed greenschist-to-amphibolite facies, representative of low- to medium-grade metamorphic rock units (Labotka, 1980; Applegate et al., 1992). The Grapevine Mountains allochthon dips gently to the northwest from the autochthonous Funeral Mountains, and the medium-grade metamorphic rocks are exposed near the fault contact in the northwestern portion of the Funeral Mountains. Previous studies have estimated extension of the detachment to be on the order of 25 - 30 km, based on correlation of hanging wall rock sequences near the fault contact in the Grapevines with footwall geology found at Winter's Peak to the southeast (Snow and Wernicke, 1989; Hoisch and Simpson, 1993).

#### 4.4.3 Study site 1: Wood Canyon & Stirling Quartzite formation outcrop

The first study site consists of an outcrop of siliceous, micaceous, and carbonate lithologies at Hell's Gate, near the southeastern terminus of Boundary Canyon. The



canyon opens to the Death Valley basin and is centered at latitude  $36^{\circ}43'27''\text{N}$ , longitude  $-116^{\circ}58'37''\text{W}$ , near the junction of Daylight Pass Road and Beatty Road (figure 2). The local geology is comprised of extensively folded and faulted late Proterozoic and Paleozoic sedimentary units of the lower Wood Canyon and upper Stirling Quartzite formations (Diehl, 1979; Wertz, 1983) (figure 3 and table 2). These units both represent low- to relatively-unmetamorphosed lithologies belonging to the Grapevine Mountains allochthon. Field surveys were conducted, and alternating quartzite, dolomite, argillite, and limited conglomerate beds within the outcrop were identified that ranged in thickness from 0.1 to 3 m.

#### 4.4.4 Study site 2: Johnnie Formation outcrop

The second study site is located further within Boundary Canyon, at approximately 2 km north of Hell's Gate. It consists of exposed lithologies belonging to the Stirling Quartzite and Johnnie Formations, and is centered near latitude  $36^{\circ}44'53''\text{N}$ , longitude  $-116^{\circ}56'19''\text{W}$  at the flank of the Grapevine Mountains and found alongside Daylight Pass Road (figure 2). The Johnnie Formation outcrops represent low- to medium-grade metamorphosed rocks of the Funeral Mountains autochthon (figure 3 and table 2). The rocks here are a mix of folded and faulted mid- to late-Proterozoic and Paleozoic siliceous, micaceous, and carbonate lithologies including pelitic schist, conglomerate, dolomite, and amphibolite.

## 4.5 Methods

### 4.5.1 Synopsis

Field surveys were conducted to gather rock samples of unique lithologies exposed within the study sites. Petrographic, Fourier transform infrared (FTIR), and x-ray diffraction (XRD) laboratory analyses were conducted on these rocks to comprehensively determine mineral constituents present for each sample. The image data were calibrated to emissivity units and validated by comparing these measurements to library and laboratory spectra of common minerals. Following this, ground and aerial SEBASS image data were analyzed using the ENVI Hourglass methodology, and then emissivity spectra and mineral maps of corresponding surfaces were compared to determine differences between these data.

Ground and aerial SEBASS measurements were then directly compared to determine the differences between mineral mapping capabilities. Separate quartz classifications were generated based upon diagnostic features in either the 8 - 12 or 12 - 13.5 regions, which illustrate the repercussions of differing levels of atmospheric water absorption upon TIR mineral mapping.

Hyperspectral image data spectra of unique rocks were next resampled to the spectral resolution of MASTER and ASTER. Spectra for each lithology were then examined to determine whether the respective rock units found in each study site were likely to be spectrally delineable from one another using the multispectral image data. Lastly, a statistical mapping algorithm was utilized to match the resampled emissivity spectra against the image data and determine mineral distributions for the study area. In this manner, it could be determined whether these indicator mineral were mappable with multispectral data.

#### 4.5.2 Field sample collection

Field surveys were conducted in areas that coincided with image data coverage. Unique rocks found during the surveys were sampled and retained for further analysis. In study site one, quartzite, argillite, and dolomite were the predominant rock types collected. In study site two, siliceous and carbonaceous conglomerates, dolomite, pelitic schist, amphibolite, and quartzite-dominated alluvium were each sampled. Rocks were recorded with respect to sample number, description under hand-lens analysis, and location coordinates (tables 3 and 4).

#### 4.5.3 Laboratory measurements

Petrographic analysis was performed on thin section samples of select rock samples within each study site. A polarizing microscope was used to identify mineral constituents in the samples, with previous geochemical assessment of rocks from the study area by Labotka (1980) guiding the analysis. XRD measurements were made with a Philips Electronics PW2273/20 instrument to corroborate the bulk mineralogy of unique rock samples. A Nicolet 6700 laboratory FTIR spectrometer was used to make infrared reflectance measurements of each sample gathered from the study sites in the 5 - 25  $\mu\text{m}$  wavelength range. A limited number of field TIR measurements were made using a Designs & Prototypes  $\mu\text{FTIR}$  (Korb et al., 1996; Hook et al., 1996). Emissivity spectra produced from these measurements were used primarily for comparison and to validate the calibrated emissivity image data.

### **4.6 Image data acquisition and calibration**

#### 4.6.1 Ground SEBASS

SEBASS is a 12-bit pushbroom hyperspectral sensor operated by The Aerospace Corporation that measures the emission of TIR energy in 128 bands across 128 spatial pixels in two ranges (Hackwell et al., 1996). Image data are generated for the midwave-infrared (MWIR), ranging from 2.0 - 5.2  $\mu\text{m}$ , and the longwave-infrared (LWIR), ranging from 7.6 - 13.5  $\mu\text{m}$ . SEBASS has a signal-to-noise ratio (SNR) of 2000:1 for the LWIR focal plane, and a noise-equivalent differential temperature ( $\text{NE}\Delta\text{T}$ ) of 0.01 C. Only the LWIR data were investigated in this research, due to complexity in separating the reflectance component of MWIR measurements during the day collection.

Ground-based SEBASS image data were collected during the day (exact time unknown) on March 9, 1998. The SEBASS instrument was vehicle-mounted and used a scanning mirror to horizontally collect line-by-line spectral measurements (Kirkland et al., 2002). Scan frequency was set to increase dwell time by measuring each line over a period of approximately 10 seconds. At the conclusion of a scan, the elevation angle of the sensor was adjusted to collect new data at a higher angle that provided slight overlap (less than 20%). Three separate scans were acquired and combined to form mosaics for both study sites. The collection vehicle was oriented approximately parallel to the faces of the imaged outcrops at distances ranging from 100 - 200 m. Resulting ground instantaneous field of view (GIFOV) for each site varied dramatically depending on the distance from the sensor to a particular surface area. For the Hell's Gate site, the GIFOV were estimated to range from 0.1 - 1 m, while in the second study site they were estimated to range from 0.2 - 2 m due to greater topographical variability and increased

distance of some imaged surfaces to the sensor. Without pixel-specific range distance information (e.g., LiDAR), GIFOV could only be roughly estimated.

Atmospheric correction and conversion of TIR radiance image data to emissivity were performed to yield spectra in equivalent units for comparison. Temperature-emissivity separation (T&S) is a process used to estimate and withdraw these units from  $n+1$  components that comprise measured emittance (Realmuto, 1990). Each pixel measurement has a temperature as well as an emissivity (per band) component. These radiance data were atmospherically-corrected and calibrated to emissivity using T&S routines provided in ITT Visualization's ENVI V. 4.6 software (Hook et al., 1992; ITT Visual Solutions, 2008). Atmospheric constituents were calculated for the radiance data using regression to fit all pixels at maximum band values. Next the data were normalized to emissivity using an assumed emissivity value of 0.96.

#### 4.6.2 Aerial SEBASS

Aerial SEBASS image data were collected over the Boundary Canyon area on July 16, 2007 at 9:15 AM PST. The flightline was oriented such that measurements would closely intersect the location of previously collected ground-based SEBASS image data. The GIFOV of this data was approximately 4 m, allowing the identification of small outcrops while still retaining a scale adequate to observe contacts between larger-scale geologic units. The data were subset to match boundaries of the study sites and multispectral image data coverage.

The aerial SEBASS data were atmospherically corrected and calibrated to emissivity using The Aerospace Corporation's proprietary In-Scene Atmospheric

Correction (ISAC) routine (Johnson, 1998; Young, 1998). This procedure was applied to the radiance data by the data provider and delivered as apparent emissivity. The emissivity image data matched library spectra well, and generally surpassed emissivity data results that were produced using the ENVI methodology utilized for the ground data.

#### 4.6.3 MASTER

The MASTER (MODIS/ASTER Airborne Simulator) instrument was created to support calibration and validation of both the Moderate Resolution Imaging Spectroradiometer (MODIS) and ASTER by simulating the respective wavelength ranges and spectral band positions of these sensors (Hook et al., 2001). MASTER image data were collected over the Boundary Canyon study area at approximately 12:00 PM PST on May 29, 2000 at 20 m GIFOV. MASTER measures ten channels in the LWIR, ranging from 7.81 - 12.92  $\mu\text{m}$ , has a SNR of 500:1, and a NE $\Delta$ T of 0.1 C. Nine of these bands (41 - 50) coincide with the range measured by SEBASS. Band 40 was subset and the remaining bands were utilized for spectral analysis. Radiance data were processed with ENVI to atmospherically-correct and then calibrate them to apparent emissivity using a normalization-to-emissivity routine. Data were georectified and subset to an area matching the study area boundaries.

#### 4.6.4 ASTER

The Advanced Spaceborne Thermal Emission and Reflection Radiometer (ASTER) is a spaceborne instrument on the Terra (EOS AM-1) satellite platform (Abrams and Hook, 1998). ASTER measures emittance in 90 m GIFOV pixels over five channels in the LWIR ranging from 8.29 - 11.31  $\mu\text{m}$ , has a SNR of 100:1, and a NE $\Delta$ T of

0.3 C. ASTER image data were acquired at 1:36 PM PST on September 7, 2003. The ASTER Standard Product for calibrated surface emissivity (AST-05) was for spectral analysis and mineral mapping. These data are corrected to emissivity using the ASTER T&S algorithm (Gillespie et al., 1998).

#### 4.6.5 Data validation

Calibrated at-surface emissivity image data generated using respective T&S routines were validated by comparing image data spectra to library and laboratory spectra of common minerals. At-sensor radiance and corresponding surface emissivity image data spectra derived from pixels representing a common surface area dominated by quartz-rich rock are plotted in figure 5 for each image data set used in the research. Each calibrated image data emissivity spectra produced satisfactory matches to quartz. Manual inspection of emissivity spectra elsewhere in the image data scenes also indicated reasonable fits to laboratory and library emissivity spectra.

#### 4.6.6 Data processing and analysis

Standard image data processing and analysis methodologies were used to identify and map mineral-related spectral endmembers in the hyperspectral data. Simple 3-band color composites were used first to indicate presence of certain minerals corresponding to high or low emissivity values; decorrelation stretching (DCS) was used to further visually enhance these images (Gillespie et al., 1986). The ENVI Hourglass series of routines were next used to sequentially reduce data dimensionality, identify mineral-related spectral endmembers, and map these endmembers using the spectral angle mapper (SAM) classification algorithm (Kruse et al., 1993; Boardman and Kruse, 1994). Image

data emissivity spectra were manually inspected for areas exhibiting distinct colors in the DCS images, or small areas where SAM indicated high mineralogical diversity, to further refine maps.

The minimum noise fraction (MNF) algorithm was used to separate variance associated with mineral endmembers from redundant and noise components of the data. Once MNF image data were produced, each band was manually inspected for either coherence or incoherence/noise. Bands that exhibited coherence were retained, and the remaining bands were not used in further processing. Selected MNF bands were next used as input into the pure pixel index (PPI) algorithm to determine the most unique emissivity spectra in the data set. Default settings provided by ENVI (10,000 iterations; 2.5 threshold factor) were used as input for the algorithm. Resulting pure pixels were then analyzed using the N-dimensional Visualizer, a program to manually delineate groups of spectrally unique endmembers. These spectral endmember groups were then averaged to yield emissivity spectra representative of a particular mineral class. A final spectral library was formed using these data.

## **4.7 Results**

### **4.7.1 Laboratory identification of minerals**

Comprehensive results of petrographic, XRD, and FTIR analyses are briefly discussed below for each lithology and are summarized in tables 3 and 4. Quartzite samples were comprised of quartz, goethite, and  $\pm$  feldspar. Dolomite, quartz, goethite, and  $\pm$  muscovite were identified in measurements of dolomite samples. Argillite was found to be composed of muscovite, quartz, and feldspar. The mineral constituents of



pelitic schist varied, with each sample yielding muscovite, quartz, chlorite, feldspar, and goethite (figure 6). In addition, low proportions of biotite and staurolite were noted in sample SC-71, while garnet was identified in sample SC-74. Amphibolite yielded magnesio-hornblende, quartz, feldspar, chlorite, and goethite.

Laboratory FTIR-derived emissivity spectra facilitated characterization of mineral spectra features directly comparable to image data spectra. Quartz exhibited an emission minima doublet in the 8.5 - 9  $\mu\text{m}$  wavelength range, and fresh surfaces yielded a sharp, narrow emission minima at 8.4  $\mu\text{m}$ . A less pronounced secondary doublet feature was also observed in the 12 - 13  $\mu\text{m}$  range. Dolomite was identified via a diagnostic narrow emission minima centered at 11.2  $\mu\text{m}$ , while for calcite the location of this minima was shifted to 11.3  $\mu\text{m}$ . Muscovite was indicated by a broad emission minima from 9 - 10.5  $\mu\text{m}$  that was punctuated by narrow minima at 9.4 and 10  $\mu\text{m}$ . Feldspar (albite and/or orthoclase) were identified via emission minima at 9.6 and 9.9  $\mu\text{m}$ . Chlorite was identified by a very narrow minima at 9.6  $\mu\text{m}$ , and hornblende exhibited a broad emission minima spanning from 9.5 - 11  $\mu\text{m}$  and centered at 10.15  $\mu\text{m}$ .

#### 4.7.2 Remote identification of minerals with hyperspectral image data

Analysis of ground and aerial SEBASS image data within both study sites resulted in the identification of numerous mineral spectral endmembers. Quartz, muscovite, dolomite, calcite, and hornblende were each identified and mapped using the ENVI Hourglass methodology (figure 7a). Quartz-mapped pixels corresponded to alluvium, quartzite, and siliceous conglomerate; in addition, weak spectral characteristics of quartz were observed in emissivity spectra representative of dolomite, argillite and

pelitic schist. Muscovite dominated the spectra for mapped pixels of pelitic schist and argillite. Dolomite was mapped solely in outcrops of dolostone, while calcite corresponded to both a carbonate conglomerate and a marble unit. Hornblende was mapped only for amphibolite rocks. The apparent emissivity features of pelitic schists were dynamic, as varying mixtures of quartz, muscovite, feldspar, and chlorite were noted during manual inspection of emissivity spectra (figure 6).

#### 4.7.3 Comparison of ground- and aerial-SEBASS image data

At-sensor radiance spectra of ground and aerial SEBASS data were plotted for co-located pixels representing a quartz-rich surface (figure 8a), and the difference between these measurements was then computed (figure 8b). The aerial spectra indicated a significant deviation of band values from quartz characteristics of the ground spectra in the 7.5 - 8.5  $\mu\text{m}$  region and moderate deviation in the 12 - 13.5  $\mu\text{m}$  region, while mineral features in the 8 - 12  $\mu\text{m}$  wavelength range of both data sets exhibited slightly offset but similar diagnostic features.

For measurements corresponding to pelitic schist, spectral features indicative of quartz, muscovite, feldspar, and chlorite were better observed in the ground image data, as these were more individually distinguishable than aerial data spectra. In bands corresponding to the 7.5 - 8 and 12 - 13.5  $\mu\text{m}$  wavelength ranges, the ground image data emissivity spectra also represented mineral features well, while the aerial data spectra in these ranges were notably degraded, which obscured interpretation of mineral spectra features.

In order to test the repercussions of this difference for mineral mapping, four separate mineral classifications of quartz were generated from the ground and aerial SEBASS image data: 1) ground SEBASS data using bands 11 - 46 (8.04 - 10.03  $\mu\text{m}$  range); 2) ground SEBASS data using bands 89 - 128 (12.03 - 13.57  $\mu\text{m}$  range); 3) aerial SEBASS data using bands 7 - 43 (8.03 - 10.01  $\mu\text{m}$ ); and 4) aerial SEBASS data using bands 88 - 128 (12.02 - 13.54  $\mu\text{m}$ ). Quartz was used as the example for this test due to diagnostic spectral features being present throughout the 7.5 - 13.5  $\mu\text{m}$  range, in addition to it being widely distributed throughout each study site. The specific band ranges chosen for spectral processing encompassed both shoulders and troughs of primary and secondary doublet features. The resulting mineral maps are shown in figures 9 and 10.

Evaluation of the quartz mineral maps derived from the ground data indicated that both the 8.04 - 10.03 and 12.03 - 13.57  $\mu\text{m}$  classifications (1 and 2, respectively) provided similar results, with an overall difference in number of SAM-identified pixels at less than 1% (figures 9A and 9B) (table 5), while the aerial image-derived quartz maps differed more significantly (figures 10A and 10B) (table 5). Classification three, created from bands in the 8.03 - 10.01  $\mu\text{m}$  range, corresponded very well to quartz-rich surface materials such as quartzite and alluvium, while classification four, generated using bands in the 12.02 - 13.54  $\mu\text{m}$  range, did not; these surface areas in the image were obscured by significant noise and banding, and a difference in total number pixels classified was noted at nearly 27%.

#### 4.7.4 Resampling of hyperspectral emissivity spectra to multispectral resolution

Minerals identified during analysis of ground-based SEBASS image data were convolved to bandpass characteristics of multispectral MASTER and ASTER data. The ground data were used for this purpose because these exhibited emissivity spectra with much less band-to-band noise attributed to atmospheric effects, and thus best represented rocks in the area. Resampled multispectral mineral spectra were plotted and compared against each other; quartzite, argillite, schist, and amphibolite appeared spectrally distinguishable at each spectral resolution because of significant band slope or offset differences. In contrast, calcite and dolomite spectra were very similar at multispectral resolution, as band slope differences in the 11.2 - 11.3  $\mu\text{m}$  diagnostic range were nearly unperceivable, rather than distinctly offset, as for emission minima observed at hyperspectral resolution.

#### 4.7.5 Multi-scale TIR mapping of minerals in the BCDF zone

Convolved SEBASS emissivity spectra representative of unique lithologies within the two study sites were used as input for the SAM classification algorithm to map minerals with MASTER and ASTER TIR image data. These mineral spectra were indicative of quartzite, dolomite, and siltstone in site one, and siliceous conglomerate, carbonate conglomerate, dolomite, pelitic schist, and amphibolite in site two. Emissivity spectra representing the same (or nearby) imaged surface areas were next examined with ground and aerial SEBASS, MASTER, and ASTER (figure 11).

In study site one, horizontally-scanned SEBASS image data were used in the field to map quartz, indicative of alluvium and quartzite; muscovite relating to argillite;

dolomite, and limited marble (figure 12C). Aerial SEBASS image data covering this area were used to map quartz, limited muscovite, dolomite, and limited calcite (figure 12G). Analysis of MASTER data helped produce a distribution map of quartz-, muscovite-, and carbonate-rich rocks (12H). Although the overall variability of these emissivity spectra was noted, the measurements were not detailed enough to discern between specific carbonate minerals (e.g., calcite and dolomite). ASTER image data emissivity spectra exhibited reduced variability compared to MASTER, and mapped pixels were limited to large, contiguous surface areas dominated by quartz, clays, and carbonates (figure 12I).

In study site two, ground SEBASS image data were used to map minerals representative of alluvium, siliceous conglomerate, carbonate conglomerate, dolomite, amphibolite, and pelitic schist (figure 13C). Quartz-dominated pixels were related to alluvium in the foreground of the scene, as well as for a siliceous conglomerate bed. Dolomite-mapped pixels corresponded to dolostone outcrops located in the background of the scene, while calcite was mapped for pixels amongst an outcrop of conglomerate that was composed of a calcite matrix. Muscovite dominated the emissivity spectra of pixels corresponding to pelitic schist, while quartz, feldspar, and chlorite were identified as minor constituents of this rock class during manual interpretation of emissivity spectra. Lastly, hornblende was mapped in pixels representing a unit of amphibolite that jutted over the pelitic schist.

Aerial SEBASS image data measurements made within 100 m of the same surfaces imaged by the ground data were used to map quartz representing alluvium and siliceous conglomerate; dolostone outcrops were able to be distinctly mapped from a larger adjacent group of calcite pixels related to marble; muscovite pixels were mapped

that represented pelitic schist; and hornblende was identified in clusters of pixels amongst muscovite-dominated surface areas (figure 13G). The MASTER data were able to map the quartz units, muscovite-dominated schist, a single carbonate mineral class, and amphibolite mapped in a limited number of pixels amongst the larger group of muscovite-mapped pixels (figure 13H). ASTER mineral mapping yielded a simple silica-clay-carbonate distribution that provided much less detail than the SEBASS- and MASTER-derived mineral maps, as even moderate-sized outcrops and some geologic unit boundaries could not be distinguished.

## **4.8 Discussion and summary**

### 4.8.1 General observations

Laboratory measurements and analyses of rock samples collected from the study area were used to comprehensively identify mineral constituents and help recognize image data limitations for mineral identification in the NEDP study area. Petrographic analyses were able to identify the presence of micro-scale mineral constituents of pelitic schists important in determining metamorphic facies. In general these minerals comprised a low proportion of total rock mass, and consequently spectral features were not identified in XRD, laboratory FTIR, or image data emissivity spectra.

Ground SEBASS emissivity spectra produced good matches to mineral spectra derived from laboratory measurements. Emissivity spectra provided for each pixel resulted in measurements of fresh-surfaced and weathered rocks positioned in different angles, demonstrating good spectral variability and emphasizing different mineral proportions. In contrast, laboratory FTIR measurements produced less spectral variation,

even when different surface areas of samples were physically adjusted in the sample tray. Clay films and coatings noted on some rock samples produced only subtle features in laboratory FTIR measurements; these were not observed in the image data spectra.

The aerial SEBASS image data spectra exhibited the ability to identify most of the same minerals as in the ground data; however, these spectra did not replicate the same variability of individual mineral components within mixtures. Narrow features indicating mixtures composed of muscovite, feldspar, chlorite, and quartz may have been subdued due to limited proportion of imaged surface, as well as emittance measurements being impacted by atmospheric effects.

Airborne MASTER data were useful in mapping major lithologic units within each study site. With exception of quartz, these emissivity spectra were indicative of broad mineral groups, rather than specific minerals (e.g., carbonate instead of either calcite and dolomite). The 20 m GIFOV of the data enabled spatial recognition of important surface features such as larger alluvial channels, moderate-sized outcrops, and transitions between geologic units. These multispectral data were useful detecting and mapping basic compositional differences between siliceous, micaceous, and carbonate units.

ASTER, with 90 m GIFOV and only five TIR bands, produced emissivity spectra that were suited for determining where the largest contiguous exposures of quartz-, clay-, and carbonate-rich rocks were located. Variability of these mineral spectra were much less than that exhibited by MASTER data. For surface materials dominated by the same mineral (e.g., alluvium versus outcrop), delineation was not successful, and this was attributed to limitations of spatial and radiometric resolution (Kruse, 2000).

#### 4.8.2 Ground and aerial hyperspectral mineral mapping

Spectral bands at wavelengths below 8  $\mu\text{m}$  and above 12  $\mu\text{m}$  in the ground SEBASS image data exhibited continuous slope features representative of minerals such as quartz, which were useful for mapping. These same band ranges in the aerial SEBASS data are degraded and exhibit noise attributed to: 1) atmospheric water vapor, which becomes increasingly more prominent at longer pathlengths, and 2) a decrease in detector sensitivity. The role of this atmospheric component upon interpretation of aerial SEBASS emissivity spectra was previously noted by Cudahy (2000) and Vaughan (2003), and was found not to be mitigated following ISAC atmospheric correction of radiance data, limiting analysis to the 8 - 12  $\mu\text{m}$  range.

The ground and aerial SEBASS image data also provided different benefits and limitations according to the perspective of measurement. In study site one, numerous ground-scanned sedimentary beds within an outcrop were shown to be spatially resolved and mineralogically distinguishable, as they are laterally-oriented. However, from the nadir perspective of aerial SEBASS image data, a large dolostone unit was observed which caps and effectively limits observation of the numerous strata beneath it.

The aerial data were useful in providing better synoptic coverage of each study area, in addition to exhibiting clear mineralogic contacts between mapped geologic units. The contact between lower Wood Canyon and upper Stirling Quartzite formation rock units is well-delineated by dolomite and quartz, respectively. However, these aerial data did not possess adequate GIFOV to distinctly resolve lithologies with limited exposure (e.g., thin argillite beds) and thus were spectrally diminished.



In study site two dolostone, quartzite, and conglomerate were noted as overlaying micaceous pelitic schist. Contacts between mapped geologic units, such as the Stirling Quartzite and Johnnie formation, as well as individual rock beds, were able to be quickly distinguished in the ground data. In comparison, mineral maps derived from the aerial data did not help to establish the vertical relationship of rock units. Whereas amphibolite outcrops were better laterally exposed and observed from the horizontal perspective, these rocks were less prominent from the nadir point-of-view.

#### 4.8.3 Extending detection and mapping of amphibolite facies rocks

Hornblende was able to be mapped outside of the limited area of coverage provided by ground and aerial SEBASS using a MASTER-derived classification image (figure 14). The aerial SEBASS mineral map of this class was used to guide thresholding of the multispectral classification image in an area of overlap within study site two. Once a feasible threshold was determined using information from SEBASS, a hornblende mineral map over the full extent of MASTER coverage was generated that indicated likely amphibolite outcrops. Field checking of mapped areas helped to corroborate the results; pixels were found to be limited to rocks of the Johnnie Formation, and were traced along the length of the fault contact found within the boundaries of the MASTER coverage. Analysis of ASTER data following the same methodology resulted in classifications that produced false positives representative of muscovite-dominated schists within the Johnnie Formation. Further investigation of these data using mixture-tuned match filter (MTMF) and linear spectral unmixing algorithms did not introduce results indicating that amphibolite could be delineated from pelitic schist.

#### 4.8.4 Repercussions for future LWIR mineral mapping studies

The restrictions imposed by atmospheric components, such as water vapor, result in significant differences between ground and aerial TIR measurements. Pathlength distance from sensor-to-surface is an important factor that has direct repercussions for emittance measurements of surface materials, and these can effectively reduce wavelength range that may be utilized for remote mineral mapping. As such, these ground-collected data demonstrated excellent spatial recognition of surface features, but can also result in more complete utilization of spectral information, due to more limited atmospheric attenuation. Although most minerals exhibit primary diagnostic spectral features in the 8 – 12  $\mu\text{m}$  range, secondary diagnostic features are observed for minerals such as alunite and beryl at wavelengths below 8  $\mu\text{m}$ , while beryl, chromite, cordierite, and hypersthene exhibit features above 12  $\mu\text{m}$ . Thus these ranges may be of utility for further identifying and mapping minerals with ground-based LWIR image data.

Convolved hyperspectral endmembers related to minerals were useful for mapping a larger area with MASTER and ASTER image data than possible with limited SEBASS data. However, spatial, spectral, and radiometric resolution constraints limited detection, identification, and mapping of a key lithology, amphibolite, as well as physical surface characteristics important to characterizing the BCDF zone with ASTER. Image data with higher spatial and radiometric resolutions will result in better mineral detection and mapping capabilities. The proposed HySPIRI instrument (JPL, 2010) is a spaceborne multispectral sensor that makes 60 m emittance measurements in eight bands. These data would effectively increase the current maximum spatial resolution for spaceborne TIR

measurements from that of 90 m of ASTER, and enhance mineralogic and temperature characterization of the Earth's surface. This development will be important for geologic applications such as: basic lithologic mapping; structural characterization; and resolving mineralization and temperature anomalies associated with geothermal potential, in basin-to-range transition zones that may not otherwise be detected at coarser pixel resolutions (Moersch et al., 2001; Coolbaugh et al., 2006; Kratt et al., 2006).

In future surveys, image data resources of varying spatial, spectral, and radiometric resolution should be strategically utilized to maximize the potential for remotely mapping targeted minerals. Ground-collected data may be valuable for spatially resolving small or horizontally-ordered rock features that cannot be viewed from the nadir perspective of aerial or spaceborne measurements, as well as facilitating more comprehensive usage of wavelength ranges, while aerial and spaceborne data can provide emittance measurements over a larger surface area at more frequent intervals. Spectral characterization of small study sites using high spatial and spectral resolution image data, and extending these data outward with lower resolution multispectral data, such as MASTER or ASTER, is an efficient and logical manner in which to maximize mineral mapping capabilities with hyperspectral data such as SEBASS.

#### **4.9 Acknowledgements**

We would like to thank Dean Riley of the Aerospace Corporation for coordinating the collection of aerial SEBASS data, as well as releasing the archived ground SEBASS data. Thanks to Simon Hook and Eric Fraim at the Jet Propulsion Laboratory for providing information regarding MASTER data collection parameters. This research was funded by a DOE grant.

#### 4.10 References

- Abrams, M., and Hook, S. (1998). ASTER User Handbook, V.1, *NASA/Jet Propulsion Laboratory*, Pasadena, CA.
- Baldrige, A. M., Hook, S. J., Grove, C. I. and Rivera, G. (2009). The ASTER Spectral Library V. 2.0., *In press, Remote Sensing of Environment*.
- Balick, L. K. Jeffery, C. A., and Henderson, B. G. (2003). Turbulence induced spatial variation of surface temperature in high resolution thermal IR satellite imagery. *Remote Sensing for Agriculture, Ecosystems, and Hydrology IV*, Edited by Owe, M., D'Urso, G. and Toullos, L., Proceedings of SPIE, 4879, pp. 221-230.
- Boardman J. W., and Kruse, F. A. (1994). Automated spectral analysis: A geologic example using AVIRIS data, north Grapevine Mountains, Nevada. *Proceedings of the Tenth Thematic Conference on Geologic Remote Sensing*, Environmental Research Institute of Michigan, Ann Arbor, MI, pp. I-407-I-418.
- Clark, R.N. (1999). Spectroscopy and Principles of Spectroscopy, *Manual of Remote Sensing*, A. Rencz, Editor, John Wiley and Sons, Inc.
- Clark, R.N., Swayze, G.A., Wise, R., Livo, E., Hoefen, T., Kokaly, R., and Sutley, S.J. (2007). USGS digital spectral library splib06a, *U.S. Geological Survey*, Digital Data Series 231.
- Collins, A.H. (1991). Thermal infrared spectra and images of altered volcanic rocks in the Virginia Range, Nevada, *International Journal of Remote Sensing*, 12 (7), pp. 1559-1574.
- Coolbaugh, M., Kratt, C., Fallacaro, A., Calvin, W., and Taranik, J.V. (2006). Detection of geothermal anomalies using Advanced Spaceborne Thermal Emission and

- Reflection Radiometer (ASTER) thermal infrared images at Brady's Hot Springs, Nevada, USA. *Remote Sensing of Environment*, 106, pp. 350-359.
- Crowley, J.K. (2000). Mapping evaporite minerals in the Death Valley salt pan using MODIS/ASTER airborne simulator (MASTER) data. *Proceedings of the Fourteenth International Conference on Applied Geologic Remote Sensing*, pp. 344-345.
- Crowley, J.K. and Hook, S. J. (1996). Mapping Playa Evaporite Minerals and Associated Sediments in Death Valley, California, with Multispectral Thermal Infrared Images. *Journal of Geophysical Research*, 101, pp. 643-660.
- Cudahy, T.J., Okada, K., Yamato, Y., Maekawa, M., Hackwell, J.A., and Huntington, J.F. (2000). Mapping skarn and porphyry alteration mineralogy at Yerington, Nevada, using airborne hyperspectral TIR SEBASS Data, *CSIRO exploration and mining report 734R*, CSIRO Exploration and Mining Co, Floreat Park, WA, Australia.
- Cudahy, T.J., Okada, K., Cornelius, A., and Hewson, R. (2000). Regional to Prospect Scale Exploration for Porphyry-Skarn-Epithermal mineralization at Yerington, Nevada, using ASTER and Airborne Hyperspectral data. *CSIRO exploration and mining report 1122*, CSIRO Exploration and Mining Co., Floreat Park, WA, Australia.
- Diehl, P.E. (1979). The stratigraphy, depositional environments, and quantitative petrography of the Precambrian-Cambrian Wood Canyon Formation, Death Valley. *Ph.D. thesis*, Pennsylvania State University.
- Elachi, C. (1987). Introduction to the Physics and Techniques of Remote Sensing, John Wiley and Sons, Inc.: Toronto.
- Farmer, V.C., Editor (1974). *The infrared spectra of minerals*. Mineralogical Society

- Monograph vol. 4, Mineralogical Society, London.
- Gillespie, A.R., Rokugawa, S., Matsunaga, J.S., Cothorn, S. and Kahle, A.B. (1998). Temperature and emissivity separation algorithm for Advanced Spaceborne Thermal Emission and Reflection Radiometer (ASTER) images, *IEEE Transactions on Geoscience and Remote Sensing*, 36 (4), pp. 1113-1126.
- Gillespie, A.R., Kahle, A.B. and Walker, R.E. (1986). Color enhancement of highly correlated images: I. Decorrelation and HIS contrast stretches. *Remote Sensing of Environment*, 20, pp. 209-235.
- Gillespie, A.R., Kahle, A.B., and Palluconi, F.D. (1984). Mapping alluvial fans in Death Valley, California, using multi channel thermal infrared images. *Geophysical Research Letters*, 11, pp. 1153-1156.
- Hackwell, J.A., Warren, D.W., Bongiovi, R.P., Hansel, S.J., Hayhurst, T.L., Mabry, D.J., Sivjee, M.G., and Skinner, J.W. (1996). LWIR/MWIR imaging hyperspectral sensor for airborne and ground-based remote sensing, *The International Society for Optical Engineering*, 2819, pp. 102-107.
- Hapke, B. (1993). *Theory of Reflectance and Emittance Spectroscopy: Topics in Remote Sensing 3*. Cambridge University Press, Cambridge. 455 pp.
- Hoisch, T.D. and Simpson, C. (1993). Rise and tilt of metamorphic rocks in the lower plate of a detachment fault in the Funeral Mountains, Death Valley, California. *Journal of Geophysical Research*, 98, pp. 6805-6827.
- Hook, S. J., Myers, J. J., Thome, K. J., Fitzgerald, M., and Kahle, A. B. (2001). The MODIS/ASTER airborne simulator (MASTER) – a new instrument for earth science studies. *Remote Sensing of Environment*, 76, pp. 93-102.

- Hook, S.J. and Kahle, A.B. (1996). The Micro Fourier Transform Interferometer ( $\mu$ FTIR) - A New Field Spectrometer for Acquisition of Infrared Data of Natural Surfaces. *Remote Sensing of Environment*, 56, pp.172-181.
- Hook, S.J., Gabell, A.R., Green, A.A., and Kealy, P.S. (1992). A comparison of techniques for extracting emissivity information from thermal infrared data for geologic studies. *Remote Sensing of Environment*, 42, pp. 123-135.
- Hunt, C.B., and Mabey, D.R. (1966). General geology of Death Valley, California. *United States Geological Survey Professional Paper*, 494-A.
- ITT Visual Solutions (2008). ENVI User's Guide, Version 4.3. ITT Visual Solutions, Boulder, Colorado.
- Jensen, J.R. (1996). *Introductory Digital Image Processing: A Remote Sensing Perspective*. 2<sup>nd</sup> Edition, Prentice-Hall, Inc.
- Johnson, B.R. (1998). In-scene atmospheric compensation: application to the SEBASS data collected at the ARM site, Part I. *Aerospace Corporation Report*, (ATR-99(8407), Part I).
- HyspIRI Group (2010). NASA 2009 HypsIRI Science Workshop Report. Jet Propulsion Laboratory Publication 10-3, pp. 73.
- Kahle, A.B. and Goetz, A.F.H. (1983). Mineralogic information from a new thermal infrared multispectral scanner, *Science*, 222, pp. 24-27.
- Kirkland, L.E., Herr, K.C., Adams, P.M., McAfee, J., and Salisbury, J. (2002). Thermal infrared hyperspectral imaging from vehicle-carried instrumentation. *Imaging Spectrometry VIII.*, *Proceedings of the SPIE*, S.S. Shen, editor, 4816, pp. 415-425.



- Korb, A.R., Dybwad, P., Wadsworth, W., and Salisbury, J.W. (1996). Portable Fourier transform infrared spectrometer for field measurements of radiance and emissivity, *Applied Optics*, 35, pp. 1679-1692.
- Kratt, C., Coolbaugh, M.F., and Calvin, W.M. (2006). Remote detection of Quaternary borate deposits with ASTER satellite imagery as geothermal exploration tool. *Geothermal Resources Council Transactions*, 30, pp. 435 - 439.
- Kruse, F.A., Lefkoff, A.B., and Dietz, J.B. (1993). Expert system-based mineral mapping in Northern Death Valley, California/Nevada, using the Airborne Visible/Infrared Imaging Spectrometer (AVIRIS). *Remote Sensing of Environment* 44, pp. 309-336.
- Kruse, F. A. (2000). The effects of spatial resolution, spectral resolution, and signal-to-noise ratio on geologic mapping using hyperspectral data, Northern Grapevine Mountains, Nevada, *Proceedings of the 9th JPL Airborne Earth Science Workshop*, Jet Propulsion Laboratory Publication 00-18, pp. 261-269.
- Kruse, F.A. (2002). Combined SWIR and LWIR Mineral Mapping using MASTER/ASTER. *Proceedings of IGARRS 2002*, 4, pp. 2267 - 2269.
- Kruse, F.A., and Perry, S.L. (2009). Improving multispectral mapping by spectral modeling with hyperspectral signatures. *Journal of Applied Remote Sensing*, 3, 033504.
- Labotka, T.C. (1980). Petrology of a medium-pressure regional metamorphic terrane, Funeral Mountains, California. *American Mineralogist*, 65 (7-8), pp. 670-689.
- Lane, M.D., and Christensen, P.R. (1997). Thermal infrared emission spectroscopy of anhydrous carbonates. *Journal of Geophysical Research*, 102, pp. 25,581-25,592.
- Lyon, R.J.P. (1965). Analysis of rocks by spectral infrared emission (8 to 25 microns).

*Economical Geology*, 60, pp. 715-736.

Lyon, R. J. P., and Green, A. A. (1975). Reflectance and emittance of terrain in the mid-infrared (6 - 25  $\mu\text{m}$ ) region. Ch 7 in: *Infrared and Raman Spectroscopy of Lunar and Terrestrial Minerals*, Academic Press, Inc., pp. 164-194.

McCabe, M.F., Balick, L.K., Theiler, J.P., Gillespie, A.R., and Mushkin, A. (2008). Forward modeling of linear mixing in thermal IR temperature retrieval. *International Journal of Remote Sensing*, 29 (17), pp. 5047-5061.

Mitchell, H.J., and Salvaggio, C. (2003). The MWIR and LWIR Spectral Signatures of Water and Associated Materials. *Proceedings of SPIE*, 5093, pp. 195-205.

Moersch, J.E., Farmer, J., and Baldrige, A. (2001). Remote Sensing of Evaporite Minerals in Badwater Basin, Death Valley, at Varying Spatial Scales and in Different Spectral Regions. *Proceedings of the Workshop on the Martian Highlands and Mojave Desert Analogs*, paper 4053.

Realmuto, V.J. (1990). Separating the effects of temperature and emissivity: emissivity spectrum normalization. *Proceedings of the 2<sup>nd</sup> TIMS Workshop*, JPL Publication 90-55, pp. 31-35.

Reynolds, M.W., Wright, L.A., and Troxel, B.W. (1986). Geology and chronology of late Cenozoic detachment faulting, Funeral and Grapevine Mountains, Death Valley, California. *Geological Society of America Abstracts with Programs*, 18, p. 175.

Salisbury, J.W., and D'Aria, D.M. (1992). Emissivity of terrestrial materials in the 8 - 14  $\mu\text{m}$  atmospheric window. *Remote Sensing of Environment*, 42, pp. 83-106.

Salisbury, J.W., and Eastes, J.W. (1985). The Effect of Particle Size and Porosity on

- Spectral Contrast in the Mid-Infrared. *Icarus*, 64, pp. 586-588.
- Snow, J.K. and Wernicke, B. (1989). Uniqueness of geological correlations: An example from the Death Valley extended terrain. *Geological Society of America Bulletin*, 101, pp. 1351-1362, 7 figs.
- Troxel, B.W. (1988). A geologic transverse of the northern Funeral Mountains, Death Valley, California, in *This Extended Land, Geological Journeys in the Southern Basin and Range*, Field Trip Guidebook, Las Vegas. D.L. Weide, and M.L. Faber, editors. Cordilleran Section, Geological Society of America, pp. 45-49.
- Vaughan, R.G., Hook, S.J., Calvin, W.M., and Taranik, J.V. (2005). Surface mineral mapping at Steamboat Springs, Nevada, USA, with multi-wavelength thermal infrared images. *Remote Sensing of Environment* 99, pp. 140-158.
- Vaughan, R. G., Calvin, W. M., and Taranik, J. V. (2003). SEBASS hyperspectral thermal infrared data: surface emissivity measurement and mineral mapping. *Remote Sensing of Environment* 85, pp. 48-63.
- Wertz, W.E. (1983). The depositional environments and petrography of the Stirling Quartzite, Death Valley Region, California and Nevada. *Ph.D. Thesis*, Pennsylvania State University.
- Workman, J.B., Menges, C.M., Page, W.R., Taylor, E.M., Ekren, E.B., Rowley, P.D., Dixon, G.L., Thompson, R.A., and Wright, L.A. (2002). Geologic map of the Death Valley ground-water model area, Nevada and California. *USGS Misc. Field Studies Map* MF-2381-A, scale 1:250,000.
- Wright, L.A., and Troxel, B.W. (1993). Geologic map of the central and northern Funeral Mountains and adjacent areas, Death Valley region, southern California. *US*

*Geological Survey Misc. Invest. Series Map I-2305.*

Young, S. J., Johnson, B. R., and Hackwell, J. A. (2002). An in-scene method for atmospheric compensation of thermal hyperspectral data. *Journal of Geophysical Research*, 107 (D24), 4774.

## Tables

Table 1.

Instrument/sensor specifications and data collection information.

Sensor	Radiometric resolution	SNR	NE $\Delta$ T (C $^{\circ}$ )	$\lambda$ range ( $\mu$ m)	LWIR Channels	Date of collection	GIFOV
Nicolet 6700 FTIR	12-bit	u/c	n/a	2.5-25	u/c	2008-2009	.01 m
Ground SEBASS <sup>1</sup>	12-bit	2000:1	0.01	7.5-13.5	128	3/9/1998	0.1-2 m
Aerial SEBASS <sup>1</sup>	12-bit	2000:1	0.01	7.5-13.5	128	7/16/2007	4 m
MASTER <sup>2</sup>	16-bit	500:1	0.1	8-14	10	5/29/2000	20 m
ASTER <sup>3</sup>	12-bit	100:1	0.3	8-12	5	9/7/2003	90 m

n/a = non-applicable;

u/c = user configurable

<sup>1</sup> Hackwell et al., 1996

<sup>2</sup> Hook et al., 2001

<sup>3</sup> Abrams and Hook, 1998

Table 2.

Geology units within the study, associated ages, and descriptions (after Workman et al. 2002).

Name	Age	Lithologies	Description
<i>Surficial deposits</i>			
Qay	Holocene to latest Pleistocene	young alluvium	medium- to coarse-grained alluvium; unconsolidated to poorly unconsolidated
Qayo	middle Holocene to latest Pleistocene	intermediate-age alluvium	mostly medium- to coarse-grained gravel and sand deposits; unconsolidated to poorly unconsolidated
Qtau	Holocene to latest Tertiary	undifferentiated older alluvium	complex suite of deposits of widely varying ages
Qao	late to middle Pleistocene	old alluvium	medium- to coarse-grained gravel and sand deposits
<i>Bedrock units</i>			
Ts4	Pliocene and Miocene	sedimentary rocks, unit 4	poorly to moderately consolidated, mostly fluvial sandstone, conglomerate, mudstone, limestone, and siltstone
Tso	Miocene to Eocene?	older sedimentary rocks	moderately consolidated, fluvial and lacustrine sandstone, conglomerate, limestone, mudstone, and siltstone whose age is poorly constrained
€Zw	lower Cambrian and late Proterozoic	Wood Canyon Formation	quartzite, sandstone, siltstone, shale, and dolomite
Zs	late Proterozoic	Stirling Quartzite Formation	quartzite and sandstone, conglomeratic quartzite, and micaceous siltstone
Zj	late Proterozoic	Johnnie Formation	quartzite, conglomeratic quartzite, siltstone, shale, and limestone and dolomite
ZYp	late and middle Proterozoic	Pahrump Group	pelitic schist, meta-conglomerate, calcite marble, amphibolite, micaceous quartzite
Xmi	early Proterozoic	metamorphic and igneous rocks	schist, meta-sedimentary rocks

Table 3.

Table of rock samples gathered in study site one and used in laboratory measurements, with corresponding descriptions, identified minerals, and coordinates.

Sample number	Description	Identified minerals	Latitude	Longitude
<i>Study site 1</i>				
HG-48	sandy siltstone on top of the outcrop	muscovite, quartz, feldspar	36°43'29.136"	-116°58'33.599"
HG-48B	quartzite on top of the outcrop	quartz, feldspar, goethite	36°43'29.136"	-116°58'33.599"
HG-49	varnished quartzite on top of the outcrop	muscovite, quartz, feldspar, goethite	36°43'29.136"	-116°58'33.599"
HG-50	smooth surfaced dolomite on top of the outcrop	dolomite, quartz, muscovite, goethite	36°43'29.136"	-116°58'33.599"
HG-51	rough surfaced dolomite on top of the outcrop	dolomite, quartz, goethite	36°43'29.136"	-116°58'33.599"
HG-52	newer incision through wash - smaller pebbles	quartz, muscovite	36°43'31.548"	-116°58'33.599"
HG-53	older alluvium in wash - larger pebbles	quartz, muscovite, dolomite	36°43'33.671"	-116°58'37.2"
HG-54	older alluvium in wash - larger pebbles	quartz, muscovite, dolomite	36°43'33.671"	-116°58'37.2"

Table 4.

Table of rock samples gathered in study site two and used in laboratory measurements, with corresponding descriptions, identified minerals, and coordinates.

Sample number	Description	Identified minerals	Latitude	Longitude
<i>Study site 2</i>				
SC-55	quartz from wash	quartz	36°44'32.96"	-116°57'54"
SC-58	dolomite from outcrop	dolomite, quartz	36°44'9.24"	-116°57'32.4"
SC-59	amphibolite	magnesio-hornblende, feldspar, chlorite	36°44'17.19"	-116°57'21.6"
SC-60	silicic conglomerate	quartz, feldspar	36°44'11.93"	-116°57'25.19"
SC-61	carbonate conglomerate	calcite, quartz	36°44'15.03"	-116°57'28.79"
SC-63	pelitic schist	muscovite, quartz, feldspar, chlorite	36°44'19.13"	-116°57'17.99"
SC-71	pelitic schist	muscovite, quartz, feldspar, chlorite, biotite, staurolite	36°44'33.24"	-116°57'53.22"
SC-74	pelitic schist	muscovite, quartz, feldspar, chlorite, garnet	36°44'00.79"	-116°57'27.13"



Table 5.

Ground and aerial SEBASS-derived quartz classification image information for each study site, and from using input bands in the 8 - 10  $\mu\text{m}$  and 12 -13.5  $\mu\text{m}$  ranges. In the SAM threshold column, values in the upper half of the box are indicated for classifications using bands in the 8 - 10  $\mu\text{m}$  range; the values in the lower half of the box indicate classifications using bands in the 12 - 13.5  $\mu\text{m}$  range.

Data	SAM threshold	Total number of pixels	Class pixels: (8-10 $\mu\text{m}$ )	% of total pixels: (8-10 $\mu\text{m}$ )	Class pixels: (12-13.5 $\mu\text{m}$ )	% of total pixels: (12-13.5 $\mu\text{m}$ )	$\pm$ %
ground SEBASS site 1	0.052 0.098	449,941	109,121	24.25	106,998	23.78	0.47
ground SEBASS site 2	0.158 0.026	453,754	61,200	13.48	54,049	11.91	1.57
aerial SEBASS site 1	0.022 0.003	79,826	27,834	34.86	6,573	8.23	26.63
aerial SEBASS site 2	0.049 0.007	81,118	13,715	16.9	7,648	9.42	7.48

**Figures**

Figure 1.

Study area location map.

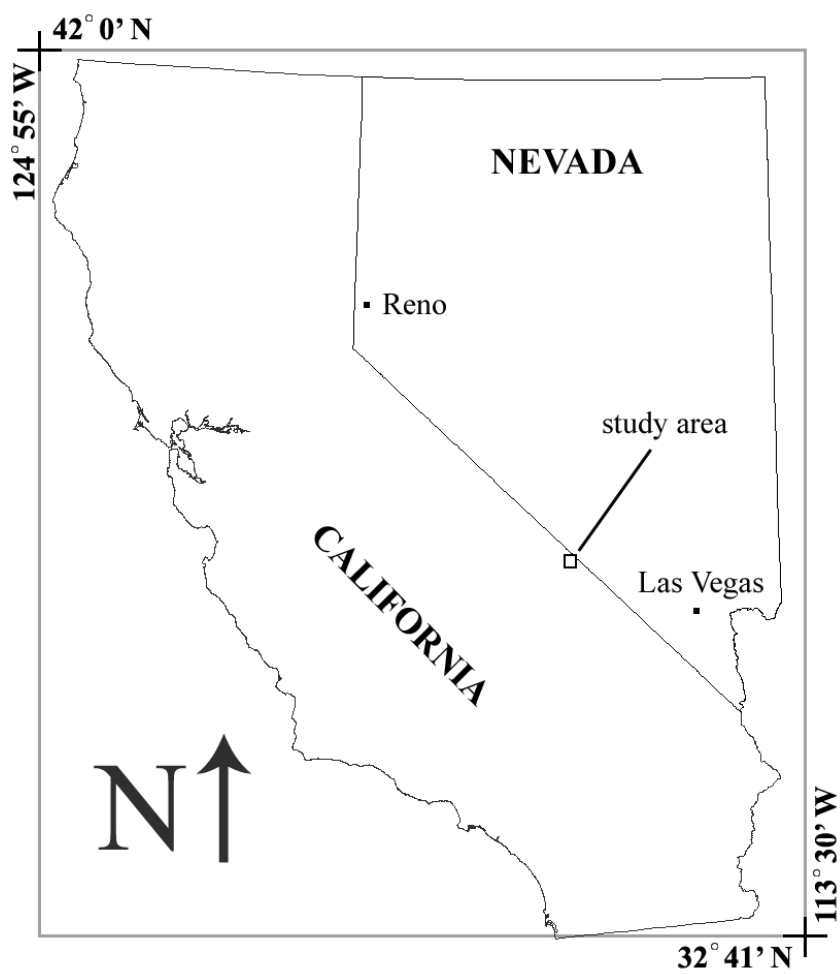


Figure 2.

Location map of study area. Investigated study sites are located in proximity to ground SEBASS image data collections, indicated by barbells. Arrows indicate ground scan direction and letters indicates a transect corresponding to beginning and ending of image data scan. Grey box indicates boundaries for aerial SEBASS image data coverage. Black squares indicate boundaries for MASTER and ASTER image data coverage.

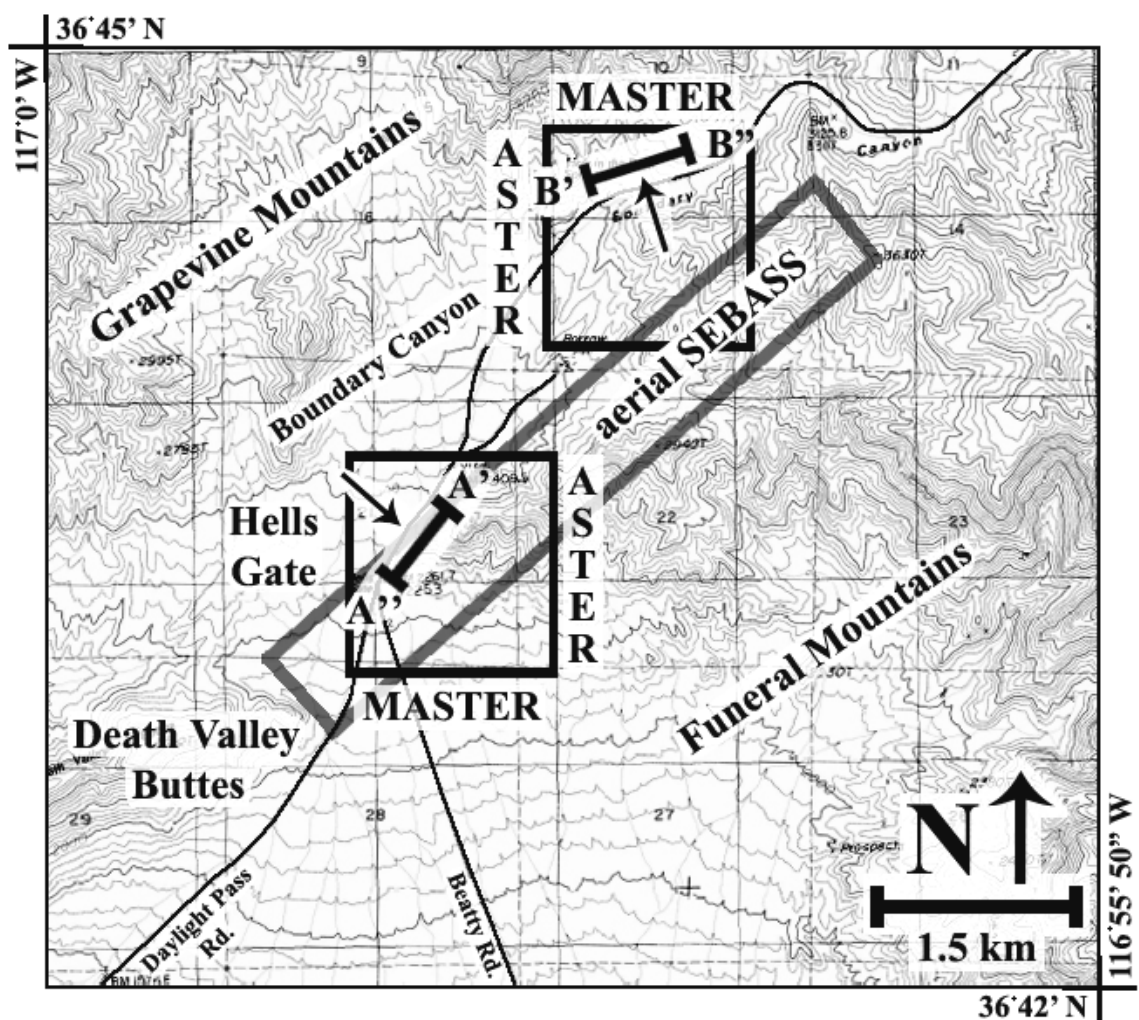


Figure 3.

Geology map of the study area (from Workman et al., 2002). Geologic unit ages and descriptions are provided in table 2.

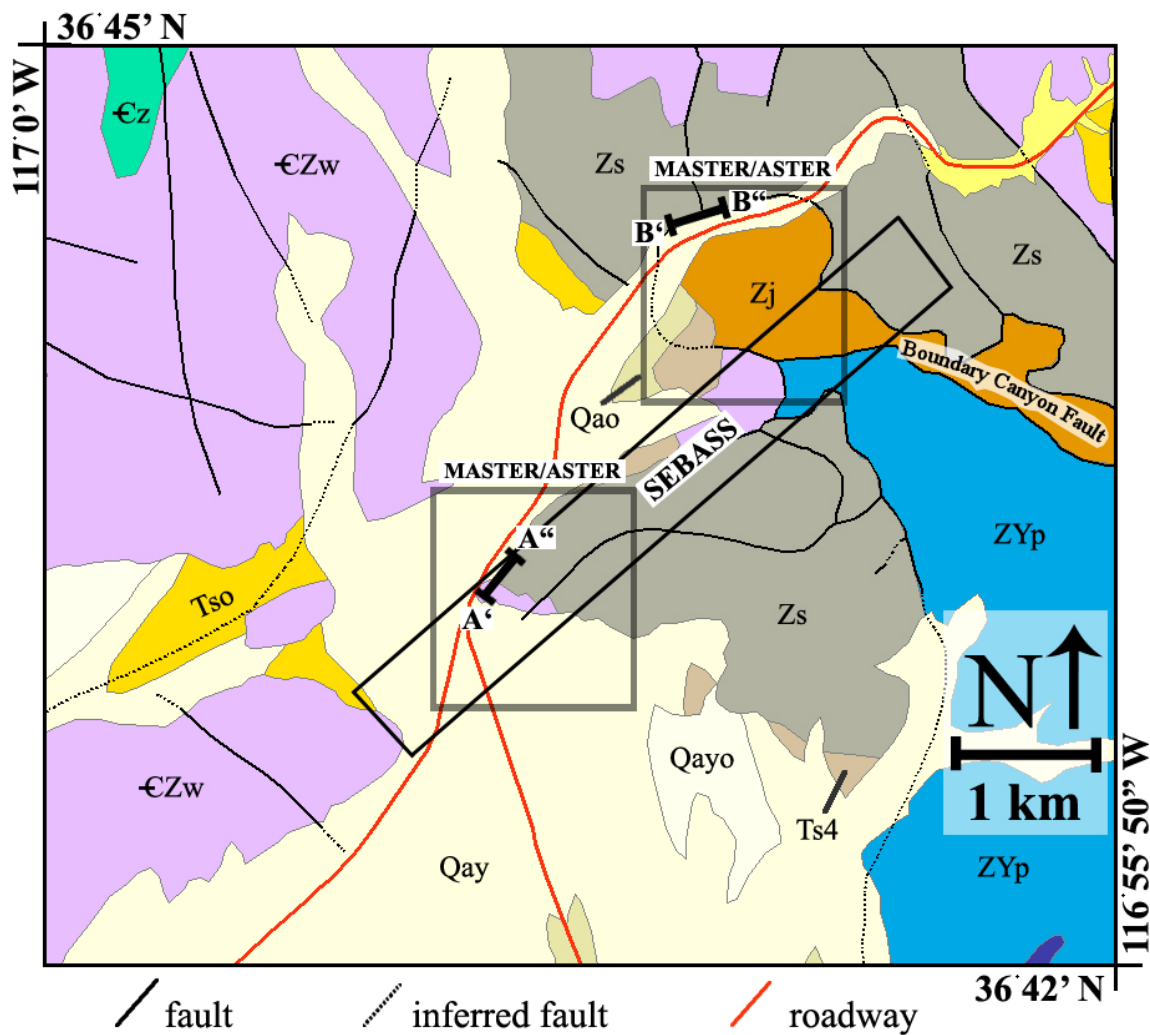


Figure 4.

Schematic illustrating relative ground instantaneous field of view (GIFOV) of image data and laboratory instrumentation used in the study.

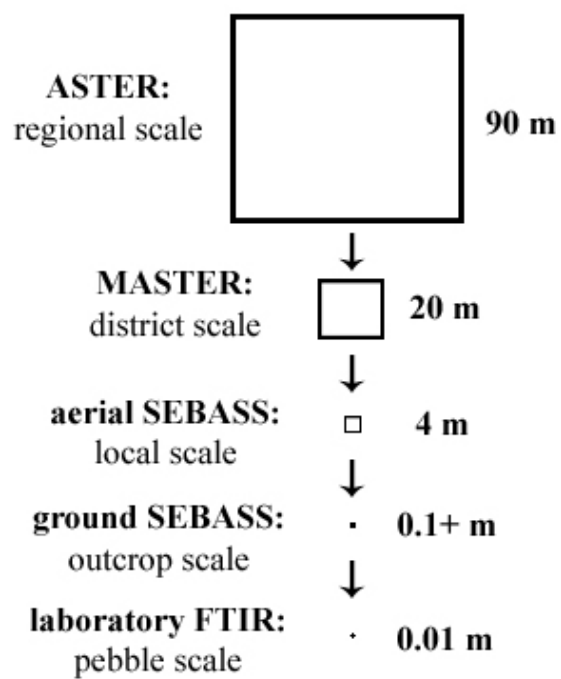


Figure 5.

At left, comparison of at-sensor radiance measurements of the same quartz-dominated surfaces areas from respective sensors. At right, calibrated apparent emissivity spectra of these same surfaces.

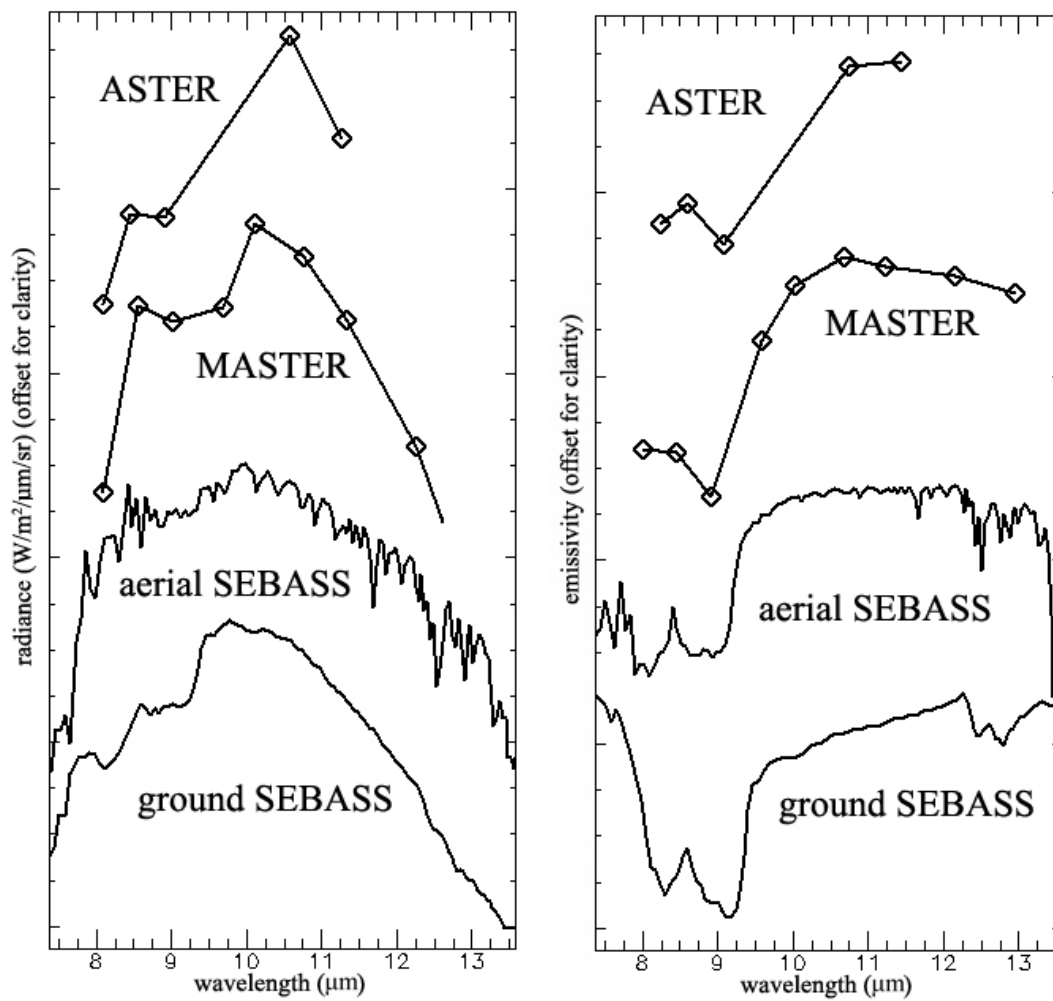


Figure 6.

Ground-collected SEBASS emissivity spectra are plotted (black), which demonstrate variability caused by mineral mixtures for imaged pelitic schists. USGS mineral library spectra are plotted (color) for comparison of pure minerals with mixtures.

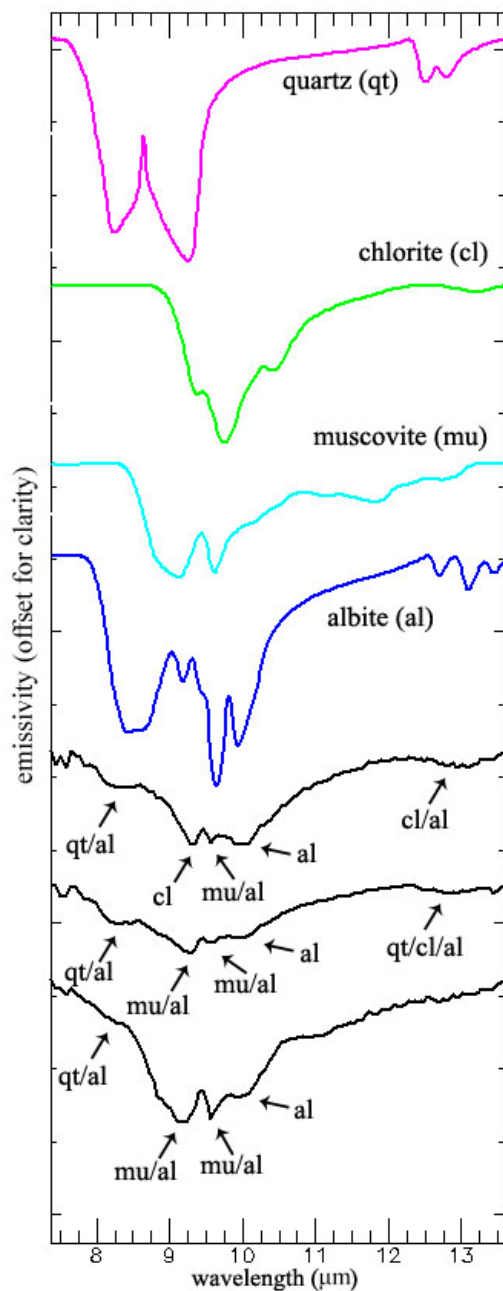


Figure 7.

Ground SEBASS emissivity spectra indicative of rock units within study sites one and two are shown in the plot at left. These spectra were then resampled to the spectral resolution of MASTER (center) and ASTER (right). Each multispectral emissivity spectra is distinct, with exception of the calcite and dolomite, which are visually similar, and effectively combined into a single carbonate spectra class.

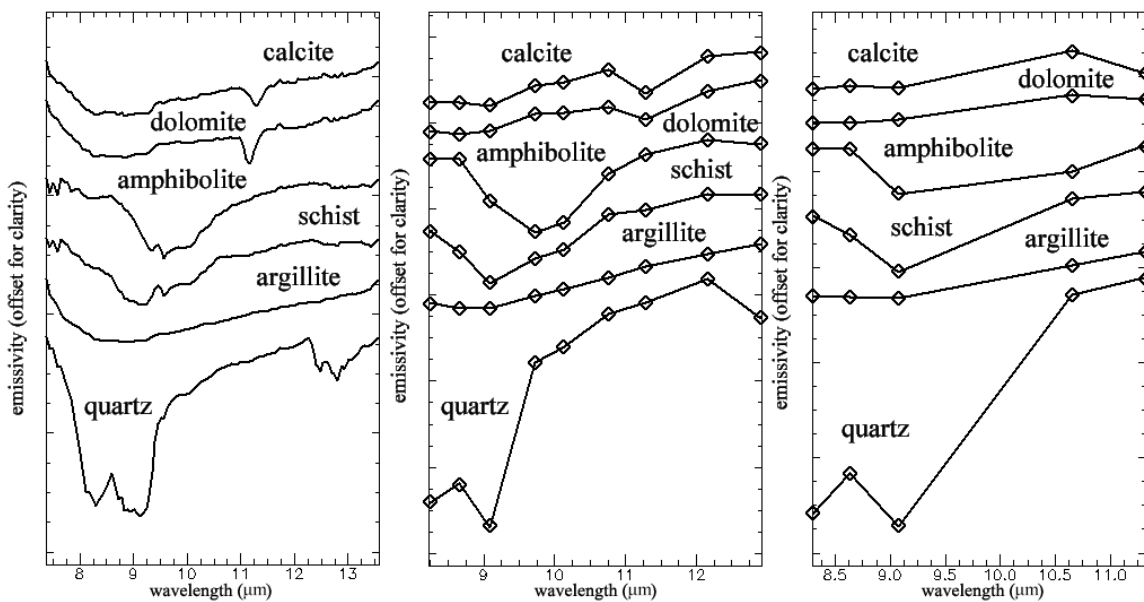




Figure 8.

Ground and aerial SEBASS at-sensor radiance spectra of a common quartz-dominated surface within study site one are plotted against a Planck curve corresponding to the average temperature of these spectra (316.5 K). The ground-based measurement was taken at a distance of approximately 100 m from an alluvial surface. The aerial measurement was acquired at nadir from a distance of approximately 4 km to the alluvial surface. At bottom, a difference value spectra was calculated from the ground and aerial radiance spectra above, indicating that the most dramatic differences occur below 8  $\mu\text{m}$ , corresponding to decreased transmissivity by atmospheric  $\text{H}_2\text{O}$ , and above 12  $\mu\text{m}$ , corresponding to  $\text{CO}_2$ .

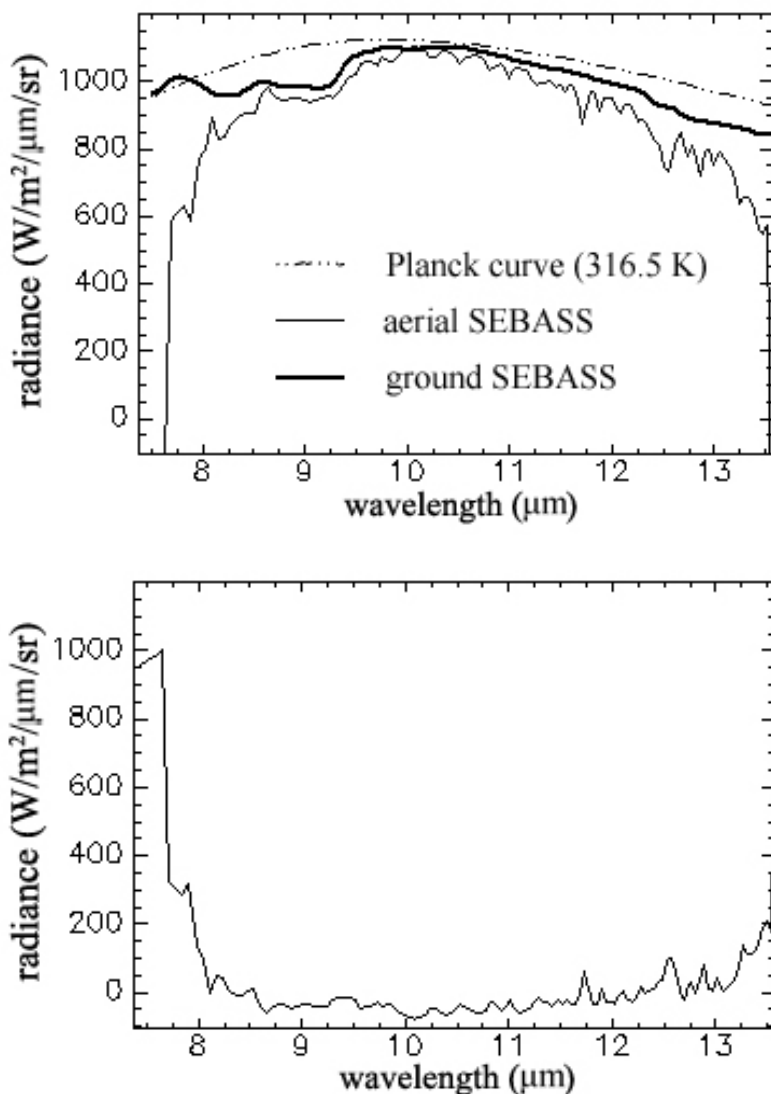


Figure 9.

Two separate SAM rule image classifications of quartz are shown. Classification one (A) was produced by using bands spanning the primary diagnostic doublet (bands 11 through 46 / 8.01 - 10.03  $\mu\text{m}$ ). A corresponding thresholded pixel map is shown for best matches (B). Classification two (C) was produced by using bands spanning the secondary quartz doublet (bands 89 through 128 / 12.03 - 13.57  $\mu\text{m}$ ). A corresponding thresholded SAM pixel map is shown for best matches (D). A minor difference in mapped pixels are observed near the top left of the outcrop.

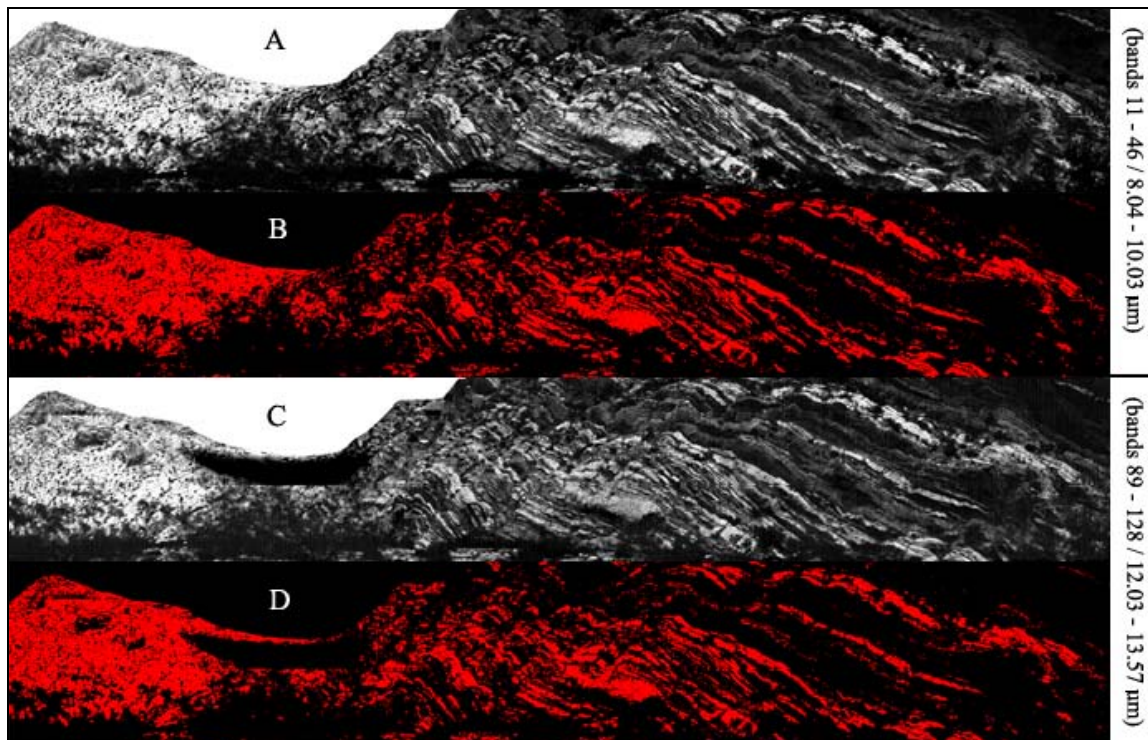


Figure 10.

Comparison of SAM quartz classification images from aerial SEBASS image data. Classification three (A) was produced by using bands spanning the primary diagnostic doublet (bands 7 through 43 / 8.03 - 10.01  $\mu\text{m}$ ). A corresponding thresholded pixel map is shown for best matches (B). Classification four (C) was produced by using bands spanning the secondary quartz doublet (bands 88 through 128 / 12.02 - 13.54  $\mu\text{m}$ ). Corresponding thresholded SAM pixel map is shown (D). Identification of quartz-dominated pixels is distinct in A/B, while these pixels are not as accurately mapped in the C/D, where detector noise and banding is observed.

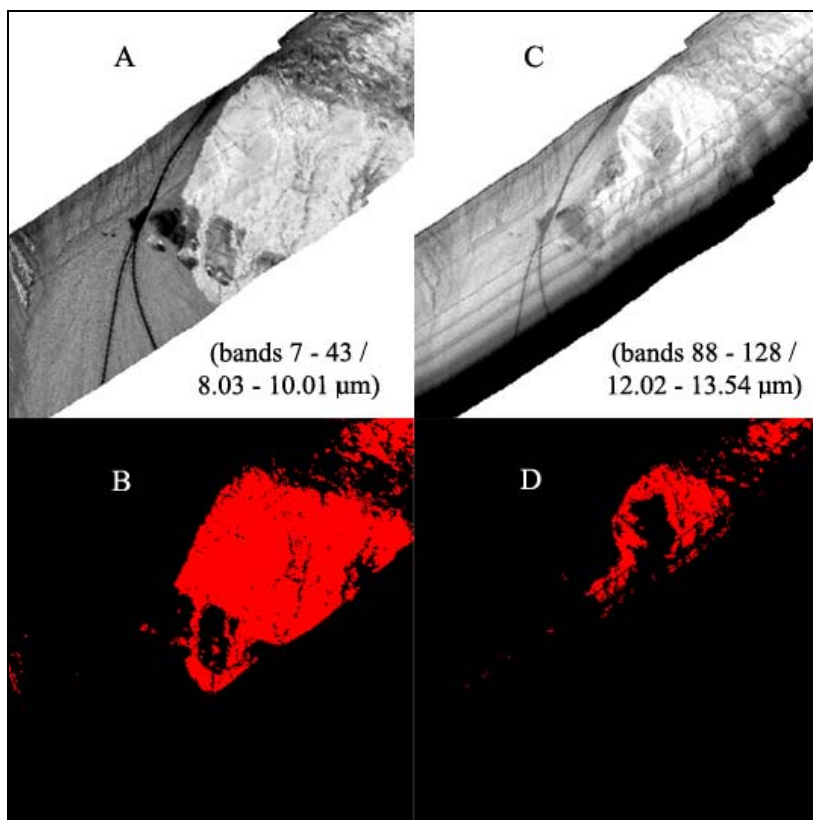


Figure 11.

Pixel emissivity spectra are plotted for lithologies identified during image data analysis. Each plot includes image data emissivity spectra from ground SEBASS (bottom), aerial SEBASS (second from bottom), MASTER (second from top), and ASTER (top), at respective spectral resolutions.

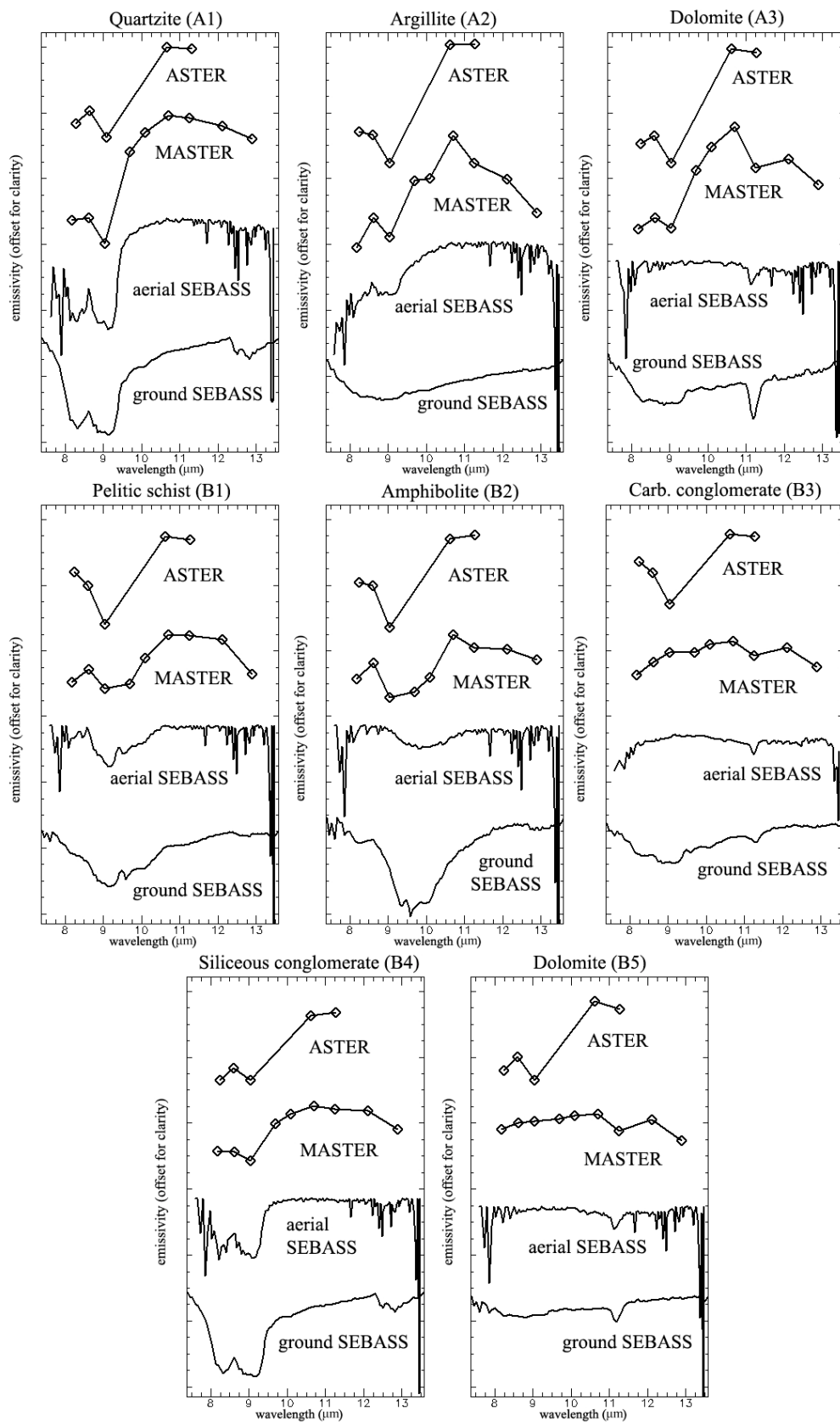


Figure 12.

A ground photograph, band composite images, and classifications of study site one are shown for comparison. In (A), a photograph is shown of the site; the black rectangle indicates image data coverage for ground-based SEBASS measurements. A' and A'' correspond to the lateral extent of transects indicated in figure 2. Ground SEBASS band composite image RGB: 42 (9.83  $\mu\text{m}$ ), 28 (9.06  $\mu\text{m}$ ), 19 (8.54  $\mu\text{m}$ ) is shown in (B), while a SAM-derived mineral map classification is shown in (C). Green pixels represent quartz-rich pixels corresponding to quartzite or alluvium; cyan pixels represent muscovite-rich argillite; magenta are dolomite-rich; and red are calcite indicative of possible marbleization. Color composite images of 4 m GIFOV aerial SEBASS (D), 20 m GIFOV MASTER (E), and 90 m GIFOV ASTER (F) are shown using bands corresponding to the ground SEBASS image (MASTER: RGB 6 (10.14  $\mu\text{m}$ ), 4 (9.09  $\mu\text{m}$ ), 3 (8.65  $\mu\text{m}$ ); ASTER: RGB 13 (10.65  $\mu\text{m}$ ), 12 (9.07  $\mu\text{m}$ ), 11 (8.63  $\mu\text{m}$ )). SAM mineral maps generated from respective image data are shown lastly. Green represents quartz; magenta is dolomite; red is calcite; and cyan is muscovite (G, H, I). For multispectral data, magenta represents a general carbonate class, instead of solely dolomite.

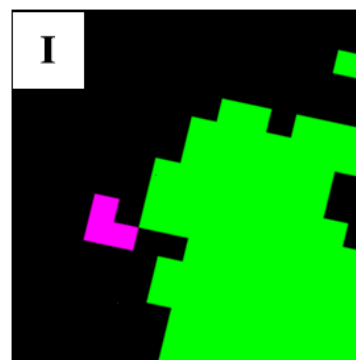
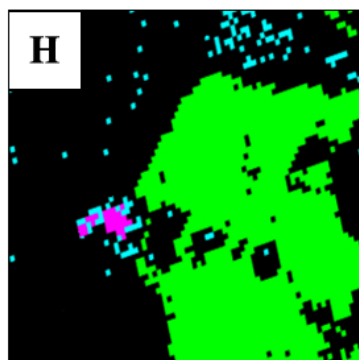
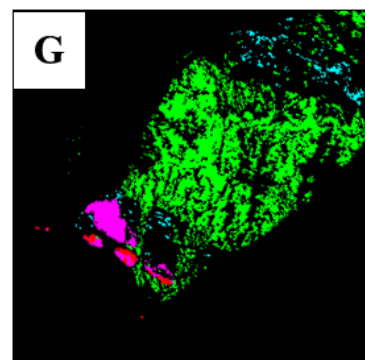
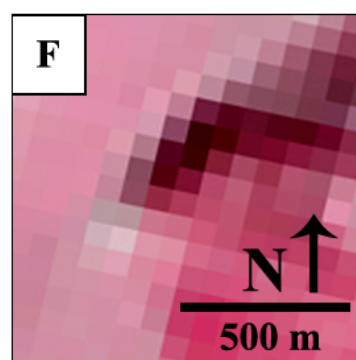
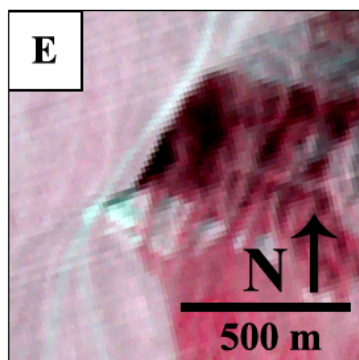
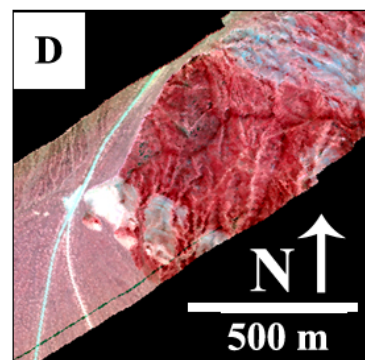
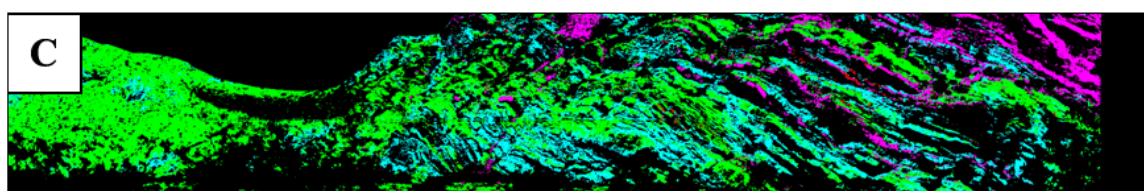
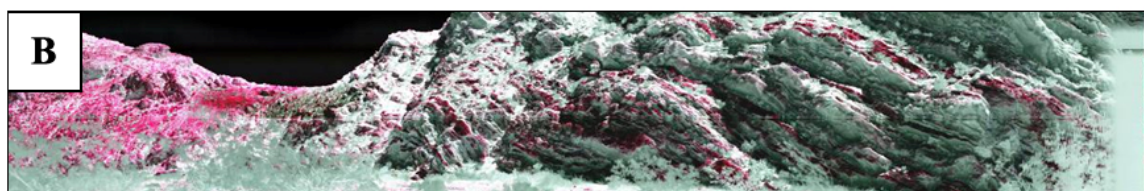
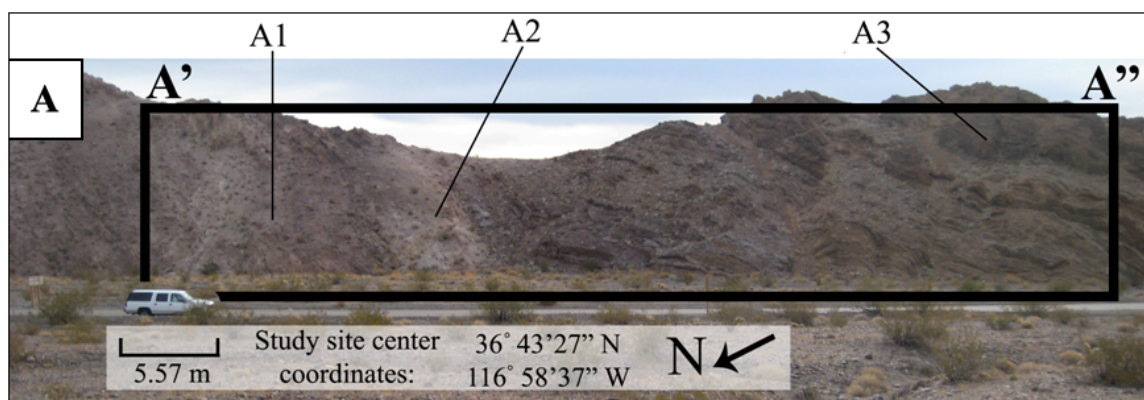


Figure 13.

A ground photograph, band composite images, and classifications of study site two are shown for comparison. In (A), a photograph is shown of the site; the black rectangle indicates image data coverage for ground-based SEBASS measurements. B' and B'' correspond to the lateral extent of transects indicated in figure 2. Ground SEBASS band composite image RGB: 42 (9.83  $\mu\text{m}$ ), 28 (9.06  $\mu\text{m}$ ), 19 (8.54  $\mu\text{m}$ ) is shown in (B), while a SAM-derived mineral map classification is shown in (C). Green pixels represent quartzite pebble alluvium, or siliceous conglomerate; blue are hornblende-rich pixels of amphibolite; cyan are muscovite-rich pixels of pelitic schist; magenta are dolomite-rich dolomite beds; and red is calcite of carbonaceous conglomerate. Color composite images of 4 m GIFOV aerial SEBASS (D), 20 m GIFOV MASTER (E), and 90 m GIFOV ASTER (F) are shown below this using bands corresponding to those used for the ground SEBASS image (MASTER: RGB 6 (10.14  $\mu\text{m}$ ), 4 (9.09  $\mu\text{m}$ ), 3 (8.65  $\mu\text{m}$ ); ASTER: RGB 13 (10.65  $\mu\text{m}$ ), 12 (9.07  $\mu\text{m}$ ), 11 (8.63  $\mu\text{m}$ )). At bottom, corresponding SAM mineral maps generated from respective aerial and spaceborne image data are shown. Green represents quartz-rich surfaces; magenta is dolomite; red is calcite; blue represent hornblende; cyan are muscovite-rich surfaces (G, H, I). For multispectral data, magenta represents a general carbonate class, instead of solely dolomite.



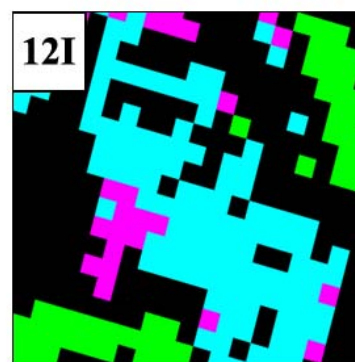
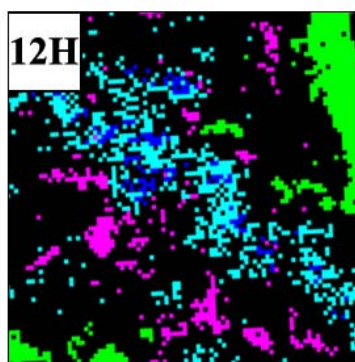
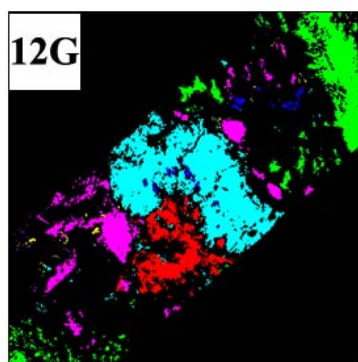
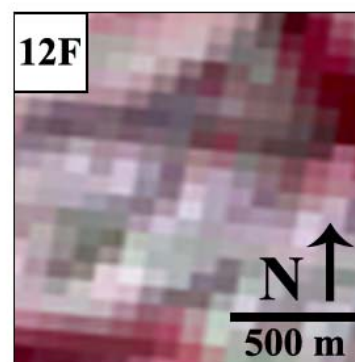
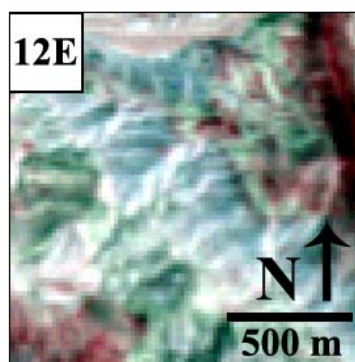
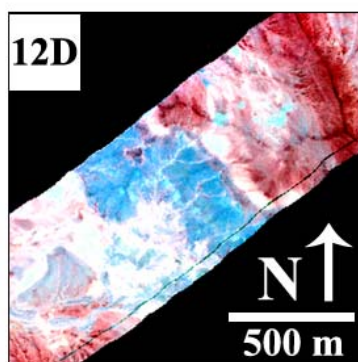
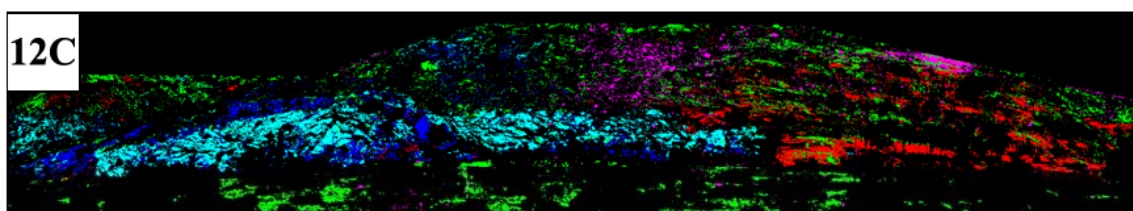
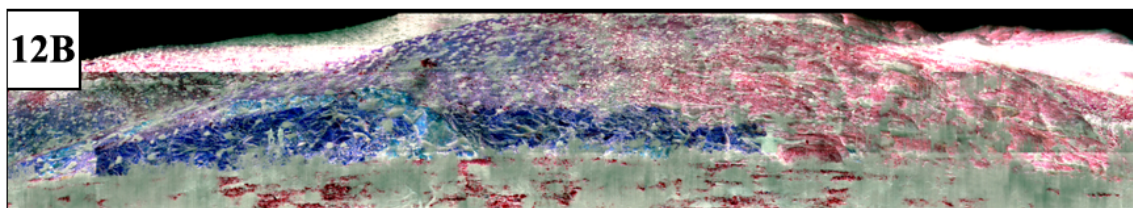
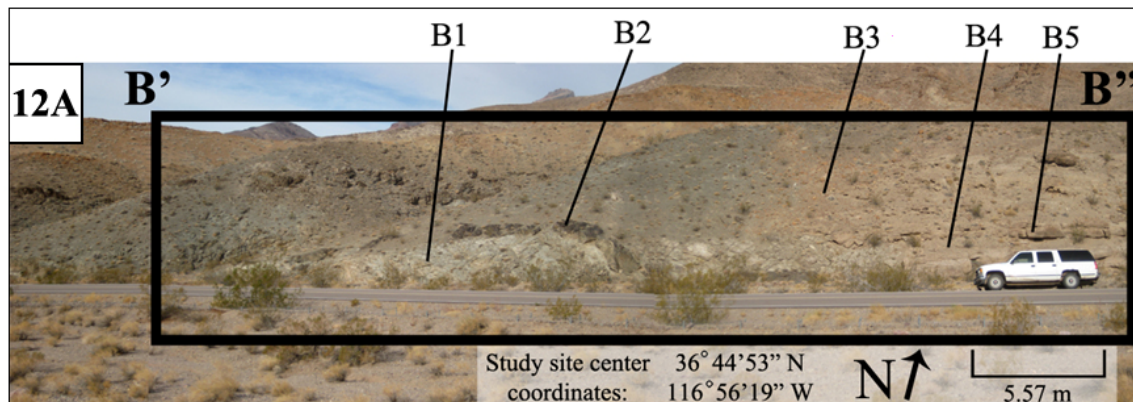
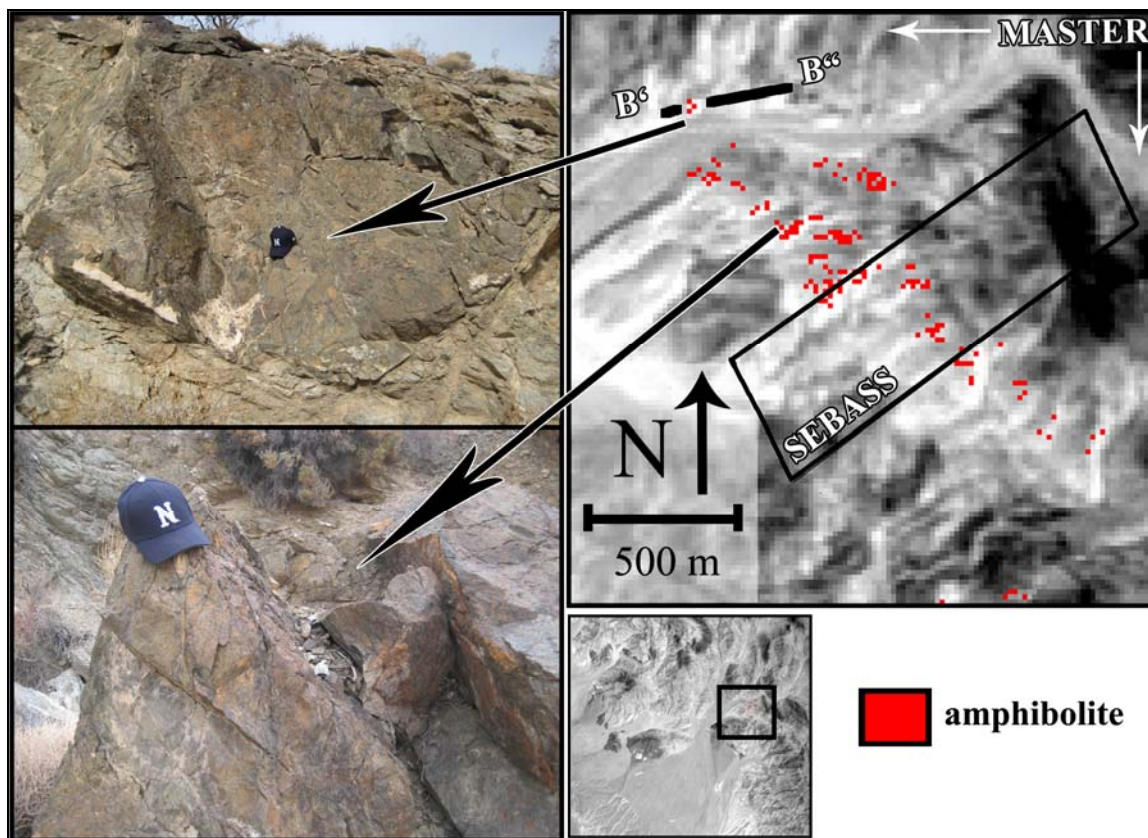


Figure 14.

A MASTER-derived amphibolite classification map for Boundary Canyon. Mapped pixels are matches to convolved SEBASS emissivity spectra of amphibolite. Rules image thresholding was guided by the high spatial and spectral resolution SEBASS-derived map. Field checks of selected pixel locations agreed with the distribution map.



## Chapter 5

### **Multi-wavelength mineral mapping in Oasis Valley, Nevada using ProSpecTIR V-S reflectance and SEBASS emittance hyperspectral image data**

Zan Aslett

Mackay School of Earth Sciences and Engineering, University of Nevada, Reno

\* Based on a manuscript to be submitted to Journal of Applied Remote Sensing

## 5.1 Abstract

Hyperspectral reflectance and emittance image data collected over Oasis Valley, Nevada on June 21, 2008 were analyzed to produce maps of surficial mineralogy that were compared to conventionally mapped geologic units. Minerals having both diagnostic absorption and emission minima spectral features in the shortwave-infrared (SWIR) and longwave-infrared (LWIR) regions of the electromagnetic spectrum were compared using ProSpectTIR V-S reflectance and SEBASS emittance hyperspectral image data that were simultaneously collected from an aircraft platform, thereby eliminating atmospheric and environmental variability that usually occurs between separate data acquisitions. SWIR and LWIR image data were compared because a variety of minerals exhibit spectral features attributed to vibrational processes in both these wavelength ranges. In contrast, VNIR spectral features are due to electronic processes, and do not occur at thermal-infrared wavelengths. Lithologies or surface features that were remotely measured within the Oasis Valley study area and exhibited diagnostic spectral features in either the SWIR or LWIR ranges include: gravels, ashflow tuff, hydrothermally-altered tuffs, basalt, siliciclastic and carbonate sedimentary rocks, and a silicified hot spring area. From these measurements muscovite, kaolinite, alunite, calcite, dolomite, zeolite, opaline silica, quartz, burkeite, gypsum, and trona were identified and mapped. The use of statistical spectral classification algorithms was found to be an efficient method to detect and map mineral spectral endmembers using SWIR data. This same methodology was also used for analysis of the LWIR image data to map pixels dominated by a single mineral. However, variability of silicate mineral mixtures (e.g., clays and feldspars) in certain rock units reduced the overall effectiveness of statistical

mapping. Instead manual inspection, identification, and mapping of these emissivity spectra in limited areas with the LWIR data resulted in better mapping of these components. While the SWIR data were able to be analyzed in a short amount of time, LWIR image data analysis was more time intensive. Combined use of SWIR and LWIR spectral endmember mineral maps allowed more comprehensive mineral maps to be defined, where clays, zeolite, certain sulfates, and opaline silica were better identified and mapped in the SWIR; and whereas rock-forming silicates, certain sulfates, and more complex mineral mixtures were better identified and mapped in the LWIR.

## **5.2 Introduction**

### 5.2.1 Overview

The use of hyperspectral image data to conduct remote mineral mapping surveys has become more prevalent in the past decade due to the increasing number of imaging spectrometers, extensive data collections, and comprehensive studies illustrating the use of these data for geological applications. Aerial hyperspectral surveys most commonly utilize sensors that measure reflected solar radiance in wavelengths ranging from 450 - 2450 nm. Established sensors such as AVIRIS (Vane et al., 1993), HyMap (Cocks et al., 1998), and the more recent ProSpecTIR V-S (SpecTIR LLC, 2009), have been used to acquire reflectance image data for detection, identification, and mapping of minerals associated with various lithologies and deposits. The emergence of hyperspectral sensors that measure thermal-infrared (TIR) emission in the 8 - 14  $\mu\text{m}$  wavelength range, such as SEBASS (Hackwell et al., 1996), has facilitated a more comprehensive approach to

remotely studying rocks and soil materials, as these data are suited for detecting and distinguishing rock-forming silicate mineralogy.

The Joint Collection using Hyperspectral Systems (JACHS) data acquisition campaign was conducted by SpecTIR and The Aerospace Corporation in the summer of 2008. Two imaging spectrometer systems were co-mounted onto a roll-stabilized frame in a Twin Otter aircraft and used to collect data throughout the western United States (Riley et al., 2008) (figure 1). The sensors used included SpecTIR's ProSpecTIR V-S, which made radiance measurements in image format over a spectral interval from 450 - 2450 nm, and The Aerospace Corporation's Spatially Enhanced Broadband Spectrograph System (SEBASS), which made radiance measurements in image format over a spectral interval of 2.5 - 5.2 and 7.5 - 13.5  $\mu\text{m}$ . These spectral measurements were made on June 21, 2008 over Oasis Valley, Nye County, Nevada in order to investigate the surficial mineralogy of the area as well as enable direct comparisons between SWIR and LWIR data-derived mineral maps. Only the SWIR and LWIR image data were compared because diagnostic absorption and emission minima spectral features in these ranges are due to vibrational processes; in contrast, absorptions in the visible spectrum are predominantly controlled by electronic processes (e.g., oxide and sulfate minerals) (Clark, 1999). The reflected solar radiance and surface-emitted radiance data sets were corrected to apparent reflectance and emissivity formats, respectively, and then independently analyzed to detect and relate the spectral data endmembers to known mineral spectra, create mineral maps, and then to compare SWIR and LWIR results. Field and laboratory measurements were used to corroborate image data spectra and map

results in addition to providing further information about the mineralogical constituents of the rocks within the study area.

Previous research has established that phyllosilicate (clay) mineral spectral features are generally better detected in the SWIR wavelength range, while rock-forming silicate mineral spectral features are better detected in the LWIR wavelength range (Lyon and Green, 1975; Clark, 1999; Vaughan et al., 2003). There are limited case studies available in the literature that reference analysis of joint reflectance and emissivity image data that were collected simultaneously at similar high spatial and spectral resolutions. Mineral spectral libraries are usually consulted to determine the wavelength location and prominence of diagnostic features such as absorptions or emission minima. However, uniqueness and spectral contrast of these features for remotely-sensed measurements is in part affected by factors such as: proportion of a single mineral within a rock; linear or intimate mineral mixtures within pixel measurements; particle size; surface roughness; atmospheric absorption and scattering; topography; sun angle; and surface temperature (Clark, 1999). Thus diagnostic features identified in analysis of library spectra may be poorly replicated in image data.

### 5.2.2 Research questions

Jointly collected hyperspectral reflectance and emittance image data were collected to facilitate the mapping of minerals and direct comparisons of reflectance and emissivity measurements in Oasis Valley. Four key questions guided the research: 1) What minerals are better suited for detection in either the SWIR or LWIR wavelength range, or are the results comparable? 2) Does combined use of both SWIR and LWIR

image data sets result in production of a more comprehensive mineral map? 3) Are consolidated rock or unconsolidated rock weathering products better suited for detection in reflectance or emissivity data? 4) What are the general capabilities and limitations of each data set for mapping mineral spectra?

### **5.3 Previous work**

#### **5.3.1 Multi-wavelength mineral mapping**

Analyses of image data spectra spanning both reflectance and TIR spectrum ranges have been previously used to conduct mineral surveys in differing geologic environments. Lang et al. (1987) utilized Thermal Infrared Multispectral Scanner (TIMS) image data to identify and associate remotely-mapped silicate, carbonate, and sulfate minerals with sedimentary lithologies in central Wyoming. These measurements were then added to Airborne Imaging Spectrometer (AIS) and Landsat Thematic Mapper (TM) reflectance image data classification results to more fully understand the mineral distribution in this area. Abrams et al. (1991) demonstrated the joint use of reflectance and thermal infrared data sets to comprehensively characterize Hawaiian lava flows; the TIR data were used to indicate the presence and erosion of silica rinds, while the reflectance data delineated areas of oxidation and vegetation cover. Variations in feldspar mineralogy were shown to be detectable with aerial HyMap reflectance and SEBASS emittance image data over Yerington, Nevada (Cudahy, 2001). Multi-wavelength data were used to detect hot spring and epithermal mineral deposits at Steamboat Springs, Nevada (Kruse, 2002), and MASTER data were successful in separating clay and silicic components of hydrothermal alteration components in this area (Vaughan et al., 2005).



Joint use of spaceborne ASTER reflectance and emissivity image data are routinely used to produce surficial mineralogy maps. These data demonstrated the spectral delineation of lithologies associated with rare earth element deposits at Mountain Pass, California (Rowan and Mars, 2003). Combined hyperspectral reflectance and multispectral emissivity data over Cuprite, Nevada were shown to increase spectral classification accuracies of certain minerals (Chen et al., 2007). Kirkland (2007) demonstrated differences between hyperspectral reflectance and emittance image data measurements of quartz-alunite outcrops in the Alunite Mining District, Nevada.

### 5.3.2 Area of study

The area of study is located in Oasis Valley, southern Nye County, Nevada, USA (figure 2). Southern Oasis Valley includes the town of Beatty, which is located approximately 170 km northwest of Las Vegas and found along Nevada Highway 95. The study area is found in a transition zone between the Great Basin and the Mojave desert and receives 15.75 cm of annual precipitation. Vegetative cover is dominated by desert shrubs in the rangelands, though surface cover is generally low. Grasses and deciduous trees are interspersed within the riparian corridor near the center of the valley, resulting in moderate vegetative cover in this area. The average elevation within the study area is 1008 m above sea level, while maximum elevation approaches 1450 m.

### 5.3.3 Geology

The local ranges bounding the study area are comprised primarily of Tertiary volcanic and Paleozoic carbonate and siliciclastic rocks, while the valley is filled with unconsolidated sediment, semi-consolidated-to-consolidated conglomerate, sandstone,

siltstone, and interbedded volcanic ash and lava flows (Fridrich et al., 1999; Workman et al., 2002) (figure 3). Middle-to-late Miocene ash-flow tuffs that emanated from adjacent calderas of the Southwestern Nevada Volcanic Field (SNVF) compose the bulk of surface cover (Carr et al., 1996). Three major tuff or ash-flow units intersect the boundaries of the study area: Timber Mountain (Pliocene); Paintbrush (Pliocene); and Crater Flat (Miocene) ash-flow tuffs and rhyolitic ash-flow. Older welded tuff, basalt, breccia, and hydrothermally altered rhyolites form a minority of the surface cover. The northeastern tip of Bare Mountain, consisting of Paleozoic carbonate and siliceous units, intersects the southeastern boundary of the study area (Smith et al., 1983). More than 70 springs and seeps are found throughout Oasis Valley. These are attributed to aquifers found in fractured volcanic rocks, changes in lithology, and thickness of rock units that contribute water to the area (Fridrich et al., 1999; Reiner et al., 2002). Springs within the study area boundaries are found in proximity to the east-west trending Hot Spring and Fleur de Lis faults and north-south trending Beatty and Hogback faults, resulting in localized hydrothermal alteration (Fridrich et al., 2007) (figure 3). Hidden structural features of the area have been inferred from previous gravity and magnetic geophysical data measurements and analysis (Mankinen et al., 2003; Fridrich et al., 2007).

## **5.4 Data and instrumentation**

### **5.4.1 Overview**

Reflected solar radiance and surface emitted radiance image data were acquired on June 21, 2008 between 9:00 AM and 2:00 PM PST at an altitude of 5 km over the study area, which yielded 5 m ground instantaneous field of view (GIFOV) pixels. Sensor

characteristics are recorded in table 1. A total of 15 flightlines were collected in two areas that intersect approximately perpendicularly to each other near the town of Beatty. These were oriented to cover a range of volcanic and sedimentary rocks in the east-west segment; data coverage was oriented to cover the valley floor in the north-south segment. Data parameters are recorded in table 2. The average length of these flightlines was 11 km. Rock samples were collected in the field that corresponded to unique reflectance and emissivity image data spectra. Laboratory measurements were used to comprehensively determine mineralogy of these samples.

#### 5.4.2 ProSpecTIR V-S imaging spectrometer

The ProSpecTIR V-S imaging spectrometer system is operated by the SpecTIR Corporation and measures at-sensor radiance across the reflectance spectrum from 400 - 2450 nm (SpecTIR LLC, 2009). Separate 12-bit VNIR and 14-bit SWIR sensors make measurements across 320 spatial pixels, and forward motion of the aircraft is used to build a datacube line-by-line. Spectral resolution can be independently modified for each range, resulting in a number of band channels that can be configured by the vendor to suit particular remote sensing applications.

Image data were collected in 178 bands at spectral resolutions of approximately 9 nm in the VNIR and 13 nm in the SWIR. The sensor was radiometrically calibrated before and after flights using a National Institute of Standards and Technology (NIST)-traceable spectral radiance calibration sphere, which resulted in data within +/- 5% of absolute radiance. The calibrated radiance data were later processed using the Atmospheric CORrection Now (ACORN) atmospheric correction routine.

#### 5.4.3 SEBASS imaging spectrometer

The Spatially Enhanced Broadband Array Spectrograph System (SEBASS) is a pushbroom imaging spectrometer operated by The Aerospace Corporation that measures at-sensor radiance across two infrared ranges using 12-bit radiometric resolution (Hackwell et al., 1996). MWIR data is measured from 2.5 - 5.2  $\mu\text{m}$ ; LWIR data is measured from 7.5 - 13.5  $\mu\text{m}$ . Both the midwave and longwave data sets measure radiance in 128 spectral channels across 128 spatial pixels. Hot and cold blackbodies are used to establish floor and ceiling temperature reference measurements at the conclusion of a flightline. The vendor-provided radiance product incorporates these temperature calibration data to yield noise equivalent change temperature difference (NE $\Delta$ T) of 0.01 C°. Due to the complexity of separating daytime reflectance and emittance components of measured at-sensor thermal infrared radiance in the MWIR region, as well as a relative lack of geologically informative spectral features, only the LWIR data were utilized for our research.

#### 5.4.4 ASD FieldSpec Pro spectroradiometer

The Applied Spectral Devices (ASD) FieldSpec Pro instrument is a dual-use field and laboratory instrument that measures reflected electromagnetic energy from 350 - 2500 nm. The spectral sampling of the instrument is 1.4 nm from 350 - 1050 nm and 2 nm from 1000 - 2500 nm. Spectral resolution is 3 nm at 700 nm; 10 nm at 1400 nm; and 12 nm at 2100 nm. Electronic/system noise is recorded, and then removed from radiance measurements. A Spectralon calibrated reference panel is then measured to convert to

reflectance units. The FieldSpec Pro was used to take measurements of rocks and other mineral instances during field surveys, in addition to characterizing samples in the laboratory. Multiple spectral measurements can be taken over time and averaged to mitigate significant noise.

#### 5.4.5 FTIR instruments

A Nicolet 6700 series Fourier Transform Infrared spectroscopic (FTIR) spectrometer was used to make laboratory reflectance measurements of samples within the TIR wavelength range. The FTIR measures bidirectional reflectance over a wavelength interval ranging from 2.5 - 25  $\mu\text{m}$  and incorporates a gold-plated background reference for calibration purposes. The band sampling interval of the instrument is user-defined, and multiple measurements can be averaged to generate relatively noise-free mineral spectra. General laboratory measurement procedure involved using bulk rock chip samples approximately 1 x 1 x 0.5 cm in size, oriented horizontally in the sample tray to approximate measurement of a flat surface.

A Designs & Prototypes (D&P)  $\mu\text{FTIR}$  field instrument was also used to make *in situ* measurements of emissivity (Hook and Kahle, 1996; Korb et al., 1996). Upwelling surface radiance, reflected downwelling radiance, and hot and cold blackbody measurements at temperatures above and below that of the approximate surface temperature were necessary for each generated spectra. Usage of the instrument during field surveys was somewhat limited in favor of sample measurements in the laboratory, due to the extensive amount of time needed to acquire each measurement, as well as difficulty with transporting the instrument in the field.

#### 5.4.6 XRD

X-ray diffraction (XRD) measurements were made with a Philips Electronics PW2273/20 instrument using a Cu radiation source at a current of 40 kV and 30 mA. These were made to verify minerals comprising samples by their diagnostic spectra peaks, attributed to particular crystal orientation. Material Data, Inc. (MDI) Datascan V. 4 software was used to process the samples and the MDI Jade V. 6.5 software, with the International Centre for Diffraction Data (ICDD) PDF-2 database, was used to analyze the data.

### **5.5 Image data calibration**

#### 5.5.1 Correction to apparent reflectance

ProSpecTIR V-S radiance data were converted to apparent reflectance using the Atmospheric CORrection Now (ACORN) V. 6 software (AIG, 2009). This MODTRAN-based software application mitigates atmospheric absorption components of measured radiance in the VNIR/SWIR image data, and yields apparent at-surface reflectance spectra. Reflectance measurements taken during field surveys with the portable ASD spectrometer were used for comparison with the apparent reflectance image data spectra. These separate measurements agreed well for the minerals found in the study area, as well as with library spectra (Clark et al., 2007) thereby validating the apparent reflectance calibration of the airborne data.

#### 5.5.2 Correction to apparent emissivity

SEBASS radiance data were converted by The Aerospace Corporation to apparent at-surface emissivity using a proprietary in-scene atmospheric correction (ISAC) routine (Johnson, 1998; Young, 1998) and as outlined in Vaughan, 2005. The Aerospace Corporation provided both apparent emissivity and temperature image data resulting from a temperature-emissivity separation (T&S) algorithm (Realmuto, 1990; Hook et al., 1992). Comparison of image data with ground and laboratory measurements showed good agreement. A separate T&S and normalization to emissivity of the SEBASS radiance data was conducted using routines in the ENVI software in order to independently generate these data. These emissivity spectra resulted in a range of good to poor matches with ground and laboratory measurements throughout the image data scene. The Aerospace Corporation-provided ISAC apparent emissivity data were thus used for all mineral mapping.

## **5.6 Data processing methodologies**

### **5.6.1 General analysis**

The ProSpecTIR V-S and SEBASS image data sets were separately analyzed to produce SWIR- and LWIR-derived mineral classification maps. Minerals that featured diagnostic spectra features in both the SWIR and LWIR were of most interest in the study; independent classification strategies were used to best compare similarities and differences between the respective data sets. Minerals were identified by interpretation and comparison of image data spectra with field, laboratory, and spectral library spectra (Hunt and Salisbury, 1971; Farmer, 1974; Lyon and Green, 1975; Salisbury and D'Aria, 1992; Gaffey et al., 1993; Lane and Christensen, 1997; Ruff et al., 1997; Clark et al.,

2007). Georectification and mosaicing of the respective data set flightlines were performed to facilitate data set-to-data set registration following spectral analyses. A gyro-stabilized mount for the sensors during data collection mitigated significant deviations in image data geometry. A small 0.1 millirad difference in aperture field-of-view (FOV) between the ProSpecTIR V-S and SEBASS imaging spectrometers and the use of separate inertial measurement units (IMU) to collect yaw, pitch, and roll (X, Y, Z) data during aerial data collection resulted in georectified SWIR and LWIR image data that generally matched with only minor offsets, overlaps, or other geometric mismatches.

In preliminary statistical mapping analysis, non-mineral endmembers were found to contribute toward false positive identifications of targeted minerals. Vegetation spectra in the SWIR are characterized by a broad absorption trough from approximately 2275 - 2400 nm, attributed to cellulose and lignin, that somewhat mimics the diagnostic absorption features of weak carbonate and Mg-OH minerals. In addition, manmade materials such as roofing were falsely identified by spectral classification algorithms. To mitigate this problem, a mask comprised of zero-value, vegetation, paved roadway, and urban areas pixels was created. This mask was then applied to both data sets to remove these pixels from any subsequent spectral processing. The ProSpecTIR data were subset to SWIR wavelengths ranging from 2050 - 2450 nm and the SEBASS data were subset to wavelengths ranging from 8 - 12  $\mu\text{m}$ . These wavelength ranges were chosen based upon the location of diagnostic spectral features for targeted minerals, as well as the exclusion of band ranges associated with atmospheric absorption or low transmissivity, and detector noise.



ENVI V. 4.6 software was used to perform spectral analysis using a supervised Hourglass routine (Kruse et al., 1993; Boardman and Kruse, 1994; ITT Visual Solutions, 2008). The minimum noise fraction (MNF) routine was used to statistically order the spectral data into bands representing highest variance in the lowest bands and grading to noise in sequentially higher bands. MNF image data were manually inspected in order to identify a threshold between coherent (high variance) and incoherent (noise or low variance) bands. The MNF bands retained for ProSpecTIR V-S data were 1-14 and 17. The bands for SEBASS were 4, 5, 8, 9 and 10. The remaining bands were removed from subsequent processing. Next, the MNF data were used as input for the Pure Pixel Index (PPI) routine in order to statistically determine the most unique spectral endmembers within the respective data sets. PPI processing of the SWIR data set initially resulted in the identification of twenty spectral endmembers, while the LWIR data set initially yielded twenty-eight. PPI image data were linked to spectral data in order to manually analyze the results. SWIR and LWIR endmembers found to be redundant or represent slight variations were removed from consideration. The SWIR endmember spectra were related to relatively pure mineral spectra and few mixtures with other minerals. The LWIR endmember spectra were apparently more related to mixtures of minerals than pure minerals. A final spectral library of mineral endmembers for each data set was created (figure 3). The match filter (Harsanyi et al., 1994) and Spectral Angle Mapper (SAM) (Boardman and Kruse, 1994) spectral classification algorithms were used to match these PPI mineral-related endmember spectra to image data. Each mineral endmember was processed with both algorithms and the results were compared; the best result was retained to produce final classification maps of minerals.

## 5.7 SWIR image data results

### 5.7.1 Overview

The SWIR data were analyzed first because familiarity with reflectance mineral spectra and data processing methodologies suggested that initial mineral maps could be produced in a reasonable amount of time. Analysis began with displaying RGB band combinations that would emphasize various mineral absorption features. RGB 168 (2326 nm), 156 (2175 nm), 148 (2074 nm) was used as a baseline to display kaolinite in purple, alunite in magenta and carbonates in cyan (figure 4). The ENVI Hourglass routine helped to statistically identify seven mineral endmembers with unique spectral features: alunite, kaolinite, muscovite, calcite, dolomite, zeolite, and opaline silica (figure 5). Each mineral has either distinct narrow absorption features (e.g., kaolinite exhibits a doublet at 2200 nm) or broad reflectance slopes (e.g., zeolite). Field and laboratory measurements of rocks within the study area assisted in corroborating these apparent reflectance spectra. A scene-wide mineral map was created for each identified mineral endmember (figure 6 and table 3), in which distributions were constrained by manual inspection of pixel spectra, as well as by field observations and measurements.

### 5.7.2 Acid-sulfate alteration

Minerals associated with acid-sulfate hydrothermal alteration were mapped in the north-south segment of the image data. In particular, alunite (hydrated aluminum-potassium sulfate,  $\text{KAl}_3(\text{SO}_4)_2(\text{OH})_6$ ), kaolinite (aluminum silicate hydroxide,  $\text{Al}_2\text{Si}_2\text{O}_5(\text{OH})_4$ ), and opaline silica (hydrated silica,  $\text{SiO}_2 \cdot n(\text{H}_2\text{O})$ ) were mapped amongst the outcrops found along the east-west trending Hot Spring and north-south

trending Beatty faults (figure 7). Gravel used on roads in this area exhibited a distinctive muscovite (potassium aluminum silicate hydroxide,  $\text{KAl}_2(\text{AlSi}_3)\text{O}_{10}(\text{F},\text{OH})_2$ ) spectra (absorption maxima at 2220 nm and minima at 2360 nm), and gravel storage piles of the same material could be traced to the area due east across Highway 95. The valley floor south of this area was characterized by a mixture of riparian vegetation such as grasses, shrubs, and small tree stands in addition to intermittent patches of evaporite crusts. Spectral identification of particular evaporite minerals was not achieved in SWIR image data analyses, but laboratory measurements of field samples identified trona (trisodium hydrogencarbonate dihydrate,  $\text{Na}_3\text{H}(\text{CO}_3)_2 \cdot 2\text{H}_2\text{O}$ ), halite (sodium chloride,  $\text{NaCl}$ ), and burkeite (sodium carbonate-sulfate,  $\text{Na}_6(\text{CO}_3)(\text{SO}_4)_2$ ).

### 5.7.3 Tertiary volcanics

Slightly-to-moderately varnished tertiary basalt flows (augite,  $(\text{Ca},\text{Mg},\text{Fe})\text{SiO}_3$  + albite,  $\text{NaAlSi}_3\text{O}_8$ , + anorthite  $\text{CaAl}_2\text{Si}_2\text{O}_8$ ) were denoted on geologic maps. These outcrops were characterized as spectrally flat and displayed low, uniform reflectance in the SWIR wavelength range. The southernmost portion of the north-south flightlines (figure 8) was characterized by ashflow tuff volcanic units. Two units dominated: 1) a low density, high albedo tuff with small vesicles and moderately-developed phenocrysts of quartz, feldspar, and hornblende that ranged from no-to-low varnish coatings and spectroscopically matched the zeolites, heulandite and/or clinoptilolite  $((\text{Na},\text{K},\text{Ca})_{2-3}\text{Al}_3(\text{Al},\text{Si})_2\text{Si}_{13}\text{O}_{36} \cdot 12\text{H}_2\text{O})$ ; 2) a higher density, largely oxidized tuff that laboratory measurements indicated was composed of quartz and orthoclase and was spectroscopically identified as opaline silica in reflectance measurements. Contacts

between the two units were frequently observed in the field and opal pixels were mapped in the image data at these contacts in some areas, which may represent a tuff cooling unit.

#### 5.7.4 Volcanics and alteration

Image data in the western portion of the east-west segment (figure 9) indicated the presence of additional tuff associated with zeolite, as well as an ancillary tuff unit associated with muscovite. Concentric patterns were mapped here that represented zeolite, opaline silica, and muscovite. Kaolinite-dominated outcrops were remotely identified at the eastern extent of the scene. Under hand lens observation these rocks were determined to consist of both kaolinite and quartz and as a result were somewhat resistant to weathering. Although unmapped in the image data, a large unit of welded tuff was observed underlying the kaolinite in this area that had been recently uncovered.

#### 5.7.5 Miocene gravel deposits

In figure 10, a Miocene gravel deposit comprised of mixed quartzite, limestone, dolostone, and assorted tuff was spectrally distinct because of abundant calcite ( $\text{CaCO}_3$ ), which has an absorption feature at 2333 nm. The northernmost tip of Bare Mountain protruded into the image data coverage area, which was predominantly characterized here as dolomite,  $\text{CaMg}(\text{CO}_3)_2$ . Previous mining activity adjacent to the range produced an older tailings pile and gravel roads leading from an abandoned open pit mine. These features indicated muscovite-dominated spectra in the image data. Kaolinite was identified in a few small areas upon Bare Mountain and was related to older adits and mined gangue material.

## 5.8 LWIR image data results

### 5.8.1 Overview

The LWIR image data were analyzed following the SWIR image data. A RGB band combination of 41 (9.89  $\mu\text{m}$ ), 27 (9.16  $\mu\text{m}$ ), 19 (8.72  $\mu\text{m}$ ) was used that corresponded to known mineral emission minima features of minerals within the scene (figure 11). Quartz was indicated in red; tuffs were displayed in purple; basalt was cyan; and carbonates were a light brown. A total of nine spectral endmembers were identified using a supervised ENVI Hourglass routine. These represented basalt, zeolite-rich tuff, quartz, quartz- and feldspar-rich tuff, alunite, kaolinite, calcite, dolomite, and burkeite (figure 5). Two additional endmembers, gypsum + trona and mascagnite, were not identified using the Hourglass method and instead were found during manual investigation of image data spectra. Each of the endmember spectra possessed either broad emission minima features in the 8 - 10  $\mu\text{m}$  range (e.g., quartz, basalt), more narrow minima in the same range (e.g., alunite); narrow minima in the 11 - 12  $\mu\text{m}$  range (e.g., calcite, dolomite); or combinations thereof. Image data spectra were often observed as mineral mixtures. A scene-wide mineral map was created for each spectral endmember (figure 12 and table 3). Minerals not found in the SWIR data set required additional field surveys to verify their presence and identity.

### 5.8.2 Acid sulfate alteration

The area of hydrothermal alteration associated with the Hot Spring and Beatty faults in (figure 7) was mapped predominantly as alunite, kaolinite, and quartz. Alunite was identified by a moderate emission minima feature centered at approximately 9  $\mu\text{m}$ ;

kaolinite featured a minima triplet with two prominent troughs at 8.77 and 9.27  $\mu\text{m}$  and a less distinctive trough at 9.9  $\mu\text{m}$ ; quartz displayed a well-defined doublet with emission minima lobes centered at 8.3 and 9.16  $\mu\text{m}$ . Mixtures of each of these minerals were observed, with quartz most commonly dominating the emissivity spectra. The gravel road and gravel storage pile were characterized by a spectral mixture dominated by quartz and a minor component of muscovite, which expanded the width of the 9.16  $\mu\text{m}$  trough and added a sharp emission minima at 9.58 in addition to a slight minima at approximately 10  $\mu\text{m}$ . Within the riparian corridor, manual investigation of spectra was used to identify a small 4 pixel (approximately 20  $\text{m}^2$ ) instance of mixed gypsum (via a diagnostic emission minima centered at 8.66  $\mu\text{m}$ ) and trona (a narrow 11.7  $\mu\text{m}$  minima). Evaporite crusts associated with burkeite were identified and mapped more extensively on the groundwater discharge area via an apparent emission maxima at 11.37  $\mu\text{m}$ .

### 5.8.3 Tertiary volcanics

The basalt flows within figure 8 exhibited a broad emission minima from approximately 9.05 - 10.33  $\mu\text{m}$ , which was punctuated by a sharp minima at 9.58  $\mu\text{m}$ . The tuff spectrally identified as zeolite in the SWIR data exhibited a broad emission minima spanning 8.4 - 10.6  $\mu\text{m}$  with a trough centered at 9.21  $\mu\text{m}$ , a sharp minima at 9.58  $\mu\text{m}$ , and a small trough at 9.95  $\mu\text{m}$ . This emissivity spectra was reminiscent of library spectra of muscovite, however the main trough at 9.21  $\mu\text{m}$  is slightly narrower. The second tuff unit identified as opaline silica in the reflectance measurements had a mixed emissivity spectra comprised of quartz, feldspar, and zeolite.

### 5.8.4 Volcanics and alteration

The western portion of the east-west flightlines (figure 9) was characterized by ashflow tuff surface cover. Zeolite-rich tuff pixels were mapped extensively while the silica-rich tuff was mapped to a lesser extent. The kaolinite outcrops located east of Highway 95 were identified via emissivity spectra as mixed kaolinite and quartz. Burkeite was mapped in small instances here and usually limited to areas with minimal vegetative cover. A sharp emission minima feature centered at 8.95  $\mu\text{m}$  was observed in the image data in close proximity to the first mapped evaporite class, and was somewhat covered by valley floor grasses. The spectra were interpreted in to represent an additional sulfate mineral class, mascagnite (ammonium sulfate,  $(\text{NH}_4)_2\text{SO}_4$ ), however this area was fenced off as private property, and a field sample was not obtained for laboratory analysis and corroboration.

#### 5.8.5 Miocene gravel deposits

The high spectral resolution of the SEBASS image data facilitated accurate spectral delineation of the two predominate carbonate minerals within the scene. In the eastern portion of the east-west flightlines (figure 10) the gravel deposit was characterized by mixed spectra of quartz-, calcite-, and dolomite-rich rocks. Spectral mixtures observed here were dominated by quartz and calcite emission minima, the latter centered at 11.28  $\mu\text{m}$ . Next, the emissivity spectra of Bare Mountain produced dolomite-dominated emission minima centered at 11.15  $\mu\text{m}$ . Quartz outcrops and float associated with a siliciclastic Paleozoic sedimentary unit of Bare Mountain was distinctly mapped on the eastern flank of the range.

### **5.9 Mapping small instances of minerals in a hot spring area**

A hot spring found due north of the area of acid-sulfate hydrothermal alteration was investigated for surficial mineralogical expression (figure 13). A mix of siliceous and carbonate sinter material was observed either naturally at the surface, or had been withdrawn when a well was drilled. A mix of vegetative species, such as grasses and large brush stands, as well as precipitated sulfo-salts, were interspersed throughout the area. Band color combinations based on the absorption feature of calcite at 2335 nm (RGB: 2368 nm, 2325 nm, 2255 nm) were used to emphasize this mineral, however these surface areas were not delineated. A DCS image was next generated from this RGB band combination, but no carbonate-rich areas were observed distinctly from areas dominated by other minerals.

A LWIR color combination image was next made using bands that corresponded to the 11.3  $\mu\text{m}$  emission minima of calcite (RGB: 11.41  $\mu\text{m}$ , 11.28  $\mu\text{m}$ , 11.11  $\mu\text{m}$ ). This resulted in an anomalous magenta-toned surface area being immediately identified. DCS was applied to this band combination image, and the resulting DCS image produced good delineation between the areas where calcite was present and surrounding pixels. SAM was used to map 51 pixels corresponding to calcite. Using these LWIR data-mapped pixels as a guide, the SWIR image data spectra were then manually re-inspected. A limited number of SWIR image data pixels indicated the presence of calcite via the absorption at 2335 nm, however the absorptions were weak, and fewer overall pixels were mapped compared to the LWIR pixels.



## 5.10 Discussion

### 5.10.1 General analysis and mineral map observations

A comparison of SWIR and LWIR mineral map results derived from statistical spectral classification algorithms and expert analysis of mineral spectra were reviewed. The ENVI Hourglass-based statistical methodology for mapping minerals provided good results from the SWIR image data. The PPI-identified spectral endmembers were able to be mapped over a large area in a relatively short amount of time, and fieldwork was used to corroborate the presence and constrain the extent of mapped minerals with the assistance of field and laboratory measurements referenced to global positioning system (GPS) coordinates. Small instances of some minerals were noted in field surveys that were not detected in the image data spectra (e.g., chlorite), presumably because their distribution within a corresponding 5 m GIFOV pixel was relatively limited.

The Hourglass methodology was also used for analysis of the LWIR image data. In a few examples endmember mineral spectra were manually discovered in small groups of pixels (usually less than 20); these spectra (e.g., gypsum) were not identified during the PPI process. When particular minerals were found in larger extents, either in pure form or when they dominated spectral mixtures, the statistical methodology produced good matches between mineral map results and geologic maps. However, the majority of mapped pixels in the LWIR data were composed of spectral mixtures that exhibited variability in apparent contribution of minor mineral constituents from pixel-to-pixel. When average spectra were used in mineral mapping to represent particular rock types, fewer number of pixels were mapped compared to the SWIR image data results. Consequently, manual inspection of emissivity spectra was used to examine and map

small areas exhibiting complex mineral mixtures. Even though this method was more time consuming, mineral mixtures were better able to be identified than when statistically mapped. In general, these procedures for LWIR image data analysis derived more comprehensive mineralogical information from measured surfaces compared to the SWIR.

Rock outcrops and talus tended to yield the best defined diagnostic image data absorption or emission minima spectral features. Areas that were comprised of fine-grained or weathered material generally resulted in stronger reflectance values in comparison to corresponding emissivity spectra. Previous laboratory measurement research supports this finding as fine-grained mineral samples in VNIR/SWIR measurements exhibit higher overall reflectance and spectral contrast than coarse-grained samples of the same mineral (Hapke, 1993; Clark, 1999). Conversely, in the thermal-infrared wavelength range, fine-grained mineral samples produce lower reflectance and spectral contrast attributed to porosity and loss of energy during internal reflections, compared to coarse grained samples (Salisbury and Eastes, 1985; Clark, 1999).

### **5.11 Comparisons of SWIR and LWIR mineral map results**

The detection of certain minerals was limited in a single spectral range for some examples, including burkeite, mascagnite, gypsum, basalt, and quartz. Minerals that were spectrally identified and mapped in both spectral ranges, with differing degrees of success, included alunite, kaolinite, muscovite, zeolite, opaline silica, calcite, and dolomite.

#### **5.11.1 Evaporites**

Halite, trona, and burkeite were identified in laboratory measurements for an area of precipitated evaporite minerals. Burkeite and trona are characterized in the SWIR by broad absorptions between 2100 - 2200 nm, a peak at around 2250 nm, and a broad absorption between 2300 - 2400 nm, while halite is spectrally flat in the SWIR. These diagnostic SWIR absorption features coincide with similar features of both vigorous and dry grass. Within this study area, evaporites and vegetation were nearly always observed together. While the evaporites exhibit high albedo and can be readily distinguished from vegetation, spectrally identifying specific evaporite minerals is difficult using SWIR data, due to lack of distinct narrow absorption features, as well as spectral mixing. In comparison, spectral identification of a particular mineral, burkeite, was accomplished with the LWIR data by apparent emission peaks at 10.04 and 11.37  $\mu\text{m}$ , which contrast well with the spectra of surrounding minerals and vegetation (figure 14).

Gypsum also exhibits diagnostic absorption features in the SWIR. It is characterized by an absorption doublet occurring at 2215 and 2265 nm. However, the presence of gypsum was not identified or mapped using SWIR image data. Healthy and dry grasses interspersed amongst this evaporite may have resulted in vegetation-dominated spectra that did not facilitate delineation and mapping of this sulfate mineral. In contrast, the LWIR image data was used to detect and identify four pixels dominated by gypsum, characterized by a distinct emission minima feature at approximately 8.66  $\mu\text{m}$  (figure 15). This feature contrasted well with surrounding mineral and vegetative surface materials. Further investigation of these spectra indicated a spectral mixture – a second emission minima at 11.7  $\mu\text{m}$  that was diagnostic of trona.

Lastly, mascagnite exhibits a relatively flat spectrum in the SWIR, which makes it spectrally distinct from other evaporate minerals in the area (figure 16). However, the vegetation found amongst this evaporative crust resulted again in image data reflectance spectra that are dominated by features of grass instead of minerals. In contrast, the distribution of this mineral is immediately distinguishable from adjacent surface materials, including vegetation using the LWIR image data. A diagnostic emission minima observed here at 8.9  $\mu\text{m}$  is exhibited by numerous pixels, and is unique to this particular portion of the study area.

#### 5.11.2 Basalt

Basalt flows were investigated with the SWIR image data. A low uniform reflectance and lack of diagnostic spectral absorption features was found to be characteristic of these rocks within the study area. However, algorithms used to match the reflectance level of the basalt resulted in false positive matches to other scene materials exhibiting low levels of albedo (e.g., asphalt). In the LWIR image data, emissivity spectra of basalt were characterized by a broad, shallow emission minima from 9.5 - 10.5  $\mu\text{m}$  (resulting from a mixture of augite, anorthite and albite) and punctuated by a sharp minima at 9.7  $\mu\text{m}$ . These spectral features were unique in the context of other minerals found elsewhere in the scene. The basalt flows were thus able to be distinctly mapped with the LWIR image data.

#### 5.11.3 Quartz

Quartz associated with ashflow tuffs, exposed basement rock, and Paleozoic quartzite was investigated using the image data. Quartz is not detectable in the SWIR, as

it exhibits no diagnostic spectral features. In the LWIR image data quartz was easily detected and mapped based on its diagnostic emission minima doublet with minima centered at 8.3 and 9.4  $\mu\text{m}$ . Conversely, mineral mixtures elsewhere in the study area that included quartz were usually dominated by it, resulting in emissivity spectra that were somewhat difficult to unmix and interpret.

#### 5.11.4 Opaline silica

Amorphous silica was identified in two different parts of the study area using the SWIR image data. First it was mapped in the hydrothermal alteration zone near the Hot Spring and Beatty faults (figure 7). During field inspection the opal-mapped pixels were found to correspond to altered rhyolitic-to-trachytic ashflow tuff outcrops (Fridrich, 2007). In the LWIR image data these outcrops corresponded to quartz-dominated emissivity spectra, however the presence of opal in the LWIR spectra was unable to be visually determined here. Quartz overprints opal in the LWIR, as the diagnostic opal emission minima occurs at approximately 9  $\mu\text{m}$ , near the second diagnostic emission minima lobe of quartz at 9.3  $\mu\text{m}$ . The overall number of quartz pixels mapped here area was far greater than that mapped as opaline silica in the SWIR, which may indicate limited areas of opalization.

Opal was also mapped in the SWIR as the primary mineralogic constituent of the second denser tuff class previously identified (figures 8 and 9). This tuff was able to be delineated well from the younger zeolite-rich tuff that frequently overlaid it. The overall number of pixels of this class mapped was lower than that of the zeolite class due to fewer exposures. The emissivity spectra of this tuff indicated the presence of quartz, and

feldspar, and fewer pixels were mapped than the same class in the SWIR, which may be attributed to variability of individual mineral constituents.

#### 5.11.5 Alunite

The SWIR reflectance spectra of alunite is characterized by a prominent absorption at 2165 nm and a smaller absorption at 2320 nm, while the LWIR spectra exhibits an emission minima centered at 8.95  $\mu\text{m}$ . The areas mapped with the SWIR data as alunite were extensive throughout the outcrops along the Hot Spring and Beatty faults and included a quarry on the western side of Highway 95 (figure 6). The SWIR alunite classification was thresholded to yield only pixels that matched pure alunite spectra. Mixtures of kaolinite and alunite were noted as occurring outside of these areas.. Mixed kaolinite and alunite spectra were able to be visually identified, as the primary absorption at 2165 nm split into a doublet as mixing increased. With the LWIR image data, alunite was not mapped as extensively as in the SWIR. Quartz mixtures with alunite made it more difficult to visually identify and statistically map, due to overprinting of the 8.95  $\mu\text{m}$  minima feature of alunite by the quartz doublet.

#### 5.11.6 Kaolinite

Kaolinite was mapped in the SWIR via the 2165 and 2205 nm troughs of an absorption doublet feature. This diagnostic feature contrasted well with the spectra of surrounding minerals and vegetation. The SWIR classification was extensive in outcrops on the western side of the highway while less so on the eastern side (figure 6). In the LWIR data fewer pixels exhibited the diagnostic kaolinite triplet feature at 8.81, 9.34, and 9.89  $\mu\text{m}$  than those identified in the SWIR image data. The mixture of kaolinite with

quartz severely minimized the apparent kaolinite component, so that the spectra appeared as quartz with a minor doublet imprinted upon the 9.4  $\mu\text{m}$  emission minima lobe.

#### 5.11.7 Muscovite

The gravel road and gravel stockpile associated with muscovite were identified in the SWIR via the diagnostic narrow absorption at 2205 nm and a minor absorption at 2355 nm. Muscovite was able to be mapped with a high degree of confidence because the diagnostic feature was sharp and varied sufficiently from adjacent instances of alunite and kaolinite, as well as being spatially constrained to man-made surface features (figure 7). The LWIR image data were more difficult to use to replicate similar results as the SWIR. Laboratory measurements of samples taken from the road and stockpiles indicated that the bulk mineralogical constituent of the gravel was quartz, while a muscovite-based clay coated the gravel. This resulted in frequent false positives as adjacent quartz-rich outcrops were misidentified during LWIR data analysis. The SWIR results were able to be used as a guide to help determine LWIR rule image thresholds.

#### 5.11.8 Zeolite

The zeolite class was mapped extensively throughout the east-west image data mosaic (figures 6 and 12). A map product was created with the SWIR image data due to the distinctive broad reflectance down-slope from 2000 - 2450 nm unique to zeolite minerals. This feature resulted in a great deal of contrast between adjacent mineral classes. The LWIR image data was also able to be used to map zeolite-rich tuff, though the diagnostic feature, a deep minima at 9.16  $\mu\text{m}$  and a sharp minima at 9.58  $\mu\text{m}$ , did not result in spectral delineation that matched as many pixels mapped as with the SWIR data

(figures 8 and 9). The tuff included varying percentages of clastic and phenocryst constituents that may have caused spectral variability, and so fewer overall pixels were mapped that matched the single data endmember spectra that represented the class.

#### 5.11.10 Carbonates

Calcite and dolomite were able to be spectrally delineated and mapped based upon subtle shifts in diagnostic spectral features. The absorption band center of calcite is 2335 and 2320 nm for dolomite; the emission minima for calcite is centered at 11.3  $\mu\text{m}$  (figure 14F) and at 11.2  $\mu\text{m}$  for dolomite. For the Miocene/Pliocene gravel deposit, which was composed of quartz-rich gravel mixed with calcite and dolomite, overall reflectance and spectral contrast for the calcite absorption feature was low in the SWIR.

Nevertheless, pixels indicative of calcite were able to be mapped over a large area, whereas in the LWIR data, the calcite emission minima varied in prominence, and was more distinctive at the ridges of the fan and subdued in the incised areas where alluvium had collected. Bare Mountain exhibited a strong dolomite absorption in the SWIR reflectance spectra, and the LWIR image data spectra also exhibited a deep emission minima diagnostic of dolomite. The talus that formed small fans at the base of the range generally indicated the spatial boundary of mapped pixels using the LWIR data, while mapped dolomite pixels in the SWIR data extended further outward from this area.

In the hot spring area, limited carbonate was surficially expressed. Spectral contrast in the 2335 nm range associated with calcite absorption was not distinct, as other materials in the scene mimicked this weak feature, including a secondary absorption feature of alunite at 2324 nm, and vegetation. In addition, mixtures of adjacent materials



such as opaline silica and evaporites may have reduced the measurable contribution of the targeted mineral. The LWIR data was shown to be of great use in this example because none of the other materials found in the area exhibited diagnostic features that overlapped or effectively attenuate the 11.3  $\mu\text{m}$  feature of calcite, thus enhancing spectral delineation.

### **5.12 Resolving ambiguity in mineral spectra interpretation**

Some LWIR mineral endmembers were misidentified during statistical mapping of the data. Emissivity spectra of zeolite-rich tuff (consisting of zeolite + feldspar + quartz) and muscovite clay-coated gravel were both characterized by a narrow emission minima feature at 9.63  $\mu\text{m}$  (figure 17). Laboratory measurements attributed this feature to feldspar in the tuff sample and muscovite in the gravel. The SWIR data was useful to corroborate the presence or absence of muscovite, via the narrow primary diagnostic absorption at 2200 nm. Because LWIR image data pixels that exhibited the 9.63  $\mu\text{m}$  emission minima could be attributed to either feldspar or muscovite, the SWIR image data spectra could thus be cross-referenced to better resolve this uncertainty. When the 2200 nm absorption was present, the respective emission feature could be attributed to either muscovite or feldspar. When absent, the feature was attributed solely to feldspar.

### **5.13 Comprehensive mineral mapping**

SWIR and LWIR image data sets can be used in a complementary manner to enhance recognition of mineral presence, such as in areas of hydrothermal alteration. By combining respective mineral classification maps from the two data sets, an optimal map delineating quartz, alunite, kaolinite and opaline silica was produced (figure 18). A wider

distribution of alunite was mapped in the SWIR than the LWIR because spectral mineral mixtures were limited. In the LWIR, alunite was mappable but the additional presence of quartz resulted in mixed emissivity spectra where quartz spectral features overlapped and diminished those of alunite.

Opaline silica was mapped with the SWIR image data in distinct portions of the studied outcrops. Although crystalline and amorphous forms of silica can be distinguished and mapped with LWIR image data (e.g., quartz and opal), amorphous opaline silica is dominated by quartz when occurring together. The combined use of these data revealed the presence of both of these minerals, where opal would have otherwise been under-represented, or possibly not mapped at all. These joint image data may be useful for further extending geologic applications such as relating surficially-expressed alteration mineral patterns to unrecognized fault structures (Kratt et al., 2005), as well as for delineating areas where minerals such as kaolinite and alunite have been silicified from those that have not.

#### **5.14 Conclusion**

This research presented results from the analysis of jointly-collected reflectance and emittance hyperspectral image data in Oasis Valley, Nye County, Nevada. ProSpecTIR-VS and SEBASS hyperspectral image data were individually analyzed to produce maps of clay, evaporite, sulfate, rock-forming silicate, and carbonate minerals. A focus of the research was to determine whether particular minerals were better suited for detection, identification, and mapping in a single or combined wavelength ranges. Certain mineral classes were mapped in more pixels in the SWIR image data than the LWIR.

These included: opaline silica, calcite, dolomite, alunite, kaolinite, muscovite, and zeolite. However, this did not necessarily indicate a shortcoming of the LWIR data, as the presence of quartz diminished some of these minerals. In addition, the LWIR data were invaluable for identifying and mapping small consolidated carbonate features associated with a hot spring, whereas these features were not identified during initial analysis of the SWIR data.

Quartz and basalt were mapped solely in the LWIR image due to lack of diagnostic features in the SWIR. Next, the evaporites burkeite, mascagnite, and gypsum were shown to be better detected and mapped in the LWIR image data, as they did not produce high contrast diagnostic spectral features in the SWIR, possibly due to being adjacent to or interspersed amongst vegetation. Manual analysis of LWIR image data resulted in the identification of subtle mineral components in emissivity spectra, and was found to be preferable to produce more comprehensive mineral maps. However these manual analyses are far more time-intensive than using statistical mapping algorithms such as SAM. Fine-grained weathering products were found to be best mapped in the SWIR, due to a higher reflectance attributed to increased proportion of surface area. The combined use of the data sets were used to corroborate map results and to identify mineral instances that had not been observed in independent analysis of either SWIR or LWIR image data. In tandem these data sets are useful for highlighting differing mineralogical constituents of measured surfaces.

### **5.15 Acknowledgements**

This research was supported by a Department of Energy (DOE) Office of Nonproliferation and Verification Research and Development (NA-22), Nuclear Fuel Cycle Remote Sensing contract, DE-FG52-08NA28771, entitled: “Quantitative Spectral Characterization of Background Spectra Using Full-Spectrum Hyperspectral Image Data. We thank the reviewers for their constructive comments which improved the final version of the manuscript. We thank Chris Kratt, Tim Minor, and Don Sabol for use of field reflectance measurement libraries that were used in addition to libraries compiled by the author. Thanks to Todd Morken and Laura Huebner for assisting in taking field thermal-infrared measurements and Fred Kruse for his assistance with successfully utilizing and evaluating atmospheric correction software.

## 5.16 References

- Abrams, M., Abbot, E., and Kahle, A.B. (1991). Combined use of visible, reflected infrared, and thermal infrared images for mapping Hawaiian lava flows. *Journal of Geophysical Research*, 96 (B1), pp. 475-484.
- Analytical Imaging and Geophysics LLC (AIG) (2009). *ACORN User's Guide, Stand-alone Version*. Analytical Imaging and Geophysics LLC. 64 pp.
- Boardman, J.W. and Kruse, F.A. (1994). Automated spectral analysis: a geologic example using AVIRIS data, North Grapevine Mountains, Nevada. *Proceedings of the tenth thematic conference on geologic remote sensing*, Environmental Research Institute of Michigan, Ann Arbor, MI, pp. I-407 – I-418.
- Carr, M.D., Sawyer, D.A., Nimz, K., Maldonado, F., and Swadley, W.C. (1996). Digital Bedrock Geologic Map Database of the Beatty 30 X 60-Minute Quadrangle, Nevada and California. *U.S. Geological Survey Open-File Report 96-291*.
- Chen, X., Warner, T.A., Campagna, D.J. (2007). Integrating visible, near-infrared and short-wave infrared hyperspectral and multispectral thermal imagery for geological mapping at Cuprite, Nevada. *Remote Sensing of Environment*, 110, pp. 344-356.
- Clark, R.N. (1999). Spectroscopy and Principles of Spectroscopy, *Manual of Remote Sensing*, A. Rencz, Editor, John Wiley and Sons, Inc.
- Clark, R.N., Swayze, G.A., Wise, R., Livo, E., Hoefen, T., Kokaly, R., Sutley, S.J. (2007). USGS digital spectral library splib06a. *U.S. Geological Survey, Digital Data Series 231*.
- Cocks, T., Jansen, R. Stewart, W.I., Shields, T. (1998). The HyMap airborne hyperspectral sensor: The system, calibration and performance. In: M. Schaepman, D.

- Schlapfer and K.I. Itten, Eds., *Proceedings of the 1st EARSeL Workshop on Imaging Spectroscopy*, Zurich.
- Cudahy, T.J., Wilson, J., Hewson, R.D., Okada, K., Linton, P., Harris, P., Sears, M., and Hackwell, J.A. (2001). Mapping variations in plagioclase feldspar mineralogy using airborne hyperspectral VNIR-SWIR-TIR imaging data. *Proceedings of IEEE 2001, International Conference on Geoscience and Remote Sensing*, Sydney 9-13 July.
- Farmer, V.C., Editor (1974). *The infrared spectra of minerals*. Mineralogical Society Monograph vol. 4, Mineralogical Society, London
- Fridrich, C.J., Minor, S.A., and Mankinen, E.A. (1999). Geologic evaluation of the Oasis Valley basin, Nye County, Nevada. *United States Geological Survey Open-File Report 99-533-A*.
- Fridrich, C.J., Minor, S.A., Slate, J.L., and Ryder, P.L. (2007). Geologic map of Oasis Valley spring-discharge area and vicinity, Nye County, Nevada. *U.S. Geological Survey Scientific Investigations Map 2957*, 25 p., scale 1:50,000.
- Gaffey, S.J., McFadden, L.A., Nash, D., and Pieters, C.M. (1993). Ultraviolet, Visible, and Near-infrared Reflectance Spectroscopy: Laboratory spectra of Geologic Materials, in *Remote Geochemical Analysis: Elemental and Mineralogical Composition* (C. M. Pieters, and P.A.J. Englert, editors.), Cambridge University Press, Cambridge, pp. 43-78.
- Hackwell, J.A., Warren, D.W., Bongiovi, R.P., Hansel, S.J., Hayhurst, T.L., Mabry, D.J., Sivjee, M.G., and Skinner, J.W. (1996). LWIR/MWIR imaging hyperspectral sensor for airborne and ground-based remote sensing, *The International Society for Optical*

- Engineering*, 2819, pp. 102-107.
- Hapke, B. (1993). *Theory of reflectance and emittance spectroscopy*: Topics in Remote Sensing 3, 455 pp.
- Harsanyi, J.C., Farrand, W., and Chang, C.I. (1994). Detection of subpixel spectral signatures in hyperspectral image sequences, *Proc. Am. Soc. Photogramm. Remote Sens. Annu. Mtg.*, pp. 236-247.
- Hook, S.J. and Kahle, A.B. (1996). The micro fourier transform interferometer ( $\mu$ FTIR) – a new field spectrometer for acquisition of infrared data of natural surfaces. *Remote Sensing of Environment*, 56, pp. 172-181.
- Hook, S.J., Gabell, A.R., Green, A.A., and Kealy, P.S. (1992). A comparison of techniques for extracting emissivity information from thermal infrared data for geologic studies. *Remote Sensing of Environment*, 42, pp. 123-135.
- Hunt, G.R., and Salisbury, J.W. (1971). Visible and near infrared spectra of minerals and rocks. II. Carbonates, *Modern Geology*, 2, pp. 23-30.
- ITT Visual Solutions (2008). *ENVI User's Guide*, Version 4.3. ITT Visual Solutions, Boulder, Colorado.
- Johnson, B.R. (1998). In-scene atmospheric compensation: application to the SEBASS data collected at the ARM site, Part I. *Aerospace Corporation Report*, (ATR-99(8407), Part I).
- Kirkland, L.E., Herr, K.C., and Adams, P.M. (2007). Straightforward results from a Mars analog site (Alunite, Nevada): Learning to combine near- and thermal-infrared spectral interpretations for Mars. *Proceedings of the 38th Lunar and Planetary Science Conference*, 1338, p. 2232

- Korb, A.R., Dybwad, P., Wadsworth, W., and Salisbury, J.W. (1996). Portable fourier transform infrared spectroradiometer for field measurements of radiance and emissivity. *Applied Optics*, 35 (10), pp. 1679-1692.
- Kratt, C., Calvin, W. M., and Coolbaugh, M. F. (2005). Geothermal Exploration With Hymap Hyperspectral Data at Brady-Desert Peak, Nevada. *Remote Sensing of Environment*, 104, pp. 313-324.
- Kruse, F. A. (2002). Combined SWIR and LWIR Mineral Mapping Using MASTER/ASTER. *Proceedings of IGARSS 2002*, Toronto, Canada. pp. 24-28.
- Kruse, F.A., Lefkoff, A.B., and Dietz, J.B. (1993). Expert system-based mineral mapping in Northern Death Valley, California/Nevada, using the Airborne Visible/Infrared Imaging Spectrometer (AVIRIS). *Remote Sensing of Environment*, 44, pp. 309-336.
- Lane, M.D., and Christensen, P.R. (1997). Thermal infrared emission spectroscopy of anhydrous carbonates. *Journal of Geophysical Research*, 102 (E11), pp. 25581-25592.
- Lang, H.R., Adams, S.L., Conel, J.E., McGuffie, B.A., Paylor, E.D., and Walker, R.E. (1987). Multispectral Remote Sensing as Stratigraphic and Structural Tool, Wind River Basin and Big Horn Basin Areas, Wyoming. *AAPG Bulletin*, 71 (4), pp. 389-402.
- Lyon, R. J. P., and Green, A. A. (1975). In Ch. 7, Reflectance and emittance of terrain in the mid-infrared (6 – 25  $\mu\text{m}$ ) region, *Infrared and Raman Spectroscopy of Lunar and Terrestrial Minerals*, Academic Press, Inc., pp. 164-194.
- Mankinen, E.A., Hildenbrand, T.G., McKee, E.H., and Schenkel, C.J. (2003). Geophysical setting of the Pahute Mesa-Oasis Valley region southern Nevada. *Nevada*



*Bureau of Mines and Geology Report 50.*

Realmuto, V.J. (1990). Separating the effects of temperature and emissivity: emissivity spectrum normalization. *Proceedings of the 2<sup>nd</sup> TIMS Workshop*, JPL Publication 90-55, pp. 31-35.

Reiner, S.R., Lacznia, R.J., Demeo, G.A., Smith, J.L., Elliott, P.E., Nylund, W.E., and Fridrich, C.J. (2002). Ground-water Discharge Determined from Measurements of Evapotranspiration, Other Available Hydrologic Components, and Shallow Water-Level Changes, Oasis Valley, Nye County, Nevada. *USGS Water-Resources Investigations Report 01-4239.*

Riley, D.N., Weatherbee, O., Jones, K.L., and Peppin, W.A. (2008). Joint Airborne Collection using Hyperspectral Systems (JACHS): Geological and environmental mineral mapping with visible-near infrared-shortwave infrared and midwave-longwave infrared hyperspectral imagers. *Presentation at 33<sup>rd</sup> International Geological Congress*, Oslo, Norway.

Rowan, L.C., and Mars, J.C. (2003). Lithologic mapping in the Mountain Pass, California area using Advanced Spaceborne Thermal Emission and Reflection Radiometer (ASTER) data. *Remote Sensing of Environment*, 84 (3), pp. 350-366.

Ruff, S.W., P.R. Christensen, P.W. Barbera, and D.L. Anderson (1997). Quantitative thermal emission spectroscopy of minerals: A laboratory technique for measurement and calibration, *Journal of Geophysical Research*, 102, pp. 14,899-14,913.

Salisbury, J.W., and Wald, A. (1992 A). The role of volume scattering in reducing spectral contrast of restrahten bands in spectra of powdered minerals. *Icarus*, 96, pp. 121-128.

- Salisbury, J.W., and D'Aria, D.M. (1992 B). Emissivity of terrestrial materials in the 8 – 14  $\mu\text{m}$  atmospheric window. *Remote Sensing of Environment*, 42, pp. 83-106.
- Salisbury, J.W., and Eastes, J.W. (1985). The Effect of Particle Size and Porosity on Spectral Contrast in the Mid-Infrared. *Icarus*, 64, pp. 586-588.
- Smith, P., Tingley, J., Bentz, J., Garside, L., Papke, K., and Quade, J. (1983). A mineral inventory of the Esmeralda-Stateline resource area, Las Vegas district, Nevada. *Nevada Bureau of Mines and Geology Official Report* 83-11, pp. 14-20.
- SpecTIR, LLC. (2009). ProSpecTIR VNIR and SWIR hyperspectral sensors. <http://spectir.com/assets/Images/Capabilities/ProspecTIR%20specs.pdf>  
Accessed on 10/1/2009.
- Vane, G., Green, R.O., Chrien, T.G., Enmark, H.T., Hansen, E.G., and Porter, W.M. (1993). The airborne visible/infrared imaging spectrometer (AVIRIS). *Remote Sensing of Environment*, 44 (2-3), pp. 127-143.
- Vaughan, R.G., Hook, S.J., Calvin, W.M., and Taranik, J.V. (2005). Surface mineral mapping at Steamboat Springs, Nevada, USA, with multi-wavelength thermal infrared images. *Remote Sensing of Environment*, 99, pp. 140-158.
- Vaughan, R. G., Calvin, W. M., and Taranik, J. V. (2003). SEBASS hyperspectral thermal infrared data: surface emissivity measurement and mineral mapping. *Remote Sensing of Environment*, 85, pp. 48-63.
- Workman, J.B., Menges, C.M., Page, W.R., Taylor, E.M., Ekren, E.B., Rowley, P.D., Dixon, G.L., Thompson, R.A., and Wright, L.A. (2002). Geologic map of the Death Valley ground-water model area, Nevada and California. *USGS Misc. Field Studies*

*Map* MF-2381-A, scale 1:250,000.

Young, S. J., Johnson, B. R., and Hackwell, J. A. (2002). An in-scene method for atmospheric compensation of thermal hyperspectral data. *Journal of Geophysical Research*, 107 (D24), 4774.

## Tables

Table 1.

Sensor specifications (from SpecTIR LLC, 2009; and Hackwell et al., 1996)

Sensor	Spectral range ( $\mu\text{m}$ )	Radiometric resolution	Spectral resolution	# of bands	# of pixels	IFOV	SNR	INS
ProSpecTIR V-S	0.4 - 2.451	VNIR: 12-bit SWIR: 14-bit	v/c; VNIR: 5 nm+ SWIR: 8 nm+	v/c; 178 to 366	320	1.0 mrad	VNIR: 500:1 SWIR: 800:1	Honeywell HG1700 w/ Novatel SPAN
SEBASS	7.65 - 13.54	12-bit	40 nm	128	128	1.1 mrad	2000:1	C-MIGITS 3

v/c = vendor configurable

Table 2.

Data acquisition parameters

Sensor	GIFOV	# flightlines	Mosaic data size
ProSpecTIR V-S	5 m	11	3.23 GB
SEBASS	5 m	11	3.4 GB

Table 3.

Number of pixels classified for each mineral per segment

Class	Classified pixels: SWIR	Classified pixels: LWIR
alunite	15368	11377
basalt	-	44813
calcite	45338	26758
dolomite	24201	17419
kaolinite	22009	17263
burkeite	-	1594
muscovite	4252	1665
opaline silica	8334	518
quartz	-	14312
zeolite	40612	29394
gypsum	-	4

## Figures

Figure 1.

ProSpecTIR V-S and SEBASS imaging spectrometer systems are mounted in the data collection aircraft (photographs courtesy of SpecTIR LLC and The Aerospace Corporation). At left, the instruments are viewed from a side perspective and shown installed in a roll-stabilized mount. At right, the apertures of the systems are viewed from below. Image data from the indicated camera system were not provided or utilized in the study.

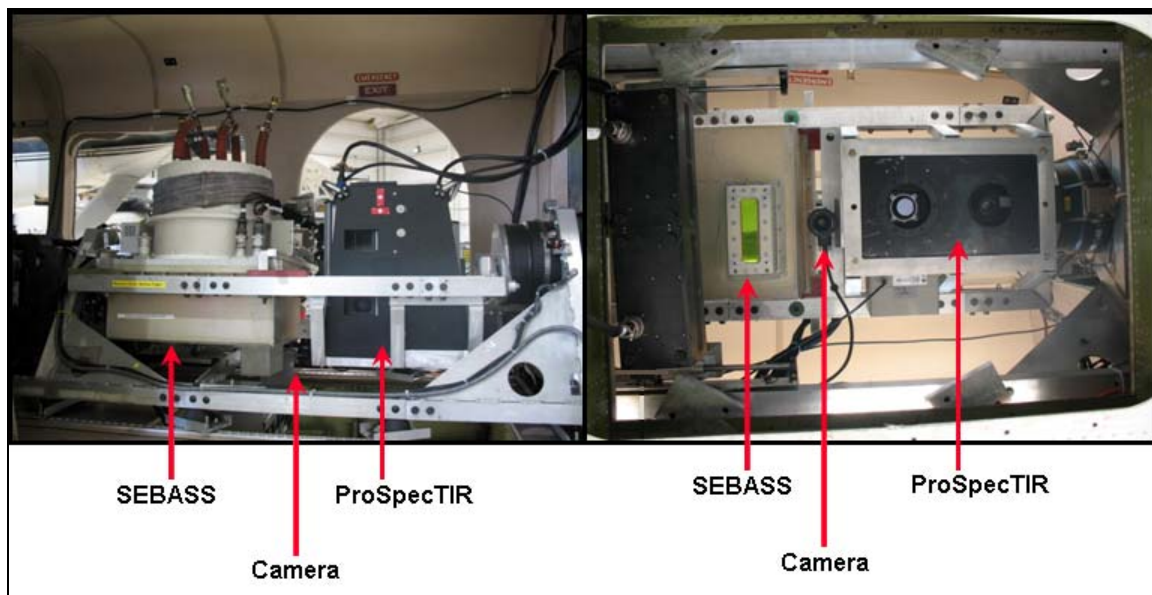


Figure 2.

Location map of the Oasis Valley, Nevada study area. 5 m GIFOV ProSpecTIR V-S and SEBASS hyperspectral image data were collected within the boundaries of the black outlined box.

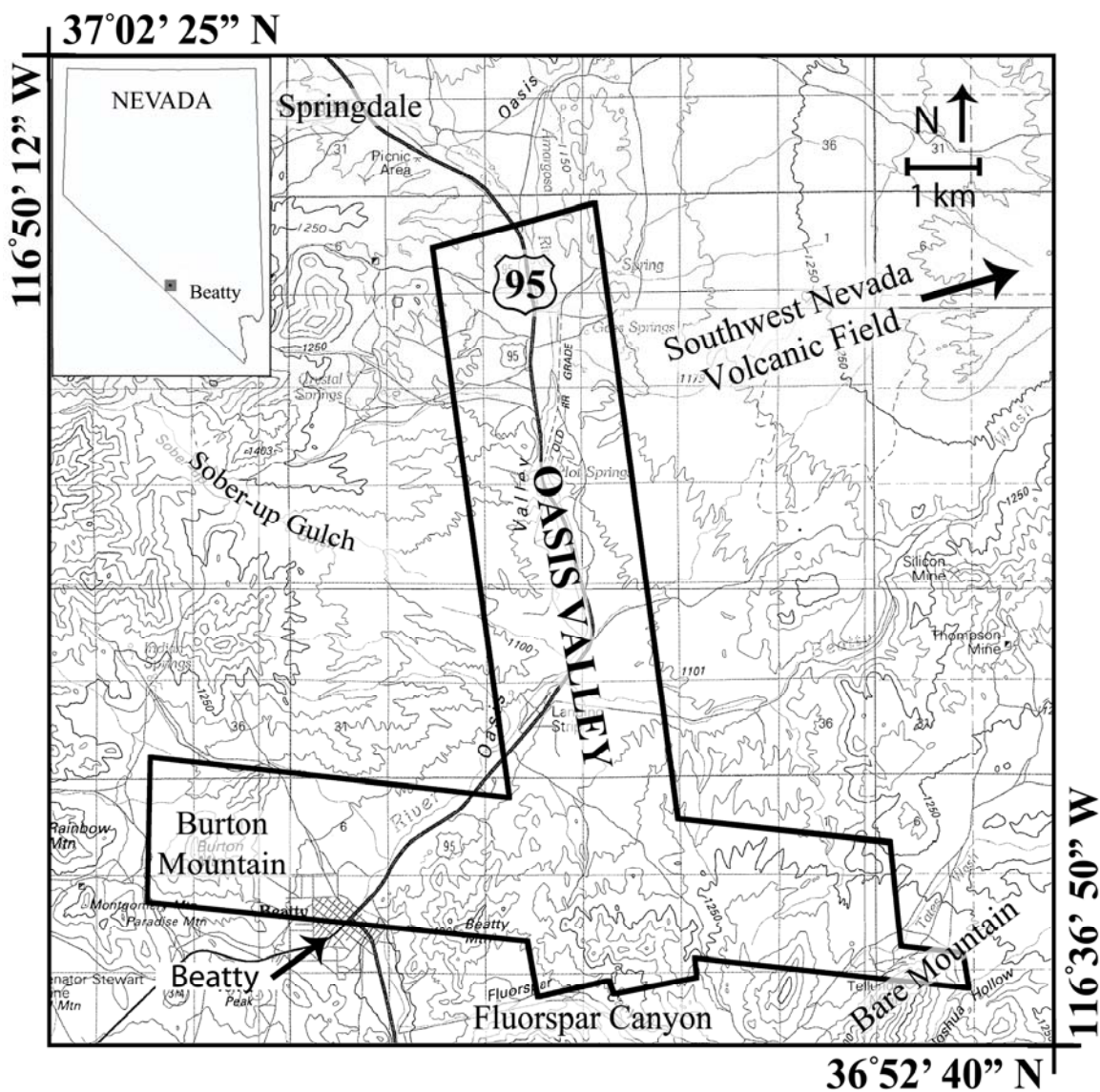
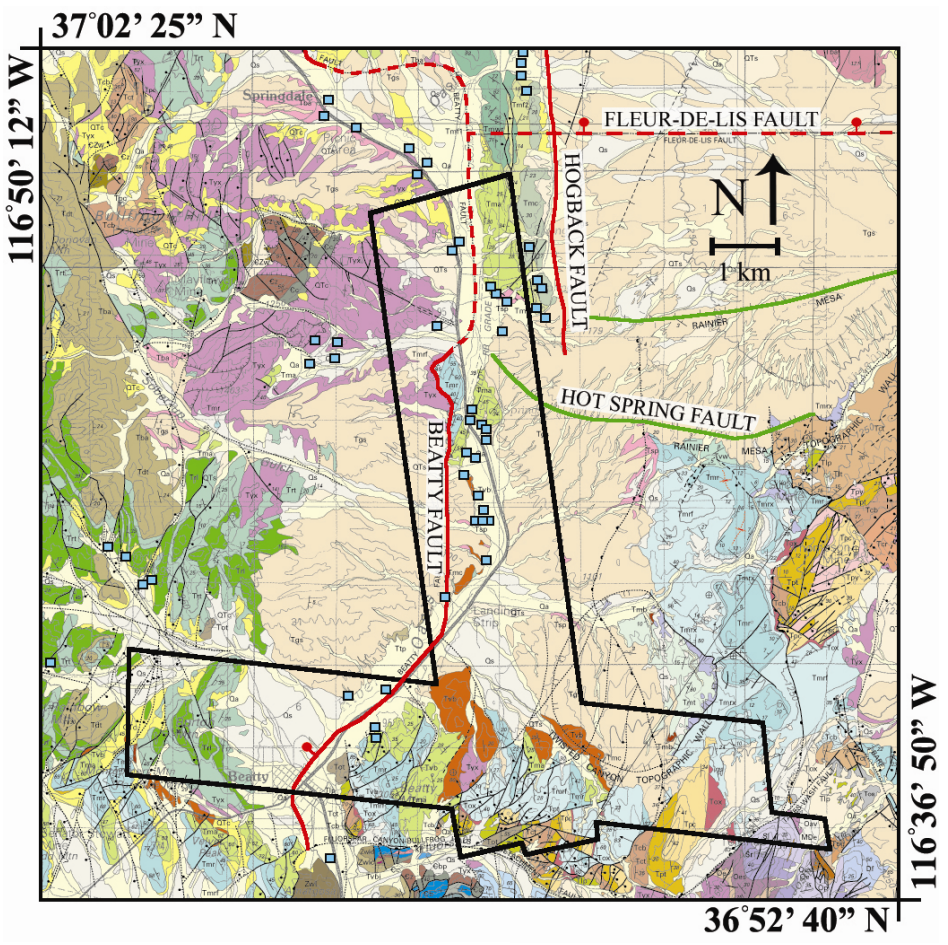


Figure 3.

Geology map of the study area (from Fridrich et al., 2007). Prominent structural features that intersect the image data boundaries (from Reiner et al., 2002) overlay the geology map. Features in solid red denote fault traces, while red dashes are inferred or otherwise blind fault continuation, and green indicates caldera ring fractures. The locations of springs are shown as turquoise squares (from Reiner et al., 2002).



Qa	Young alluvial deposits (Holocene)
Qs	Middle alluvial deposits (Pleistocene)
QTc	Colluvium (Holocene to Pliocene)
QTs	Old alluvial deposits (early Pleistocene and Pliocene)
Tgs	Older gravels (lower Pliocene and Miocene)
Ttp	Pahute Mesa Tuff
Tso	Rhyolite of Oasis Valley (Miocene)
Tdt	Trachyte of Donovan Mountain (Miocene)
Trl	Rhyolite Lavas of Rainbow Mountain (Miocene)
Trt	Rhyolite Tuffs of Rainbow Mountain (Miocene)
Tyx	Younger landslide breccias (Miocene)
Tvb	Basalts (Miocene)
Tma	Ammonia Tanks Tuff
Tmr	Rainier Mesa Tuff
Tmrf	Pre-Rainier Mesa rhyolite
Tot	Older tuffs and intercalated sediments
Sl	Lone Mountain Dolomite (Silurian)
Sr	Roberts Mountain Formation (Silurian)
Oes	Ely Springs Dolomite (Ordovician)
Oe	Eureka Quartzite (Ordovician)



Figure 4.

ProSpecTIR V-S image data map. RGB band combination: 168 (2326 nm), 156 (2175 nm), 148 (2074 nm displays kaolinite in purple, alunite in magenta and carbonates in cyan.

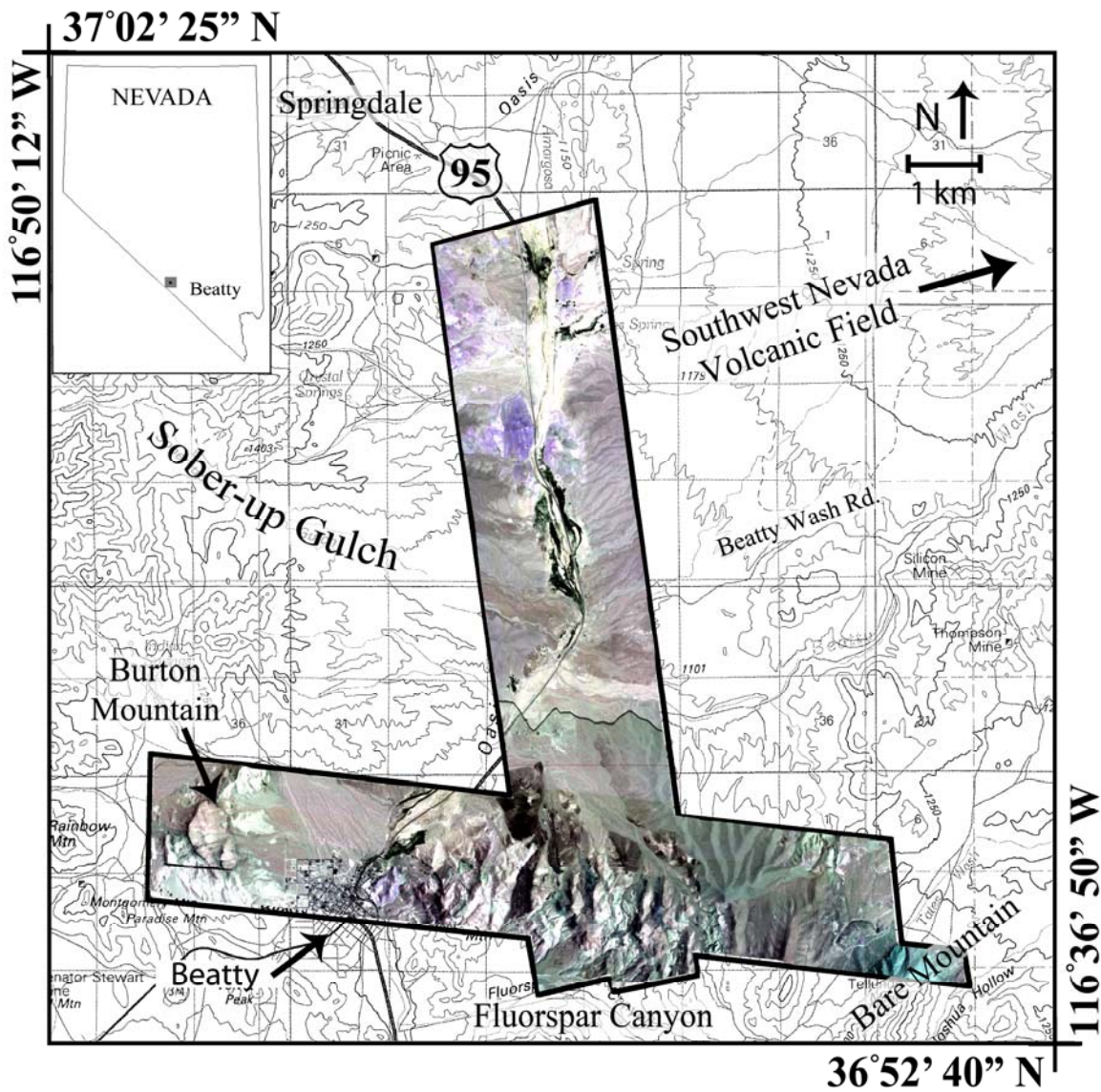


Figure 5.

ProSpecTIR V-S SWIR image data endmember spectra (left) and SEBASS LWIR image data endmember spectra (right).

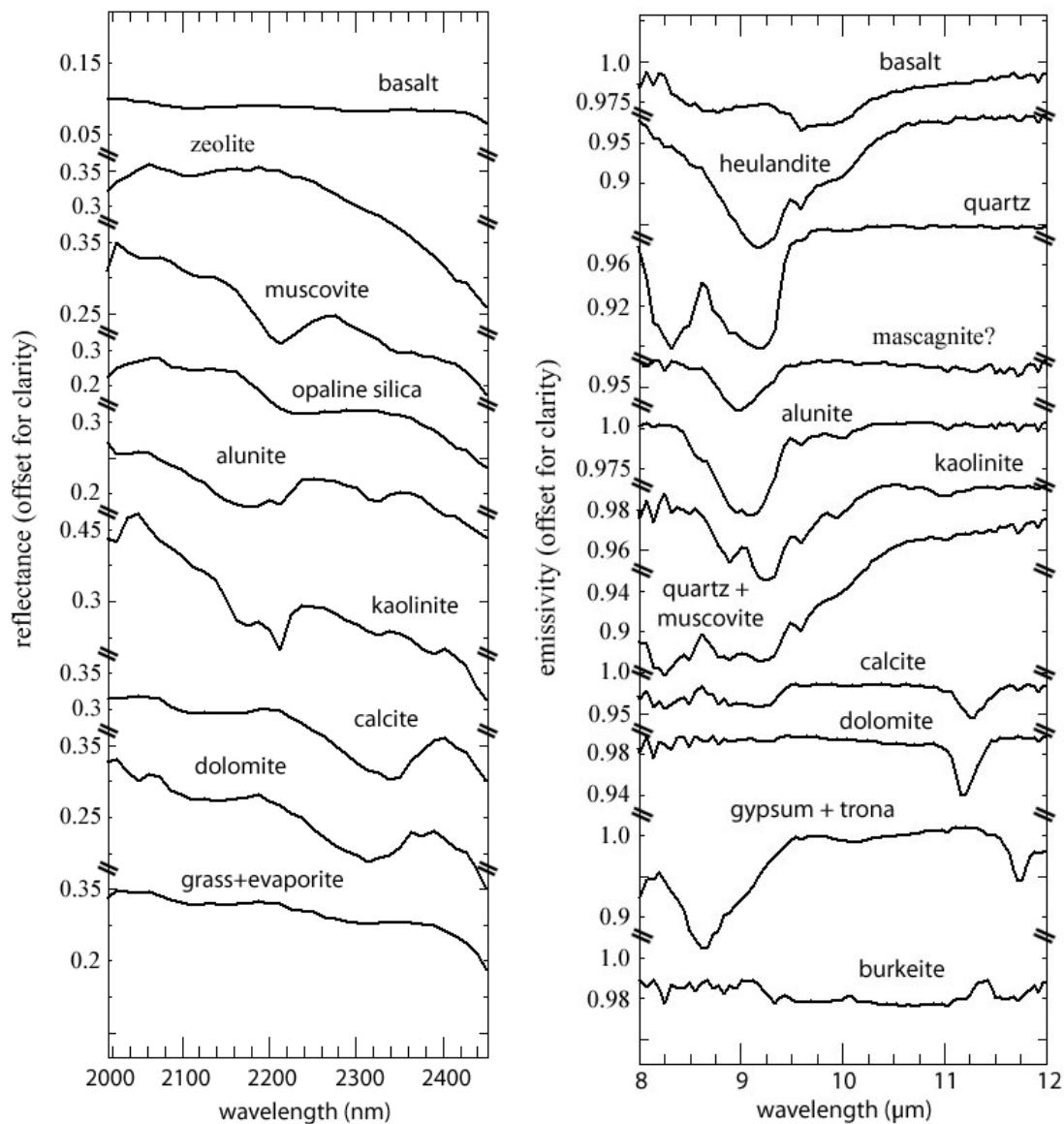


Figure 6.

Mineral map derived from analysis of ProSpecTIR V-S SWIR image data bands ranging from 2050 - 2450 nm. Background image is a high-resolution orthophoto.

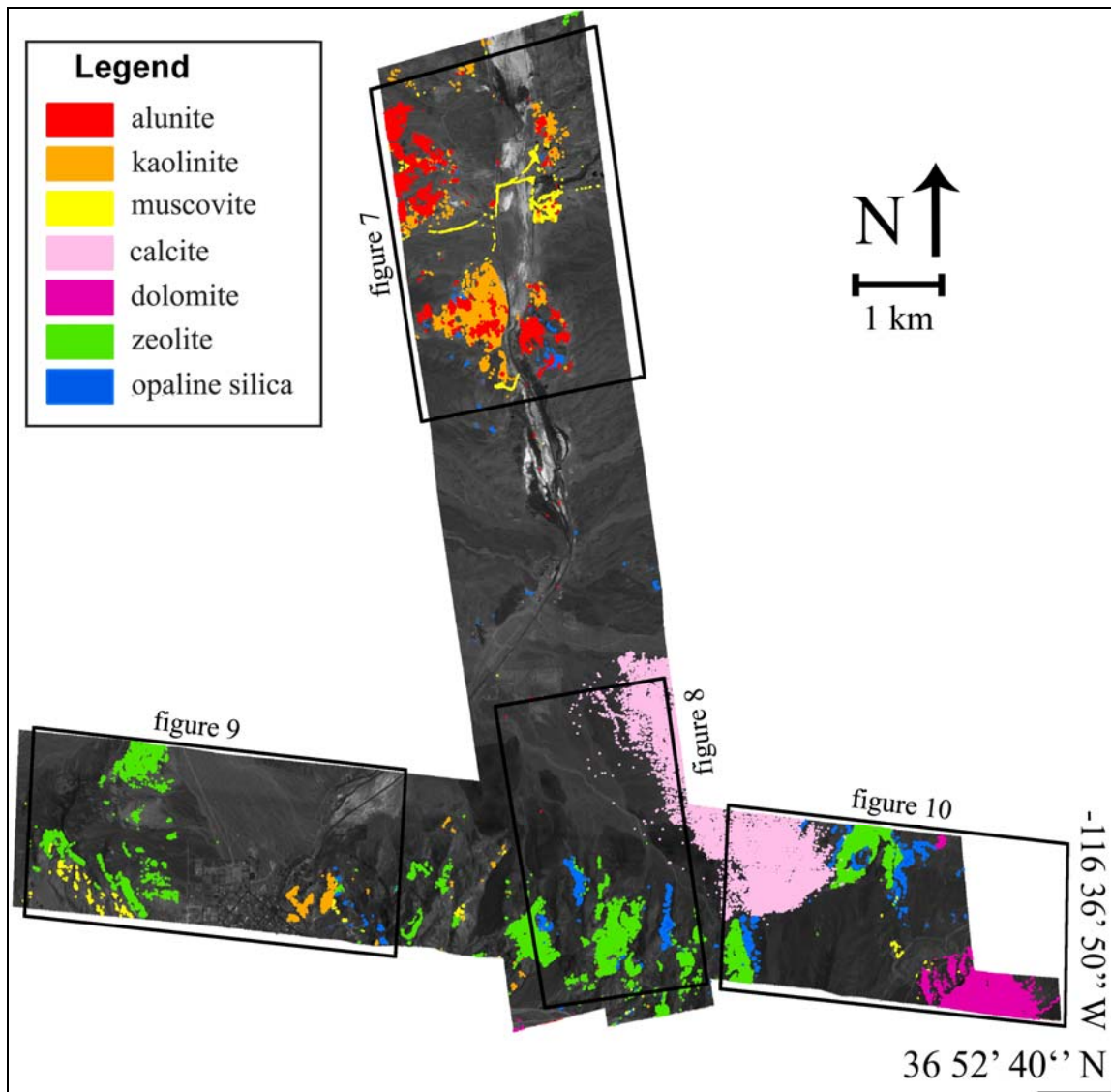


Figure 7.

Scene 1: acid-sulfate hydrothermal system; dirt road; quartz/silica outcrops; alunite quarry.

Colored spectra correspond to image data and black spectra are from laboratory.

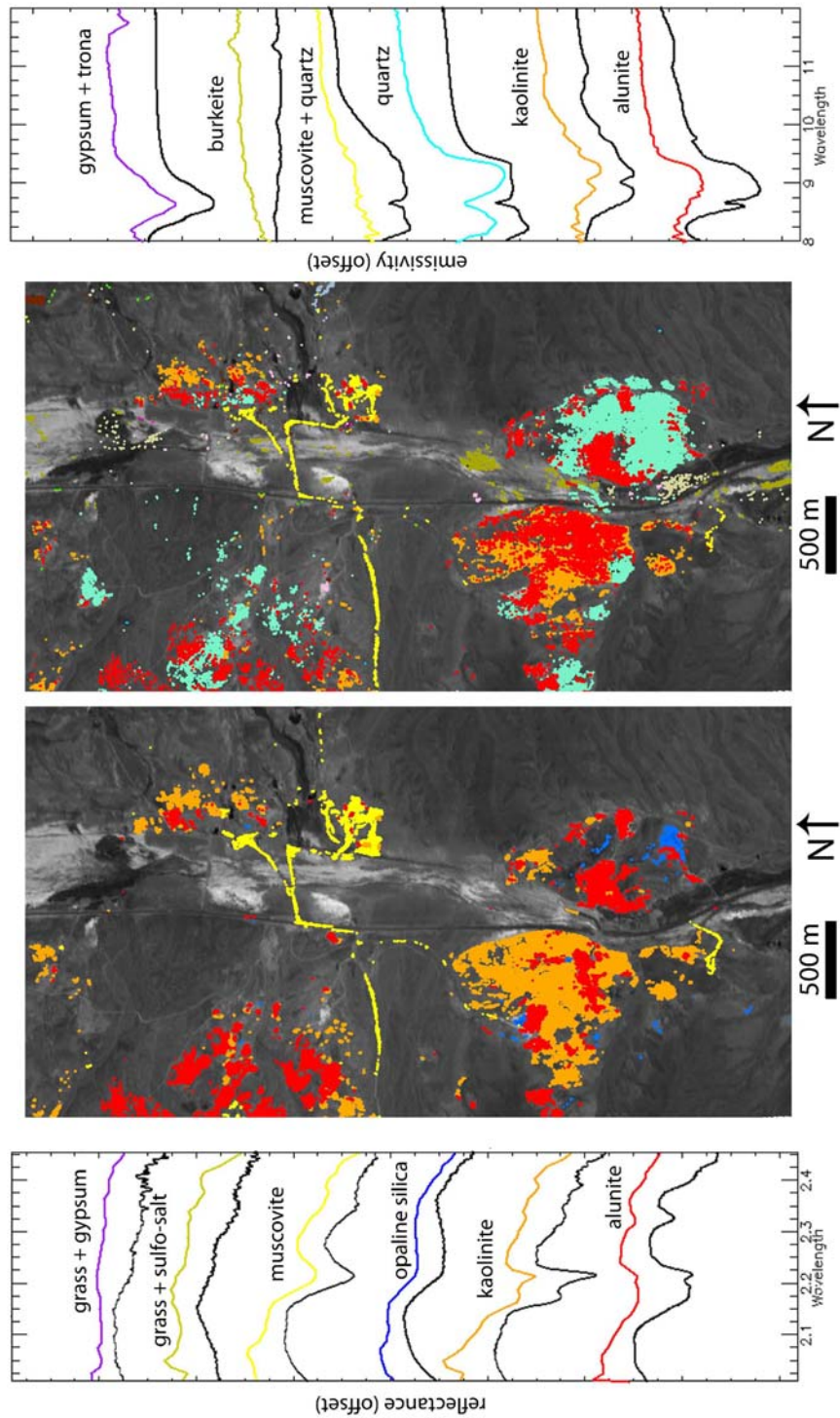


Figure 8.

Scene 2: basalt flows; zeolite and silica-rich tuff; carbonate-rich alluvial fan. Colored spectra correspond to image data and black spectra are from laboratory.

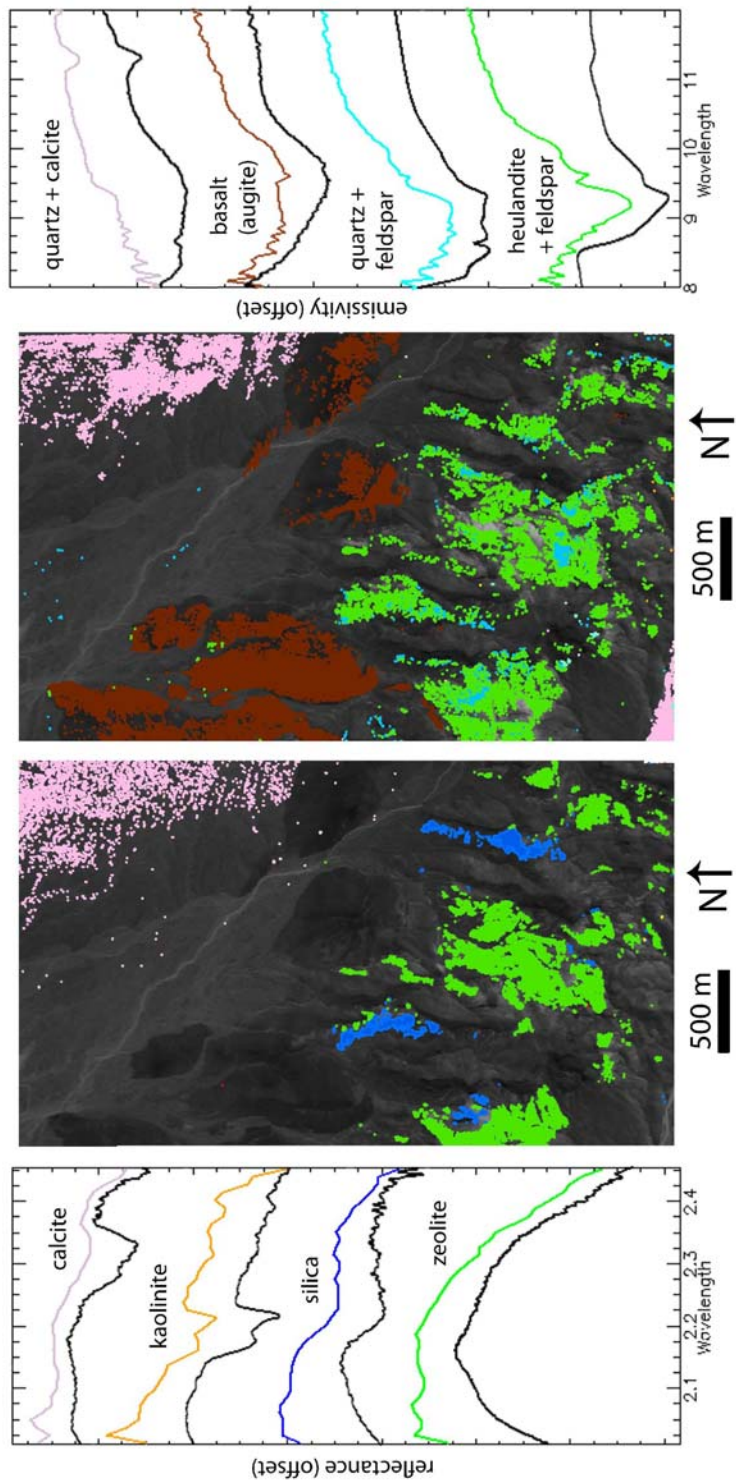


Figure 9.

Scene 3: zeolite extrusive; illite related to outflow; kaolinite outcrop; sulfate in field. Colored spectra correspond to image data and black spectra are from laboratory.

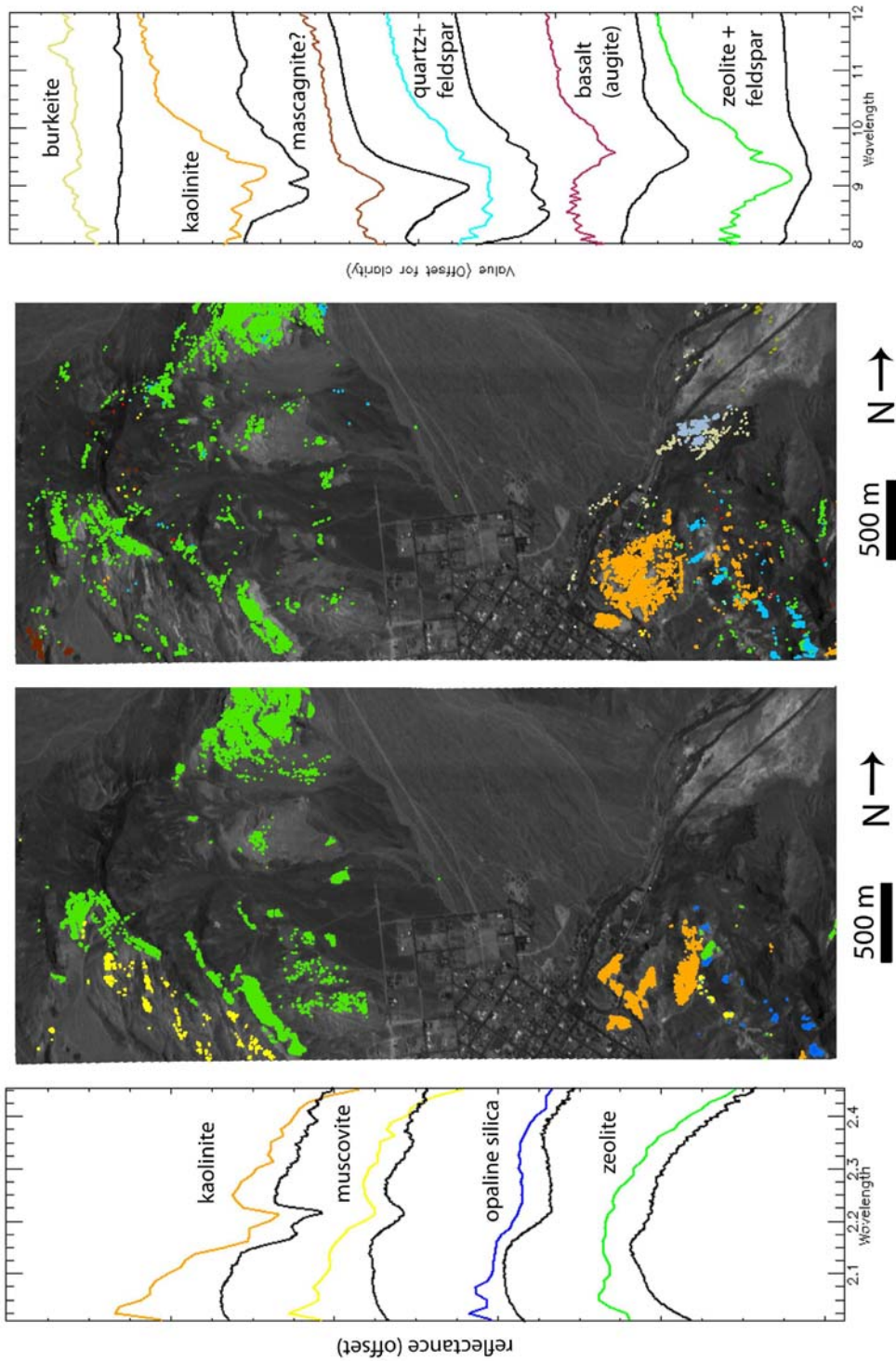


Figure 10.

Scene 4: Bare Mountain dolostone; carbonate-rich alluvial fan; zeolite/tuff contact.  
Colored spectra correspond to image data and black spectra are from laboratory.

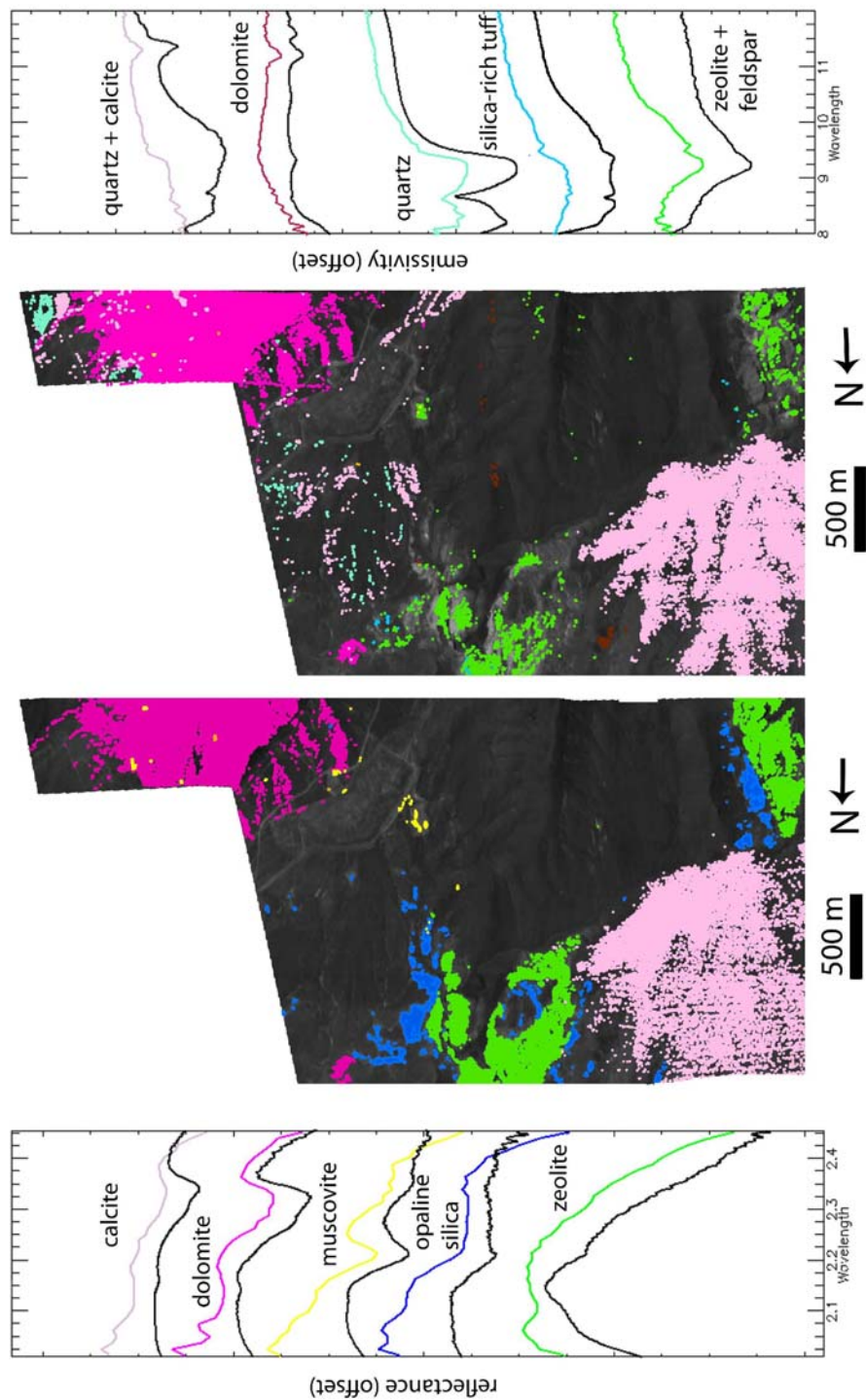


Figure 11.

SEBASS image data map. RGB color band combination: 41 (9.89  $\mu\text{m}$ ), 27 (9.16  $\mu\text{m}$ ), 19 (8.72  $\mu\text{m}$  displays quartz in red, tuff in purple, basalt in cyan and carbonates in light brown.

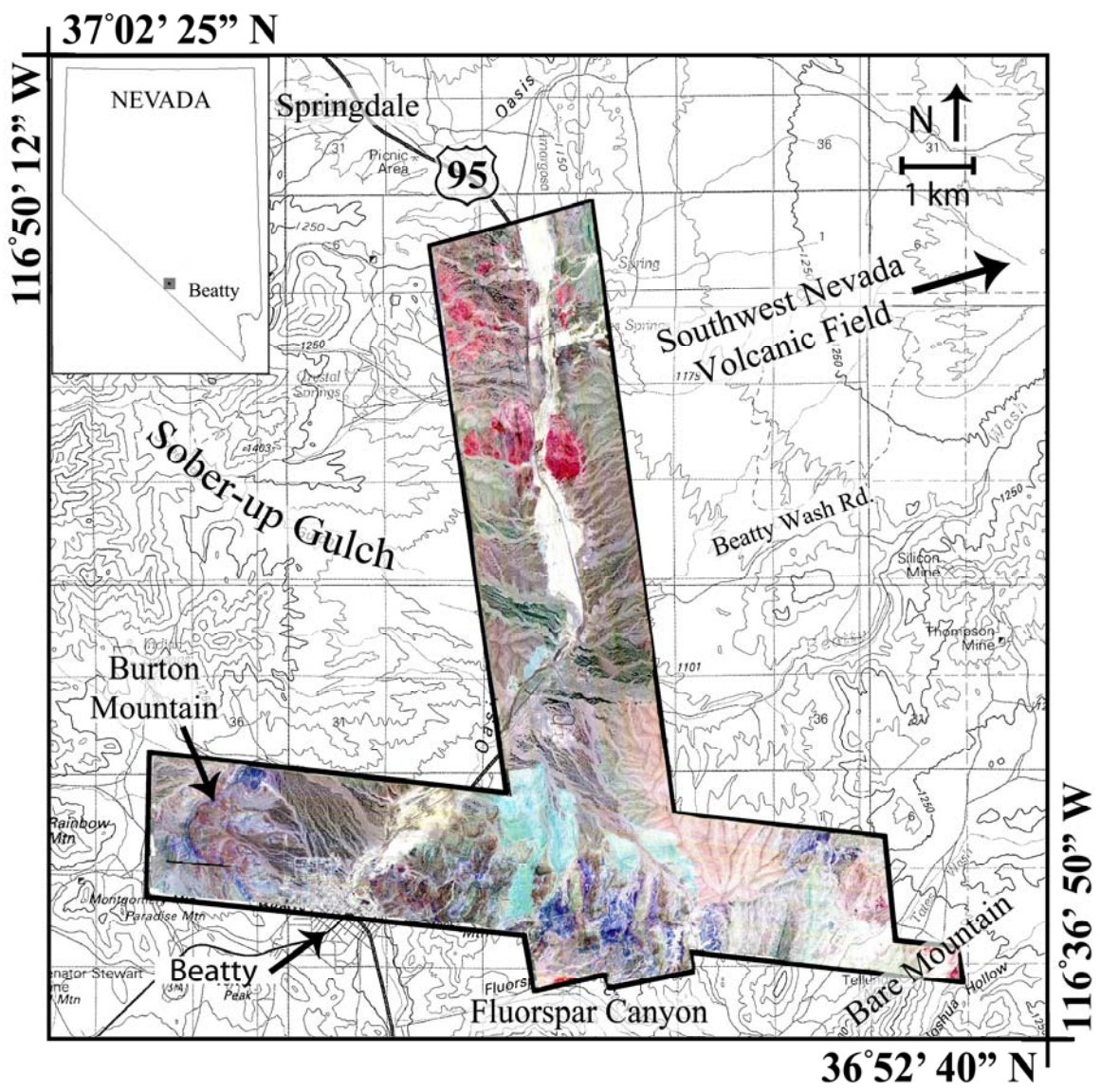




Figure 12.

Mineral map derived from analysis of SEBASS LWIR image data using bands ranging from 8 to 12  $\mu\text{m}$ . Background image is a high-resolution orthophoto.

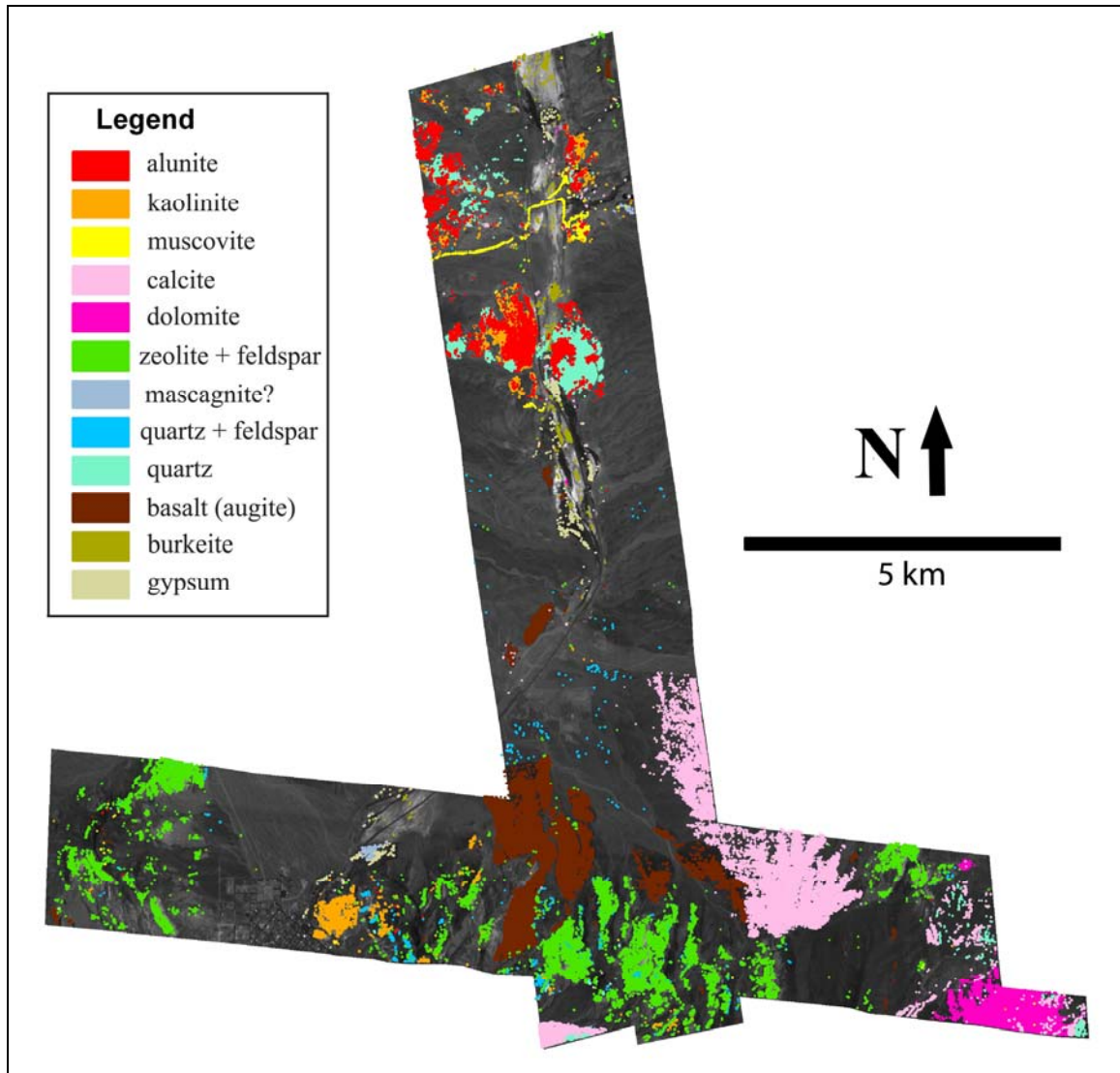


Figure 13.

At top-left, SWIR data band combination RGB: 2368 nm, 2325 nm, 2255 nm is used to emphasize carbonate minerals. A decorrelation stretch of this image is shown at bottom-left. These statistical methods to visually emphasize the carbonate mineral class are not successful due mixing of other minerals and/or vegetation, and resultant lack of spectral contrast. At top-right, LWIR data RGB band combination: 11.41  $\mu\text{m}$ , 11.28  $\mu\text{m}$ , 11.11  $\mu\text{m}$  is used to emphasize carbonate minerals. Magenta-toned pixels are noted near "A". A decorrelation stretch of this image is shown at bottom-right. An anomalous region is emphasized and is distinguished well from the surrounding surface areas. These pixels correspond to carbonaceous sinter material withdrawn from the sub-surface during installation of a well at the spring.

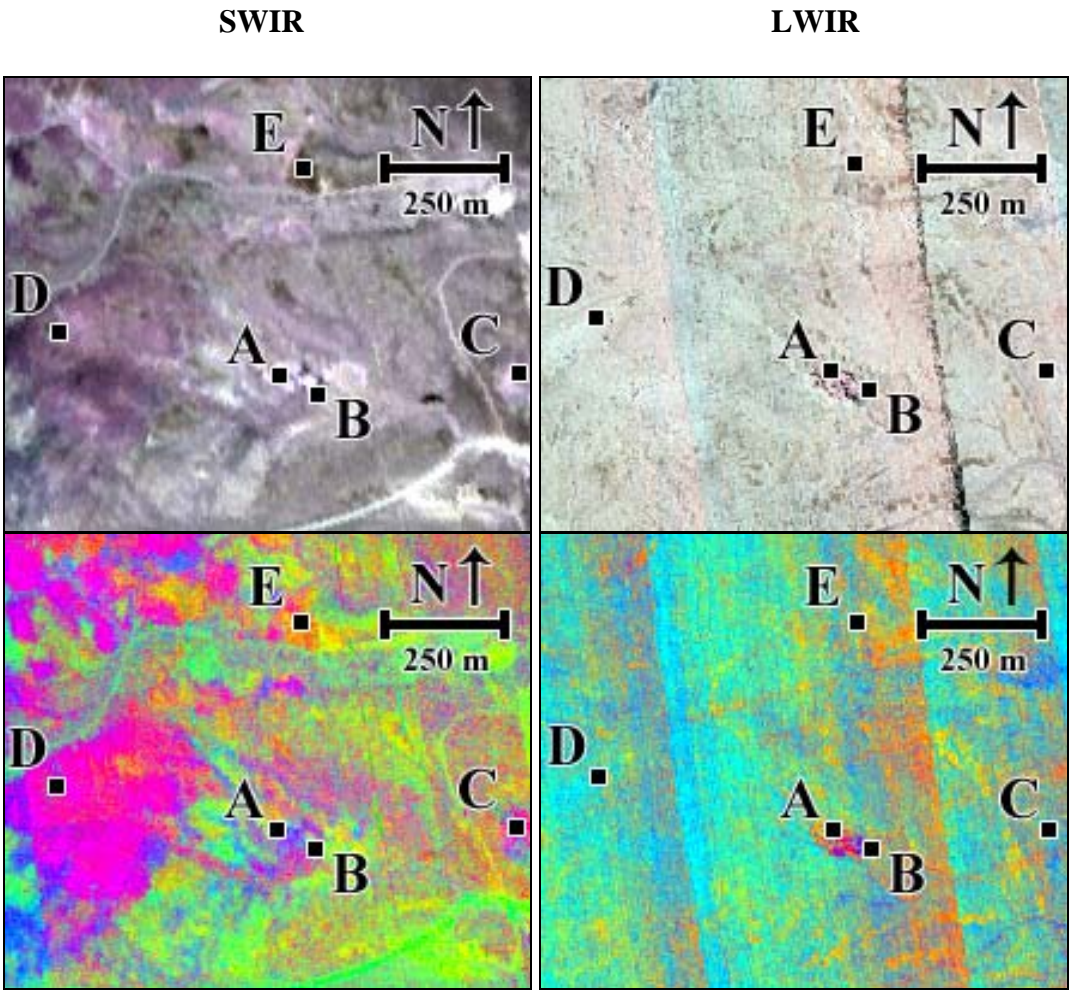


Figure 13. (continued).

At left, a plot of image data reflectance spectra is shown corresponding to indicated surface areas. Mixed vegetation, evaporite, and calcite (A), kaolinite (B), alunite 1 (C), alunite 2 (D), and mixed opaline silica (E) are shown. A LWIR image data spectra plot is shown at bottom-right. Mixed quartz and calcite (A), mixed opaline silica and kaolinite (B), alunite 1 (C), alunite 2 (D), and opaline silica (E) are shown.

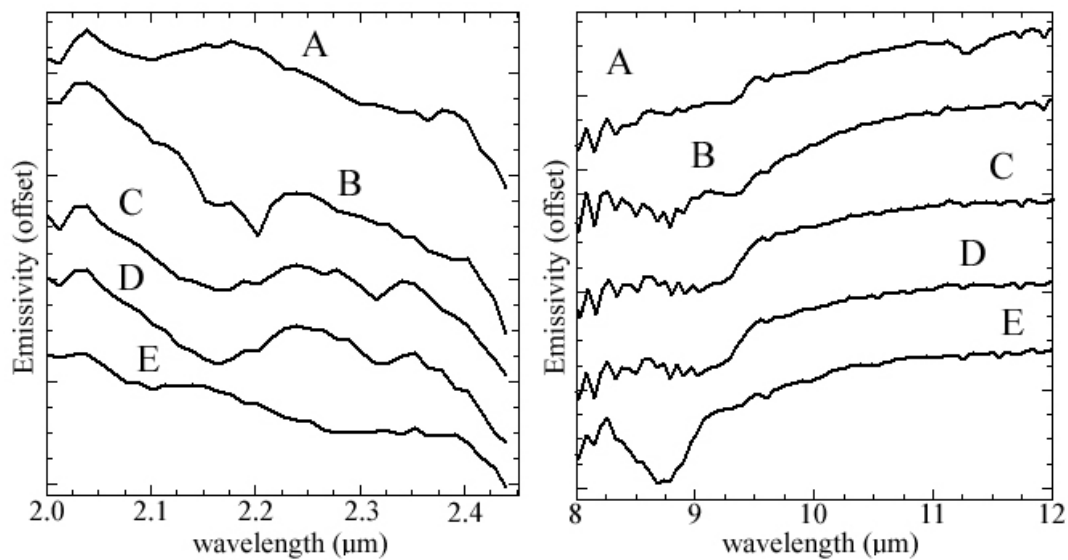


Figure 14.

A surface area covered by evaporative crusts was analyzed using the SWIR and LWIR image data. The SWIR spectra indicates features dominated by vegetation, while the LWIR emissivity spectra exhibits two apparent emission peaks, one at 10.04 and another at 11.37  $\mu\text{m}$ , which are indicative of burkeite. These features contrast with the surrounding surface materials, including vegetation. Laboratory XRD measurements identified the evaporite as a mix of halite, trona, and burkeite.

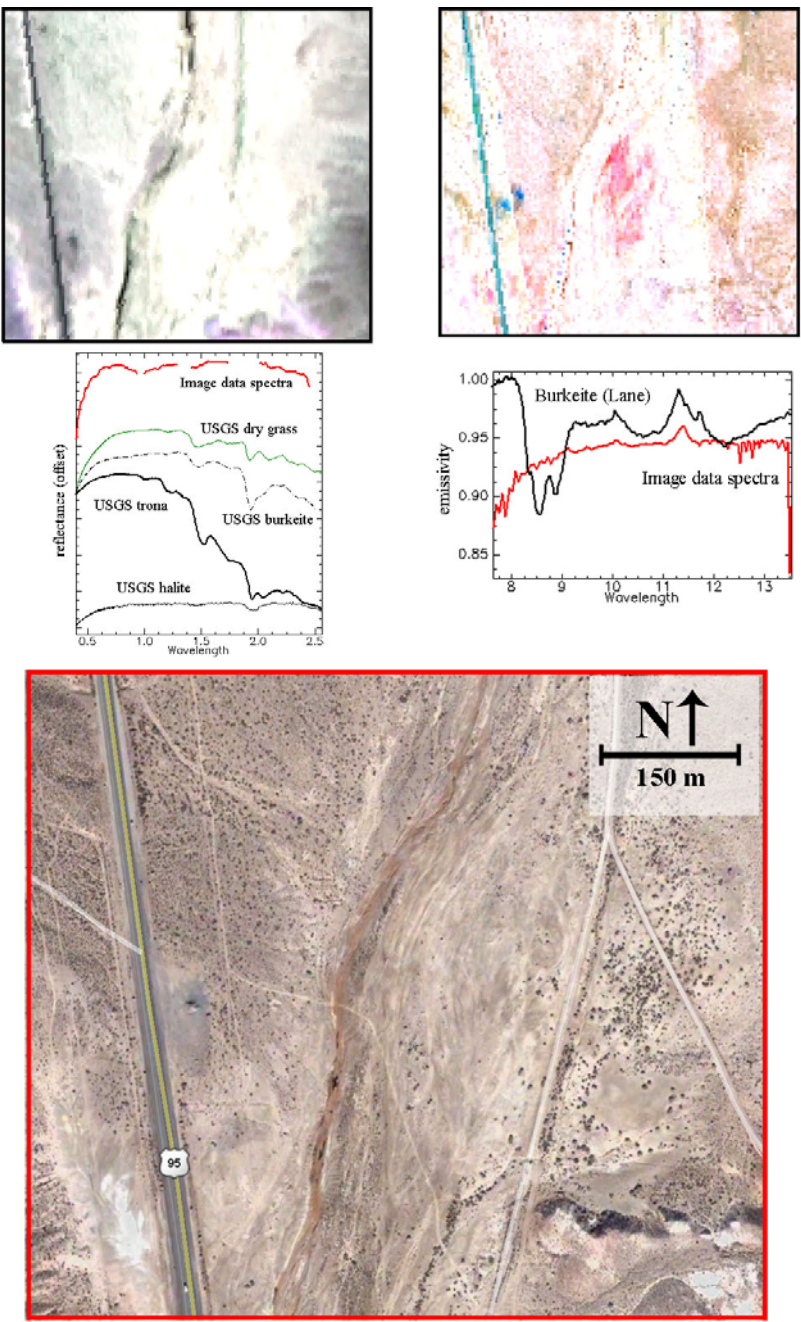


Figure 15.

A water discharge area northeast of the town of Beatty, Nevada exhibits precipitation of evaporite minerals. At left, a color-infrared band combination shows the general distribution of healthy vegetation (red), dryer vegetation (cyan and brown), and evaporite minerals (white). The SWIR image data spectra corresponding to these sulfo-salt crusts exhibit features that match dry grass more than a particular mineral. Also note that the 2.0 - 2.5  $\mu\text{m}$  wavelength range is spectrally flat. The LWIR image data spectra show a distinct emission minima at 8.94  $\mu\text{m}$  that were attributed to mascagsite  $((\text{NH}_4)_2\text{SO}_4)$ , a sulfate associated with geothermal systems. However, field samples were not able to be collected from this area to corroborate the mineral identification.

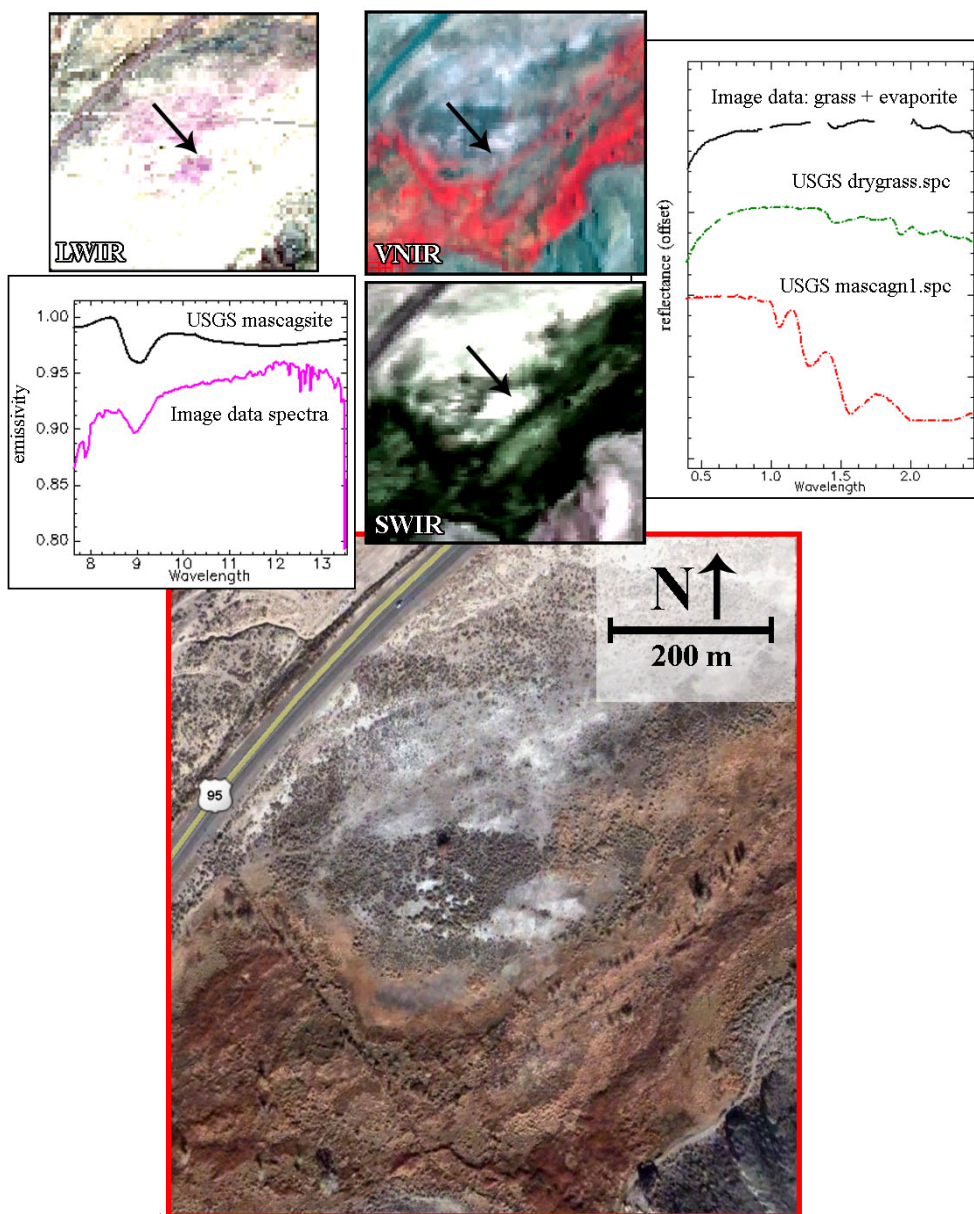


Figure 16.

A small patch of evaporite crust (less than 20 m<sup>2</sup>) was initially analyzed using the SWIR image data. The SWIR spectra did not exhibit absorption or slope features that were diagnostic of a particular mineral; rather dry vegetation was indicated. The same area was investigated with the LWIR data, and these image data spectra exhibited two prominent features: an emission minima centered at 8.66  $\mu\text{m}$  attributed to gypsum, and a narrow minima at 11.7  $\mu\text{m}$  that is diagnostic of trona.

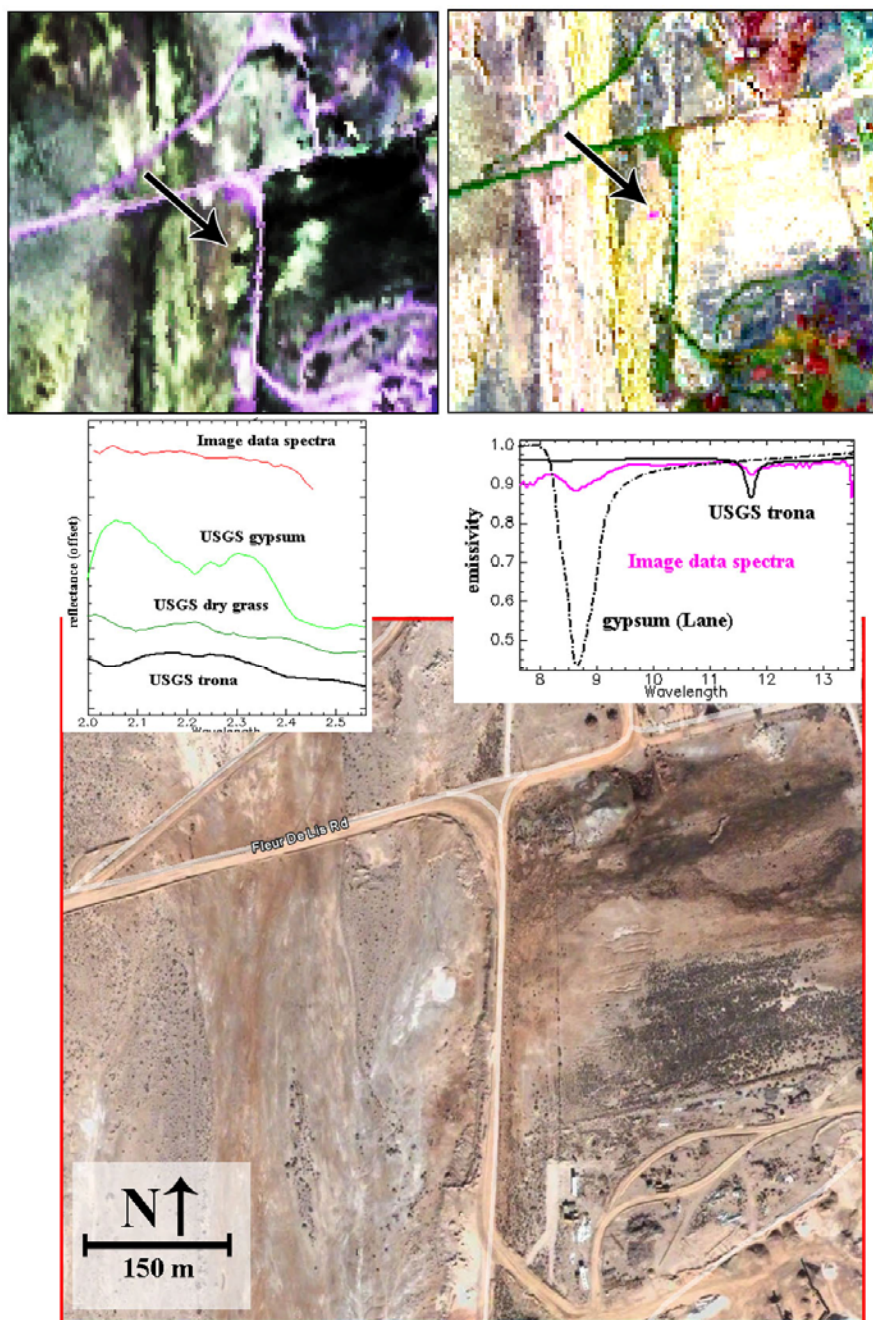


Figure 17.

SEBASS image data spectra of gravel (quartz- and muscovite-dominated) and zeolite tuff (feldspar-rich) are compared with pure emissivity spectra of corresponding rock constituents (from USGS spectral library). Narrow emission minima features at approximately  $9.6 \mu\text{m}$  are unique to both muscovite and feldspar (e.g., albite), and are observed in the image data spectra. Because the features overlap, determining which (or whether both) mineral(s) is present requires either examination of rock samples, or SWIR image data spectra to indicate if muscovite is either present or absent.

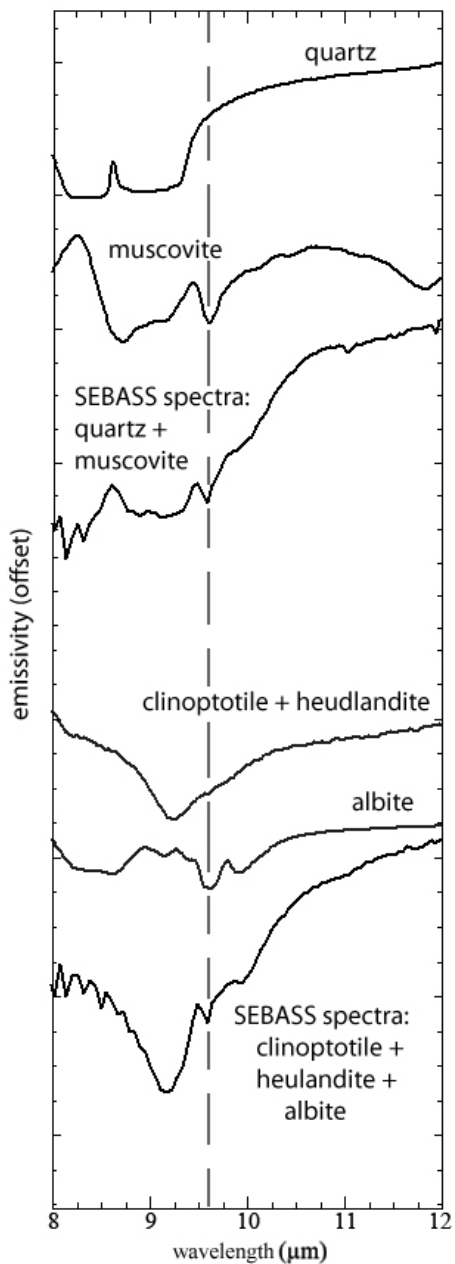
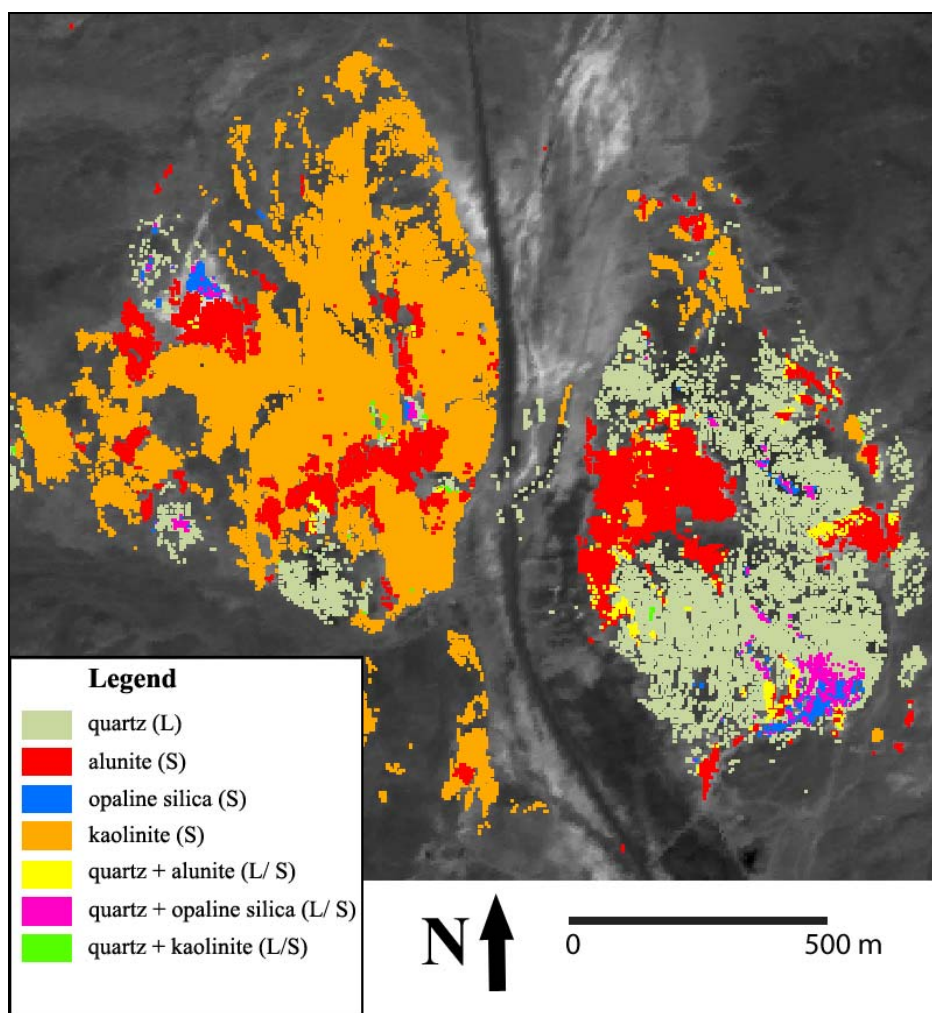


Figure 18.

Individual SWIR and LWIR mineral maps derived from image data analysis were input into a geographic information system (GIS). Union and intersection functions were used to indicate pixels that are associated with more than one mineral by either image data set. Mineral map layers were then output that retain integrity of individual mineral maps while adding to the comprehensive knowledge of surficial mineralogy for the study area. In the legend below, “S” indicates a SWIR image data-derived classification, while “L” indicates a LWIR-derived map. “L/S” indicates a jointly-created mineral map. The results of this simple comprehensive map indicate two areas where mixtures of opaline silica, quartz, and either kaolinite or alunite occur in close proximity to one another. Ground surveys of these areas indicated silicified alunite and silicified kaolinite outcrops.





## Chapter 6. Summary and Conclusions

The dissertation sought to investigate LWIR emittance multi- and hyper- spectral image data collected from ground, aerial, and spaceborne platforms to characterize the surficial mineralogic expression of rocks within Boundary Canyon, northeastern Death Valley National Park, California and compare both SWIR reflectance and LWIR emittance hyperspectral image data measurements collected over Oasis Valley, Nevada. Questions regarding the ability of LWIR image data to enhance the geologic knowledge of this well-studied corridor of Death Valley, as well as to understand the optimal wavelength ranges in which to best detect, identify, and map minerals in the diverse geologic environment of Oasis Valley, Nevada were posed to drive the research. Individual case studies produced analyses used to answer initially posed research questions that may be of interest to those in the geology and remote sensing communities.

### 6.1 Important aspects of the research

- 1) Ground-based SEBASS LWIR image data collected from the perspective of a field geologist were used to successfully map minerals associated with sedimentary and meta-sedimentary lithologies, including quartzite, dolomite, argillite, and marble. Quartzite was the most distinct mapped lithology, while muscovite-dominated argillite was more difficult to map, owing to the overlapping of diagnostic spectral features of muscovite and quartz, in addition to limited spatial representation of these thin beds in the data.
- 2) Aerial SEBASS image data were used to mineralogically characterize the Boundary Canyon Detachment Fault contact, drawing attention to the contrast between relatively

unmetamorphosed dolomite and metamorphosed calcite marble, as well as delineating pelitic schist associated with low-grade greenschist facies from amphibolite of medium-grade amphibolite facies.

3) Comparisons of ground- and aerially-collected SEBASS LWIR image data spectra demonstrated that the entire measured 7.5 - 13.6  $\mu\text{m}$  wavelength range was utilizable for mineral mapping in the ground data, while wavelength bands below 8 and above 12  $\mu\text{m}$  in the aerial data were generally dominated by atmospheric-related noise attributed to water vapor, and thus unusable. This distinction enabled the ground SEBASS data to better detect and map quartz using only bands coinciding with the secondary emission minima doublet in the 12 - 13  $\mu\text{m}$  range.

4) Hyperspectral-resolution emissivity spectra corresponding to lithologies within the Boundary Canyon detachment fault study area were resampled to multispectral resolution of MASTER and ASTER and then mapped with these image data. Amphibolite, a unique mineral identifier of exposed Johnnie Formation rocks was able to be identified and mapped with MASTER data, by using SEBASS classification images as a thresholding guide, thereby extending the map of this rock class to a larger area.

5) SWIR and LWIR image data demonstrated that minerals such as kaolinite, alunite, and zeolite are detectable in both wavelength ranges, but these data present different levels of complexity and effectiveness for mapping. The reflectance image data can provide quick and simple classification maps due to prominent, distinct absorptions, attributed to the lack of spectral mixtures; the emittance data exhibited additional silicate mineral

components (e.g., quartz and feldspar) in the spectra for these same measured surfaces, which varied in prominence from pixel to pixel, effectively increasing the time needed to analyze the data, and reducing the overall effectiveness of statistical mapping methods, as well as number of pixels mapped for the targeted minerals.

6) Carbonate mineral detection was shown to be enhanced in the LWIR data compared to the SWIR, as variability attributed to adjacent non-carbonate surface materials (e.g., alunite, opaline silica, and vegetation) effectively reduced spectral contrast of carbonate-rich materials. In contrast, features diagnostic of carbonate minerals in the LWIR did not overlap with other scene materials, resulting in quick and accurate identification and mapping of these classes.

## **6.2 Brief review of case studies**

In Chapter 2, analysis of ground-based LWIR image data collected at the late Proterozoic-early Paleozoic Hell's Gate outcrop indicated that each prominent lithology identified during field surveys could be remotely mapped based upon diagnostic spectral features. Quartzite, argillite, and dolomite comprised the major rock types within the outcrop. A limited exposure of marble was also remotely identified and mapped; during field mapping this rock type went unnoticed from surrounding dolomite. Analysis of emissivity spectra for each rock type indicated that the average emissivity value for diagnostic feature bands varied according to what mineral these were composed of. Quartz resulted in the lowest emissivity values for diagnostic feature bands, while muscovite, dolomite, and calcite produced less spectral contrast. However, the dolomite and calcite were more readily identified and separable during image data mapping than

muscovite, because they are characterized by narrow emission minima that do not overlap with other mineral-related spectral features. In contrast, diagnostic features of muscovite-dominated argillite overlapped with quartz, resulting in more frequent quartz-dominated spectra. Differing levels of rock resistance also played a significant role in differentiating these rocks. Quartzite was most resistant, dolomite was next most resistant, and argillite was least-resistant. The argillite beds were very thin and exhibited pronounced recession from between the more resistant beds. Cumulatively, these factors resulted in reduced overall indication of this lithology. A pixel-based mineral classification map was successfully generated which indicated the presence of each of these rock types.

In Chapter 3, analysis of aerial SEBASS LWIR data collected over the Boundary Canyon area indicated a relatively limited mineralogical diversity in comparison to the numerous outcropping lithologies identified in field surveys. Siliceous rocks such as quartzite, sandstone, conglomerate, and alluvium exhibited only minor differences in depth of emissivity values for diagnostic bands of quartz spectra, resulting in limited spectral delineation. Micaceous lithologies, including siltstone, schist, and slate also exhibited relatively similar spectra. However, carbonate-dominated lithologies such as limestone or marble, and dolomite were able to be spectrally separated. The integration of geologic unit boundary maps with image data-derived mineral maps in a geographic information system allowed the combined information to enhance the understanding of local geology. A boundary mapped amid pixels of large dolomite and calcite marble units indicated the detachment fault between the Grapevine Mountains allochthon and Funeral Mountains autochthon. In addition, transition between greenschist and amphibolite

metamorphic facies was able to be detected and mapped via muscovite (associated with pelitic schist) and hornblende (associated with amphibolite), respectively.

In Chapter 4, a comparison of ground- and aerial-SEBASS LWIR image data was used to determine what repercussions GIFOV and atmospheric effects had upon mineral detection and mapping in the 7.5 - 13.5  $\mu\text{m}$  wavelength range. Emissivity spectra derived from quartz-dominated pixels of both image data sets were directly compared. The ground-based emissivity spectra indicated low contribution from atmospheric components, and subsequently quartz could be mapped using only bands corresponding to a secondary doublet in the 12 - 13.5  $\mu\text{m}$  range. In the aerial data, the quartz-dominated emissivity spectra closely matched ground measurements within the 8 - 12  $\mu\text{m}$  wavelength range. However band values matching or indicating surface mineralogy were instead diminished by atmospheric water vapor in the 7.5 - 8  $\mu\text{m}$  range and  $\text{CO}_2$  in the 12 - 13.5  $\mu\text{m}$  wavelength range, effectively restricting full utilization of image data. Because ground-based SEBASS LWIR data can better utilize all 128 bands measured in the 7.5 - 13.5  $\mu\text{m}$  range, these data may enhance mapping of minerals or other surface materials that possess diagnostic features in these outlying wavelength ranges.

Resampling of hyperspectral mineral spectra identified during analysis of ground data to the multispectral resolutions of MASTER and ASTER helped to determine that these associated lithologies were spectrally distinctive enough to facilitate remote mapping of some minerals using these lower spectral resolution image data. Specific carbonate minerals were not able to be differentiated using either MASTER or ASTER, however, silica-, clay-, and general carbonate-rich surfaces were able to be distinguished with both data sets. Amphibolite was able to be mapped with MASTER and effectively

extend the surface area of this mapped mineral class from the limited coverage of the SEBASS data set that was used as reference. Because this class was not detected or mapped with ASTER, and these rocks are relatively limited in exposures, spatial and radiometric resolution were deemed to be a constraining factor.

In Chapter 5, surficial mineralogy was comprehensively investigated in the Oasis Valley study area using SWIR and LWIR image data. SWIR data were analyzed to map calcite, dolomite, muscovite/montmorillonite, alunite, kaolinite, opaline silica, and zeolite. Analysis of LWIR image data resulted in maps of quartz, kaolinite, opal, calcite, dolomite, alunite, burkeite, gypsum, trona, and muscovite/montmorillonite. Comparison of the respective mineral maps and reflectance and emissivity spectra indicated that certain minerals were better detected in one data set than another. These included muscovite, kaolinite, alunite, and opaline silica in the SWIR data. In the LWIR data, burkeite, calcite, dolomite, gypsum + trona, and quartz were best detected. The presence of minerals with overlapping diagnostic features in the LWIR data occurred for alunite, kaolinite, opal, and quartz, where quartz dominated these mixtures. In addition, unconsolidated clays such as muscovite were not mapped with as much success using the LWIR data. Silicate mineral mixture components associated with Tertiary volcanic units were identified with LWIR data, however these increased the complexity involved in analysis.

Both data sets were used to increase overall confidence in mapped minerals. When used together, areas of complex mineralogy, such as the acid-sulfate alteration center near Bailey's Hot Springs, could be better understood. In this example, alunite, kaolinite, and opaline silica were mapped with the SWIR data, while quartz was mapped

in the LWIR. The results were then input into a geographical information system (GIS) and mineral map layers were integrated to yield pixels with the presence of multiple minerals (e.g., quartz + alunite; quartz + kaolinite; and quartz + opaline silica). This process resulted in better delineation of clay-rich areas, including kaolinite and alunite, from areas of silicified counterparts, which could not be distinguished well through analysis of a single data set due to the overlapping of features with quartz in the 9  $\mu\text{m}$  region. Significant additional field work would likely be needed to spectrally delineate, map, and corroborate these minerals using a single data set.

Certain small instances of carbonate minerals were found to be better identified with the LWIR data; the SWIR data were limited to higher albedo materials, as well as instances comprising a larger surface area. SWIR spectra of vegetation was shown to be similar in spectral slope to weak calcite, which presented detection problems for these often intermingled surface materials. The LWIR data were particularly useful in finding small instances of carbonate minerals that were either pure calcite or dolomite, or even when mixed with other minerals, such as quartz. Decrease in sensor detector sensitivity in the far SWIR, where carbonate absorptions occur, and the overlapping spectral features of other minerals or mixtures that may be associated with carbonates, comparatively reduced the effectiveness of SWIR detection and mapping. In the LWIR, no minerals were found that exhibited overlapping diagnostic emission features and introduced ambiguity to the identification of carbonate minerals.

### 6.3 Implications of research

Ground-based LWIR measurements can provide unique benefits for remote sensing of geology. These image data can be used at close distance from an outcrop surface to spatially resolve small features and identify mineralogically unique areas that may be visually inconspicuous. The relatively low atmospheric contribution observed in these data also provides enhanced spectral utility. These measurements are of particular use for characterizing rocks that are horizontally-ordered, such as sedimentary beds, or when a targeted rock is otherwise found underlying another rock unit. Thus, these data would be of use in an environment that is spatially limited, yet mineralogically diverse and dynamic. This could include an open pit mine, whereby walls are continually excavated, and rock material are usually geochemically assayed to test if targeted minerals are being optimally collected and processed. An imaging spectrometer based on-site may assist in providing mineralogical assessments of freshly-exposed surfaces, resulting in immediate information for decision-makers.

Aerial LWIR surveys of sedimentary and meta-sedimentary lithologies that generally exhibit homogenous bulk mineralogies can still provide useful information to the geologist. Silica-, clay-, and carbonate-dominated rocks were able to be mapped, and although these were not necessarily indicative of a particular lithology, the location and juxtaposition of clusters of mapped minerals were useful in delineating sharp boundaries indicative of lithologic transitions, and in the example given in the research, a detachment fault contact. Visually-similar carbonate rocks can be assessed in the field using hydrochloric acid tests, however the hyperspectral image data provide the benefit of mapping these units quickly and quantifiably, allowing a geologist to make more



intelligent use of limited field time. The 4 m spatial resolution of these data was a good compromise between surface area coverage and resolving smaller outcrops. The presence of metamorphic index minerals that composed a low percentage of total composition of pelitic schists were noted in a previous study (Labotka, 1980) and evaluated in petrographic analyses. Minerals such as biotite, staurolite, and garnet were not observed via spectral features in laboratory or image data emissivity spectra, thus suggesting a basic limitation for the remote sensing of these minerals within the study area.

Spatial and radiometric resolutions were found to be more important to delineating broad lithologic units in the DVNP study area than spectral resolution. Hyperspectral data-derived mineral spectra resampled to multispectral resolution exhibited sufficient variability to be identifiable in MASTER and ASTER data. However, limited exposure of targeted surface material prevented amphibolite from being mapped with ASTER. Thus future spaceborne emittance-measuring sensors, if mapping similar rocks to this study area, should collect image data at the maximum radiometric and spatial resolutions possible.

Reflectance and emittance image data sets are complementary and can be used to corroborate and further understand unfamiliar spectral features, thereby reducing ambiguity of a mapped class. These combined data increase overall ability to characterize a surface area by recognition of more mineralogically-complex surface compositions that may otherwise be assumed basic or homogenous.

## 6.4 Recommendations and conclusion

Ground-collected LWIR hyperspectral data can be a tremendous tool for particular geologic applications, but the data are relatively limited. Newer portable LWIR hyperspectral sensors, such as the FIRST (Chamberland et al., 2005), provide these data, and suggest that future surveys that utilize these data and analyses will grow. Parameters of these data collections and calibration of these data should be further researched. First, atmospheric correction of these radiance data should be examined to more aptly suit the differences in geometric relationships between ground and aerial TIR measurements, as current ISAC routines were created for aerial data. Next, the repercussions of increasing distance between sensor and measured surfaces should be understood to result in optimal TIR data collection and quality of mineral-related emittance spectra. As the Earth's atmosphere is thickest at the surface, pathlength will generally have a more profound effect from this horizontal perspective than for a measurement made at equal distance from surface to aerial sensor.

Aerially-collected SEBASS image data measurements used in this research were measured over a limited area of Boundary Canyon, and thus only a small portion of the Funeral Mountains metamorphic core complex was characterized. It is recommended that these data be collected in the area stemming from Boundary Canyon southeastward to Winter's Peak, thereby collecting emittance data over the extent of the Funeral Mountains metamorphic core complex, and determining if outcrops here exhibit higher percentages of minerals indicative of various facies.

The further use of jointly-collected VNIR/SWIR and LWIR image data is recommended for comprehensive mineral surveys. These data sets should be noted for

their extremely large sizes. As a result, logical and efficient data processing methodologies should be implemented to address the opportunity cost of computer processing time. Further study of optimal wavelength ranges in which to identify and map minerals should focus on seasonal effects, which may change the prominence of diagnostic spectral features, and result in variable mapping capability at different times of the year, or weather conditions.

**Chapter 7. Appendices**


## Appendix I. Mineral Chemical Formulas

Name	Formula
albite	$\text{NaAlSi}_3\text{O}_8$
almandine	$\text{Fe}_3\text{Al}_2(\text{SiO}_4)_3$
alunite	$\text{KAl}_3(\text{SO}_4)_2(\text{OH})_6$
analcime	$\text{NaAlSi}_2\text{O}_6 \cdot \text{H}_2\text{O}$
anorthite	$\text{CaAl}_2\text{Si}_2\text{O}_8$
augite	$(\text{Ca}, \text{Na})(\text{Mg}, \text{Fe}, \text{Al})(\text{Si}, \text{Al})_2\text{O}_6$
biotite	$\text{K}(\text{Mg}, \text{Fe})_2(\text{AlSi}_3\text{O}_{10})(\text{F}, \text{OH})_2$
burkeite	$\text{Na}_6(\text{SO}_4)_2(\text{CO}_3)$
calcite	$\text{CaCO}_3$
chlorite	$(\text{Mg}, \text{Fe})_3(\text{SiAl})_4\text{O}_{10}(\text{OH})_2 \cdot (\text{Mg}, \text{Fe})_3(\text{OH})_6$
clinochlore	$(\text{Mg}_5\text{Al})(\text{AlSi}_3)\text{O}_{10}(\text{OH})_8$
clinoptilolite	$(\text{Na}, \text{K}, \text{Ca})_{2-3}\text{Al}_3(\text{Al}, \text{Si})_2\text{Si}_{13}\text{O}_{36} \cdot 12(\text{H}_2\text{O})$
cristobalite	$\text{SiO}_2$
dolomite	$\text{CaMg}(\text{CO}_3)_2$
goethite	$\text{FeO}(\text{OH})$
grossular	$\text{Ca}_3\text{Al}_2(\text{SiO}_4)_3$
gypsum	$\text{CaSO}_4 \cdot 2\text{H}_2\text{O}$
halite	$\text{NaCl}$
hematite	$\text{Fe}_2\text{O}_3$
heulandite	$(\text{Ca}, \text{Na})_{2-3}\text{Al}_3(\text{Al}, \text{Si})_2\text{Si}_{13}\text{O}_{36} \cdot 12\text{H}_2\text{O}$
hornblende	$\text{Ca}_2(\text{Mg}, \text{Fe}, \text{Al})_5(\text{Al}, \text{Si})_8\text{O}_{22}(\text{OH})_2$
illite	$(\text{K}, \text{H}_3\text{O})(\text{Al}, \text{Mg}, \text{Fe})_2(\text{Si}, \text{Al})_4\text{O}_{10}[(\text{OH})_2, (\text{H}_2\text{O})]$
kaolinite	$\text{Al}_2\text{Si}_2\text{O}_5(\text{OH})_4$
magnesio-hornblende	$\text{Ca}_2[(\text{Mg}, \text{Fe}^{2+})_4\text{Al}](\text{Si}_7\text{Al})\text{O}_{22}(\text{OH})_2$
margarite	$\text{CaAl}_2(\text{Al}_2\text{Si}_2)\text{O}_{10}(\text{OH})_2$
mascagnite	$(\text{NH}_4)_2\text{SO}_4$
microcline	$(\text{KAlSi}_3\text{O}_8)$
mirabilite	$\text{Na}_2\text{SO}_4 \cdot 10\text{H}_2\text{O}$
molybdophyllite	$\text{Pb}_2\text{Mg}_2[(\text{OH})_2\text{Si}_2\text{O}_7]$
montmorillonite	$(\text{Na}, \text{Ca})(\text{Al}, \text{Mg})_6(\text{Si}_4\text{O}_{10})_3(\text{OH})_6 \cdot n\text{H}_2\text{O}$
muscovite	$\text{KAl}_2(\text{AlSi}_3\text{O}_{10})(\text{F}, \text{OH})_2$
opaline silica	$\text{SiO}_2 \cdot n\text{H}_2\text{O}$
orthoclase	$\text{KAlSi}_3\text{O}_8$
paragonite	$\text{NaAl}_2(\text{AlSi}_3\text{O}_{10})(\text{OH})_2$
quartz	$\text{SiO}_2$
sanidine	$(\text{K}, \text{Na})(\text{Si}, \text{Al})_4\text{O}_8$
serpentine	$(\text{Mg}, \text{Fe})_3\text{Si}_2\text{O}_5(\text{OH})_4$
smectite	$(\text{Ca}, \text{Na})(\text{Al}, \text{Mg})_6(\text{Si}_4\text{O}_{10})_3(\text{OH})_6 - n\text{H}_2\text{O}$
spessartine	$\text{Mn}(\text{II})_3\text{Al}_2(\text{SiO}_4)_3$
staurolite	$(\text{Fe}^{2+}, \text{Mg})_2\text{Al}_9(\text{Si}, \text{Al})_4\text{O}_{20}(\text{O}, \text{OH})_4$
sulfur	$\text{S}$
trona	$\text{Na}_3\text{H}(\text{CO}_3)_2 \cdot 2\text{H}_2\text{O}$
zeolite	$\text{Na}_2\text{Al}_2\text{Si}_3\text{O}_{10} \cdot 2\text{H}_2\text{O}$

## Appendix II. Mineral spectra used from public spectral libraries

Chapter	Figure	Mineral/ material	Library	$\lambda$ Range	Spectra number
2	6	quartz	ASU	8 - 12 $\mu\text{m}$	quartz479
4	6	quartz	USGS	8 - 12 $\mu\text{m}$	19086, GDS74
	“	chlorite	USGS	8 - 12 $\mu\text{m}$	4862, SMR-13.A
	“	muscovite	USGS	8 - 12 $\mu\text{m}$	15072, GDS113
	“	albite	USGS	8 - 12 $\mu\text{m}$	469, HS66.3B
5	14	dry grass	USGS	0.4 - 2.5 $\mu\text{m}$	drygrass.spc
	“	burkeite	Evaporites	0.4 - 2.5 $\mu\text{m}$	burkeite.txt
	“	halite	Evaporites	0.4 - 2.5 $\mu\text{m}$	halite.txt
	“	trona	Evaporites	0.4 - 2.5 $\mu\text{m}$	trona.txt
	“	burkeite	Lane	8 - 12 $\mu\text{m}$	S71
5	15	dry grass	USGS	0.4 - 2.5 $\mu\text{m}$	drygrass.spc
	“	mascagnite	USGS	0.4 - 2.5 $\mu\text{m}$	mascagn1.spc
	“	mascagnite	USGS	8 - 12 $\mu\text{m}$	13468, GDS65
5	16	dry grass	USGS	0.4 - 2.5 $\mu\text{m}$	drygrass.spc
	“	gypsum			gypsum1.spc
	“	trona	Evaporites	0.4 - 2.5 $\mu\text{m}$	trona.txt
	“	trona	USGS	8 - 12 $\mu\text{m}$	23174, GDS148
	“	gypsum	USGS	8 - 12 $\mu\text{m}$	HS333
5	17	quartz	USGS	8 - 12 $\mu\text{m}$	19086, GDS74
	“	muscovite	USGS	8 - 12 $\mu\text{m}$	15072, GDS113
	“	clinoptolite (50%)	USGS	8 - 12 $\mu\text{m}$	5908, GDS2
	“	heulandite (50%)	USGS	8 - 12 $\mu\text{m}$	9800, GDS3
	“	albite	USGS	8 - 12 $\mu\text{m}$	469, HS66.3B

## Appendix III. Permit for field work in Death Valley National Park

DEATH VALLEY NATL P		12:33:56 p.m. 02-19-2010		2 / 3	
 <p><b>SCIENTIFIC RESEARCH AND COLLECTING PERMIT</b> Grants permission in accordance with the attached general and special conditions. United States Department of the Interior National Park Service Death Valley NP</p>			<p>Study#: DEVA-00207 Permit#: DEVA-2008-SCI-0037 Start Date: Jul 18, 2008 Expiration Date: Aug 15, 2008 Coop Agreement#: n/a Optional Park Code: n/a</p>		
<b>Name of principal investigator:</b>					
Name: Zan Aslett Phone: 7757704102 Email: n/a					
<b>Name of institution represented:</b>					
University of Nevada - Reno					
<b>Co-Investigators:</b>					
No co-investigators					
<b>Project title:</b>					
Study of stratigraphy at the Hell's Gate outcrop with ground-based thermal-infrared image data					
<b>Purpose of study:</b>					
To find the sensitivity of ground-based hyperspectral TIR image data to detect particular minerals remotely.					
<b>Subject/Discipline:</b>					
Geo-Sedimentology / Stratigraphy					
<b>Locations authorized:</b>					
The Hell's Gate outcrop across from the Visitors Center (part of the Funeral Mountains)					
<b>Transportation method to research site(s):</b>					
I can walk to the outcrop from the Visitors Center					
<b>Collection of the following specimens or materials, quantities, and any limitations on collecting:</b>					
n/a					
<b>Name of repository for specimens or sample materials if applicable:</b>					
Repository type: Will be destroyed through analysis or discarded after analysis Objects collected: Sedimentary rocks in the Wood Canyon formation. Individual samples will be no more than a size of a pebble. I would like to take 1 sample per bed, which would total from 10 to 20 samples. These will all be taken along a transect which will be marked by a measuring tape from the top of the outcrop to the base.					
<b>Specific conditions or restrictions (also see attached conditions):</b>					
All data, reports and publications resulting from this study shall be provided to the park.					

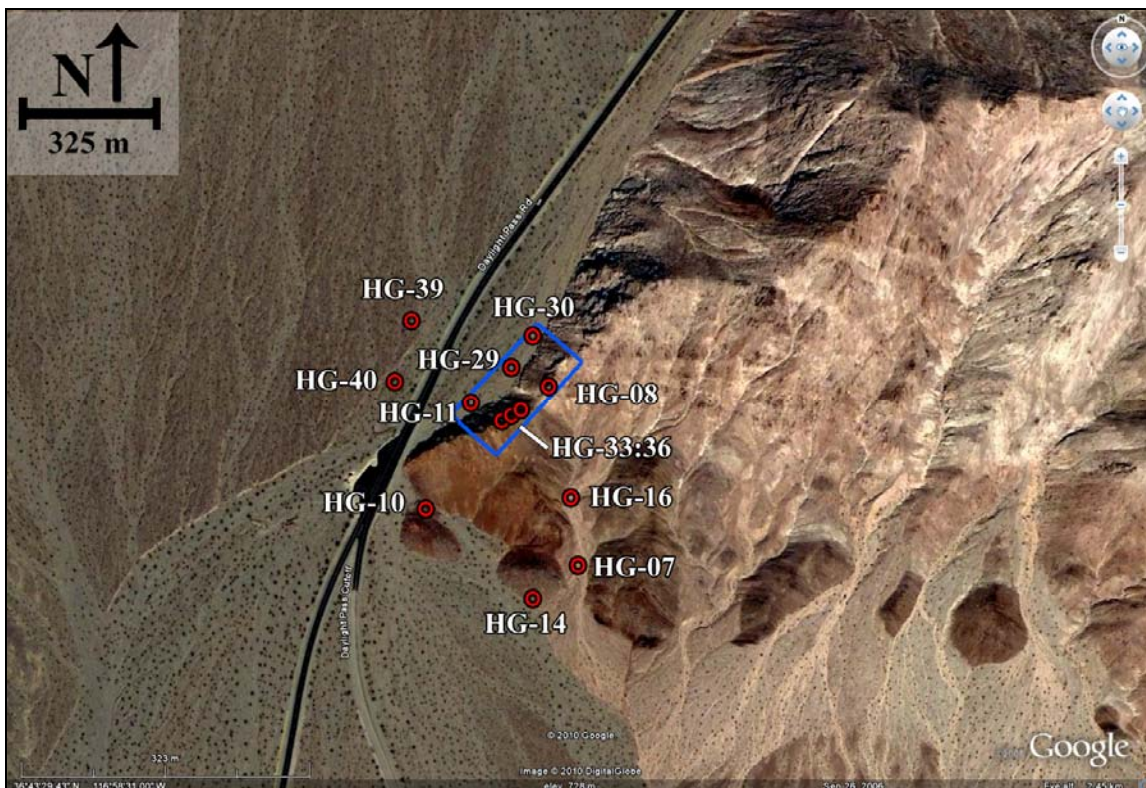
Appendix IV.  
Image data and rock sample information for field site 1: Hell's Gate

Ground-based SEBASS image data parameters

data set	bands	$\lambda$ range	GIFOV	data type	data size	dimensions
gates1.dat	128	7.5 - 13.5 $\mu\text{m}$	0.1 - 1 m (estimated)	BIP	115 MB	128 x 1800
gates1_emis.dat	128	7.5 - 13.5 $\mu\text{m}$	“	“	115 MB	“
gates1_temp.dat	1	temperature	“	-	90 Kb	“
gates2.dat	128	7.5 - 13.5 $\mu\text{m}$	“	“	115 MB	“
gates2_emis.dat	128	7.5 - 13.5 $\mu\text{m}$	“	“	115 MB	“
gates2_temp.dat	1	temperature	“	-	90 Kb	“
gates3.dat	128	7.5 - 13.5 $\mu\text{m}$	“	“	115 MB	“
gates3_emis.dat	128	7.5 - 13.5 $\mu\text{m}$	“	“	115 MB	“
gates3_temp.dat	1	temperature	“	-	90 Kb	“
gates_mosaic.dat	128	7.5 - 13.5 $\mu\text{m}$	“	“	260 MB	290 x 1800

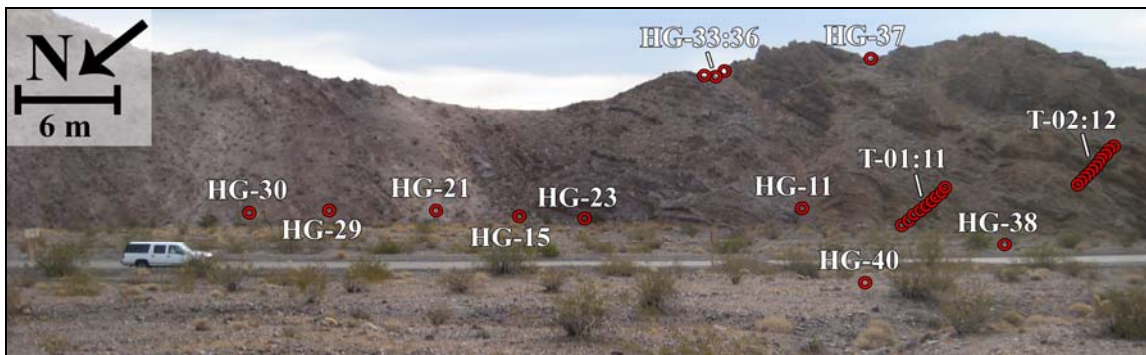


Sample location map



(from Google Earth, 2010)

Sample location map 2



Rock sample photographs

Quartzite



Desert varnish



Dolomite



Marble



Argillite



Alluvium



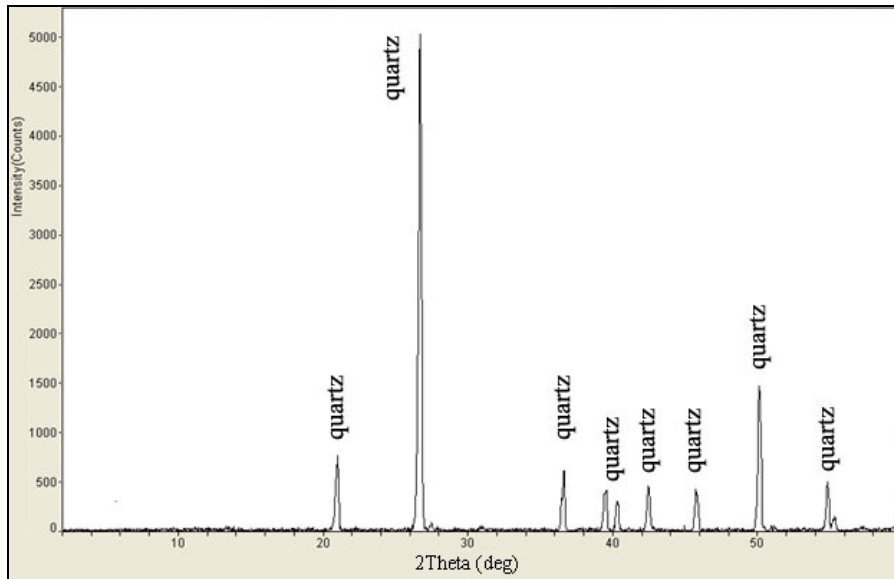
Sample identification number, description, location coordinates, and minerals identified in reflectance (0.4 - 2.45  $\mu\text{m}$ ), thermal-infrared (7.5 - 13.5  $\mu\text{m}$ ), and XRD measurements.

Sample number	Description	Latitude	Longitude	Minerals
T1-01	quartzite	36°43'28.95"N	116°58'35.09"W	goethite, kaolinite, muscovite, quartz
T1-02	silty stratified micaceous argillite	"	"	goethite, kaolinite, kaosmectite, microcline, muscovite, quartz
T1-03	quartzite with slight oxidized clay surface	"	"	goethite, kaolinite, quartz
T1-04	quartzite	"	"	goethite, muscovite, quartz
T1-05	silty stratified micaceous argillite	"	"	goethite, kaolinite, microcline, muscovite, quartz
T1-06	silty massive argillite	"	"	kaolinite, microcline, muscovite, quartz
T1-07	argillite	"	"	goethite, kaosmectite, microcline, muscovite, quartz
T1-08	quartzite	"	"	goethite, kaolinite, quartz
T1-09	silty stratified argillite	"	"	goethite, microcline, muscovite, quartz
T1-10	quartzite	"	"	dolomite, goethite, kaolinite, kaosmectite, quartz
T1-11	quartzite with slight oxidized clay surface	"	"	goethite, muscovite, quartz
T2-01	fractured quartzite with oxidized clay surface	36°43'28.75"N	116°58'35.06"W	goethite, quartz, muscovite
T2-02	quartzite with oxidized clay surface	"	"	calcite, dolomite, goethite, muscovite, quartz
T2-03	dolomite with quartz sand grains; oxidized clayey surface	"	"	dolomite, goethite, quartz, muscovite, quartz, paragonite
T2-04	quartzite	"	"	dolomite, goethite, quartz
T2-05	fissile silty argillite	"	"	goethite, kaolinite, muscovite, quartz
T2-06	dolomite with quartz sand grains; oxidized clayey surface	"	"	dolomite, goethite, quartz, muscovite
T2-07	dolomite with quartz sand grains; oxidized clayey surface	"	"	dolomite, goethite, kaolinite, microcline, muscovite, quartz
T2-08	dolomite with quartz sand grains; oxidized clayey surface	"	"	calcite, dolomite, goethite, quartz
T2-09	oxidized argillite	"	"	goethite, kaolinite, muscovite, orthoclase, quartz
T2-10	fractured quartzite with oxidized clay surface	"	"	goethite, quartz, muscovite
T2-11	fissile silty argillite	"	"	dolomite, goethite, kaolinite, muscovite, orthoclase, quartz
T2-12	dolomite with quartz sand grains; low oxidation	"	"	dolomite, goethite, muscovite, quartz
HG-01	stratified argillite	"	"	goethite, muscovite, quartz
HG-02	quartzite with feldspar grains and oxidation	"	"	feldspar, goethite, muscovite, quartz
HG-03	oxidized dolostone	"	"	dolomite, goethite, muscovite
HG-04	volcanic glass	36°43'28.59"W	116°58'37.22"W	opaline silica
HG-05	pelitic schist	"	"	chlorite, muscovite, quartz
HG-06	heavy desert varnish on dolomite	36°43'28.6"W	116°58'35.97"W	dolomite, goethite, muscovite
HG-07	clayey fractured quartzite	"	"	goethite, muscovite, quartz
HG-08	fractured quartzite	"	"	goethite, muscovite, quartz
HG-09	massive argillite	"	"	feldspar, goethite, muscovite
HG-10	dolostone with crystalline veining	"	"	dolomite, goethite, quartz

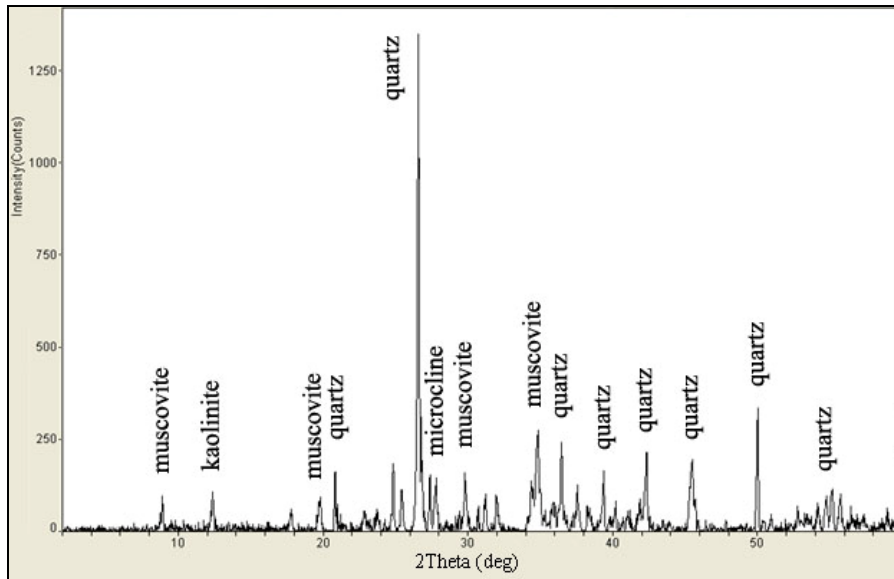
HG-11	fault gouge: clay-dominated; oxidized quartzite	36°43'29.74"N	116°58'33.45"W	goethite, muscovite, quartz
HG-12a	clayey, slightly oxidized conglomerate	36°43'29.12"W	116°58'34.91"W	goethite, kaolinite, quartz
HG-13	varnished quartzite - alluvium	"	"	goethite, muscovite, quartz
HG-14	oxidized dolostone	"	"	dolomite, goethite, muscovite
HG-15	heavily oxidized, clayey dolostone	"	"	dolomite, goethite, muscovite
HG-16	oxidized, platy argillite	"	"	feldspar, goethite, muscovite, quartz
HG-17	very clayey quartzite	"	"	goethite, muscovite, quartz
HG-18	oxidized massive dolostone	"	"	dolomite, goethite
HG-19	varnished dolostone	"	"	dolomite, goethite, muscovite
HG-20	porous, fissile, clayey conglomerate	"	"	goethite, kaolinite, quartz
HG-21	slightly fractured, clayey quartzite	"	"	goethite, muscovite, quartz
HG-22	heavily oxidized dolostone	"	"	dolomite, goethite, muscovite
HG-23	heavily oxidized, rough-surfaced dolostone	"	"	dolomite, goethite, muscovite
HG-24	gravel from canyon wash, primarily quartzite	"	"	goethite, quartz
HG-28	clayey fractured quartzite	"	"	goethite, muscovite, quartz
HG-29	pinkish, clayey sandstone or slightly metamorphosed quartzite	36°43'25.17"N	116°58'30.85"W	goethite, feldspar (undetermined type), muscovite, quartz
HG-30	quartzite with weathered feldspar - oxidized cavities	"	"	goethite, quartz
HG-33	sandy argillite on top of the outcrop	36°43'28.68"W	116°58'34.37"W	feldspar, goethite, muscovite, quartz
HG-34	quartzite on top of the outcrop	"	"	muscovite, quartz
HG-35	varnished quartzite on top of the outcrop	"	"	goethite, muscovite, quartz
HG-36	smooth-surfaced dolostone on top of the outcrop	"	"	dolomite, goethite, muscovite
HG-37	rough-surfaced dolostone on top of the outcrop	"	"	dolomite, goethite, muscovite
HG-38	newer incision at base of outcrop - smaller pebbles	36°43'29.92"N	116°58'34.25"W	goethite, quartz
HG-39	older alluvium in wash - larger pebbles	36°43'31.29"N	116°58'38.45"W	goethite, muscovite, quartz
HG-40	older alluvium in wash - larger pebbles	36°43'33.29"N	116°58'38.65"W	goethite, muscovite, quartz

## XRD measurements for mineralogically unique rock samples

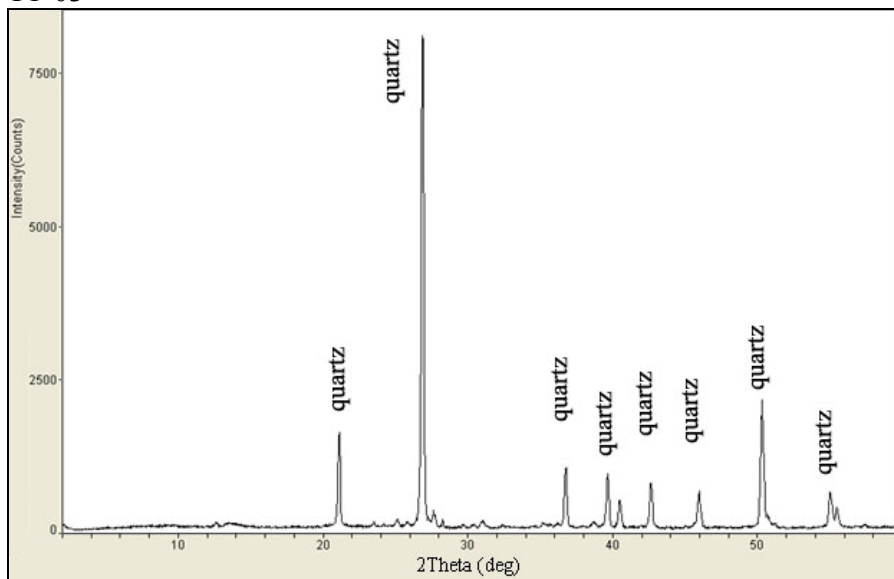
T1-01



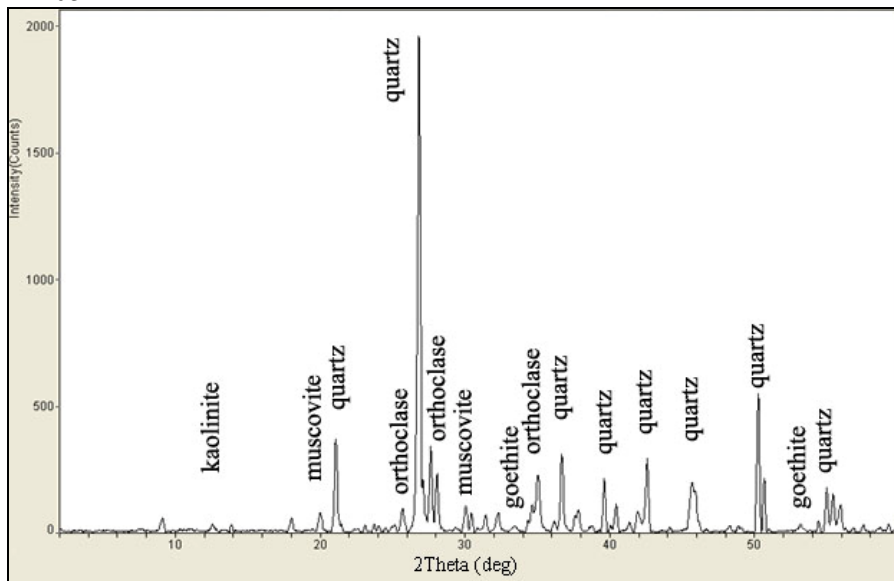
T1-02



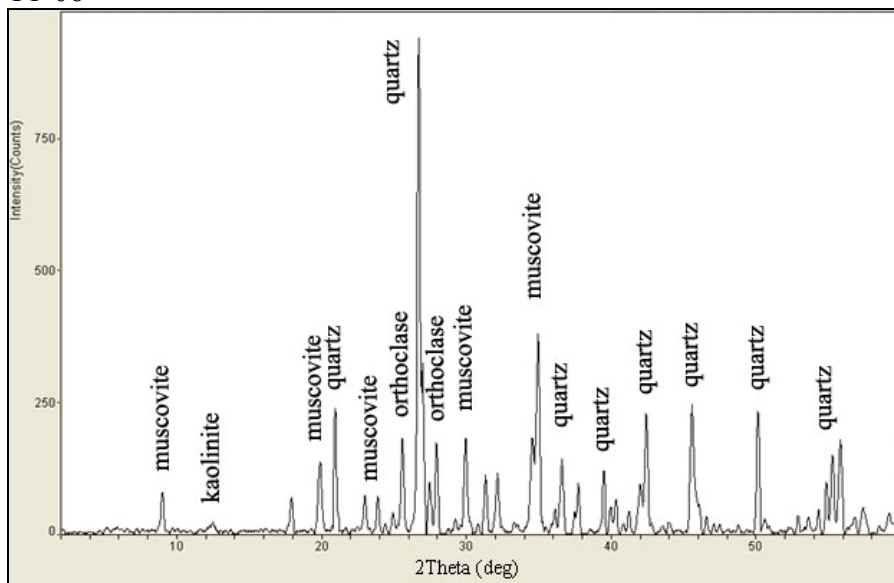
T1-03



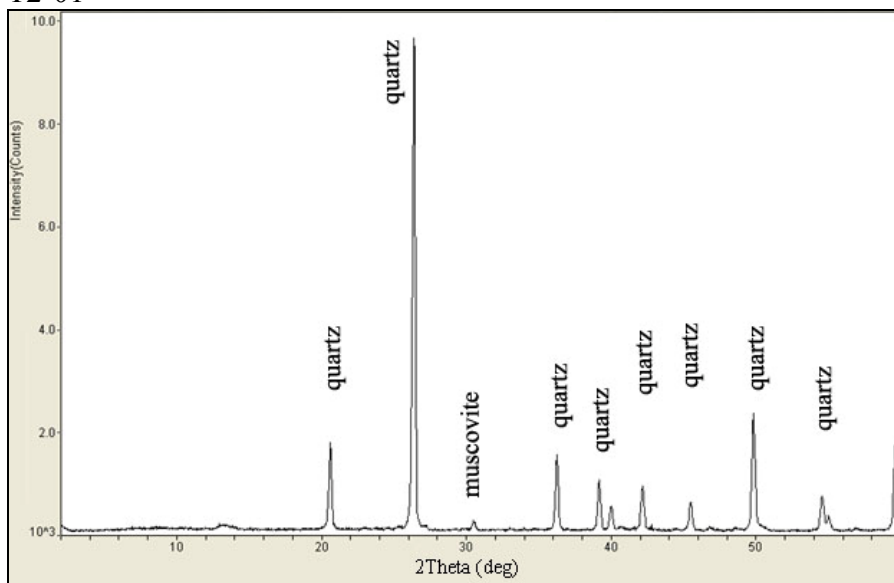
T1-05



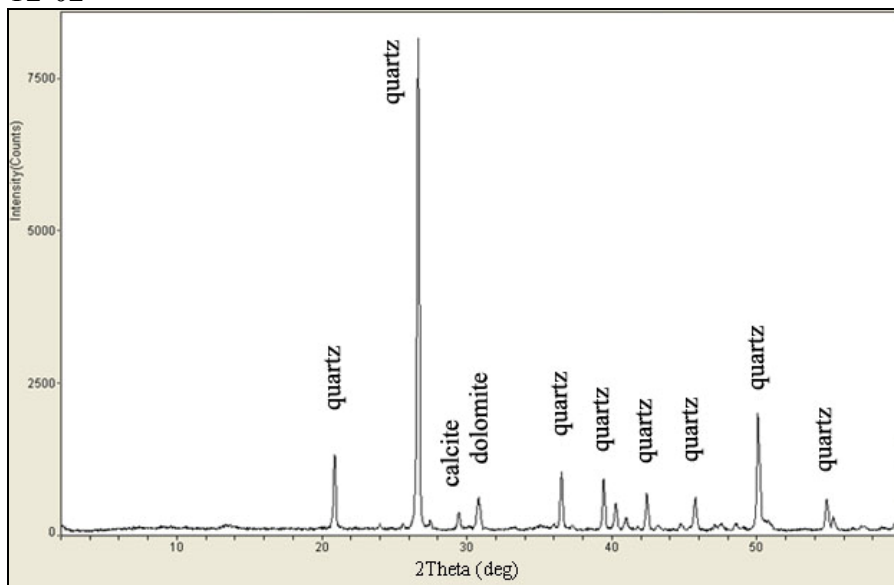
T1-06



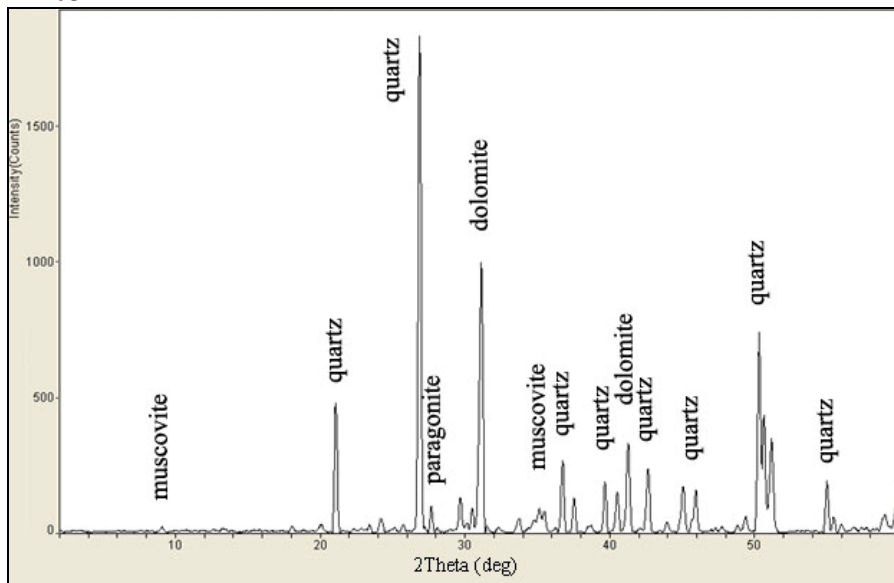
T2-01



T2-02

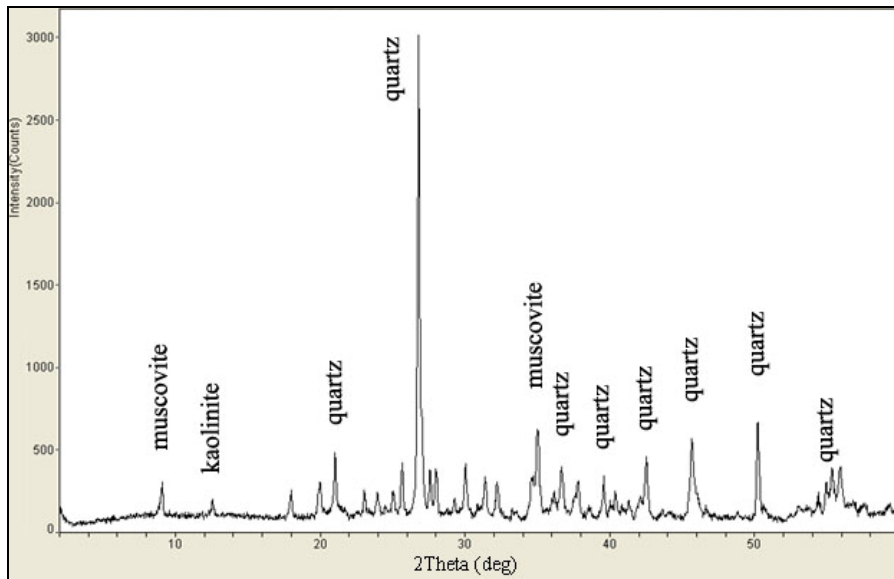


T2-03

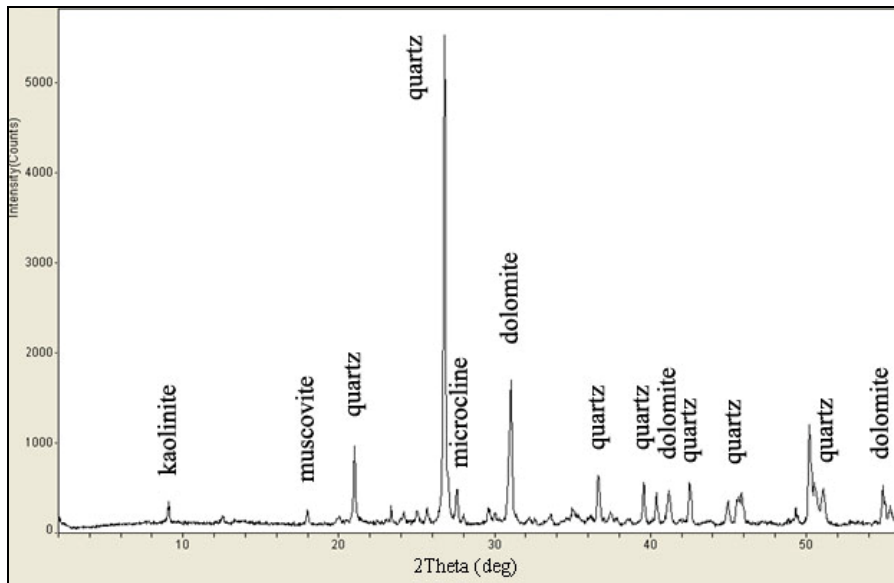




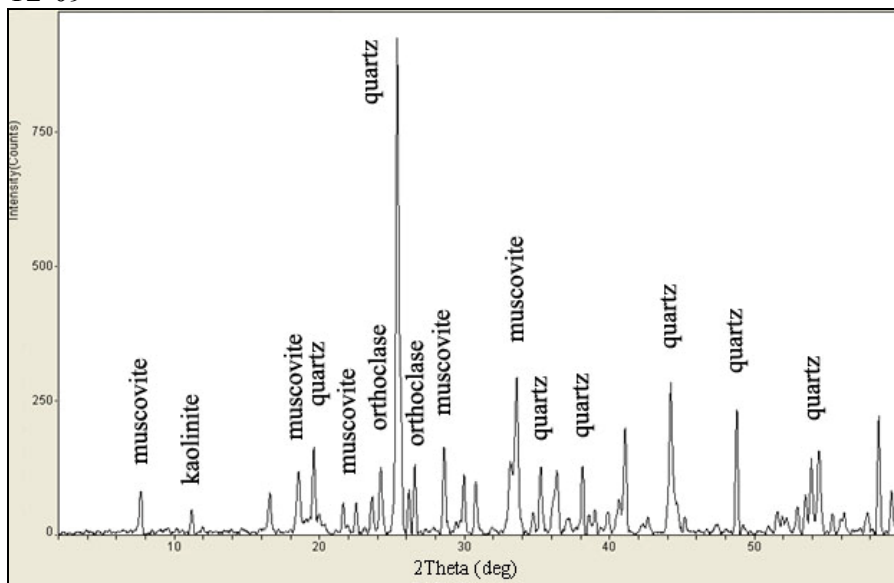
T2-05



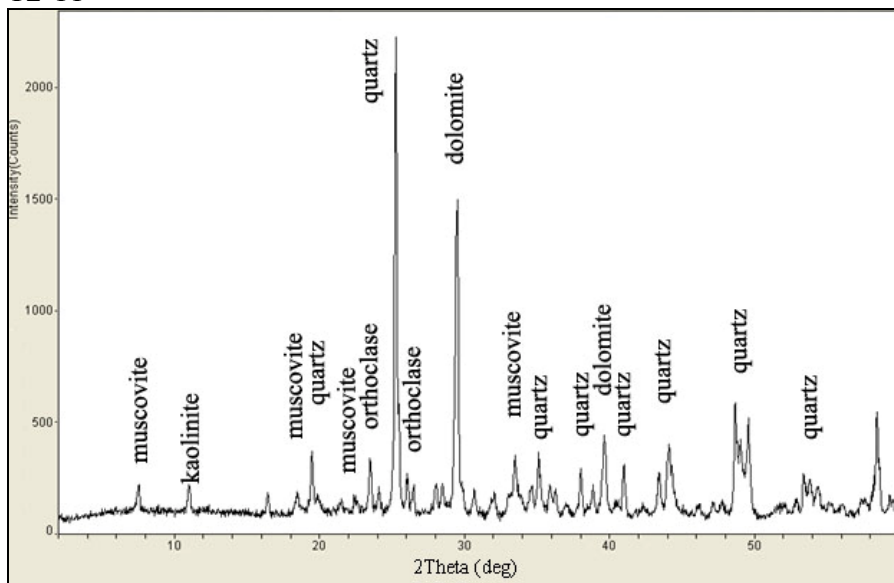
T2-07



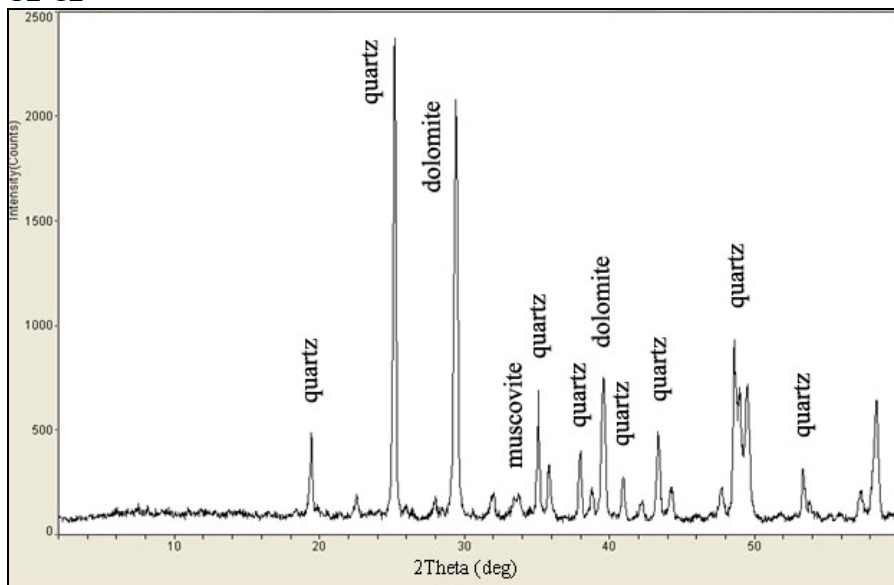
T2-09



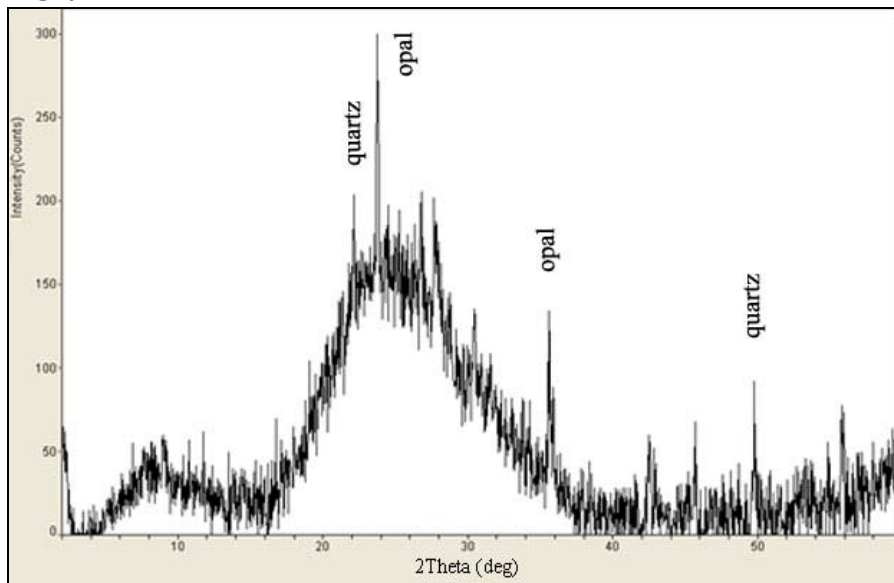
T2-11



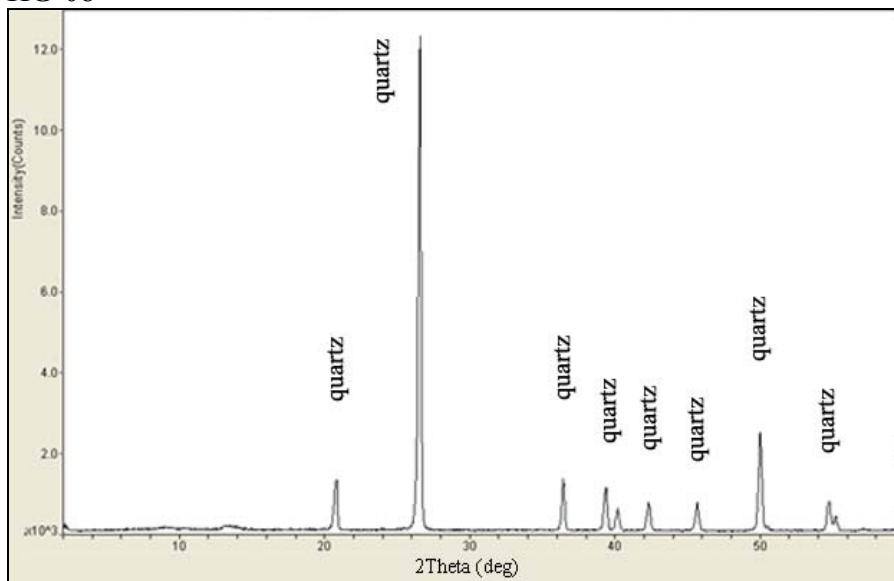
T2-12



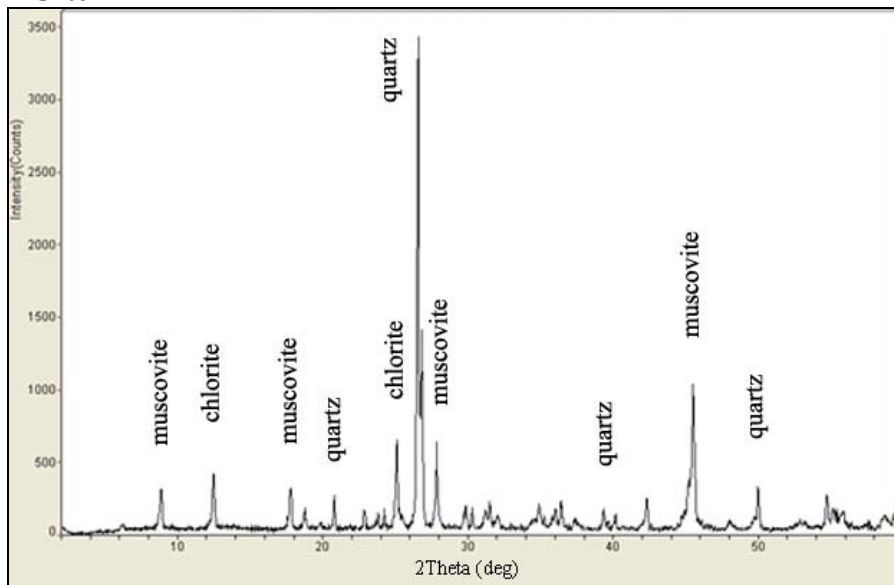
HG-04



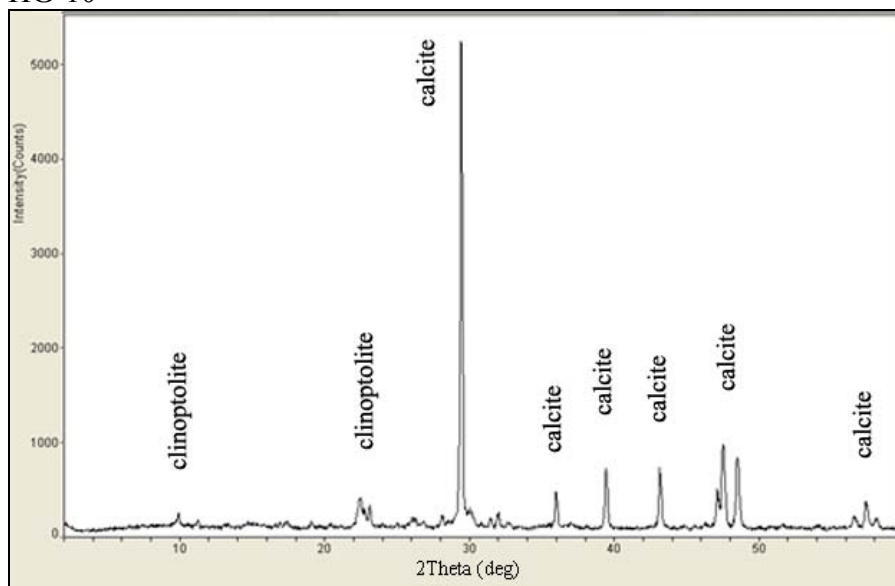
HG-08



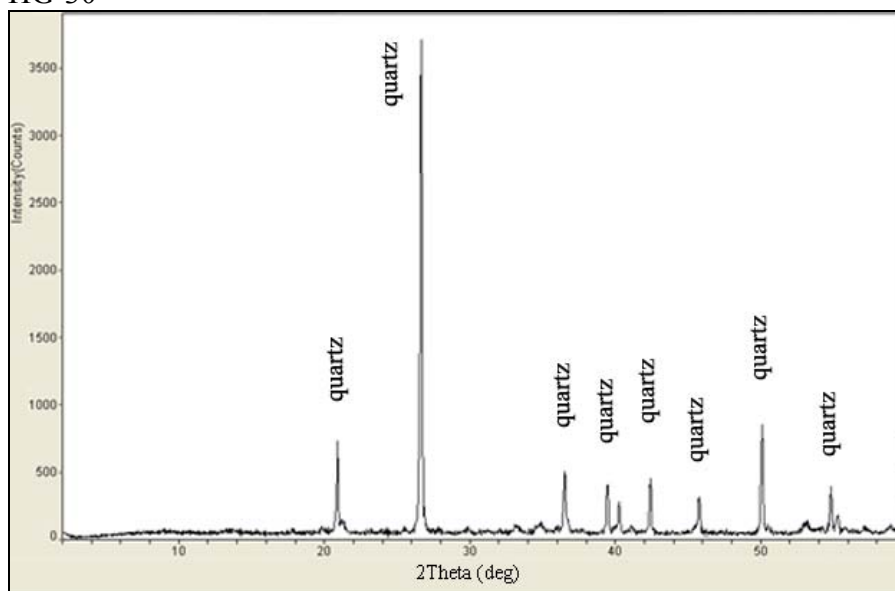
HG-09



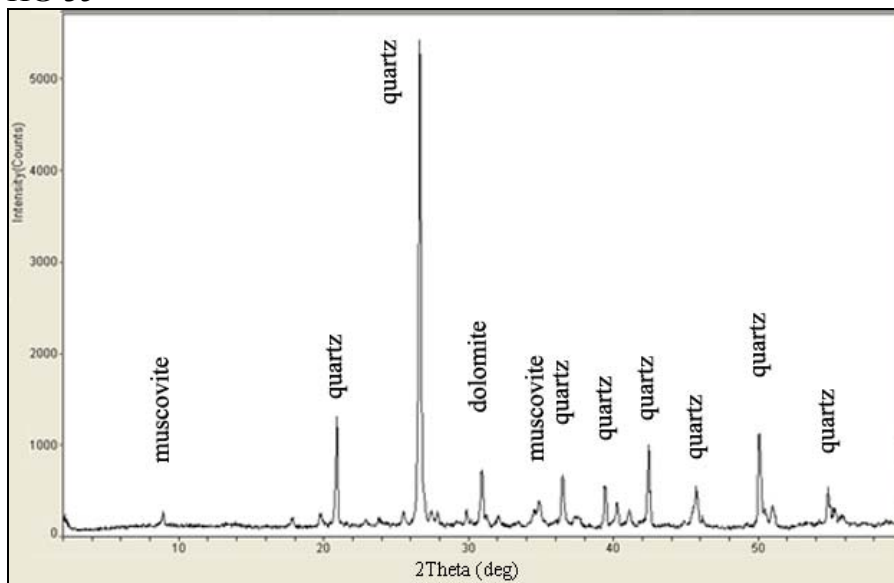
HG-10



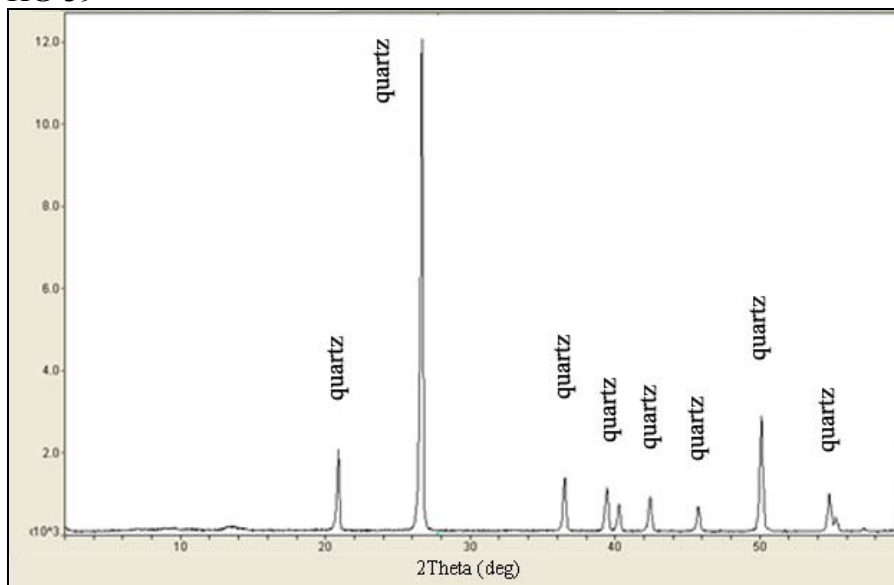
HG-30



HG-35



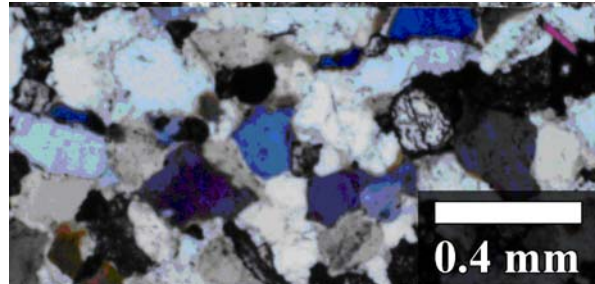
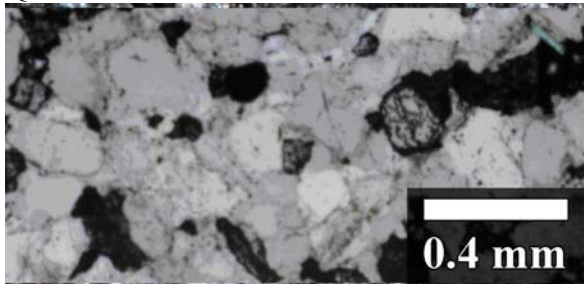
HG-39



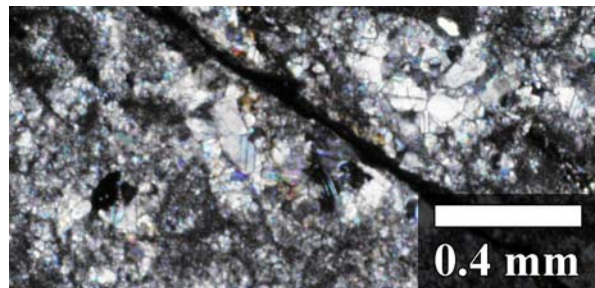
## Thin sections

*Plane-polarized**Cross-polarized*

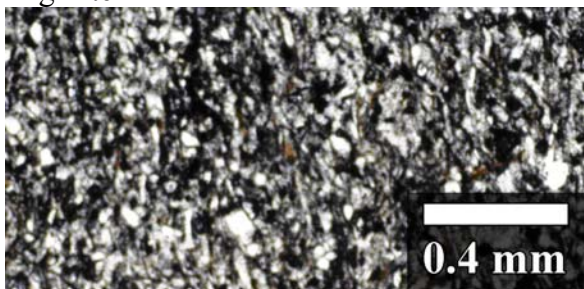
## Quartzite



## Dolomite



## Argillite



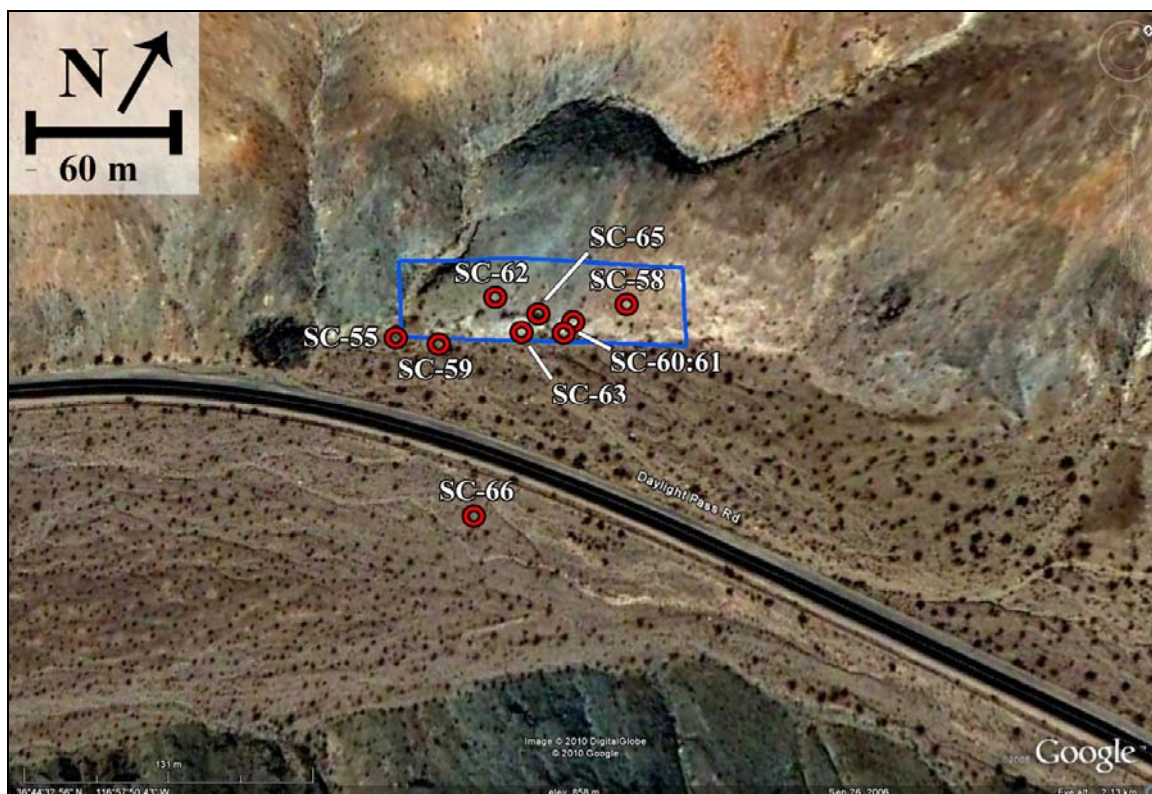
Appendix V.  
Image data and rock sample information for field site 2: schist outcrop

Ground-based SEBASS image data parameters

data set	bands	$\lambda$ range	GIFOV	data type	data size	dimensions
schist1.dat	128	7.5 - 13.5 $\mu\text{m}$	0.2 - 2 m (estimated)	BIP	115 MB	128 x 1800
schist1_emis.dat	128	7.5 - 13.5 $\mu\text{m}$	“	“	115 MB	“
schist1_temp.dat	1	temperature	“	-	90 Kb	“
schist2.dat	128	7.5 - 13.5 $\mu\text{m}$	“	“	115 MB	“
schist2_emis.dat	128	7.5 - 13.5 $\mu\text{m}$	“	“	115 MB	“
schist2_temp.dat	1	temperature	“	-	90 Kb	“
schist3.dat	128	7.5 - 13.5 $\mu\text{m}$	“	“	115 MB	“
schist3_emis.dat	128	7.5 - 13.5 $\mu\text{m}$	“	“	115 MB	“
schist3_temp.dat	1	temperature	“	-	90 Kb	“
schist_mosaic.dat	128	7.5 - 13.5 $\mu\text{m}$	“	“	287 MB	319 x 1800

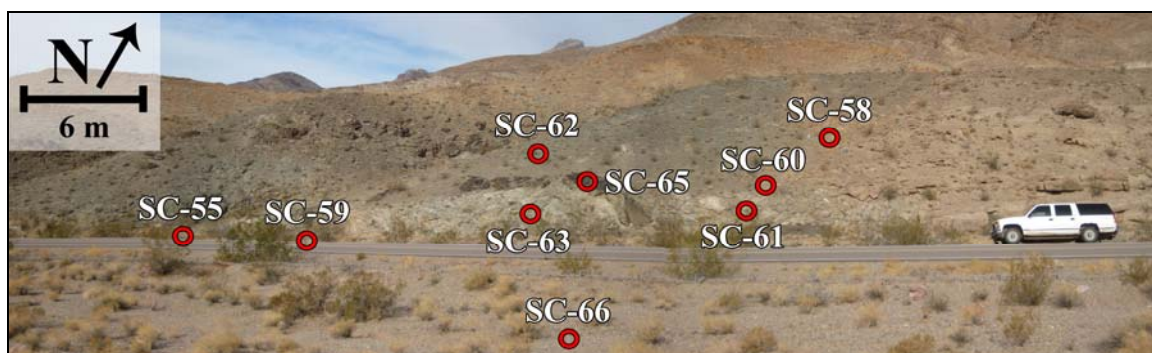


Sample location map



(from Google Earth, 2010)

Sample location map 2



Rock sample photographs

Pelitic schist 1



Pelitic schist 2



Siliceous conglomerate



Carbonate conglomerate



Dolomite



Amphibolite



Alluvium

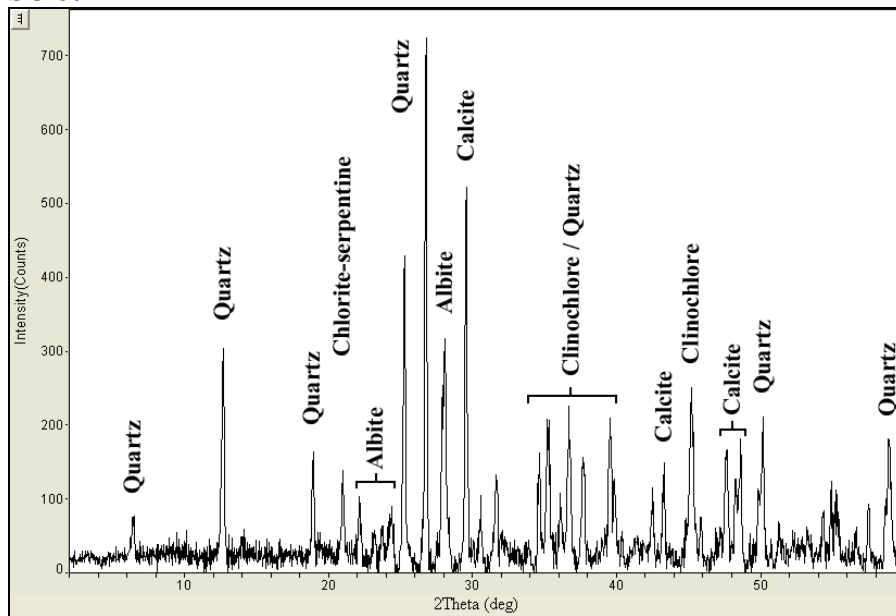


Sample identification number, description, location coordinates, and minerals identified in reflectance (0.4 - 2.45  $\mu\text{m}$ ), thermal-infrared (7.5 - 13.5  $\mu\text{m}$ ), and XRD measurements.

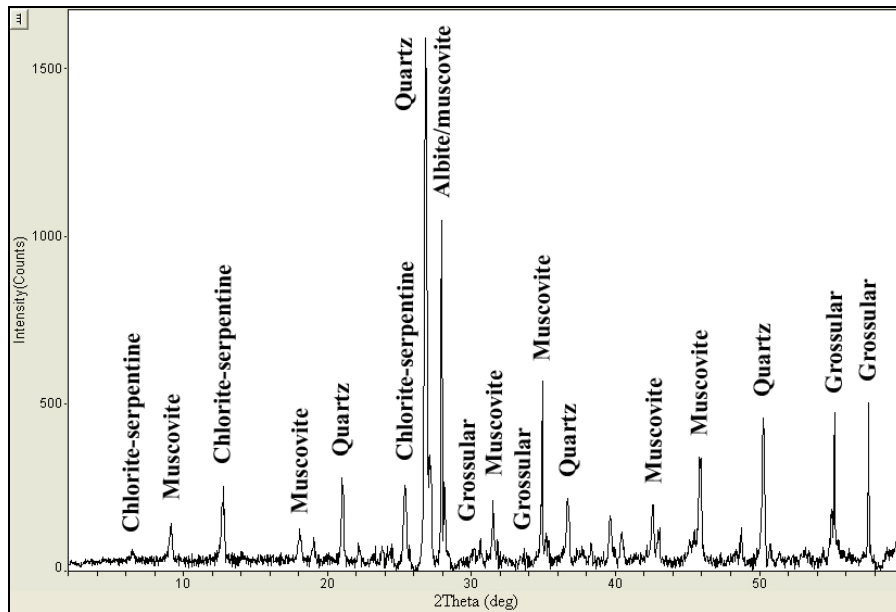
Sample number	Description	Latitude	Longitude	Minerals
SC-55	limestone from alluvium in foreground	36°44'31.46"N	116°57'53.51"W	calcite, quartz
SC-58	oxidized dolostone	36°44'33.93"N	116°57'51.15"W	dolomite, goethite, quartz
SC-59	chloritized siltstone from alluvium in foreground	36°44'31.32"N	116°57'53.75"W	clinocllore, muscovite, quartz
SC-60	siliceous conglomerate	36°44'33.49"N	116°57'50.90"W	goethite, quartz
SC-61	conglomerate with calcite matrix	"	"	goethite, muscovite, quartz
SC-62	silver-ish schist with dark porphyroblasts	36°44'32.65"N	116°57'52.62"W	albite, chlorite, grossular, muscovite, quartz
SC-63	silver-ish schist	36°44'32.75"N	116°57'51.98"W	albite, chlorite, muscovite, quartz
SC-65	amphibolite	36°44'32.96"N	116°57'52.01"W	almandine, chlorite, magnesian- hornblende, molybdophyllite, quartz
SC-66	compacted alluvium (quartzite)	36°44'30.40"N	116°57'50.75"W	goethite, muscovite, quartz

## XRD measurements for mineralogically-unique rock samples

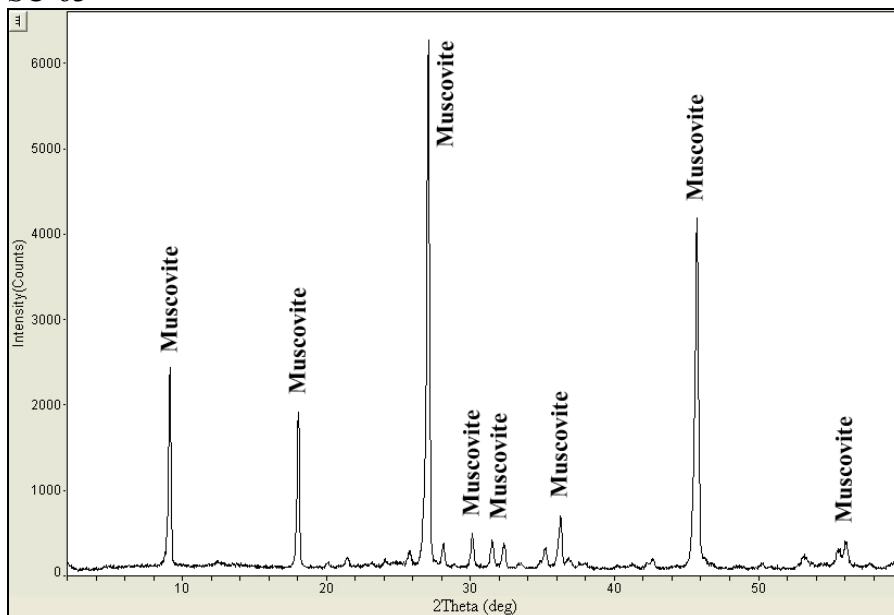
SC-59



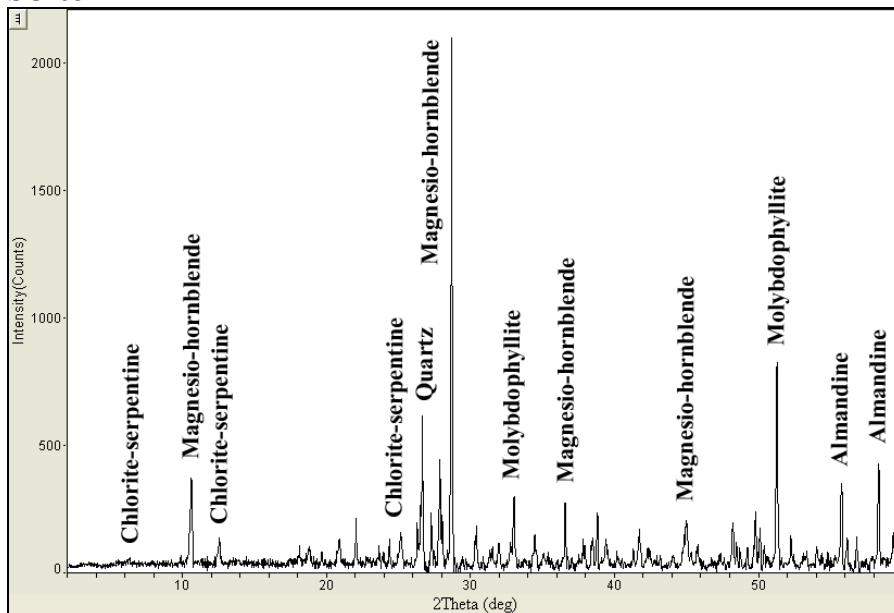
SC-62



SC-63



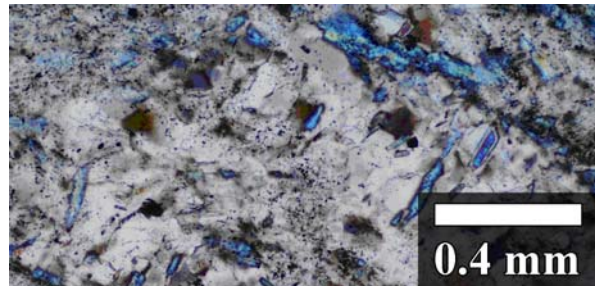
SC-65



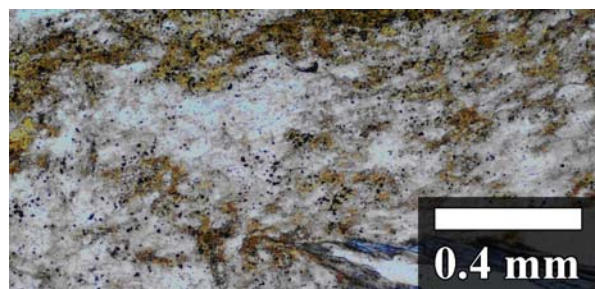
## Thin sections

*Plane-polarized**Cross-polarized*

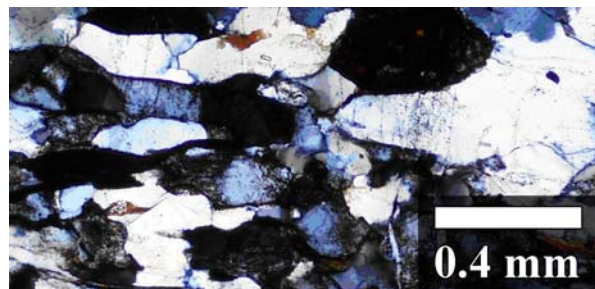
## Green schist



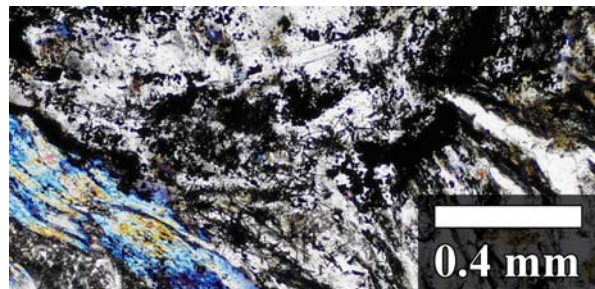
## Red schist



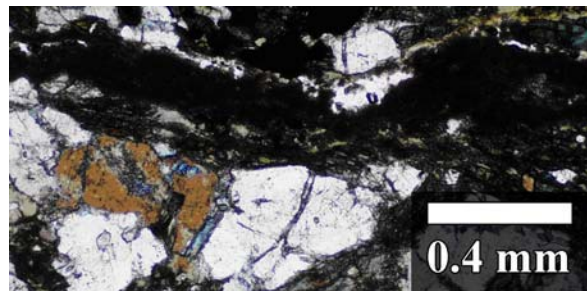
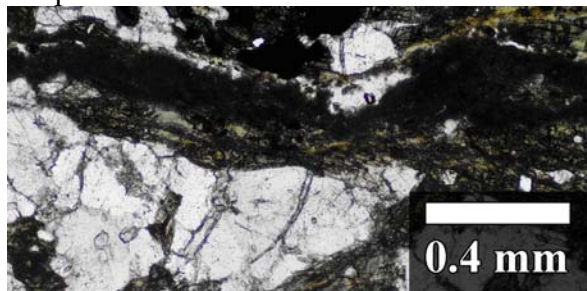
## Porphyroblastic schist



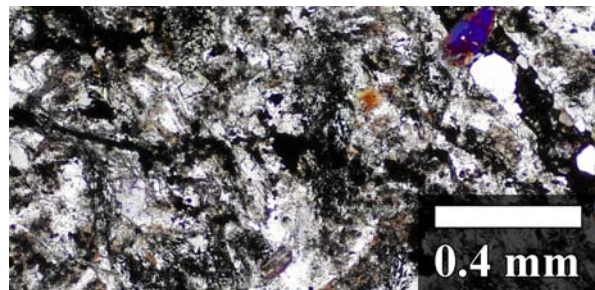
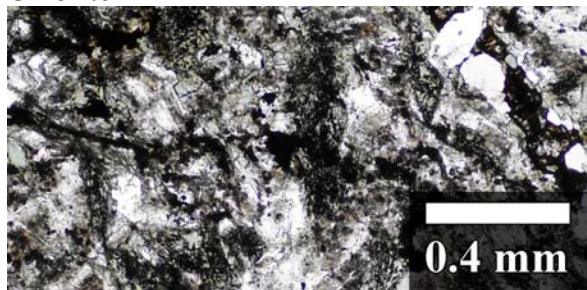
## Silver schist



Amphibolite



Chlorite



Appendix VI.  
Image data and rock sample information for field site 3: Boundary Canyon

Aerial SEBASS image data parameters

data set	bands	$\lambda$ range	GIFOV	data type	data size	dimensions
006_070716_141003_HELLGT_1_L2S.dat	128	7.5 - 13.5 $\mu\text{m}$	3.7 m	BIP	256 MB	128 x 4000
006_070716_141003_HELLGT_1_aux.dat	1	-	-	-	-	-
HELLGT_1_L2S_isac_emissivity.dat	128	7.5 - 13.5 $\mu\text{m}$	"	"	256 MB	"
HELLGT_1_L2S_isac_emissivity_temp.dat	1	temperature	"	"	2 MB	"
HELLGT_1_L2S_ENVI_atmos.dat	128	7.5 - 13.5 $\mu\text{m}$	"	"	256 MB	"
HELLGT_1_L2S_ENVI_ISAC.dat	128	7.5 - 13.5 $\mu\text{m}$	"	"	256 MB	"

MASTER image data parameters

data set	bands	$\lambda$ range	GIFOV	data type	data size	dimensions
MASTERL1b_0000213_03_20000617_1851_1908_V01.hdf	50	0.46 - 12.92 $\mu\text{m}$	20 m	BIL	554 MB	716 x 6267
MASTER_2000_subset_ENVI_atmos.dat	9	8.22 - 12.92 $\mu\text{m}$	"	"	17 MB	716 x 659
MASTER_2000_subset_ENVI_emiss.dat	9	"	"	"	"	"

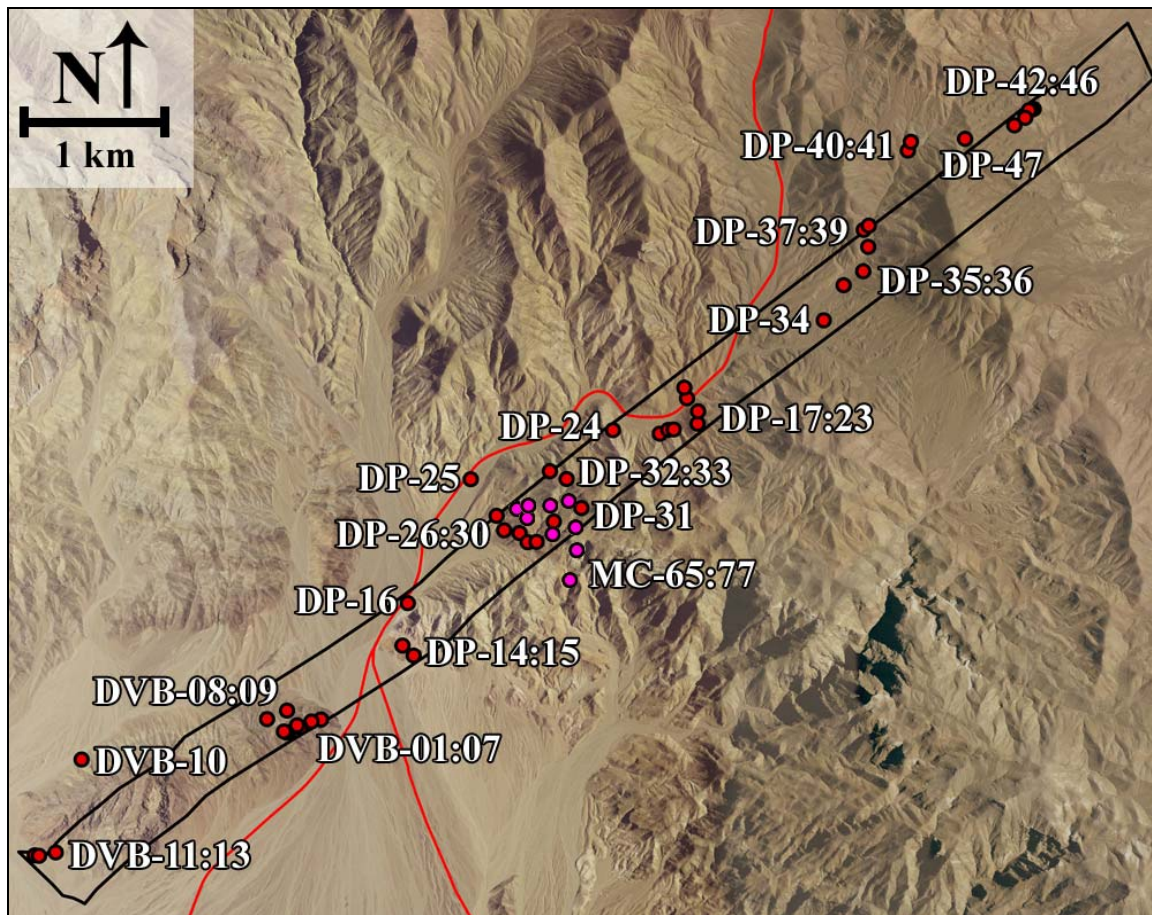
ASTER image data set parameters

data set	bands	$\lambda$ range	GIFOV	data type	data size	dimensions
AST_05_003092420031838370000000.hdf	5	8.29 - 11.32 $\mu\text{m}$	90 m	BSQ	9 MB	830 x 700
AST_05_ENVI_subset_atmos.dat	"	"	"	"	"	"
AST_05_ENVI_subset_emiss.dat	"	"	"	"	"	"



## Sample location map

Red circles indicate samples gathered around the Death Valley Buttes and within Boundary Canyon. Magenta circles indicate samples corresponding to lithologies in and around the Boundary Canyon detachment fault.



Rock sample photographs

Quartzite



Dolomite



Sandstone



Conglomerate



Alluvium



Chloritized sandstone



Pelitic schist



Slate



Argillite



Amphibolite



Chloritized siltstone



Montmorillonite



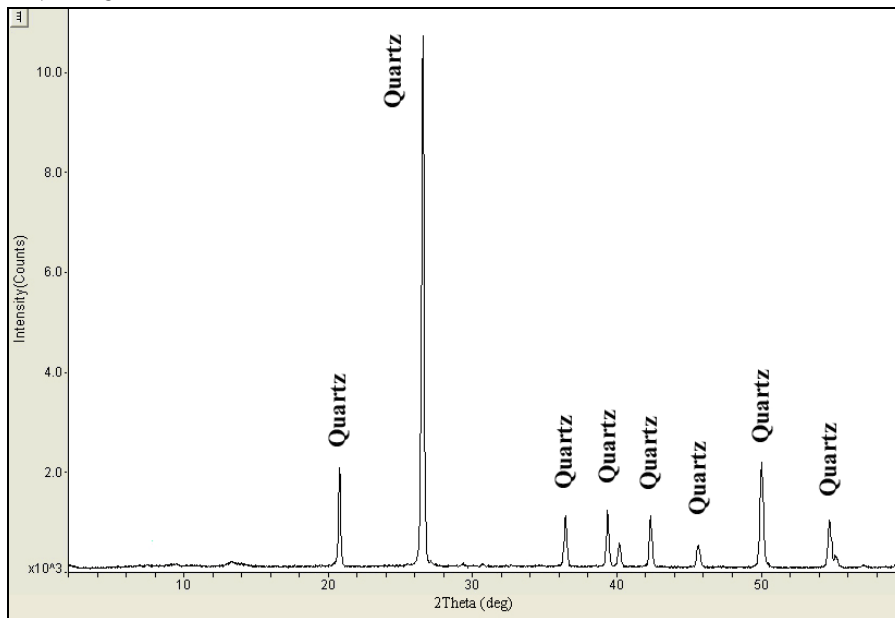
Sample identification number, description, location coordinates, and minerals identified in reflectance (0.4 - 2.45  $\mu\text{m}$ ), thermal-infrared (7.5 - 13.5  $\mu\text{m}$ ), and XRD measurements.

Sample number	Description	Latitude	Longitude	Minerals
DVB-1a	dark, foliated rock with fine-to-fine-medium sized phenocrysts in a fine matrix	36° 43' 2.46"N	-116° 59' 1.14"W	chlorite, goethite, muscovite, quartz
DVB-1b	interlayered quartzite	"	"	goethite, quartz
DVB-2a	altered quartzites with either clayey or oxidized exterior and friable portions	36° 43' 1.80"N	-116° 59' 5.24"W	kaosmectite, muscovite, quartz
DVB-2b	dark, fine grained siltstone/mudstone	"	"	chlorite, muscovite
DVB-3	dark chloritic siltstone/mudstone with oxidized exterior	36° 42' 59.74"N	-116° 59' 9.92"W	clinocllore, muscovite, quartz
DVB-4	quartzite with well-sutured grains; varnished surface	36° 42' 58.08"N	-116° 59' 14.96"W	muscovite, quartz
DVB-5	thinly laminated grayish siltstone	36° 42' 58.04"N	-116° 59' 16.06"W	hematite, muscovite, quartz
DVB-6	laminated, darkish, platy siltstone	36° 42' 58.33"N	-116° 59' 16.91"W	chlorite, muscovite, quartz
DVB-7a	thinly laminated light grayish siltstone	36° 43' 0.48"N	-116° 59' 11.32"W	goethite, muscovite, quartz
DVB-7b	dark, fine-grained sedimentary rock	"	"	chlorite, muscovite, quartz
DBB-7c	altered sandstone? - quartz grains are large, but not sutured; matrix is clayey	"	"	goethite, muscovite, quartz
DVB-8	heavily varnished, dark quartzite	36° 43' 5.56"N	-116° 59' 15.61"W	muscovite, quartz
DVB-9	dark, chloritic siltstone	36° 43' 2.61"N	-116° 59' 24.11"W	clinocllore, muscovite, quartz
DVB-10	oxidized dolostone	36° 42' 48.69"N	-117° 0' 42.89"W	goethite, quartz
DVB-11	slightly oxidized crystalline quartzite	36° 42' 15.73"N	-117° 1' 2.77"W	quartz
DVB-12	non-oxidized, weathered quartzite	36° 42' 15.55"N	-117° 1' 0.97"W	quartz
DVB-13a	very rough-surfaced, grayish dolomite with calcite veining	36° 42' 16.71"N	-117° 0' 53.88"W	calcite, dolomite
DVB-13b	oxidized, very rough-surfaced, grayish dolomite	"	"	dolomite, goethite
DVB-13c	lightly oxidized, rough-surfaced, light grayish dolomite	"	"	goethite, quartz
DVB-13d	lightly oxidized limestone	"	"	calcite, dolomite, goethite
DP-14	pinkish orthoquartzite.	36° 43' 27.92"N	-116° 58' 26.52"W	quartz
DP-15	reddish oxidized dolostone with micaceous flecks and rough surface texture	36° 43' 24.47"N	-116° 58' 21.78"W	dolomite, goethite, muscovite
DP-16	whitish quartzite that has been fractured into small fragments.	36° 43' 42.50"N	-116° 58' 24.27"W	muscovite, quartz
DP-17a	heavily weathered and varnished dolostone	36° 44' 40.81"N	-116° 56' 37.15"W	dolomite, goethite, muscovite
DP-17b	quartz-rich conglomerate.	"	"	dolomite, goethite, quartz
DP-18	light-brown oxidized dolostone with rough surface and sandy internal structure.	36° 44' 42.15"N	-116° 56' 33.50"W	dolomite, goethite, quartz
DP-19	light-brown conglomerate with clayey skin and quartz-based pebbles with medium to sharp edges.	36° 44' 42.26"N	-116° 56' 31.23"W	goethite, muscovite, quartz
DP-20	micaceous sandstone with oxidized dolomitic exterior	36° 44' 44.25"N	-116° 56' 21.10"W	dolomite, feldspar, goethite, quartz
DP-21	conglomerate with sharp pebbles and a calcite matrix	36° 44' 48.49"N	-116° 56' 20.91"W	calcite, quartz
DP-22a	sandstone with visible grains of mica	36° 44' 52.99"N	-116° 56' 25.59"W	feldspar, goethite, muscovite, quartz
DP-22b	alluvium: mixed pebbles and sand	"	"	dolomite, quartz
DP-23	dark gray dolostone with rough-textured surface	36° 44' 56.66"N	-116° 56' 26.73"W	dolomite, goethite
DP-24	sandstone or possible lightly metamorphosed quartzite	36° 44' 42.04"N	-116° 56' 57.06"W	muscovite, quartz
DP-25a	interlayered schist and quartzite (measured quartzite)	36° 44' 25.19"N	-116° 57' 57.50"W	muscovite, quartz
DP-25b	interlayered schist and quartz (measured schist)	"	"	chlorite-serpentine,

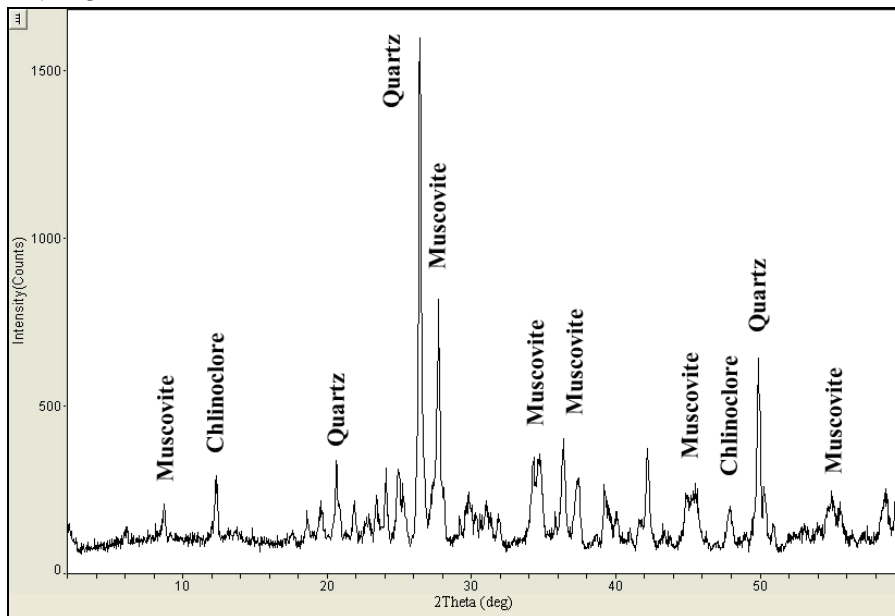
				muscovite, quartz
DP-26	altered quartzite dominated by clay matrix and sparse original fragments of quartzite	36° 44' 12.58"N	-116° 57' 46.54"W	goethite, muscovite, quartz
DP-27	light-brown dolostone	36° 44' 7.56"N	-116° 57' 43.34"W	dolomite, goethite
DP-28	varnished dolostone	36° 44' 6.62"N	-116° 57' 36.77"W	dolomite, muscovite
DP-29	light-gray, non-oxidized dolostone with calcite veining	36° 44' 3.47"N	-116° 57' 33.35"W	calcite, dolomite
DP-30a	slightly foliated dolostone; possibly marble and schist (measured the dolostone/marble)	36° 44' 3.60"N	-116° 57' 29.56"W	calcite
DP-30b	slightly foliated dolostone / possibly marble and schist (measured the schist)	"	"	chlorite-serpentine, muscovite, quartz
DP-31	interlayered dolostone and schist	36° 44' 15.26"N	-116° 57' 10.49"W	dolomite, goethite, muscovite, quartz
DP-32	mixed quartzite and weathered dolostone	36° 44' 25.22"N	-116° 57' 16.77"W	dolomite, goethite, quartz
DP-33	varying pelitic schist layers	36° 44' 27.95"N	-116° 57' 23.88"W	clinocllore, muscovite, quartz
DP-34	conglomerate with sandy/clayey matrix and small pebbles	36° 45' 19.82"N	-116° 55' 27.44"W	muscovite, quartz
DP-35a	desert pavement-like alluvial surfaces (quartzite pebbles)	36° 45' 31.87"N	-116° 55' 18.97"W	goethite, muscovite, quartz
DP-35b	dark shale or lightly metamorphosed slate	"	"	chlorite, muscovite, quartz
DP-36	light brown dolostone	36° 45' 36.68"N	-116° 55' 10.66"W	dolomite, goethite
DP-37	conglomerate with sharp pebbles	36° 45' 45.09"N	-116° 55' 8.54"W	quartz
DP-38	medium gray sandstone with lightly oxidized skin	36° 45' 50.94"N	-116° 55' 10.41"W	microcline, quartz
DP-39	fractured, clayey quartzite	36° 45' 52.40"N	-116° 55' 8.25"W	muscovite, quartz
DP-40	purple-ish sandstone; very friable	36° 46' 18.21"N	-116° 54' 51.63"W	goethite, muscovite, quartz
DP-41	green chloritic sandstone	36° 46' 21.24"N	-116° 54' 50.35"W	albite, quartz
DP-42	varnished feldspathic sandstone	36° 46' 32.51"N	-116° 53' 58.14"W	feldspar, goethite, muscovite, quartz
DP-43	white-ish siltstone	36° 46' 32.09"N	-116° 53' 59.42"W	dolomite, muscovite, quartz
DP-44	thin, platy white-ish siltstone	36° 46' 32.08"N	-116° 54' 0.11"W	dolomite, quartz
DP-45	dark conglomerate	36° 46' 29.48"N	-116° 54' 1.77"W	goethite, quartz
DP-46	light limestone	36° 46' 26.86"N	-116° 54' 6.32"W	calcite, quartz
DP-47	mixed pebbles (primarily quartzite) in a desert pavement-like surface	36° 46' 22.24"N	-116° 54' 27.29"W	goethite, muscovite, quartz
MC-65	rough-textured dolostone	36°45'17.62"N	-116°53'39.98"W	dolostone, goethite
MC-66	chloritized sandstone	36°45'15.88"N	-116°53'16.67"W	chlorite, muscovite, quartz
MC-67	chloritized sandstone	36°45'10.63"N	-116°53'11.54"W	chlorite, muscovite, quartz
MC-68	marble	36°44'04.72"N	-116°57'24.35"W	calcite, goethite
MC-69	intermixed schist and quartz	36°44'16.27"N	-116°56'34.72"W	goethite, muscovite, quartz
MC-70	oxidized carbonate conglomerate	36°44'40.50"N	-116°56'54.63"W	calcite, quartz
MC-71	reddish schist with dark porphyroblasts	36°44'26.30"N	-116°57'35.24"W	goethite, muscovite, quartz
MC-72	reddish weathered schist	"	"	goethite, muscovite, quartz
MC-73	dolostone with rough surface	36°44'22.12"N	-116°57'11.05"W	dolomite, goethite
MC-74	silver-green pelitic schist	36°44'17.45"N	-116°57'21.82"W	clinocllore, muscovite, quartz
MC-75	weathered silver-greenish pelitic schist	"	"	clinocllore, muscovite, quartz
MC-76	amphibolite	36°44'16.12"N	-116°57'24.00"W	chlorite, magnesio-hornblende, quartz
MC-77	weathered yellowish schist	36°44'21.58"N	-116°57'19.71"W	clinocllore, muscovite, quartz

## XRD measurements for mineralogically unique rock samples

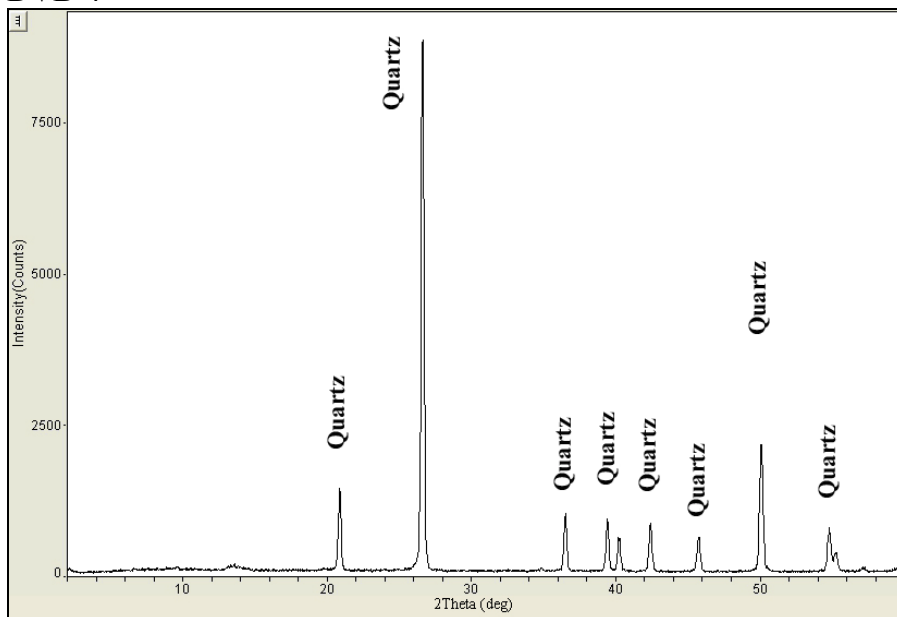
DVB-1b



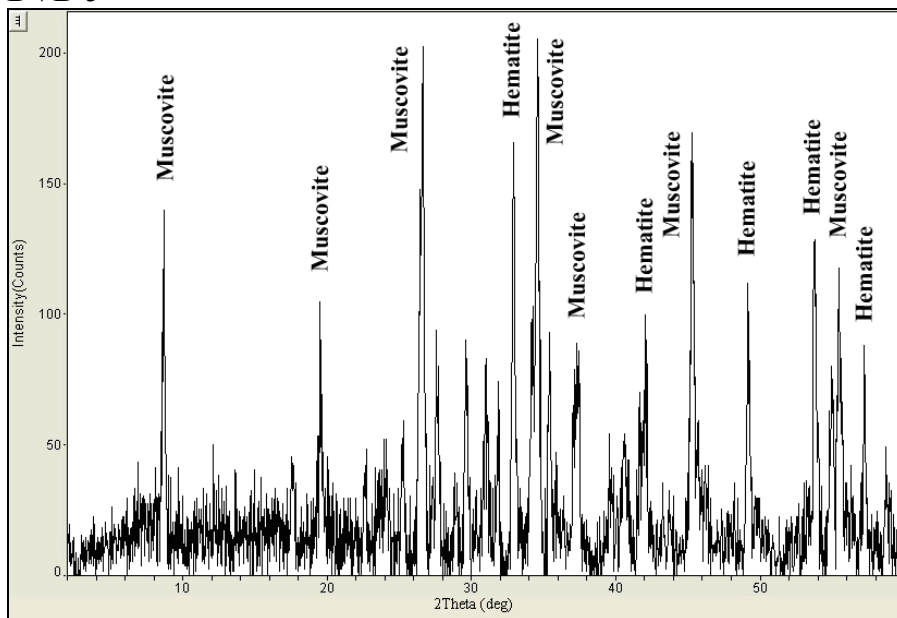
DVB-3



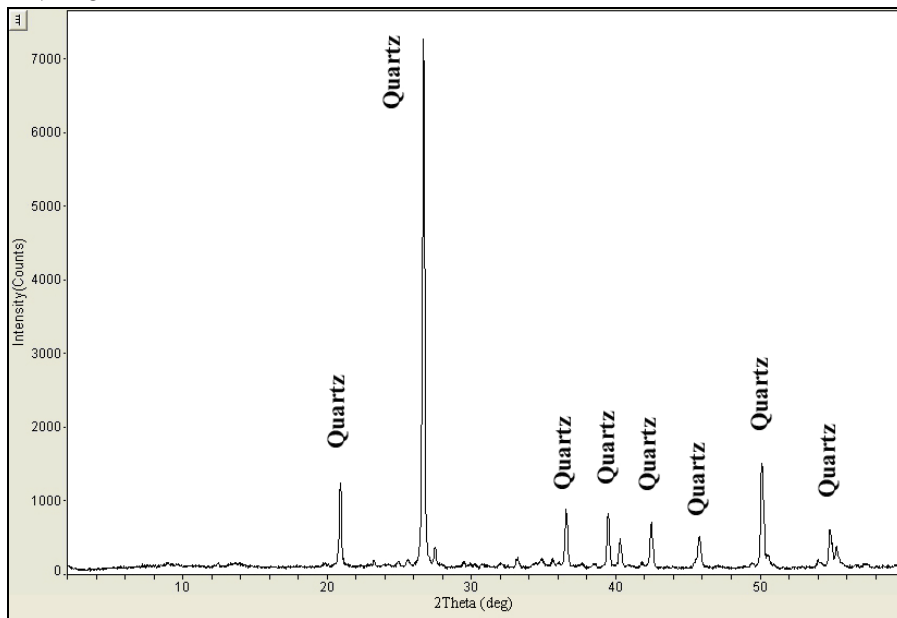
DVB-4



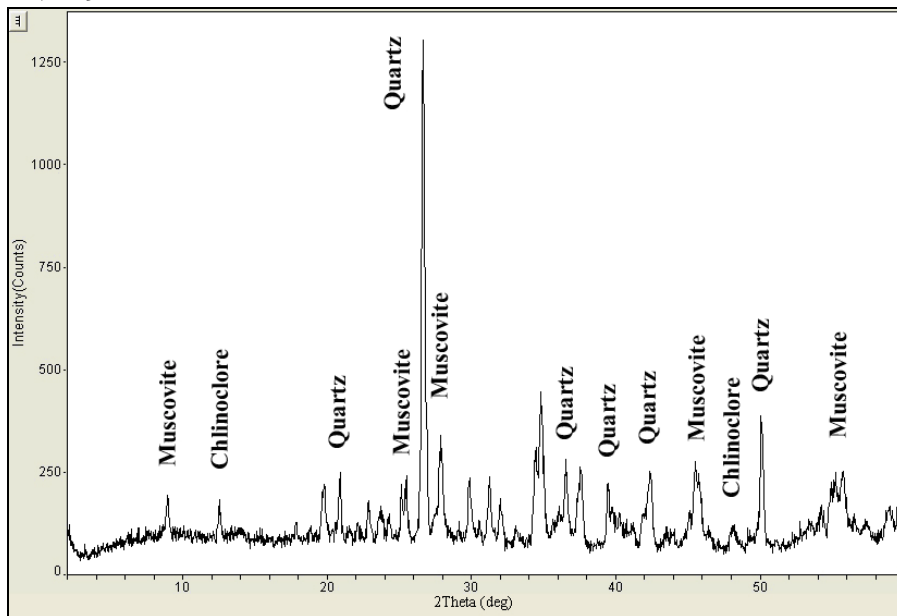
DVB-5



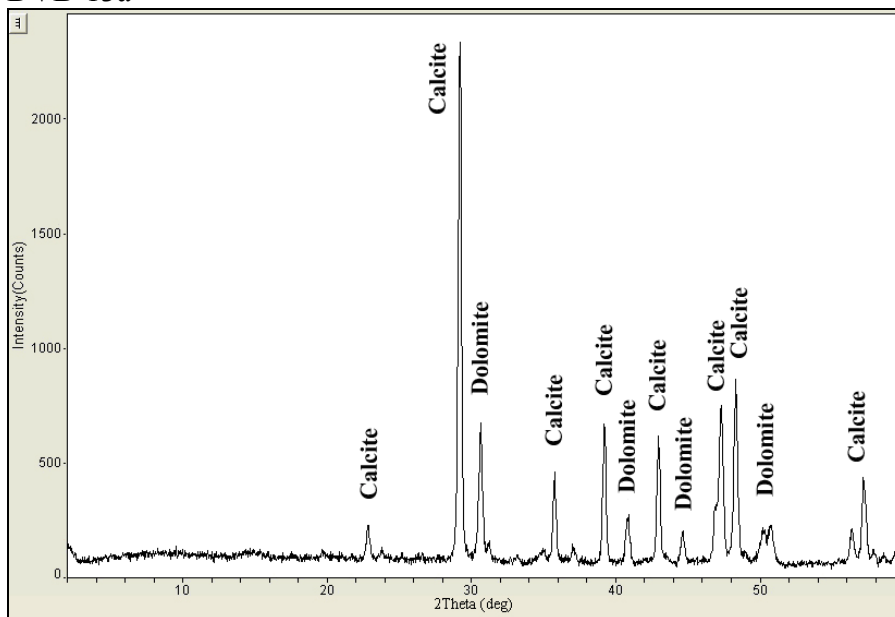
DVB-8



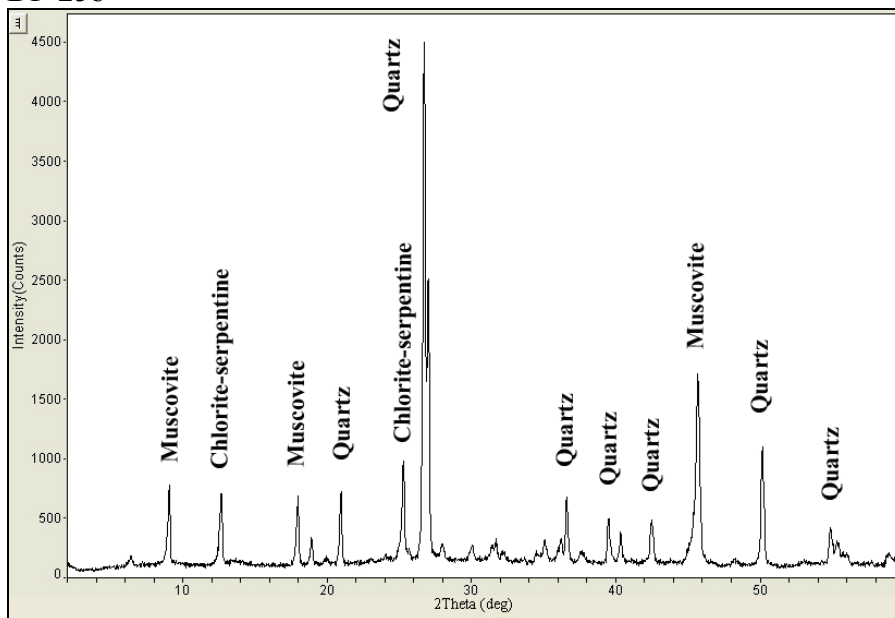
DVB-9



DVB-13a

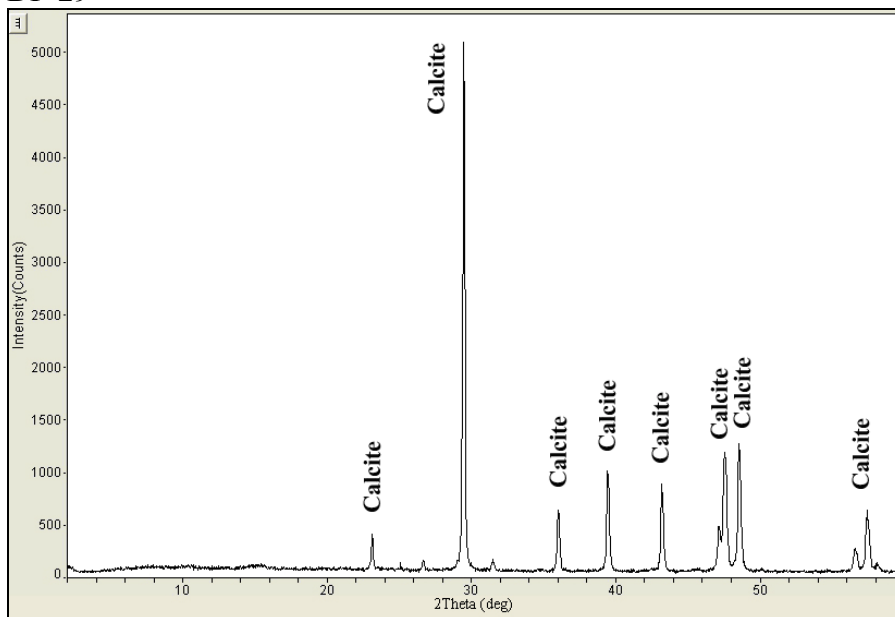


DP-25b

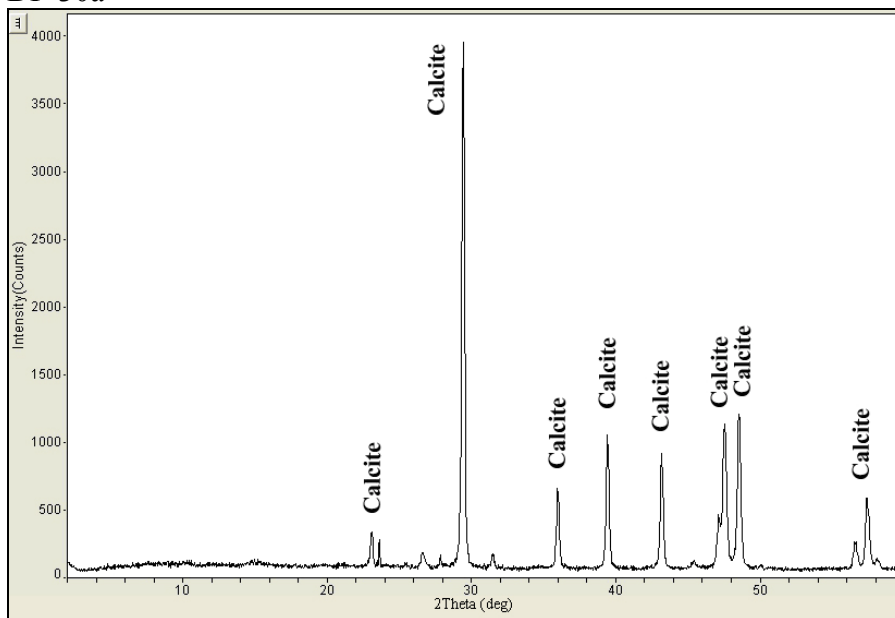




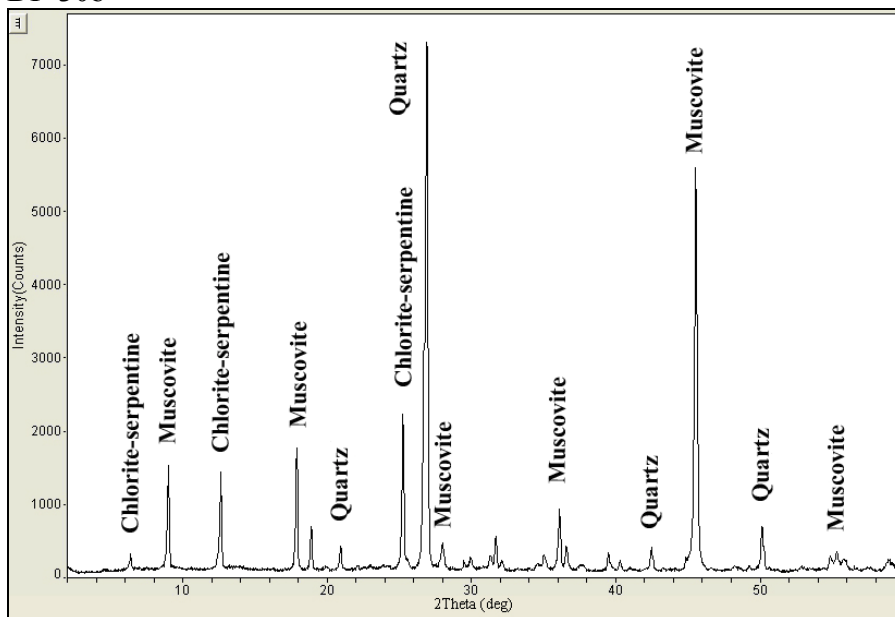
DP-29



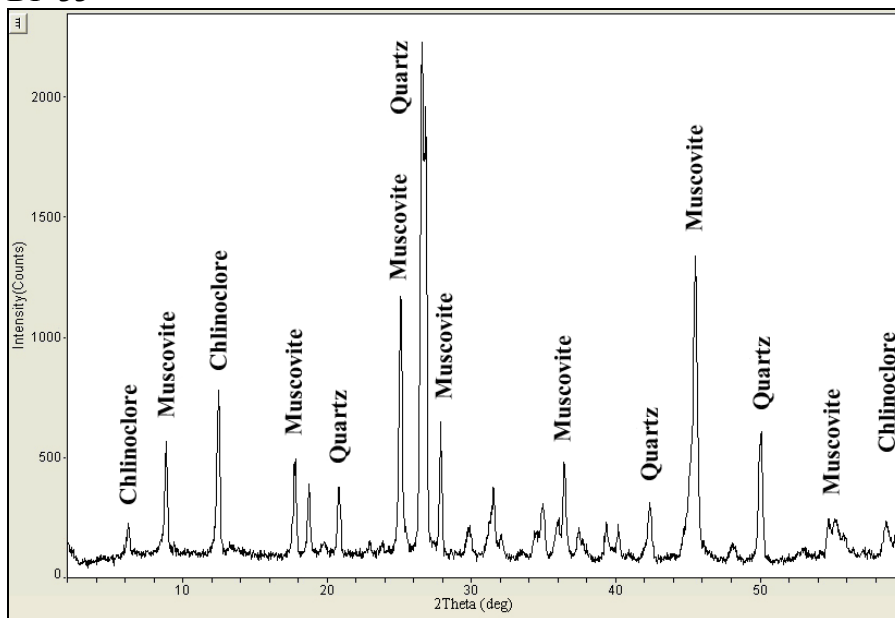
DP-30a



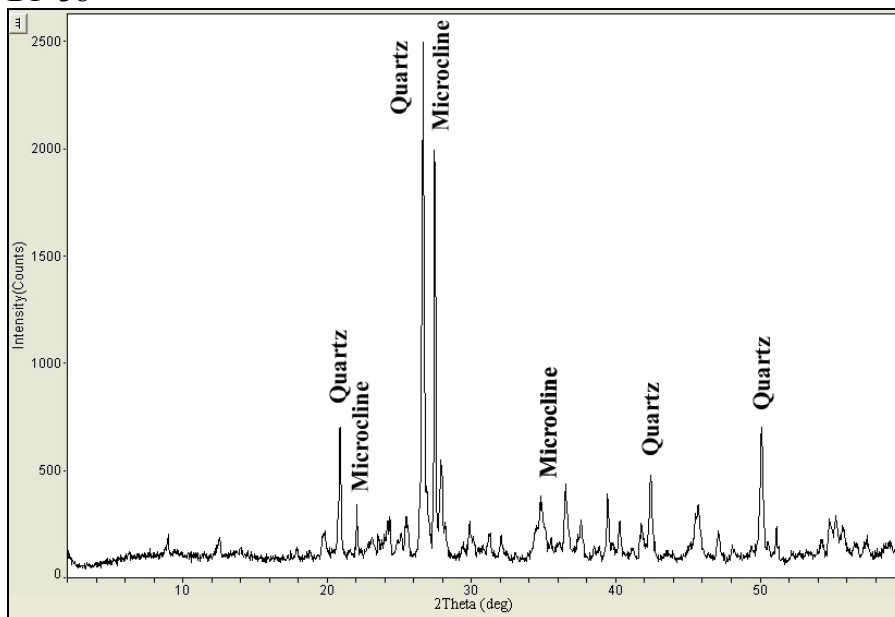
DP-30b



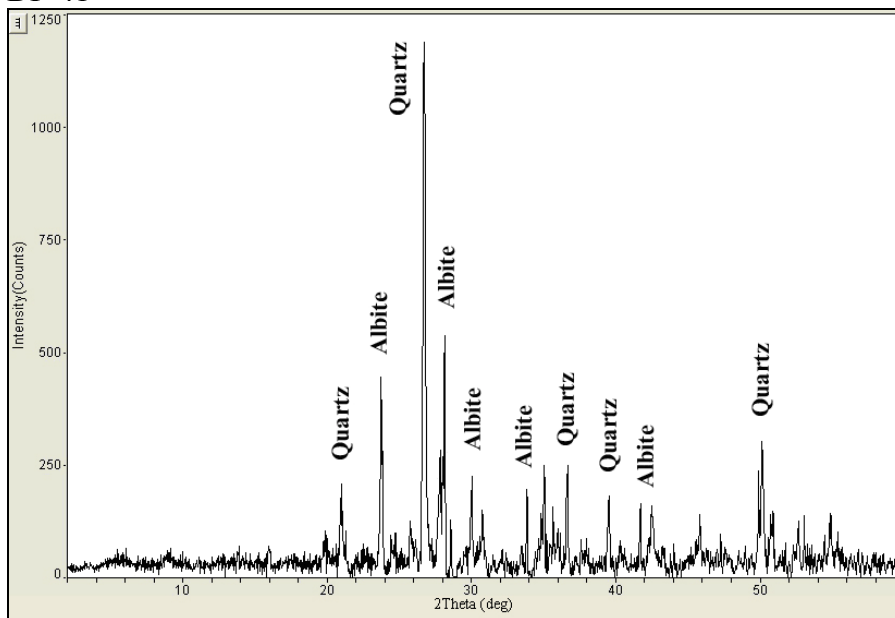
DP-33



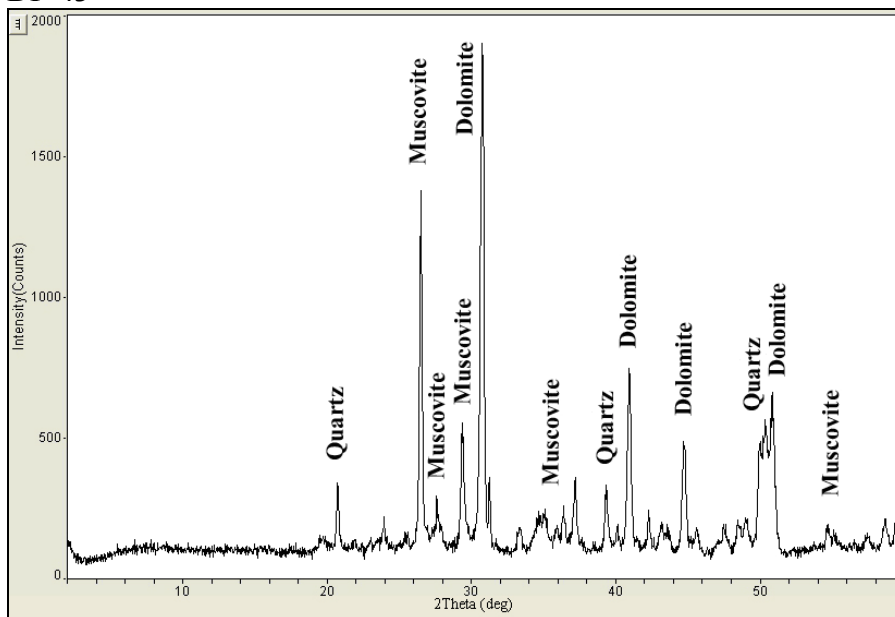
DP-38



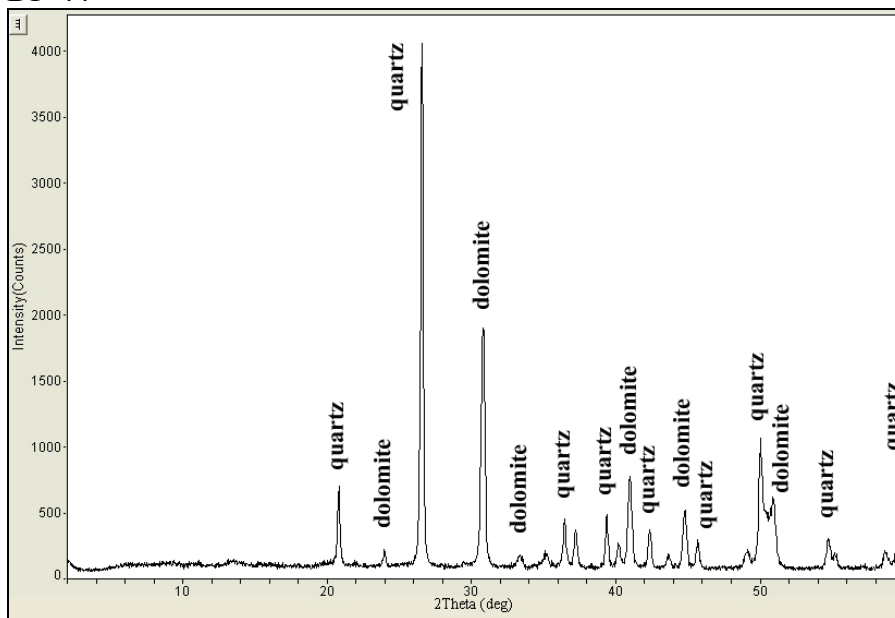
DP-41



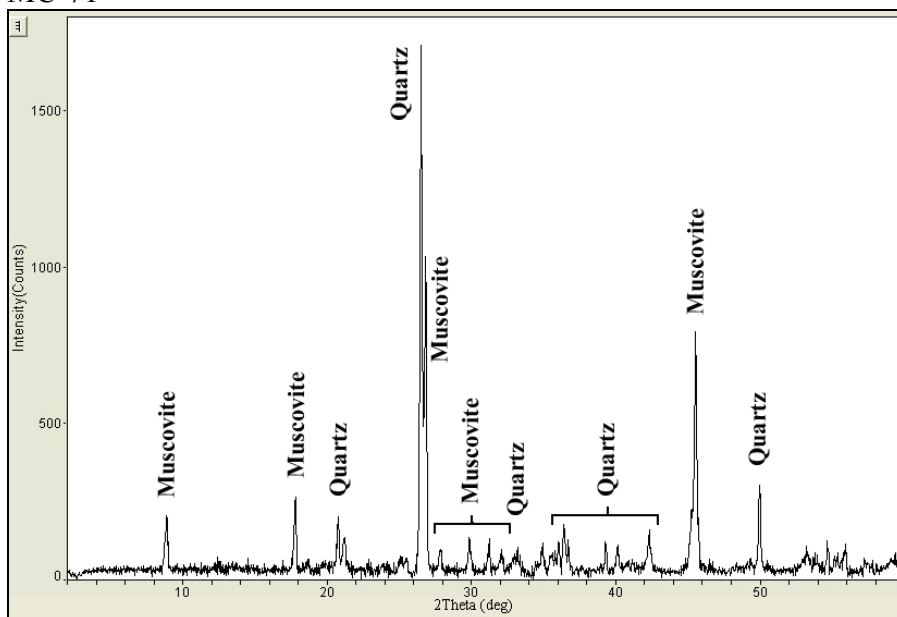
DP-43



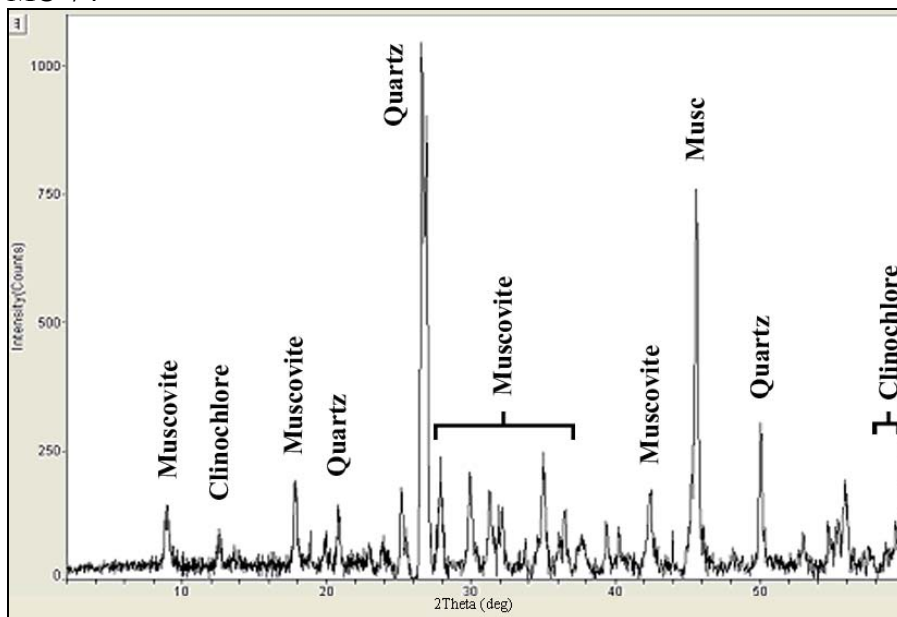
DP-44



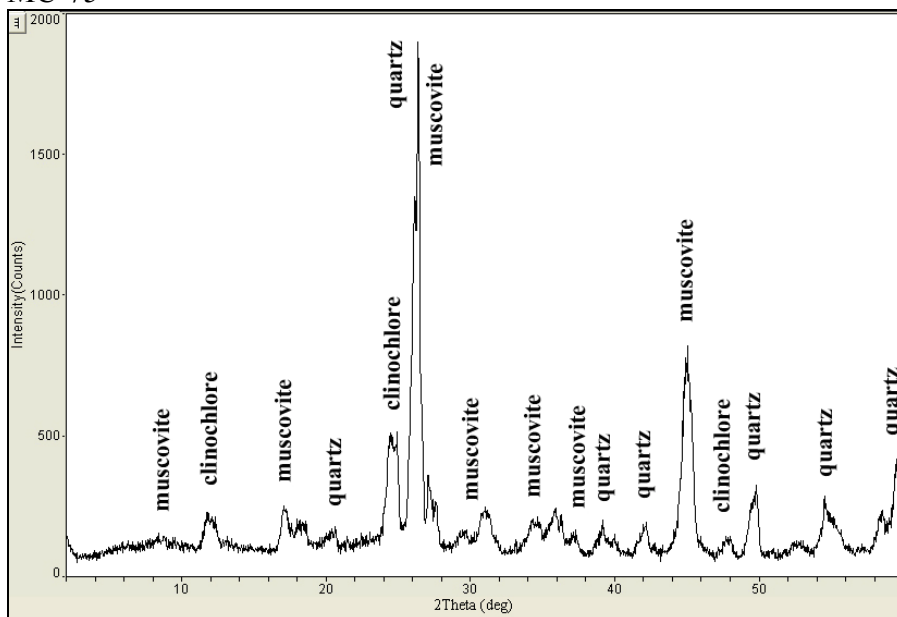
MC-71



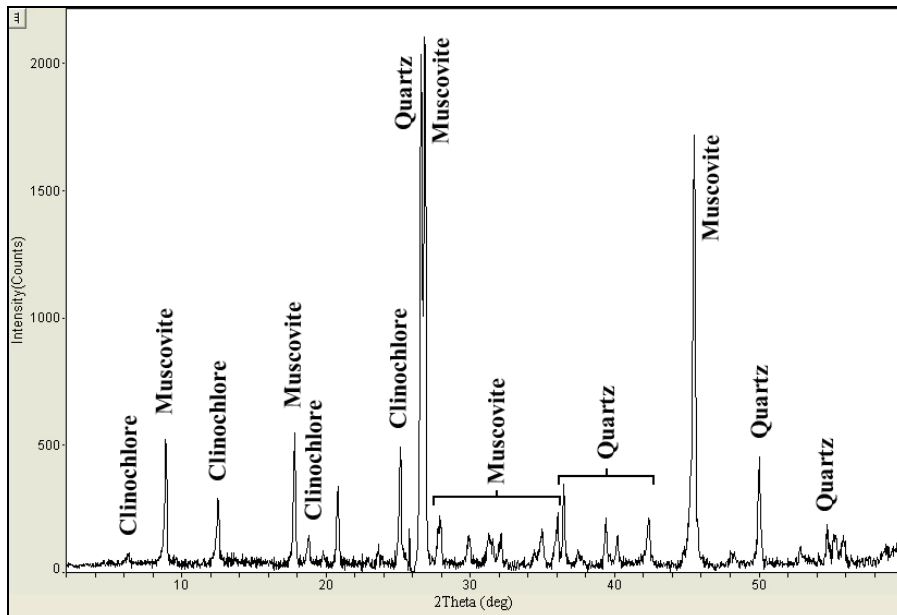
MC-74



MC-75



MC-77



Appendix VII.  
Image data and rock sample information for study site 4: Oasis Valley

Oasis Valley ProSpecTIR V-S image data sets and parameters

data set	bands	$\lambda$ range	GIFOV	data type	data size	dimensions
0612-1017 EW rad.dat	178	400 - 2451 nm	5 m	BIL	316 MB	320 x 2912
0612-1017 EW ACORN.dat	“	“	“	“	“	“
0612-1030 EW rad.dat	“	“	“	“	334 MB	320 x 3079
0612-1030 EW ACORN.dat	“	“	“	“	“	“
0612-1042 EW rad.dat	“	“	“	“	321 MB	320 x 2959
0612-1042 EW ACORN.dat	“	“	“	“	“	“
0612-1106 EW rad.dat	“	“	“	“	299 MB	320 x 2757
0612-1106 EW ACORN.dat	“	“	“	“	“	“
0612-1117 EW rad.dat	“	“	“	“	305 MB	320 x 2809
0612-1117 EW ACORN.dat	“	“	“	“	“	“
0612-1137 EW rad.dat	“	“	“	“	314 MB	320 x 2893
0612-1137 NS ACORN.dat	“	“	“	“	“	“
0612-1149 EW rad.dat	“	“	“	“	320 MB	320 x 2954
0612-1149 NS ACORN.dat	“	“	“	“	“	“
0612-1201 EW rad.dat	“	“	“	“	310 MB	320 x 2858
0612-1201 NS ACORN.dat	“	“	“	“	“	“
0612-1212 EW rad.dat	“	“	“	“	321 MB	320 x 2963
0612-1212 NS ACORN.dat	“	“	“	“	“	“
0612-1223 EW rad.dat	“	“	“	“	296 MB	320 x 2727
0612-1223 NS ACORN.dat	“	“	“	“	“	“
OasisValley EW ACORN mosaic.dat	“	“	“	BSQ	1.31 GB	3259 x 1221
OasisValley NS ACORN mosaic.dat	“	“	“	“	1.04 GB	1056 x 2991
OasisValley ACORN subsetmosaic.dat	“	“	“	“	3.23 GB	2705 x 2638

Oasis Valley SEBASS image data sets and parameters

data set	bands	$\lambda$ range	GIFOV	data type	data size	dimensions
0612-1314 rad EW.dat	128	7.5 - 13.5 $\mu$ m	5 m	BSQ	250 MB	128 x 4000
0612-1314 ISAC EW.dat	“	“	“	“	“	“
0612-1327 rad EW.dat	“	“	“	“	218 MB	128 x 3500
0612-1327 ISAC EW.dat	“	“	“	“	“	“
0612-1339 rad EW.dat	“	“	“	“	218 MB	128 x 3500
0612-1339 ISAC EW.dat	“	“	“	“	“	“
0612-1403 rad EW.dat	“	“	“	“	218 MB	128 x 3500
0612-1403 ISAC EW.dat	“	“	“	“	“	“
0612-1414 rad EW.dat	“	“	“	“	218 MB	128 x 3500
0612-1414 ISAC EW.dat	“	“	“	“	“	“
0612-1426 rad EW.dat	“	“	“	“	218 MB	128 x 3500
0612-1426 ISAC EW.dat	“	“	“	“	“	“
0612-1436 rad NS.dat	“	“	“	“	250 MB	128 x 4000
0612-1436 ISAC NS.dat	“	“	“	“	“	“
0612-1447 rad NS.dat	“	“	“	“	234 MB	128 x 3750
0612-1447 ISAC NS.dat	“	“	“	“	“	“
0612-1458 rad NS.dat	“	“	“	“	234 MB	128 x 3750
0612-1458 ISAC NS.dat	“	“	“	“	“	“
0612-1509 rad NS.dat	“	“	“	“	234 MB	128 x 3750
0612-1509 ISAC NS.dat	“	“	“	“	“	“
0612-1521 rad NS.dat	“	“	“	“	234 MB	128 x 3750
0612-1521 ISAC NS.dat	“	“	“	“	“	“
0612-1532 rad NS.dat	“	“	“	“	234 MB	128 x 3750
0612-1532 ISAC NS.dat	“	“	“	“	“	“
OasisValley EW ISAC mosaic.dat	“	“	“	“	1.81 GB	4160 x 916
OasisValley NS ISAC mosaic.dat	“	“	“	“	2.96 GB	1537 x 4046
OasisValley ISAC mosiac.dat	“	“	“	“	3.4 GB	2704 x 2639





## Rock sample photographs

Alunite



Kaolinite



Opaline silica



Quartzite



Dolomite



Burkeite



Basalt



Muscovite



Tuff 1



Tuff 2



Gravel deposit



Carbonate sinter



Aggregate



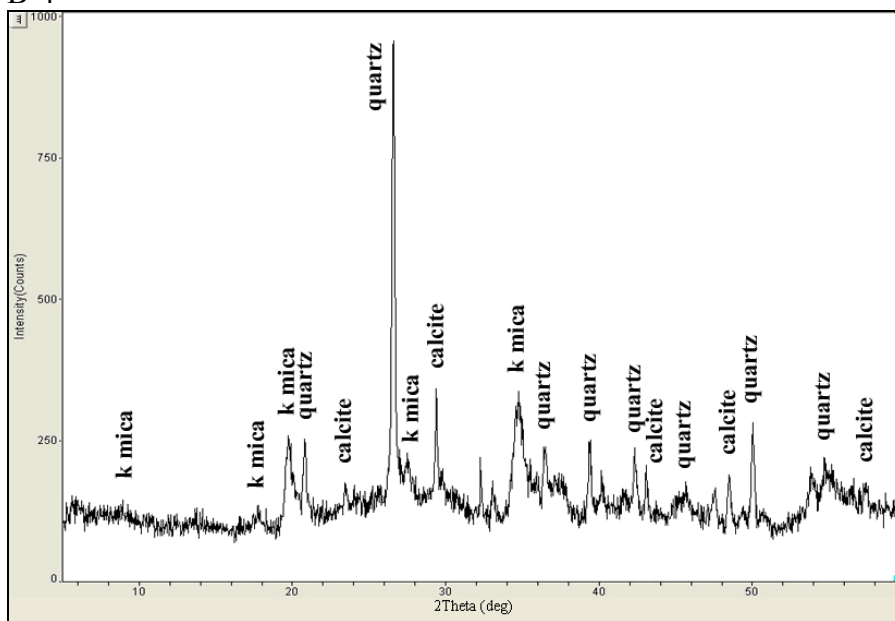
Sample identification number, description, location coordinates, and minerals identified in reflectance (0.4 - 2.45  $\mu\text{m}$ ), thermal-infrared (7.5 - 13.5  $\mu\text{m}$ ), and XRD measurements.

Sample number	Description	Latitude	Longitude	Minerals
B-1	gangue pile 1	36° 54' 52.90"N	-116° 47' 58.10"W	goethite, muscovite, quartz
B-2	gangue pile 2a	36° 54' 57.90"N	-116° 48' 5.68"W	goethite, muscovite, quartz
B-3	gangue pile 2b	"	"	goethite, muscovite
B-4	gangue pile 2c	"	"	goethite, Na-mica, quartz, calcite
B-5	gangue pile 3a	36° 55' 0.83"N	-116° 48' 8.22"W	goethite, montmorillonite
B-6	gangue pile 3b	"	"	goethite, muscovite
B-7	gangue pile 4a (pink)	36° 55' 2.07"N	-116° 48' 13.63"W	goethite, montmorillonite, Na-mica, quartz
B-8	gangue pile 4b (gray)	"	"	goethite, montmorillonite, quartz, sanidine
B-9	gangue pile 5	36° 54' 54.30"N	-116° 48' 20.68"W	goethite, quartz, sanidine
B-10	tuff talus	36° 54' 55.04"N	-116° 48' 21.25"W	zeolite
B-11	chloritic rocks from pit	36° 54' 54.75"N	-116° 48' 22.66"W	chlorite, clinoptilolite, heulandite
B-12	gangue material filling mine shaft	36° 54' 58.43"N	-116° 47' 52.63"W	analcime, calcite, goethite, margarite, quartz, sanidine
B-13	rhyolytic tuff	36° 54' 56.71"N	-116° 47' 48.71"W	orthoclase, quartz
B-14	gray gangue material	36° 55' 3.39"N	-116° 47' 47.56"W	goethite, muscovite, quartz
B-15	varnished tuff	36° 55' 13.18"N	-116° 47' 38.80"W	muscovite, quartz, sanidine
B-16	gangue pile	36° 55' 12.30"N	-116° 47' 38.56"W	goethite, montmorillonite
B-17	quartz-kaolinite outcrop	36° 54' 40.42"N	-116° 45' 15.91"W	goethite, kaolinite, orthoclase, quartz
B-18	quartz-kaolinite talus	36° 54' 39.74"N	-116° 45' 15.91"W	goethite, kaolinite, orthoclase, quartz
B-19	volcanic glass/obsidian	"	"	opal, quartz
B-20	light-colored ashflow tuff	36° 54' 20.84"N	-116° 41' 35.80"W	quartz, sanidine
B-21	oxidized ashflow tuff	"	"	goethite, quartz, zeolite
B-22	ashflow tuff	36° 54' 42.94"N	-116° 41' 59.78"W	clinoptilolite, heulandite, quartz
B-23	grayish clay (pit wall)	36° 54' 21.50"N	-116° 39' 10.22"W	calcite, Ca-iron oxide, quartz
B-24	oxidized clay (pit floor)	36° 54' 21.50"N	-116° 39' 10.34"W	goethite, montmorillonite
B-25	red clay (pit floor)	36° 54' 20.88"N	-116° 39' 10.34"W	goethite, montmorillonite
B-26	light-colored clay	36° 54' 19.62"N	-116° 39' 9.86"W	kaosmectite
B-27	light-colored clay (pit)	36° 54' 18.59"N	-116° 39' 4.85"W	kaolinite
B-28	laminated dolostone (pit)	36° 54' 23.78"N	-116° 39' 3.82"W	dolomite, quartz
B-29	oxidized clay (pit)	36° 54' 23.24"N	-116° 39' 6.97"W	goethite, kaolinite
B-30	silicified alunite	36° 58' 46.33"N	-116° 43' 50.26"W	alunite, kaolinite, opal-A, quartz
B-31	somewhat friable alunite	36° 58' 47.14"N	-116° 43' 49.59"W	alunite, kaolinite
B-32	fine-grained clayish gravel on road	36° 59' 2.41"N	-116° 43' 42.76"W	muscovite, quartz, orthoclase
B-33	oxidized kaolinite	36° 54' 38.73"N	-116° 45' 16.70"W	goethite, kaolinite, quartz, opal
B-34	silicified kaolinite	36° 58' 46.02"N	-116° 43' 54.76"W	kaolinite, opal, quartz
B-35	volcanic glass	36° 54' 39.25"N	-116° 45' 15.39"W	quartz
B-36	sinter at hot spring	36° 58' 30.52"N	-116° 43' 40.26"W	opal, quartz
B-37	silicified rocks along fault trace	36° 58' 30.37"N	-116° 43' 39.28"W	quartz, sanidine
B-38	silicified talus	36° 58' 30.76"N	-116° 43' 38.91"W	calcite, opal, orthoclase, quartz
B-39	varnished siliciclastic outcrop	36° 58' 31.41"N	-116° 43' 40.19"W	goethite, quartz
B-40	siliciclastic outcrop	36° 58' 35.06"N	-116° 43' 24.23"W	quartz, sanidine
B-41	rhyolytic tuff	36° 58' 40.99"N	-116° 43' 52.43"W	quartz, sanidine
B-42	light-colored tuff	36° 55' 36.72"N	-116° 46' 28.23"W	crystalite or opal, microcline, quartz
B-43	oxidized tuff	36° 53' 30.49"N	-116° 41' 26.57"W	goethite, orthoclase, quartz

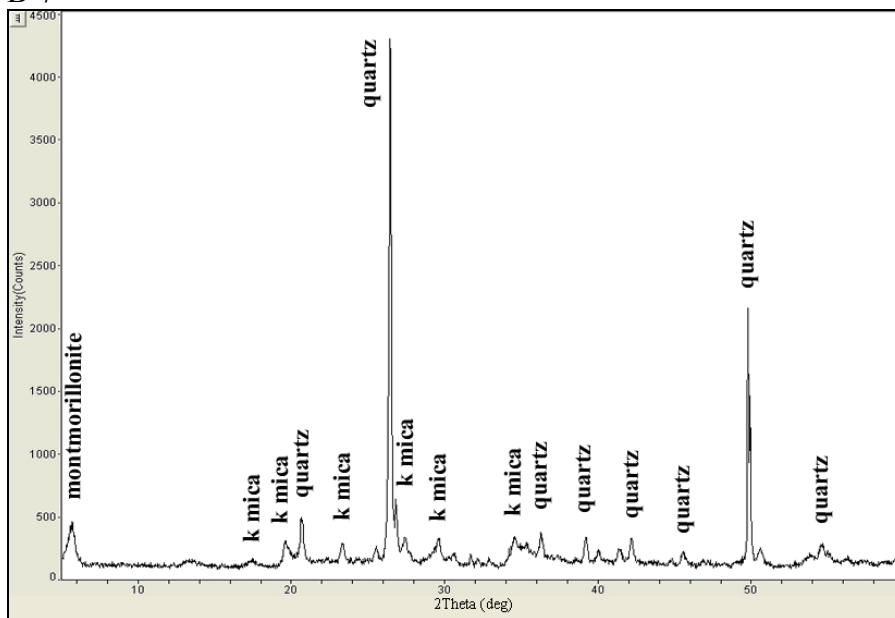
B-44	evaporite along periphery of discharge area	36°58'36.48"N	-116°43'24.40"W	burkeite, halite, quartz, trona
B-45	light-colored clay	36°54'25.21"N	-116°39'21.68"W	montmorillonite
B-46	oxidized breccia	36°59'27.80"N	-116°43'53.70"W	goethite, quartz, opaline silica
B-47	withdrawn material from spring area	36°59'28.56"N	-116°43'51.72"W	calcite, chlorite, opaline silica
B-48	sinter	36°59'29.07"N	-116°43'51.62"W	calcite, dolomite, quartz
B-49	fine-grained clay	36°59'18.59"N	-116°43'50.64"W	goethite, montmorillonite
B-50	sulfur-smelling sinter material	36°59'28.97"N	-116°43'51.90"W	calcite, quartz, sulfur?
B-51	sulfur-smelling clay	36°59'29.78"N	-116°43'53.34"W	muscovite, sulfur?
B-52	aggregate gravel	36°58'59.76"N	-116°43'25.98"W	calcite, dolomite, quartz, sulfur?
B-53	chloritized claystone	36°54'53.86"N	-116°48'24.80"W	chlorite, muscovite
B-54	dolostone talus from Bare Mountain	36°53'07.66"N	-116°40'50.27"W	dolomite
B-55	weathered clay debris outside pit mine	36°53'25.17"N	-116°40'57.65"W	goethite, kaolinite
B-56	new asphalt	36°54'51.29"N	-116°45'13.50"W	undetermined carbonate (calcite/dolomite?), quartz
B-57	old asphalt	36°54'52.52"N	-116°45'14.05"W	undetermined carbonate (calcite/dolomite?), quartz
B-58	gravel deposit 1	36°54'41.94"N	-116°41'19.50"W	goethite, dolomite, muscovite
B-59	gravel deposit 2	"	"	goethite, zeolite
B-60	gravel deposit 3	"	"	quartz, sanidine
B-61	gravel deposit 4	"	"	goethite, dolomite
B-62	gravel deposit 5	"	"	dolomite
B-63	basalt 1	36°55'43.92"N	-116°43'20.66"W	albite, anorthite, augite
B-64	basalt 2	36°55'44.08"N	-116°43'21.34"W	albite, anorthite, augite
B-65	oxidized tuff	37°00'46.33"N	-116°43'43.10"W	goethite, orthoclase, quartz
B-66	gravel dump	36°59'29.46"N	-116°43'04.06"W	calcite, dolomite, muscovite, orthoclase, quartz
B-67	clay-ish talus	36°56'44.65"N	-116°43'12.67"W	goethite, montmorillonite

## XRD measurements for mineralogically unique rock samples

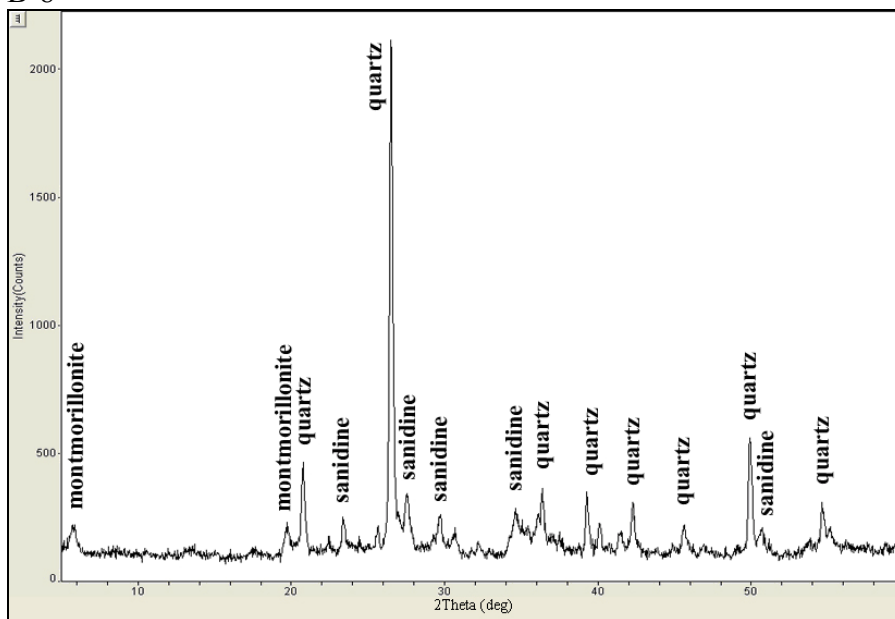
B-4



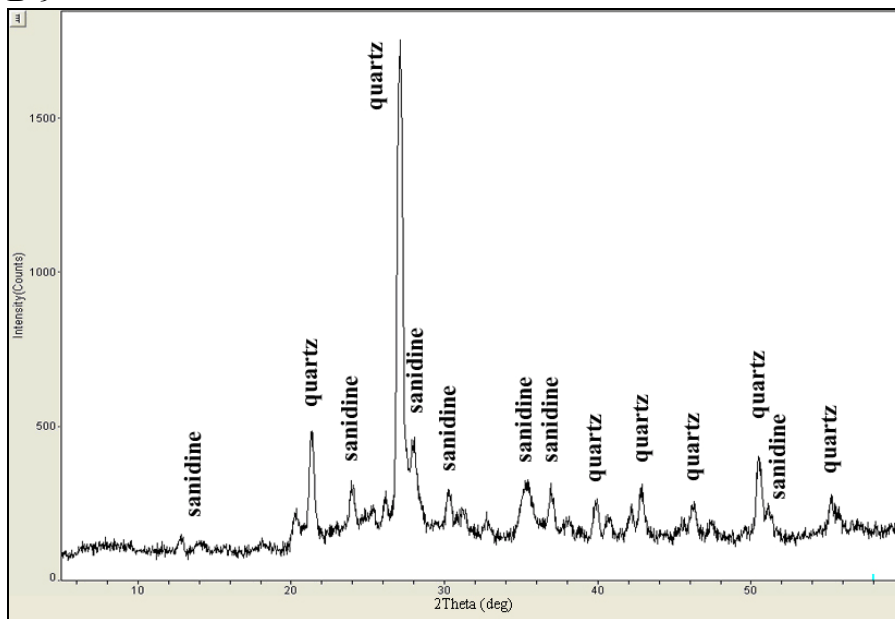
B-7



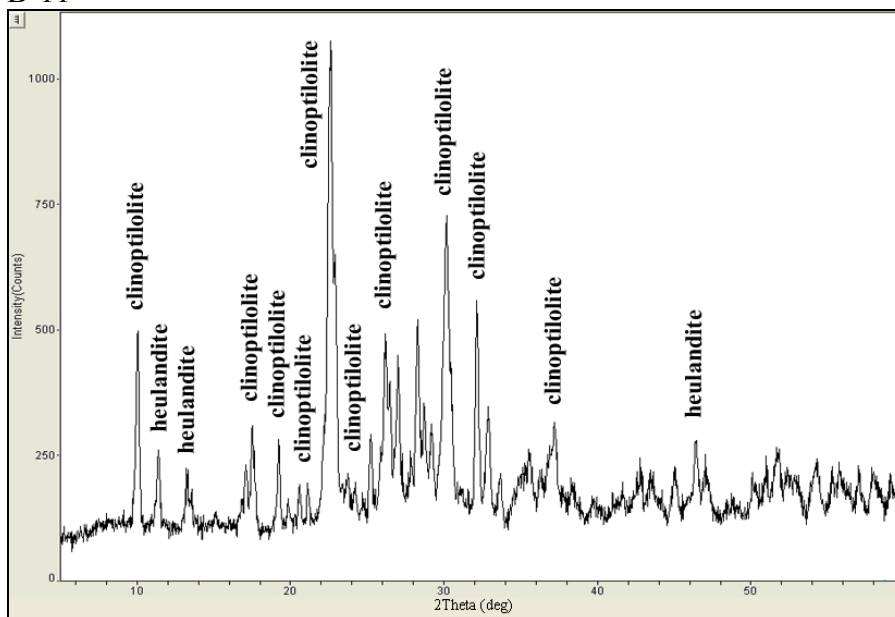
B-8



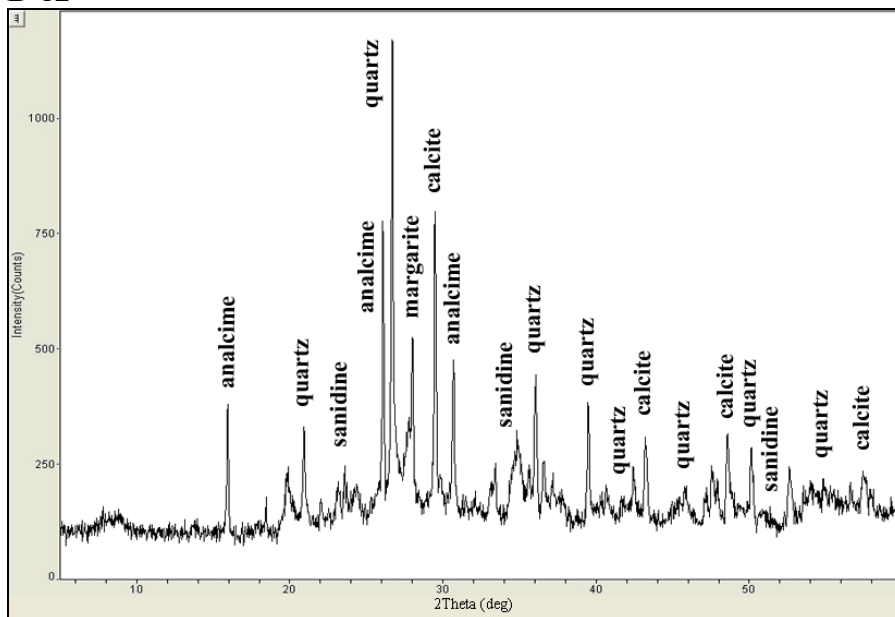
B-9



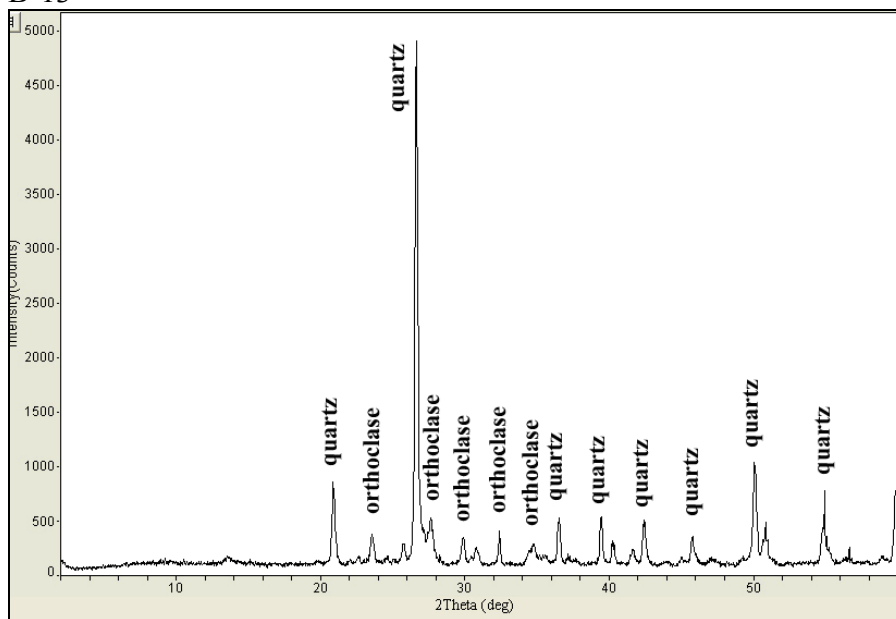
B-11



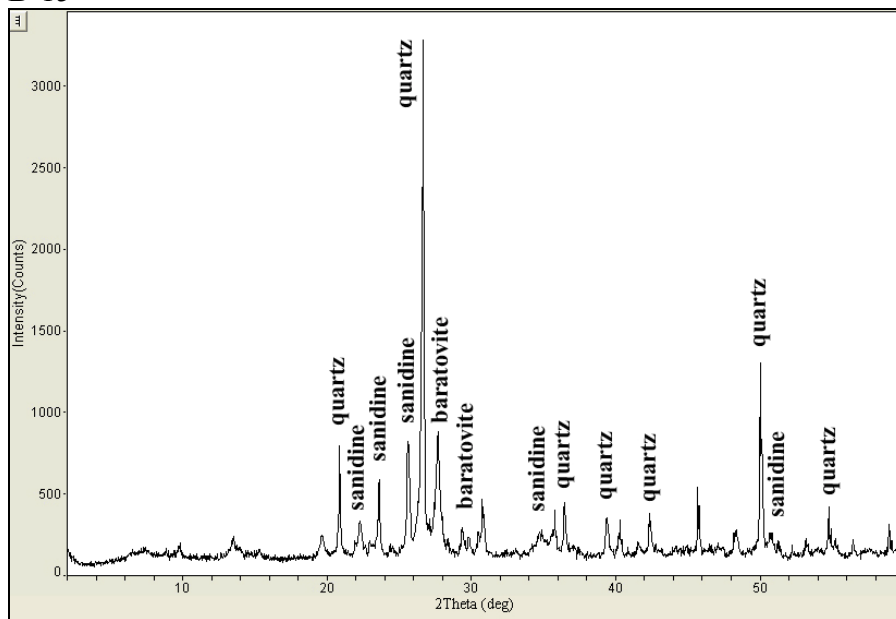
B-12



B-13



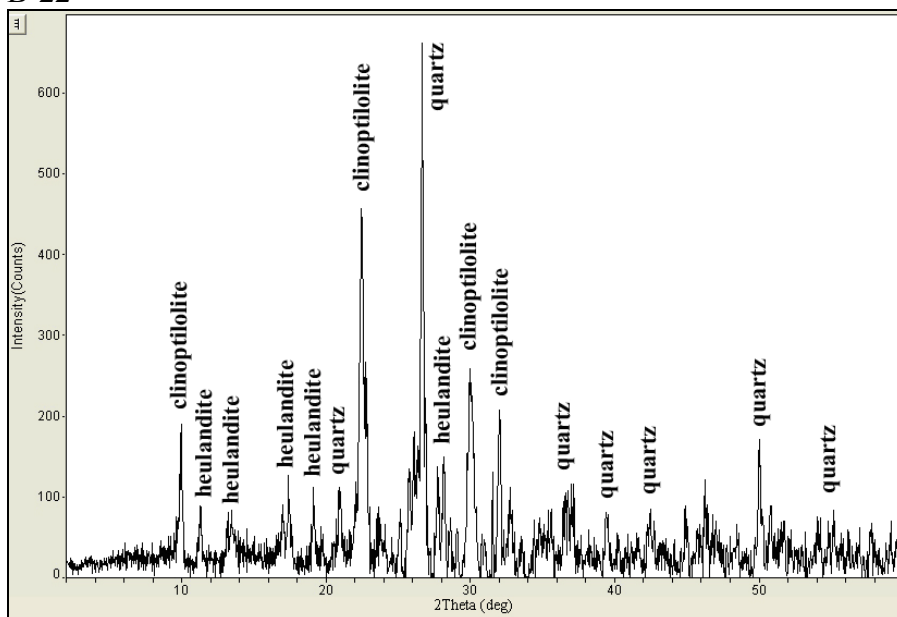
B-15



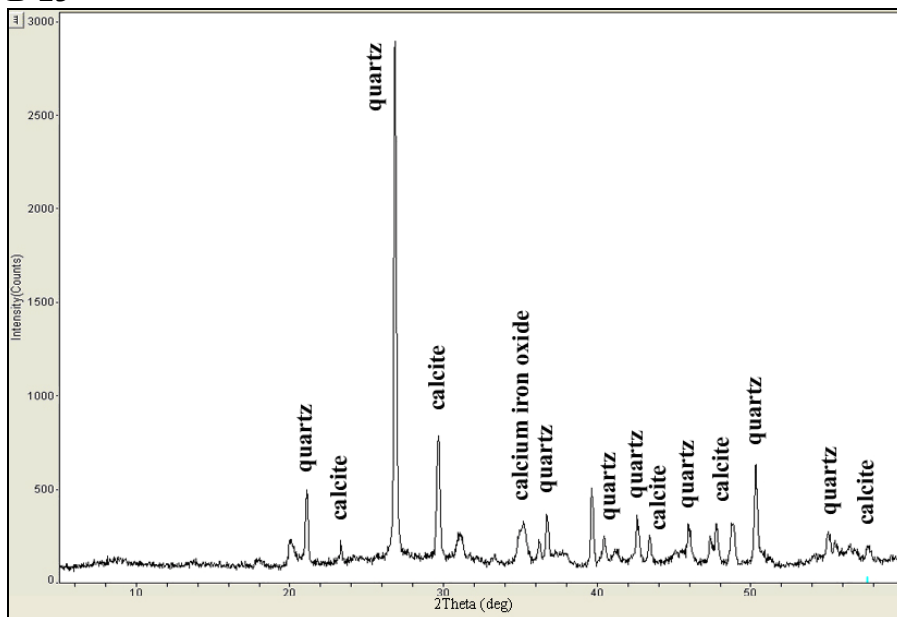




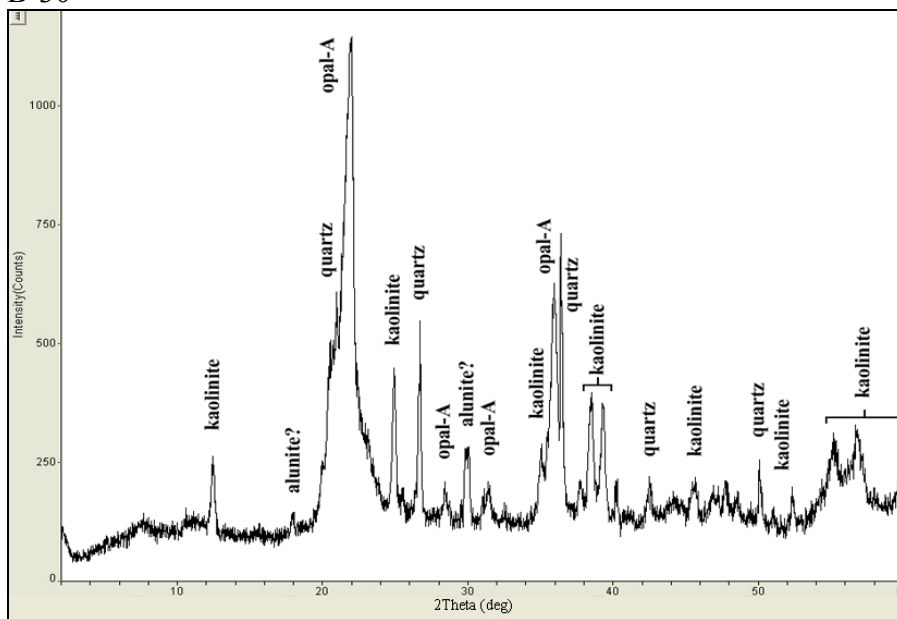
B-22



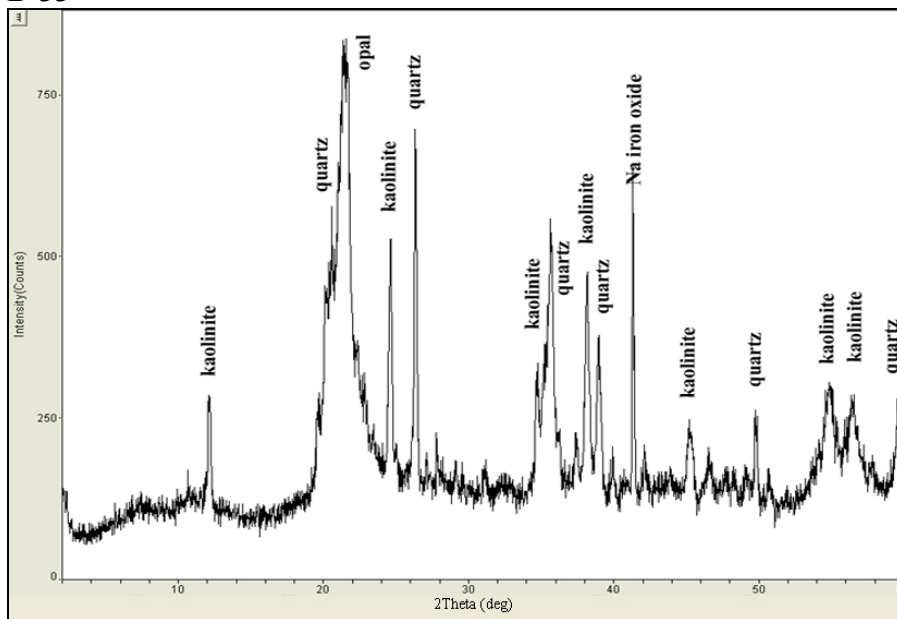
B-23



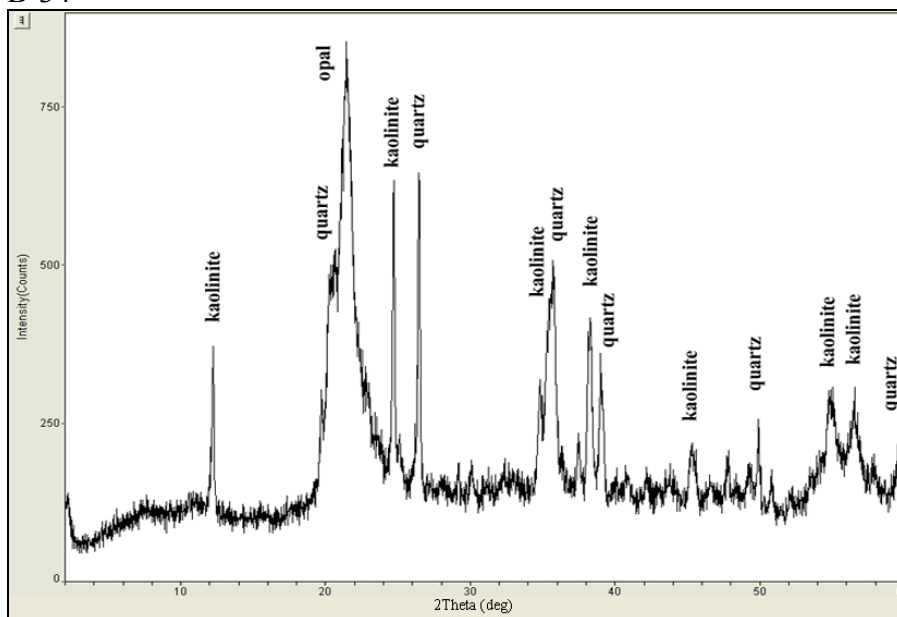
B-30



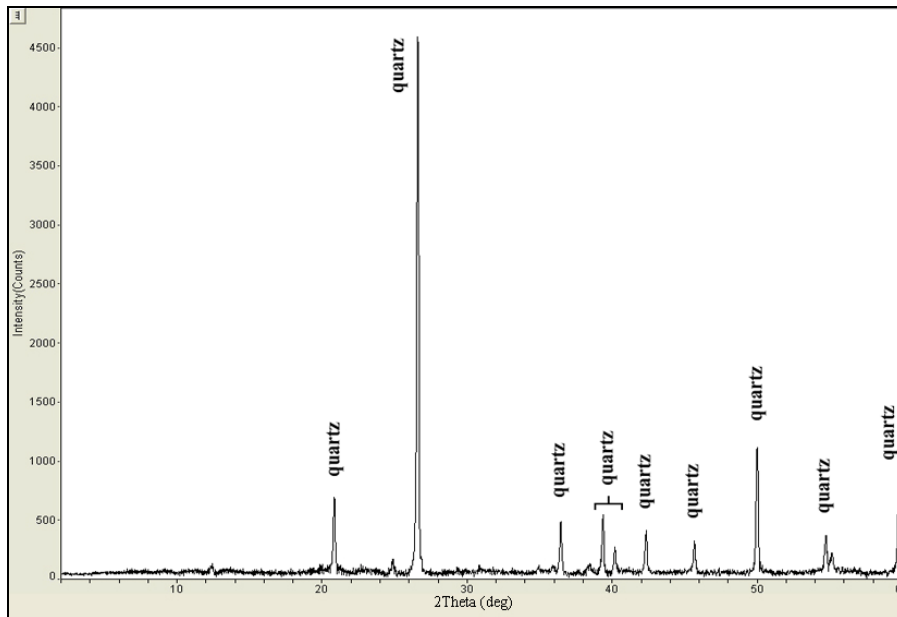
B-33



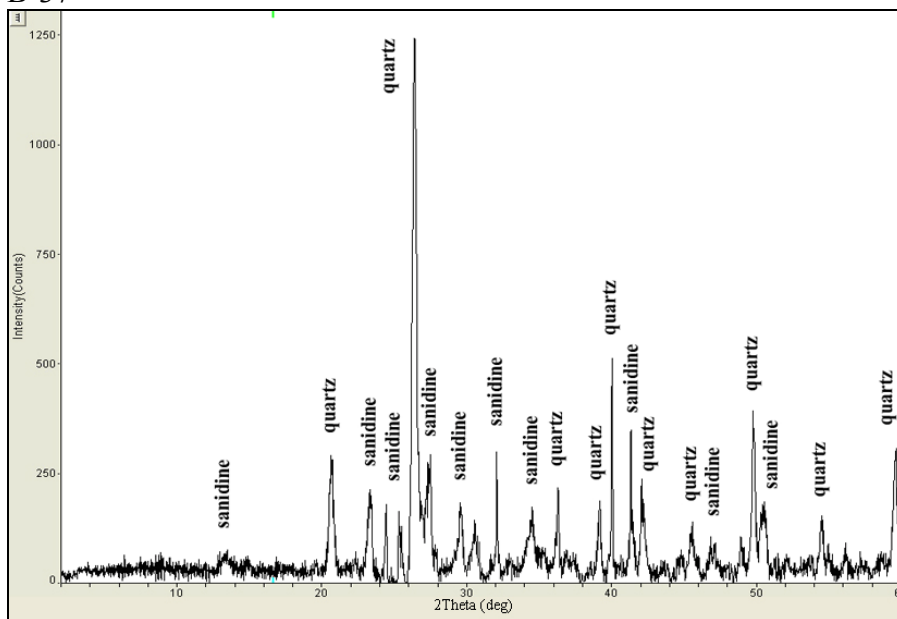
B-34



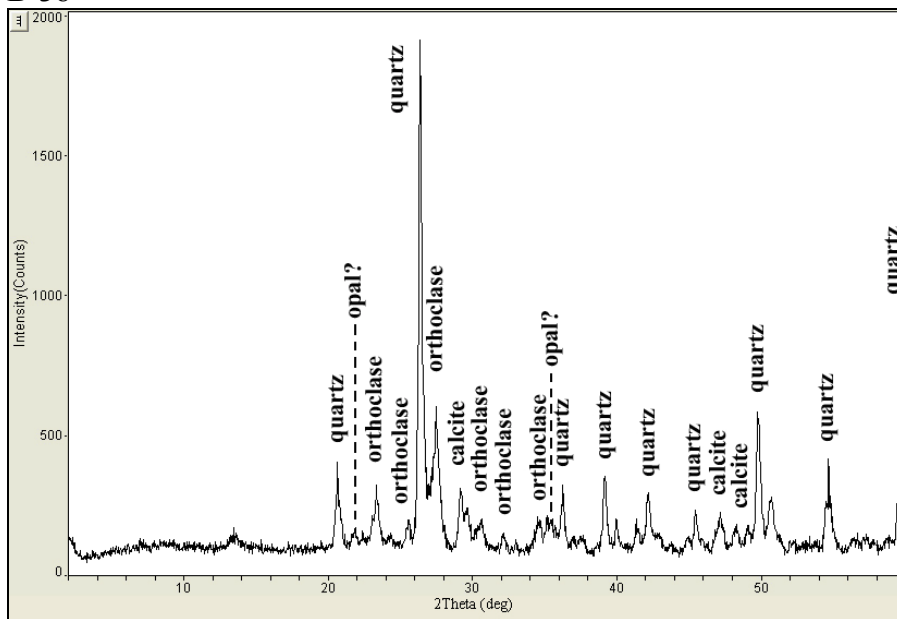
B-35



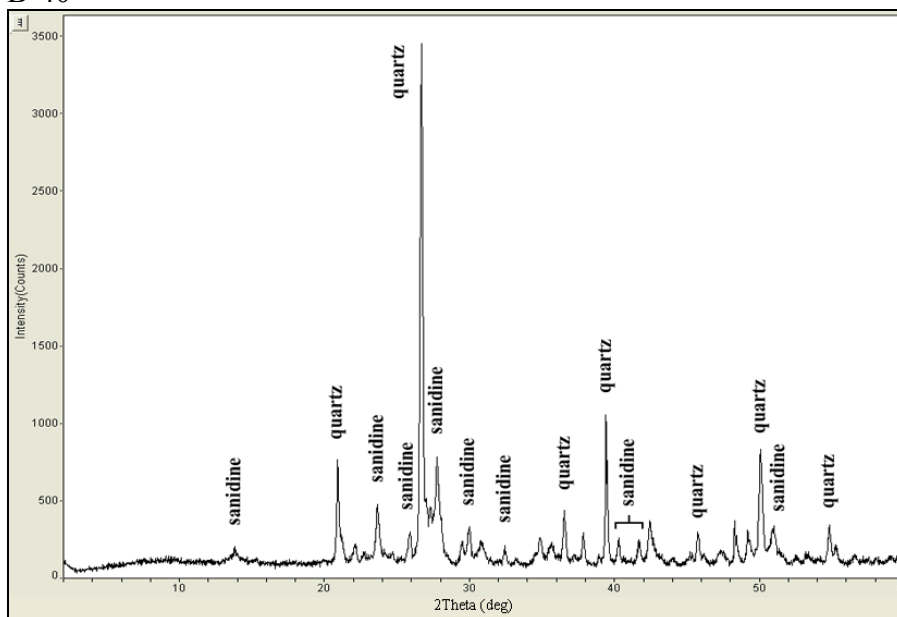
B-37



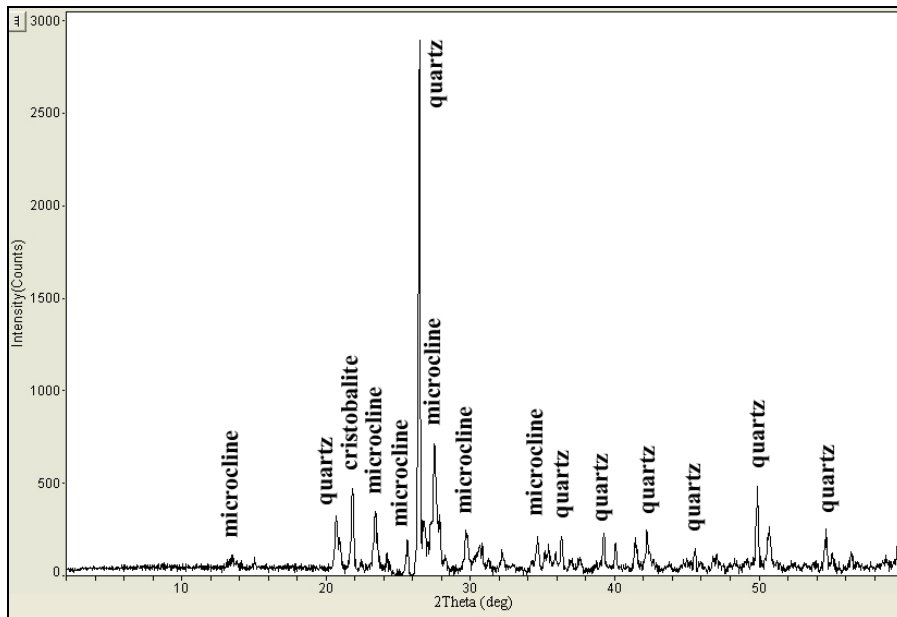
B-38



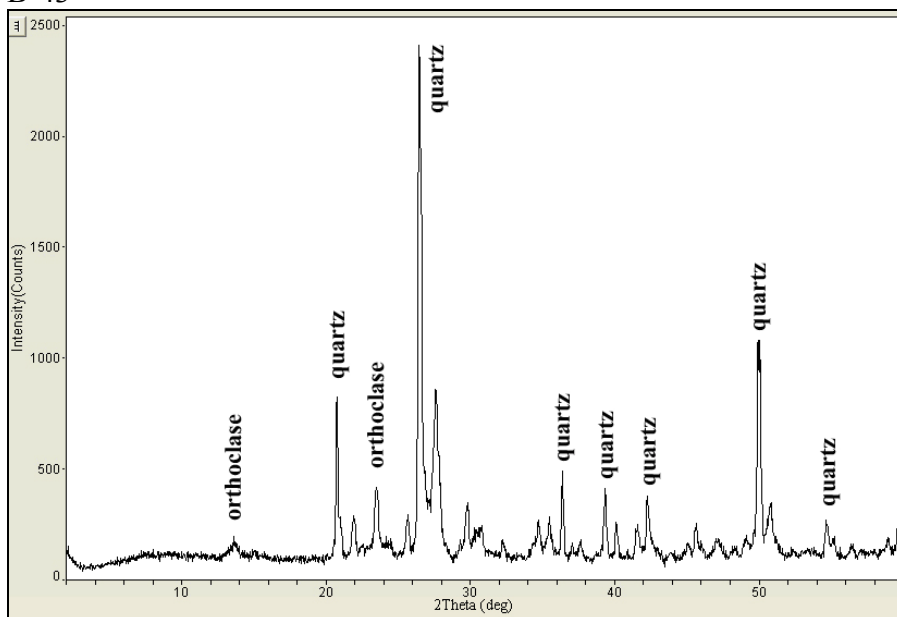
B-40



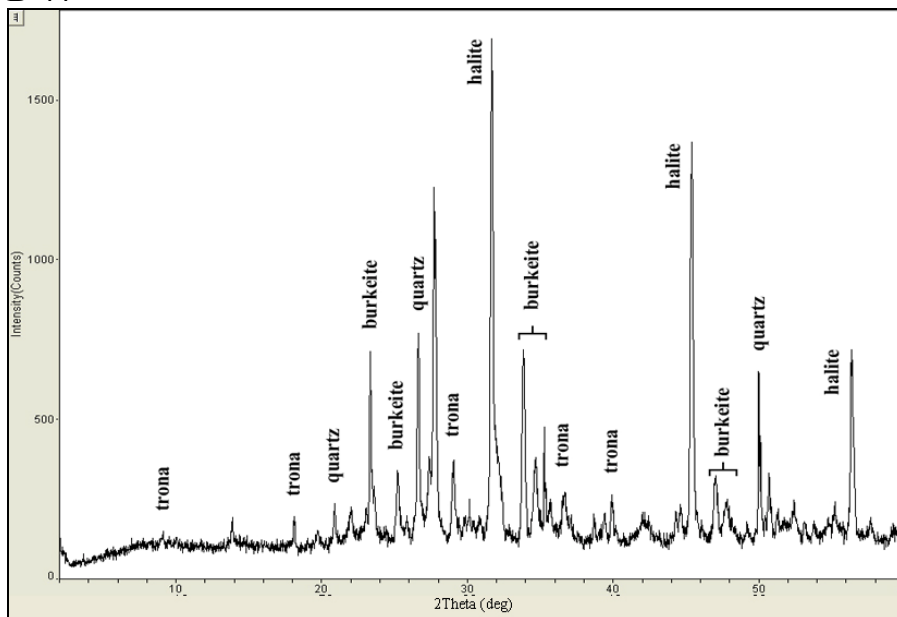
B-42



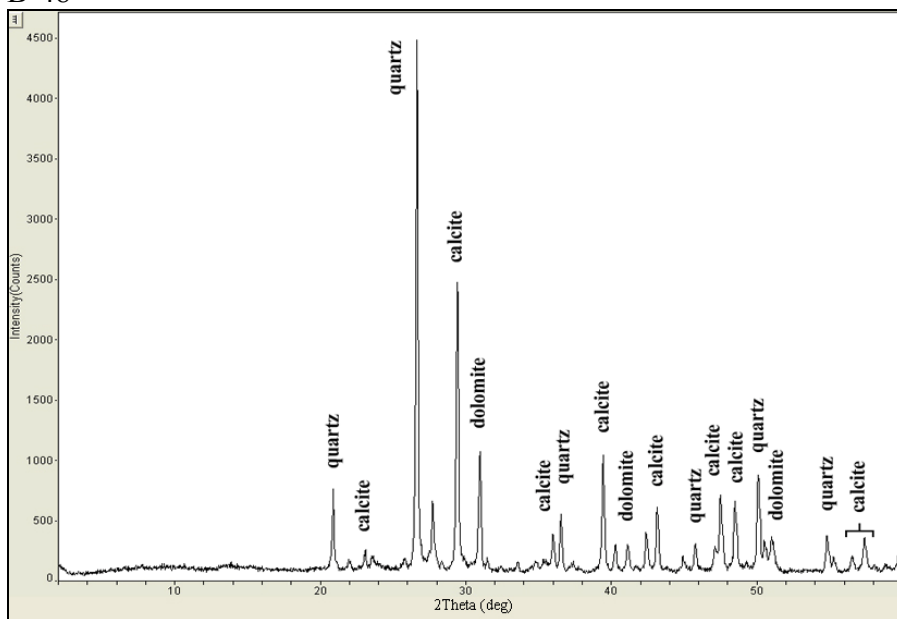
B-43



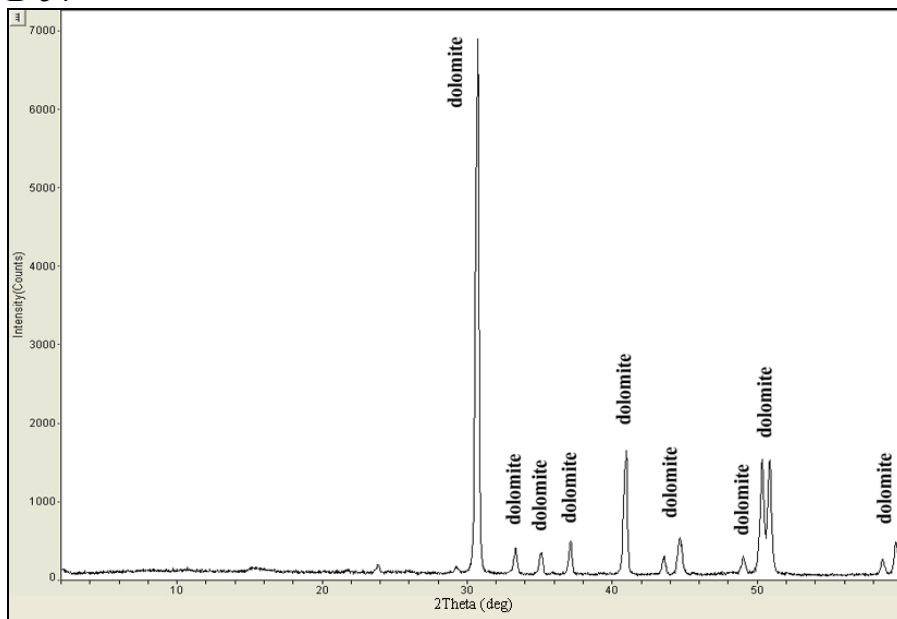
B-44



B-48

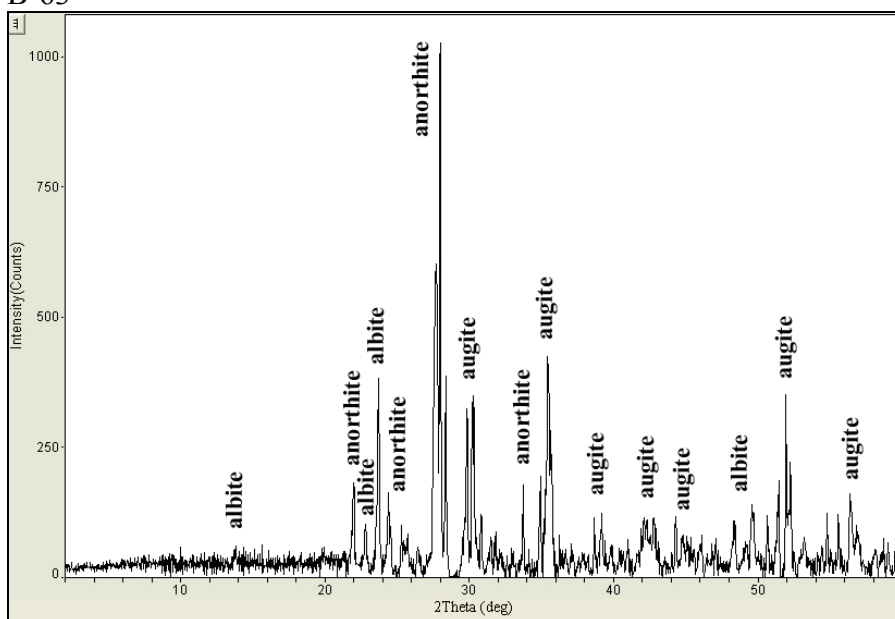


B-54

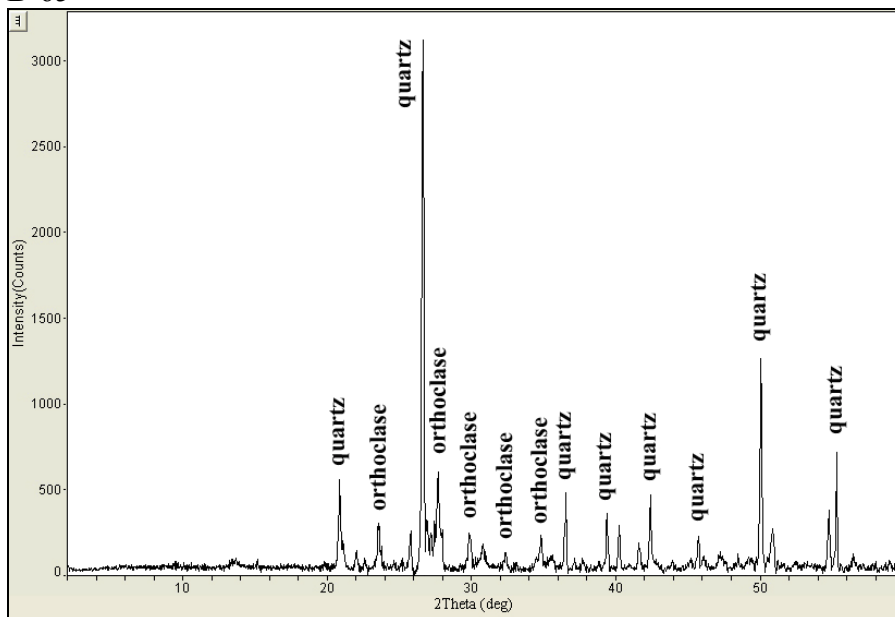




B-63



B-65



B-66

